FIRST MEASUREMENT OF FORM FACTORS OF THE BETA DECAY OF THE NEUTRAL XI HYPERON

BY

STEPHEN TALIAFERRO BRIGHT

JUNE 2000

U.S. Gov't Property

FERMILAB-THESIS-2000-21
Bright, Stephen Taliaferro
First measurement of form-factors
of the beta decay of the neutral
Xi hyperon

Gift Thesis Fermilab-Thesis-2000-21

THE UNIVERSITY OF CHICAGO

FERMILAB
LIBRARY

FIRST MEASUREMENT OF FORM FACTORS OF THE BETA DECAY OF THE NEUTRAL XI HYPERON

A DISSERTATION SUBMITTED TO
THE FACULTY OF THE DIVISION OF THE PHYSICAL SCIENCES
IN CANDIDACY FOR THE DEGREE OF
DOCTOR OF PHILOSOPHY

DEPARTMENT OF PHYSICS

BY
STEPHEN TALIAFERRO BRIGHT

CHICAGO, ILLINOIS
JUNE 2000

Abstract

We present the first measurement of the ratios of form factors g_1/f_1, $g_2/f_1$and $f_2/f_1$for the decay $\Xi^0 \to \Sigma^+ e^- \overline{\nu}_e$. Using the polarization of the Σ^+via the decay $\Sigma^+ \to p\,\pi^0$, and the $e^- - \overline{\nu}$ correlation, we measure $g_1/f_1$to be $1.32 \pm^{.21}_{.17} (stat) \pm .05(syst)$, assuming the absence of a second class current term $g_2/f_1$and the $SU(3)_f$ value of $f_2(2.6)$. Our value is consistent with exact $SU(3)_f$ symmetry. Relaxing the constraint $g_2/f_1 = 0$ we find no evidence for a second-class current term. From the energy spectrum of the electron in the Σ^+frame, we measure the weak magnetism term $f_2/f_1$to be $2.0 \pm 1.2(stat) \pm 0.5(syst)$, in agreement with the CVC hypothesis.

Acknowledgments

This result would not have been possible without the efforts of many different individuals. My deepest thanks go out to the members of the KTeV collaboration. I am especially indebted to my advisor Roland Winston for his guidance and patience over the last five years. I also owe a debt of gratitude to Yau Wah for serving on my thesis committee and helping me work through many challenging problems. I would also like to thank Thomas Rosenbaum and Peter Freund for rounding out my committee.

The other KTeV hyperon group regulars, consisting of Roland Winston, Earl Swallow, Nick Solomey, Emmanuel Monnier, Mark Timko, Doug Jensen, Erik Ramberg, Theo Alexopoulous, Albert Erwin, Ashkan Alavi-Harati put forth a tremendous amount of effort into making the KTeV hyperon program the success that it is.

My graduate school experience was certainly enhanced by the presence of my graduate student colleagues at Chicago, Peter Shawhan, Greg Graham, Eric Zimmerman, Breese Quinn, Colin Bown, Val Prasad, and Jim Graham, and I wish them the best. Special thanks to Ashkan Alavi-Harati and Eric Zimmerman for allowing me use of their drawings.

Finally, I would like to thank my family and friends for their support these last six years.

STEPHEN T. BRIGHT

Chicago, Illinois

June 2000

Table of Contents

Abstract ii

Acknowledgments iii

List of Figures viii

List of Tables xii

1 HYPERON BETA DECAYS AND $SU(3)_f$ 1
- 1.1 Quark Beta Decay . . . 1
- 1.2 Isopin Symmetry and the CVC Hypothesis . . . 1
- 1.3 $SU(3)_f$ and the Cabibbo Hypothesis . . . 5
- 1.4 $SU(3)_f$ Breaking and Experimental Data . . . 8
- 1.5 Theoretical Predictions for $\Xi^0 \to \Sigma^+ e^- \overline{\nu}_e$ . . . 8
  - 1.5.1 Predictions for g_1/f_1 . . . 8
  - 1.5.2 Predictions for g_2/f_1 . . . 9
  - 1.5.3 Predictions for f_2/f_1 . . . 10
- 1.6 Extraction of V_{us} from Hyperon Beta Decays . . . 10
- 1.7 Previous Experiments . . . 10

2 THE E799-II DETECTOR 12
- 2.1 The Primary Proton Beam . . . 12
- 2.2 The Hyperon (and K_L) Beams . . . 12
- 2.3 The Sweeping Magnets and Collimators . . . 13
- 2.4 The Decay Volume and Vacuum Window . . . 16
- 2.5 The Drift Chambers (DC) . . . 16
- 2.6 The Spectrometer Magnet . . . 17
- 2.7 The Transition Radiation Detectors (TRD) . . . 17
- 2.8 The Trigger Hodoscopes . . . 19
- 2.9 The Cesium Iodide Calorimeter (CsI) . . . 20
- 2.10 The Hole Counters and Hole Guards . . . 20
- 2.11 Photon Vetoes . . . 20
- 2.12 The Hadron Anti . . . 22
- 2.13 The Muon System . . . 24

3 THE 1997 E799-II SUMMER DATA SET AND HYPERON TRIGGERS 27
- 3.1 The Hyperon Triggers . . . 27
  - 3.1.1 Level 1 Hyperon Trigger Elements . . . 28
  - 3.1.2 Level 2 Hyperon Trigger Elements . . . 30
  - 3.1.3 Level 3 Hyperon Trigger Elements . . . 32

3.2 "Winter" and "Summer" Data 35
3.3 Runs Used 36
3.4 Reduction of the Data Samples (Crunch) 37

4 THE MONTE CARLO SIMULATION 38
4.1 Production of Ξ^0 38
4.2 Simulation of Decay Processes 39
4.3 Simulation of KTeV Detector Elements 39
4.3.1 Drift Chambers 39
4.3.2 Calorimeter 41
4.4 Accidental Overlays 41
4.5 Simulation of Hyperon Triggers 42
4.5.1 Hole Counters (HC) 42
4.5.2 Drift Chamber Fast Ors (DCFO) 42
4.5.3 Stiff Track Trigger (STT) 42
4.6 Simulation of Drift Chamber Inefficiencies and Hi-Sods 42

5 EVENT RECONSTRUCTION 44
5.1 Track Finding 44
5.1.1 Hit Pairs 44
5.1.2 Vertex Finding 45
5.1.3 Calibration of Chambers 46
5.2 Cluster Finding 47
5.2.1 Corrections to Cluster Energy and Position 48
5.2.2 Calorimeter Calibration 49

6 THE DECAY $\Lambda \to p\pi^-$ 50
6.1 Polarization of Λ 50
6.2 Reconstruction and Event Selection 50
6.3 Efficiency of Drift Chamber Fast Ors (DCFO) 54
6.4 Data / Monte Carlo Comparisons 56

7 THE DECAY $\Xi^0 \to \Lambda\pi^0$ WITH $\Lambda \to p\pi^-$ 61
7.1 Polarization of Ξ^0 61
7.2 Phenomenology of $\Xi^0 \to \Lambda\pi^0$ 61
7.3 Reconstruction and Event Selection 63
7.4 Events Lost Due to Bad Spills 67
7.5 Data / Monte Carlo Comparisons 70
7.6 Extraction of $\alpha_{\Xi^0}\alpha_\Lambda$from $\Xi^0 \to \Lambda\pi^0$ with $\Lambda \to p\pi^-$ 70
7.7 Other Physical Parameters of the Ξ^0 80
7.7.1 Ξ^0 Lifetime 80
7.7.2 Ξ^0 Mass 80

7.8 STT Random Accepts 82

8 THE DECAY $\Xi^0 \to \Sigma^+ e^- \overline{\nu}_e$ WITH $\Sigma^+ \to p\,\pi^0$ 87
8.1 Simulation of $\Xi^0 \to \Sigma^+ e^- \overline{\nu}_e$ Decays 87
8.1.1 Radiative Corrections to $\Xi^0 \to \Sigma^+ e^- \overline{\nu}_e$ 87
8.2 Reconstruction 90
8.3 Backgrounds 92
8.3.1 Background from Ξ^0 Decays 92
8.3.2 Background from Λ Decays 94
8.3.3 Background from K_L Decays 94
8.4 Event Selection 101
8.4.1 Backgrounds After Selection Criteria 105
8.5 Data / Monte Carlo Comparisons 105

9 EXTRACTION OF THE FORM FACTORS OF $\Xi^0 \to \Sigma^+ e^- \overline{\nu}_e$ 115
9.1 Kinematic Variables 115
9.2 Integrated Observables 115
9.3 Transverse Kinematic Variables 117
9.4 Extraction of g_1/f_1 119
9.4.1 Correcting for Background 120
9.5 Systematic Errors on g_1/f_1 120
9.5.1 Backgrounds 120
9.5.2 Residual Errors in Drift Chamber Alignment 126
9.5.3 Mass of the Ξ^0 126
9.5.4 $Z_{\Sigma^+} - Z_{\Xi^0}$ cut 126
9.5.5 HA 126
9.5.6 Lifetime of the Ξ^0 126
9.5.7 Neutral Energy Scale 128
9.5.8 TRD Inefficiency 128
9.5.9 $p^2_{\nu\|}$Cut 128
9.5.10 Measured CsI Non-orthogonality 128
9.5.11 Radiative Corrections 129
9.5.12 Beam Shape / Edges 129
9.5.13 Drift Chamber Inefficiency 129
9.5.14 Error on α_{Σ^+} 129
9.5.15 q^2Dependence of f_1 and g_1 131
9.5.16 Misc. Checks for g_1/f_1 131
9.6 Extraction of g_2/f_1 134
9.7 Extraction of $f_2/f_1$from Beta Spectrum 134

10 CONCLUSIONS 142
10.1 Results for g_1/f_1 142
10.2 Results for g_2/f_1 143
10.3 Results for f_2/f_1 143
10.4 Extraction of f_1 and g_1 Separately 143
10.5 Future Prospects 144

A APPENDIX A 146

B APPENDIX B 153
B.1 Hardware 153
B.2 STT Algorithm (Summer) 153
B.2.1 CAMAC Read/Write Bits 154
B.3 Integration With the KTeV Trigger System 155
B.4 STT Algorithm (Winter) 156
B.4.1 CAMAC Read/Write Bits for Winter STT 158

Bibliography 160

List of Figures

1.1 Feynman Diagrams for $n \to p\, e^- \overline{\nu}_e$ (top) and $\Xi^0 \to \Sigma^+ e^- \overline{\nu}_e$ (bottom). The only difference between the two is that the d quarks are replaced by s quarks. 2
1.2 The fundamental $SU(3)_f$ baryon octet. 7

2.1 Target, sweeping magnet and collimator elements in the KTeV target enclosure. 15
2.2 Diagram of TRD chamber and radiator. 18
2.3 The V and V' banks. These scintillator banks are used to trigger on decays with charged particles. 19
2.4 The CsI calorimeter consisting of 3100 50 cm long CsI crystals. The two beam holes allow the neutral beam (and protons from hyperon decays) to pass through. 21
2.5 Diagram of a Ring Counter. There detectors veto events where a photon leaves the detector volume at trigger level. 23
2.6 The Collar Anti (CA) viewed from the front, facing downstream. . . 24
2.7 The Hadron Anti (HA) vetoes events where a charged pion starts to shower in the lead wall in front of it. 25
2.8 The KTeV Detector 26

3.1 Wires instrumented by the beam region DC Fast Ors are in the shaded boxes. 31
3.2 Wires instrumented by the STT are indicated by large light dots. . . 33

4.1 The energy spectrum of Ξ^0 produced at the KTeV target, using equation (4.1). The filled histogram shows Ξ^0 that survive to $z = 90\, m$. 40
4.2 The efficiency of the hole counter paddles for the summer run, divided up into 4 slices in x and y. 43

5.1 Illustration of 'Corkscrew' rotation between chambers 1 and 2. . . . 47

6.1 The $\pi^+\pi^-$ mass - K_L mass for events passing $\Lambda \to p\pi^-$selection criteria. 53
6.2 The X position of the positive track at DC1 for trigger 12 $\Lambda \to p\pi^-$ decays. 55
6.3 Data-Monte Carlo comparison of the Λ vertex $p_\perp^2$(top) and $p\pi^-$ mass $-\Lambda$ mass (bottom)(the dots are data and the histogram is Monte Carlo) 57
6.4 Data-Monte Carlo comparison of x/z of the Λ vertices (top) and y/z of the Λ vertices (bottom)(the dots are data and the histogram is Monte Carlo). 58

6.5 Data-Monte Carlo comparison of Λ energy (top) and z position of the Λ vertex (bottom)(the dots are data and the histogram is Monte Carlo). 59
6.6 Data-Monte Carlo comparison of proton energy (top) and π^-energy (bottom)(the dots are data and the histogram is Monte Carlo). . . 60

7.1 The $\pi^+\pi^-\pi^0$mass for Data (dots) compared with the distribution for $\Xi^0 \to \Lambda\pi^0$ Monte-Carlo (histogram) and $K_L \to \pi^+\pi^-\pi^0$ Monte Carlo normalized to measured K_L flux (filled histogram). 65
7.2 The charged vertex $p_\perp^2$mass for Data (dots) compared with the distribution for $\Xi^0 \to \Lambda\pi^0$ Monte-Carlo (histogram). 66
7.3 The measured value of $\alpha_{\Xi^0}\alpha_\Lambda$for various Hi-SOD and chamber inefficiency map weights (top), and the Data / MC slope in Ξ^0 z vertex position (bottom). 68
7.4 Data-Monte Carlo comparison of the z positions of the Ξ^0 (top) and Λ vertices (bottom) (the dots are data and the histogram is Monte Carlo) 71
7.5 Data-Monte Carlo comparison of the proton (top) and π^-energies (bottom) (the dots are data and the histogram is Monte Carlo) 72
7.6 Data-Monte Carlo comparison of the π^0(top) and Ξ^0 energies (bottom)(the dots are data and the histogram is Monte Carlo) 73
7.7 Data-Monte Carlo comparison of x/z of the Ξ^0 vertices (top) and Λ vertices (bottom) (the dots are data and the histogram is Monte Carlo). 74
7.8 Data-Monte Carlo comparison of y/z of the Ξ^0 vertices (top) and Λ vertices (bottom) (the dots are data and the histogram is Monte Carlo). 75
7.9 Data-Monte Carlo comparison of x (top) and y (bottom) positions of the photons at the CsI (the dots are data and the histogram is Monte Carlo). 76
7.10 Data-Monte Carlo comparison of the charged vertex $p_\perp^2$(top), and the $\log p_\perp^2$ for the Ξ^0 vertex (bottom) (the dots are data and the histogram is Monte Carlo). 77
7.11 Data / Monte Carlo comparison of the number of $\Xi^0 \to \Lambda\pi^0$ events found in each run listed (in ascending order, excluding run 10957) in section 3.3 (the dots are data and the histogram is Monte Carlo). 78
7.12 Acceptance corrected $(-\hat{p}\cdot\hat{\pi^0})^\Lambda$ distribution for $\Xi^0 \to \Lambda\pi^0$. 79
7.13 Data-Monte Carlo comparison of the z positions of the Ξ^0 vertices with the default Monte Carlo (top), and with Monte Carlo $c\tau$increased by 5 % (bottom). 81

7.14 The proton π^-mass minus the Λ mass for all events passing the selection criteria. The top plot is data and the bottom plot is Monte Carlo. 83
7.15 The Λ π^0mass minus the Ξ^0 mass for all events passing the selection criteria. The top plot is data and the bottom plot is Monte Carlo. . 84
7.16 The Ξ^0 mass $-1315MeV/c^2$ as a function of the $\pi^-\gamma$ separation cut. The circles are data, and the squares are Monte Carlo. 85
7.17 The Ξ^0 mass $-1315MeV/c^2$ as a function of the $\pi^-\gamma$ separation cut, for $\Xi^0 \to \Lambda\pi^0$ events where the π^-deposited less than $1GeV$ of energy in the CsI. The circles are data, and the squares are Monte Carlo. . 86

8.1 The Monte Carlo generated spectrum of the energy of the e^-in the Σ^+frame. 91
8.2 Data (dots) / Monte Carlo (histogram) comparison for $K_L \to \pi^+\pi^-\pi^0$ mass for B11 $K_L \to \pi^+\pi^-\pi^0$ candidates (Top). Also shown are comparisons for total K_L energy (bottom left) and K_L z vertex position (bottom right). 96
8.3 $K_L \to \pi^+\pi^-\pi^0$ mass distribution 98
8.4 $K_L \to \pi^0\pi^+e^-\overline{\nu}_e$ Background 99
8.5 $K_L \to \pi^+e^-\overline{\nu}_e$ background and $p^2_{\nu\|}$distribution. 100
8.6 Data / Monte Carlo comparison of *Brem* (described in the text). . 102
8.7 Data and Monte Carlo background, based on measured K_L and Ξ^0 flux. All selection criteria have been applied. 106
8.8 Data and Monte Carlo background, based on measured K_L and Ξ^0 flux. All selection criteria have been applied, expect events having $p^2_{\nu\|} < 0$ are kept. 107
8.9 Data-Monte Carlo comparison of the z positions of the Σ^+(top) and Ξ^0 vertices (bottom). 108
8.10 Data-Monte Carlo comparison of x/z of the Ξ^0 vertices (top) and y/z of the Ξ^0 vertices (bottom). 109
8.11 Data-Monte Carlo comparison of the proton (top) and e^-energies (bottom). 110
8.12 Data-Monte Carlo comparison of the π^0(top) and Ξ^0 energies (bottom). 111
8.13 Data-Monte Carlo comparison of the difference between the Ξ^0 and Σ^+z vertex positions (top) and total Ξ^0 $p^2_\perp$(bottom). 112
8.14 Data-Monte Carlo comparison of x (top) and y (bottom) positions of the photons at the CsI. 113

9.1 Maximum Likelihood fit to g_1/f_1corrected for background. 121
9.2 g_1/f_1Comparison of DATA-MC distributions of $x^{[\Sigma]}_{pe}$, $x^{[Q]}_{p\nu\perp}$and $x^{[Q]}_{e\nu\perp}$(MC generated with $g_1/f_1 = 1.27$). 122

9.3 Background Correction to g_1/f_1, the filled circles are the corrections found with the MC background with the high momentum track being positive. 123
9.4 Background Correction to g_1/f_1, the filled circles are the corrections found with the MC background with the high momentum track being negative (for K_L background). 124
9.5 The background correction to $g_1/f_1$is evaluated by taking the mean of the corrections from the 4 background sets to the 90 Monte Carlo data sized datasets (360 total). 125
9.6 OFFMAG for $\Xi^0 \to \Lambda\pi^0$ events. 127
9.7 Beam shape for $\Xi^0 \to \Lambda\pi^0$ events. 130
9.8 The measured value for g_1/f_1as a function of the $p^2_{\nu||}$cut (top), and a function of the $z_{\Sigma^+} - z_{\Xi^0}$ cut (bottom). 132
9.9 The measured value for $g_1/f_1$with different selection criteria. 133
9.10 Confidence interval plot for g_1/f_1-g_2/f_1. 135
9.11 Extraction of f_2/f_1using maximum likelihood of energy spectrum of electron in Σ^+frame ($E_e^{[\Sigma]}$). 137
9.12 Energy spectrum of electron in Σ^+frame ($E_e^{[\Sigma]}$). 138
9.13 The measured value for f_2/f_1as a function of the $p^2_{\nu||}$cut (top), and a function of the $z_{\Sigma^+} - z_{\Xi^0}$ cut (bottom). 139
9.14 The measured value for f_2/f_1as a function of different selection criteria. 140

10.1 Confidence interval plot for f_1 and g_1. 145

A.1 Integrated observable quantities for the decay $\Xi^0 \to \Sigma^+ e^- \overline{\nu}_e$ as a function of g_1/f_1. 152

B.1 STT Winter Algorithm 157

List of Tables

1.1 Predictions for g_1/f_1 9

2.1 Strength and Precession of Ξ^0 from Sweeping Magnets in figure 2.1. 14

3.1 The 1996-1997 KTeV Run 28

6.1 Bits used to reject bad spills for $\Lambda \to p\pi^-$and $\Xi^0 \to \Lambda\pi^0$ candidate events 51
6.2 Λ flux 54

7.1 Ξ^0 flux 67
7.2 Ξ^0 Events Lost Due to Bad Spills 69
7.3 Systematic Error for $\alpha_{\Xi^0}\alpha_\Lambda$ 70
7.4 STT Acceptance for $\Xi^0 \to \Lambda\pi^0$ events with the STT random accept bit set. 82

8.1 Number of Ξ^0 decays 92
8.2 Number of Λ decays estimated to occur during the Summer E799 run. 94
8.3 Number of K_L decays estimated to occur during the Summer E799 run (for $E_K > 100\,GeV$). 101
8.4 Bits used to reject bad spills for $\Xi^0 \to \Sigma^+ e^- \overline{\nu}_e$ (in addition to those in Table 2). 101
8.5 Tabulated Background where events with unphysical neutrino momentum are kept. 105
8.6 Tabulated Background where events with unphysical neutrino momentum are excluded. 114

9.1 Variation of $g_1/f_1$with M_V and M_A 131
9.2 Systematic Error for g_1/f_1 134
9.3 Changes in Data Selection criteria. The fit using the 'Old' x(t) maps only obtains g_1/f_1in increments of .02. 136
9.4 Systematic Error for g_2/f_1 141
9.5 Systematic Error for f_2/f_1 141

10.1 Predictions for g_1/f_1 142

B.1 Description of STT front panel inputs and outputs. C0 refers to signals mapped from drift chamber 1, etc. 154
B.2 CAMAC Read/Write bits for STT (Summer) 155
B.3 CAMAC Read/Write bits for STT (Winter) 158

Chapter 1

HYPERON BETA DECAYS AND $SU(3)_f$

Hyperon beta decays provide an excellent laboratory for the study of the details of the strong interaction, and for testing our understanding of the weak interaction. Experimentally, they are the closest thing we have to quark beta decay, in that both the baryons and quarks have spin 1/2. Although baryons are very complicated objects, the fact that the up (u), down (d) and strange (s) quarks are close in mass indicates a symmetry between them, and hence a symmetry in the interactions of the baryons made of u, d and s quarks (referred to as $SU(3)_f$).

1.1 Quark Beta Decay

The beta decay of the neutral Xi hyperon (usually called 'cascade zero', written as Ξ^0) produces a positively charged Sigma hyperon (called 'sigma plus', written as Σ^+), an electron (e^-) and an electron anti-neutrino ($\overline{\nu}_e$). The fundamental interaction ($s \rightarrow u\, e^- \overline{\nu}_e$) proceeds through a virtual W^- as in figure 1.1.

1.2 Isopin Symmetry and the CVC Hypothesis

The phenomenology for hyperon beta decays is rooted in the unification of the electromagnetic and weak interactions. Following Commins [1] we consider the electromagnetic proton transition current.

$$\langle \Psi_p(p') \mid J^{\mu}_{EM} \mid \Psi_p(p) \rangle = e\, \overline{u}_p(p')[C_p(q^2)\gamma^{\mu} + \frac{K_p(q^2)}{M_p}\sigma^{\mu\nu}q_{\nu} + \frac{F_{3p}(q^2)}{M_p}q^{\mu}]u_p(p) \quad (1.1)$$

where M_p is proton mass and $q = p - p'$ is the most general vector interaction (We will use the convention of reference [2] throughout for the γ matrices, spinors, and form factors). The vanishing of the divergence of the electromagnetic current will force

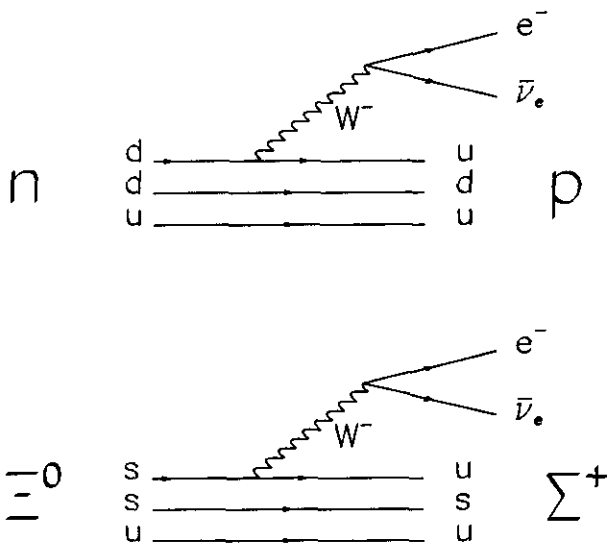

Figure 1.1: Feynman Diagrams for $n \to p\, e^- \, \overline{\nu}_e$ (top) and $\Xi^0 \to \Sigma^+ \, e^- \, \overline{\nu}_e$ (bottom). The only difference between the two is that the d quarks are replaced by s quarks.

$$F_{3p}(q^2) = 0 \tag{1.2}$$

In order to recover the correct charge and anomalous magnetic moment, we must have $C_p(0) = 1$ and $K_p = (\mu_p - \mu_0)/(2\mu_0)$, where μ_p is the proton's magnetic moment, $\mu_p = 2.79\mu_0$, and $\mu_0 =\mid e \mid \hbar/2M_pc$.

For the neutron, we have:

$$\langle \Psi_n(p') \mid J^{\mu}_{EM} \mid \Psi_n(p) \rangle = e\,\overline{u}_n(p')[C_n(q^2)\gamma^{\mu} + \frac{K_n(q^2)}{M_p}\sigma^{\mu\nu}q_{\nu}]u_n(p) \tag{1.3}$$

with $C_n(0) = 0$ and $K_n = \mu_n/(2\mu_0)$, $\mu_n = -1.91\mu_0$.

The neutron and proton can be regarded as the $-1/2$ and $+1/2$ components of an iso-doublet.

$$\frac{1}{2}(1+\tau_3)u = u_p \tag{1.4}$$

$$\frac{1}{2}(1-\tau_3)u = u_n \tag{1.5}$$

$$\tag{1.6}$$

Here τ_3 is the 3rd component if isospin, and the electromagnetic current is

$$\begin{aligned}\langle \Psi(p') \mid J^{\mu}_{EM} \mid \Psi(p) \rangle &= e\,u(p')[\frac{1}{2}(C_n(q^2) + C_p(q^2))\gamma^{\mu} + \frac{K_n(q^2) + K_p(q^2)}{M_p}\sigma^{\mu\nu}q_{\nu} \\ &+ [(C_p(q^2) - C_n(q^2))\gamma^{\mu} \\ &+ \frac{K_p(q^2) - K_n(q^2)}{M_p}\sigma^{\mu\nu}q_{\nu}]\tau_3]u(p)\end{aligned} \tag{1.7}$$

The weak current between the proton and neutron states is constructed from the most general $V - A$ interaction:

$$\langle \Psi_p(p') \mid J^{\mu}_{W} \mid \Psi_n(p) \rangle = \frac{G_F}{\sqrt{2}}V_{ud}\overline{u}(p')[f_1\gamma^{\mu} + \frac{f_2}{M_B}\sigma^{\mu\nu}q_{\nu} + \frac{f_3}{M_B}q^{\mu}$$

$$+ \quad (g_1\gamma^\mu + \frac{g_2}{M_B}\sigma^{\mu\nu}q_\nu + \frac{g_3}{M_B}q^\mu)\gamma_5]\tau_+ \, u(p) \tag{1.8}$$

We obtain the most general transition amplitude for the semileptonic decay of a spin 1/2 baryon ($B \to b\, e^- \, \overline{\nu}_e$):

$$\mathcal{M} = G_F V_{CKM} \frac{\sqrt{2}}{2} \overline{u}_b (O^V_\alpha + O^A_\alpha) u_B \overline{u_e} \gamma^\alpha (1+\gamma_5) v_\nu + H.c., \tag{1.9}$$

where

$$\begin{aligned} O^V_\alpha &= f_1\gamma_\alpha + \frac{f_2}{M_B}\sigma_{\alpha\beta}q^\beta + \frac{f_3}{M_B}q_\alpha, \\ O^A_\alpha &= (g_1\gamma_\alpha + \frac{g_2}{M_B}\sigma_{\alpha\beta}q^\beta + \frac{g_3}{M_B}q_\alpha)\gamma_5, \\ q^\alpha &= (p_e + p_\nu)^\alpha = (p_B - p_b)^\alpha, \end{aligned} \tag{1.10}$$

G_F is the Fermi Constant ($1.16639 \times 10^{-5} GeV^{-2}$), and V_{CKM} is the appropriate CKM matrix element. For strangeness changing decays, V_{CKM} is V_{us}, which is approximately equal to the sine of the Cabibbo angle ($V_{us} \approx \sin(\theta_C) \approx .22$). For strangeness conserving decays, V_{CKM} is V_{ud}, ($V_{ud} \approx \sqrt{1 - \mid V_{us} \mid^2}$).

The CVC hypothesis states that the vector part of the weak current is in the same triplet as the isovector part of the electromagnetic current, therefore:

$$f_1(q^2) = C_p(q^2) - C_n(q^2) = 1 \tag{1.11}$$

$$f_2(q^2) = K_p(q^2) - K_n(q^2) = 1.8 \tag{1.12}$$

$$f_3(q^2) = 0 \tag{1.13}$$

Although no such connection exists for the weak axial vector current, we can further constrain the axial vector form factors. For example, no effect from a g_3 term will be visible, as the form factors f_3 and g_3 will always have contributions proportional to $\frac{M_e^2}{M_B(M_B - M_b)}$ ($\approx 1.6 \times 10^{-6}$ for $\Xi^0 \to \Sigma^+ \, e^- \, \overline{\nu}_e$). We will therefore neglect the presence of a g_3 term.

Furthermore, the g_2 is constrained by $\mathcal{G}$ parity. The weak currents are classified as first-class if

$$\mathcal{G}O^V_\alpha\mathcal{G}^{-1} = O^V_\alpha \tag{1.14}$$
$$\mathcal{G}O^A_\alpha\mathcal{G}^{-1} = -O^A_\alpha \tag{1.15}$$

and second class if

$$\mathcal{G}O^V_\alpha\mathcal{G}^{-1} = -O^V_\alpha \tag{1.16}$$
$$\mathcal{G}O^A_\alpha\mathcal{G}^{-1} = O^A_\alpha, \tag{1.17}$$

where the $\mathcal{G}$ parity operator is constructed from the charge conjugation operator $\mathcal{C}$, and a rotation about the 2nd component of isospin (I_2)

$$\mathcal{G} = \mathcal{C}\exp i\pi I_2. \tag{1.18}$$

The first class currents are f_1, g_1, f_2 and g_3. The terms g_2 and f_3 are second class. The strong interaction preserves $\mathcal{G}$ parity , and second class weak currents do not naturally occur in the quark model [2]. However, small non-zero second class current terms may be induced by the electromagnetic interaction, since the electromagnetic interaction violates $\mathcal{G}$ parity.

Assuming the absence of second class current terms, there is only the g_1 term that is left undetermined.

1.3 $SU(3)_f$ and the Cabibbo Hypothesis

The Cabibbo Theory can be regarded as an extension of CVC hypothesis to the fundamental baryon octet.

As the states can be described in an $SU(2)$ algebra, the lowest energy u, d, s baryons form an $SU(3)$ octet. The weak hadronic current transforms according to

the eightfold representation of $SU(3)$, and the vector part of the weak hadronic current is in the same octet as the electromagnetic current.

A consequence of the transformation properties is that any operator can be expressed as

$$\langle B_j \mid O_k \mid B_l \rangle = i f_{jkl} F + d_{jkl} D \tag{1.19}$$

For the fundamental baryon octet, in the limit of exact $SU(3)_f$ symmetry, any one of the form factors is given by:

$$\begin{aligned} f_i &= C(B,b)_F * F_i + C(B,b)_D * D_i \\ g_i &= C(B,b)_F * F_{i+3} + C(B,b)_D * D_{i+3} \end{aligned} \tag{1.20}$$

Where $C(B,b)_F$ and $C(B,b)_D$ act as Clebsch-Gordan coefficients [2]. For the decays $\Xi^0 \to \Sigma^+ e^- \overline{\nu}_e$ and $n \to p e^- \overline{\nu}_e$ we have $C(B,b)_F = 1$ and $C(B,b)_D = 1$. Thus, in this limit, the decay $\Xi^0 \to \Sigma^+ e^- \overline{\nu}_e$ should have the same form factors as $n \to p e^- \overline{\nu}_e$. Deviations from this exact symmetry should arise from the mass and charge difference between the quarks. Details of $SU(3)_f$ breaking can be studied through the experimental determination of the form factors.

In this framework, assuming the absence of second class currents, a measurement of g_1 for any two beta decays with different $C(B,b)_F$ or $C(B,b)_D$ would completely determine the form factors for all of the beta decays. The ratios g_1/f_1, g_2/f_1, and f_2/f_1can be found from the kinematic distributions. The total rate for the process must be known in order to extract the value of f_1. The observed hyperon beta decays are shown in figure 1.2 with the appropriate F and D coefficients.

Thus, we have a way to describe the decays of strongly interacting particles without understanding any details of the strong interaction. The prediction for the form factors for the decay $\Xi^0 \to \Sigma^+ e^- \overline{\nu}_e$ is nearly almost 40 years old.

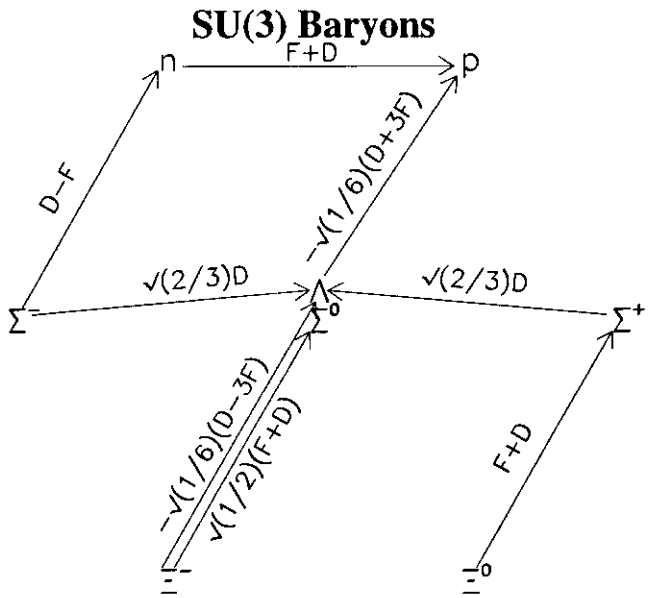

Figure 1.2: The fundamental $SU(3)_f$ baryon octet.

1.4 $SU(3)_f$ Breaking and Experimental Data

Of course, knowing that the u, d and s quarks which make up the baryons have different masses and charges, we might expect some deviation of the form factors from exact $SU(3)_f$ symmetry. Additionally, understanding the deviations of the form factors from their exact $SU(3)_f$ values can give same information about the details of the strong interaction.

The form factors can be measured by measuring the rates and angular distributions of the decay products.

Of the 12 allowed beta decays, the processes $\Sigma^0 \to pe^-\overline{\nu}_e$, $\Sigma^0 \to \Sigma^+e^-\overline{\nu}_e$, $\Sigma^- \to \Sigma^0e^-\overline{\nu}_e$, and $\Xi^- \to \Xi^0e^-\overline{\nu}_e$ are not likely to be observed in the near future, as their predicted branching ratios are all $< 10^{-10}$.

Using the remaining 7 observed decay rates and their angular distributions, we can fit for F_4 and D_4 to see how the well the exact $SU(3)_f$ predictions are matched. The $SU(3)_f$ fit in Ref. [24] gives a χ^2 of 62.3 for 23 degrees of freedom. This indicates that either one or more of the previous experiments is incorrect or that there is some symmetry breaking.

Various theoretical models attempt to describe the $SU(3)_f$ breaking. These models attempt to understand the strong interaction dynamics and the internal structure of the baryons.

1.5 Theoretical Predictions for $\Xi^0 \to \Sigma^+ e^- \overline{\nu}_e$

1.5.1 Predictions for g_1/f_1

In the limit of exact $SU(3)_f$ symmetry, $g_1/f_1$for $\Xi^0 \to \Sigma^+ e^- \overline{\nu}_e$ should be the same as for $n \to p e^- \overline{\nu}_e$. The Particle Data Group [10] value for $g_1/f_1$is 1.2670 ± 0.0035. This value is the weighted average of four experiments, [11, 12, 13, 14], and the error includes a scale factor of 1.9. Also, the Particle Data Group refers to f_1 as g_V, and g_1 as g_A, and uses the opposite sign convention for γ^5 and hence g_1/f_1.

Since the u, d and s quarks have different charges and masses, the symmetry $SU(3)_f$ is expected to be broken, and various models of $SU(3)_f$ breaking give different

predictions for the $\Xi^0 \to \Sigma^+ e^- \overline{\nu}_e$ form factors. The value of f_1 for $n \to p e^- \overline{\nu}_e$ is obtained from the CVC hypothesis, that is, we can relate the electromagnetic form factors to obtain $f_1 = 1$. Also, f_1 is protected from $SU(3)_f$ breaking effects to lowest order by the Ademollo-Gatto theorem [15], though operationally the second order can contribute to first order effects in f_1 [16, 17] (the 'order' refers to the strange quark mass, $\approx M_s/M_p$). The value of g_1 is susceptible to first order $SU(3)_f$ breaking effects.

Reference [24] presents several predictions for f_1 and g_1. Their fit A only takes into account first order symmetry breaking, and fits the measured rates and angular asymmetries of the measured hyperon beta decays ($n \to p e^- \overline{\nu}_e$, $\Sigma^+ \to \Lambda e^+ \nu_e$. $\Sigma^- \to \Lambda e^- \overline{\nu}_e$, $\Lambda \to p e^- \overline{\nu}_e$, $\Sigma^- \to n e^- \overline{\nu}_e$, $\Xi^- \to \Lambda e^- \overline{\nu}_e$, $\Xi^- \to \Sigma^0 e^- \overline{\nu}_e$), and the measured decuplet decay widths ($\Delta \to N\pi$, $\Sigma^* \to \Lambda\pi$, $\Sigma^* \to \Sigma\pi$, $\Xi^* \to \Xi\pi$). Their fits $B-D$ allow for the renormalization of f_1, fits C and D allows V_{us} and V_{ud} to float, and fit D uses a different normalization for the decuplet decay widths. Reference [23] uses a recoil center-of-mass correction, and a bag model correction (fits A and B) to g_1/f_1, neglecting any correction to f_1.

Theory	f_1	g_1	g_1/f_1
Exact $SU(3)_f$ and CVC	1.00	1.27	1.27
Flores-Mendieta (A) [24]	1.00	1.03 ± .02	1.03 ± .02
Flores-Mendieta (B) [24]	1.12 ± .05	1.02 ± .02	.91 ± .04
Flores-Mendieta (C) [24]	1.12 ± .05	1.02 ± .03	.91 ± .05
Flores-Mendieta (D) [24]	1.12 ± .05	1.07 ± .03	.96 ± .05
Ratcliffe (A) [23]	1.00	1.17 ± .03	1.17 ± .03
Ratcliffe (B) [23]	1.00	1.14 ± .03	1.14 ± .03

Table 1.1: Predictions for g_1/f_1

1.5.2 Predictions for g_2/f_1

As mentioned before, the g_2 is forbidden in the weak interaction. second class weak currents do not naturally occur in the quark model [2]. However, small non-zero second class current terms may be induced by the electromagnetic interaction, since the electromagnetic interaction violates $\mathcal{G}$ parity.

For example, for the decay $\Sigma^- \to n\, e^-\, \overline{\nu}_e$, predictions for g_2 for $\Sigma^- \to n\, e^-\, \overline{\nu}_e$ range from -0.1 to .46 [25, 26, 27, 28]. The experimental value for $\Sigma^- \to n\, e^-\, \overline{\nu}_e$ is $g_2 \approx -.6 \pm .4$[29]. Predications for $g_2/f_1$for $\Xi^0 \to \Sigma^+\, e^-\, \overline{\nu}_e$ are on the order of 0.1 [19, 20].

1.5.3 Predictions for f_2/f_1

For $n \to p\, e^-\, \overline{\nu}_e$ f_2 is obtained using the CVC hypothesis from the magnetic moments of the neutron and proton. The value is corrected for the M_B in the denominator of equation (1.9) [3].

$$f_2 = \frac{M_{\Xi^0}}{M_p} \frac{(\mu_p - \mu_n - 1)}{2\mu_0} = 2.6 \tag{1.21}$$

Variations in this value on the order of ± 1 can arise from the presence of the strong interaction [19, 20].

1.6 Extraction of V_{us} from Hyperon Beta Decays

With the three $\Delta S = 1$ hyperon beta decays, for which data for f_1 and g_1 exist, ($\Lambda \to pe^-\overline{\nu}_e$, $\Sigma^- \to ne^-\overline{\nu}_e$ and $\Xi^- \to \Lambda e^-\overline{\nu}_e$, only rate data exists for $\Xi^- \to \Sigma^0 e^-\overline{\nu}_e$) one can calculate the value of V_{us} assuming the $SU(3)_f$ breaking effects are understood [18, 21, 22]. These values can then be compared to those obtained from $K \to \pi l \overline{\nu}_l$ decays ($V_{us} = 0.2188 \pm 0.0016$ [4]). The most recent, Ref. [22] obtains a consistent value for V_{us}($.2176 \pm .0026$) ,

A complete understanding of $SU(3)_f$ breaking in hyperon beta decays could lead to an independent measurement of $V_{us}$of equal or better precision than that obtained from K decays. Experimental data on $\Xi^0 \to \Sigma^+\, e^-\, \overline{\nu}_e$ (a $\Delta\, S = 1$ decay) will be useful in that regard.

1.7 Previous Experiments

The first observation of this decay was made at KTeV [6]. Previous experiments set an upper limit of $1.1 \times 10^{-3}(90\% c.l.)$ [7, 8, 9]. The last experiment which looked

for this decay mode [7] used a $1.75\,GeV/c\,K^-$ beam to produce Ξ^0 and Ξ^- in the Brookhaven 31 *in.* hydrogen bubble chamber. Since the K^- energy and flux was so low, only about 3000 Ξ^0 were produced. Our experiment (E799-II), on the other hand, produced over 10^8 Ξ^0 which decayed in the detector volume.

Chapter 2
THE E799-II DETECTOR

The KTeV detector apparatus was used by experiments E799 and E832. The E832 experiment was built to measure direct CP violation in $K_{S,L} \to \pi^+\pi^-$ and $K_{S,L} \to \pi^0\pi^0$ decays [30, 76]. The E799 experiment was designed to look at rare $K_{S,L}$ decays, such as $K_L \to \pi^0 e^+ e^-$, electromagnetic $K_{S,L}$ decays, such as $K_L \to \mu^+\mu^-\gamma$, $K_L \to \mu^+\mu^- e^+ e^-$, $K_L \to e^+e^-e^+e^-$, electromagnetic decays of π^0 from $K_L \to 3\pi^0$ decays in flight, such as $\pi^0 \to e^+e^-e^+e^-$ and $\pi^0 \to e^+e^-$ [31], and the decay $K_L \to \pi^+\pi^-e^+e^-$, another decay mode in which CP violation has been observed [32, 33]. Since there are also a large number of Λ and Ξ^0 produced (and their anti-particles), decays such as $\Xi^0 \to \Sigma^+ e^- \overline{\nu}_e$, and the radiative decay modes $\Xi^0 \to \Sigma^0\gamma$ and $\Xi^0 \to \Lambda^0\gamma$ can also be studied in E799.

To accomplish all this, the KTeV detector apparatus was designed to produce a neutral beam of $K_{S,L}$ and hyperons, reconstruct the momenta of the decay products of the $K_{S,L}$ and hyperons, and detect decay products leaving the detector volume.

2.1 The Primary Proton Beam

The experiment ran at the KTeV hall located at the Fermi National Accelerator Laboratory (Fermilab, or FNAL). From September 1996 to September 1997, the Tevatron provided a beam consisting of $800\,GeV$ protons to KTeV and many other fixed target experiments.

In the KTeV coordinate system used throughout this thesis, 'z' refers to the direction along the beam, 'y' refers to 'up', and 'x' is the horizontal axis such that x, y, and z form a right handed coordinate system.

2.2 The Hyperon (and K_L) Beams

The KTeV secondary beam is produced by the Fermilab Tevatron's $800\,GeV$ proton beam. Every 'spill' (about 60 second), about 3.5×10^{12} $800\,GeV$ protons are

split off from the Tevatron and sent to the KTeV target hall (figure 2.1). For a 20 second period, about 3000 protons were directed towards the KTeV target every $19\,ns$ 'bucket'. The beam is directed at the target at a downward angle of $4.8\,mrad$, the spot of the beam hitting the target was about $500\,\mu m$. The KTeV target is a $30\,cm$ piece of Beryllium Oxide (BeO). The length and material was chosen to maximize kaon production [34]. Many particles, both charged and neutral are produces in this interaction with lab momenta approaching the primary beam energy.

2.3 The Sweeping Magnets and Collimators

A series of magnets sweep the charged particles out of the beam (table 2.1). They also served the dual purpose of precessing the spin of the Ξ^0 produced at the target.

The direction of the incoming proton beam is:

$$\hat{p} \approx \hat{z} - 4.8 \times 10^{-3}\hat{y} \tag{2.1}$$

and the direction of the produced Ξ^0 will be

$$\hat{\Xi^0} \approx \hat{z} \tag{2.2}$$

Since Ξ^0 are produced by the strong interaction, which conserves parity, the Ξ^0 can only be polarized along the $\hat{p} \times \hat{\Xi^0}$ direction, that is, along the $\hat{x}$ axis.

Table 2.1 [62] shows the integrated field of each of the sweeping magnets, and how much the polarization of the Ξ^0 precesses at it passes through each one, assuming the Particle Data Group value for the magnetic moment of the Ξ^0 ($\mu_{\Xi^0} = (-1.250 \pm .014)\mu_N$) [10].

Once the Ξ^0 reached the Spin Rotator (NM2SR) they were polarized in the z direction. The Spin Rotator precessed the Ξ^0 spin into $\pm y$ direction, depending on the polarity, which was switched regularly to obtain equal amounts of data for the two polarization directions.

The final sweeping magnet (NM3S) at $z \approx 90\,m$ was used to remove the remaining charged particles from the beam. At this point the Ξ^0 polarization was in

Magnet	$z_i(m)$	$z_f(m)$	$\int Bdl(T-m)$	ϕ	$I(amps)$
NM2S1	0.56	4.37	1.58	36.2	536.6
NM2S2	12.23	18.19	11.90	272.4	1500.0
NM2S3	21.85	27.85	6.18	141.4	317.0
Total (NM2S1 - NM2S3)				450.0	
NM2SR	30.47	36.53	4.00	91.5	2652.5
NM3S	90.27	92.10	2.62	No effect	2000.0

Table 2.1: Strength and Precession of Ξ^0 from Sweeping Magnets in figure 2.1. Here z_i and z_f refer to the z positions of the start and end of each magnet (in m). $\int Bdl$ is the field integral (in $(T-m)$) and ϕ is precession angle (in ^{0}) of the Ξ^0 . I is the current supplied to each magnet (in *amps*).

the $\pm y$ direction, so the Ξ^0 passed through with no effect.

Between magnets NM2S2 and NM2S3 was a $3\,in$ lead absorber which removed photons in the beams and a primary collimator which defined two beams [36]. Before the final sweeping magnet (NM3S), the defining collimators further reduced the size of the beam. Two different sizes of defining collimators were used at different parts of the run. The 'small' collimator defined two beams of $0.25\,\mu sr$ and the 'large' collimator defined two beams of $0.35\,\mu sr$.

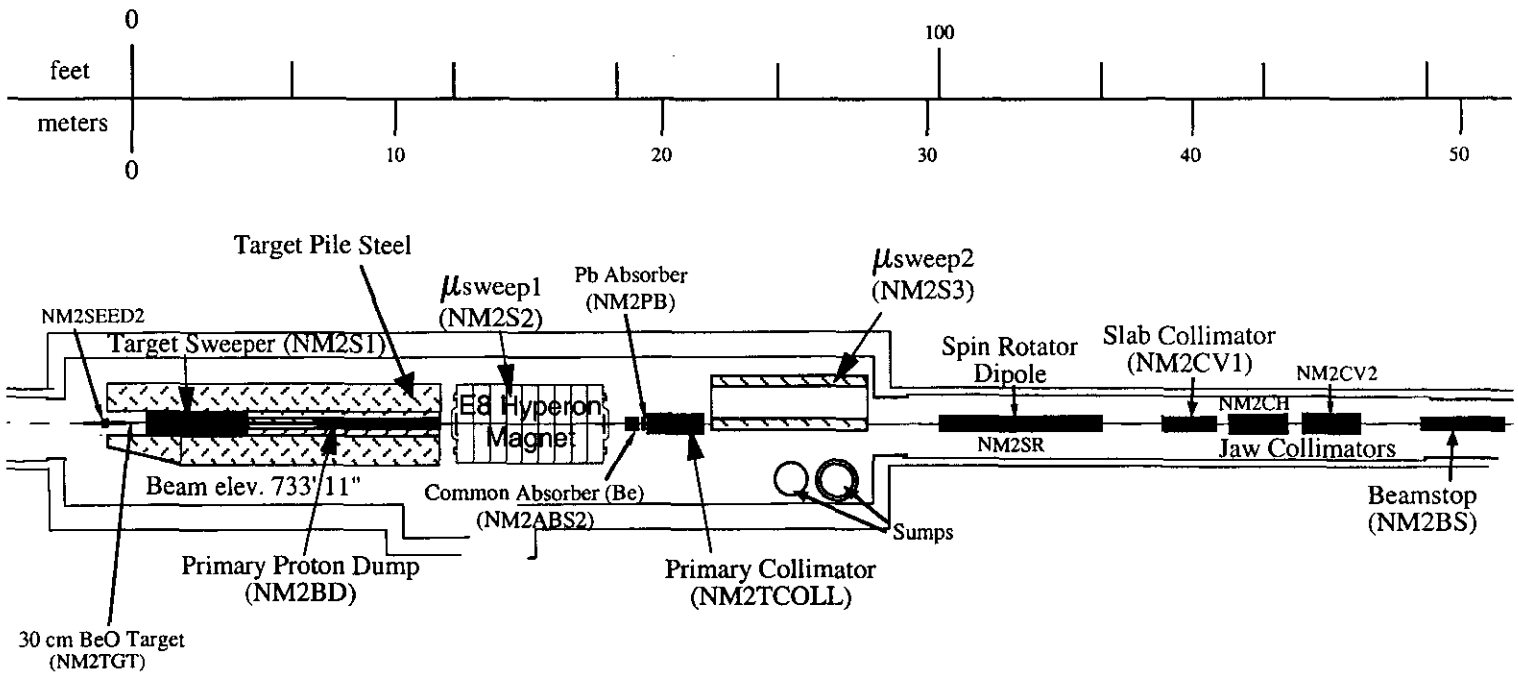

Figure 2.1: Target, sweeping magnet and collimator elements in the KTeV target enclosure.

2.4 The Decay Volume and Vacuum Window

At $93\,m$ our decay volume begins. It is a $66\,m$ long pipe whose diameter ranged from $18\,in$ at its beginning to $96\,in$ at the end. The upstream end was covered with a window of aluminized mylar reinforced with kevlar. The decay volume was kept at a pressure of $10^{-6}\,torr$ in order to minimize interactions with the neutral beam in the decay volume.

2.5 The Drift Chambers (DC)

Immediately downstream of the vacuum window is a large plastic bag filled with helium. These bags fill the area between the drift chambers. Downstream of the first helium bag is a gap to allow the shutter to cover the vacuum window. Another helium bag is just before the first drift chamber (DC). The KTeV drift chambers range in size from $1.26 \times 1.26\,m^2$ to $1.77 \times 1.77\,m^2$. each chamber contains wires in the x and y views, each view contains two planes. The wires in each plane are arranged in a hexagonal pattern with six field wires on the outside, and one sense wire at the center of each cell. The two planes are offset by one half of a cell size ($6.35\,mm$). These chamber were used in the previous generation of kaon experiments, and their geometry and construction is described in more detail in Refs. [37] and [38]. There is a voltage of $2450 - 2550\,V$ applied between the field and sense wires. The drift chambers are sealed by mylar windows, and filled with a gas mixture of argon/ethane (49.5/49.5) with 1 % iso-propyl alcohol by volume added. The alcohol absorbs UV light emitted in the ionization, which protects the wires from damage (due to the high rate).

When charged particles pass through the chamber they ionize the atoms in the gas, the field produces an 'avalanche' of electrons which produce a signal on the sense wire. The time at which the avalanche reaches the wire is read out. The time is used to calculate the precise ($\approx 100\,\mu m$) distance between the wires the particle passed through.

Since complimentary plane pairs are $6.35\,mm$ apart, when the drift chamber

times are read out and translated into a distance, the sum of distances (SOD) on two complimentary wires should equal $6.35\,mm$. For some fraction of events, the first bunch of ions produced are not recorded, and hence the SOD is significantly greater than $6.35\,mm$ (by at least $1\,mm$). This so-called 'hi-SOD' problem will worsen the chamber resolution, and cause some tracks to not be reconstructed at all.

2.6 The Spectrometer Magnet

Between the two upstream and two downstream chambers, there is a large dipole magnet. The field provides a transverse momentum 'kick' of $\pm 205\,MeV$ to charged particles passing through it. By calculating the 'bend' of charged tracks, we measure the momenta of charged particles.

2.7 The Transition Radiation Detectors (TRD)

Downstream of the last drift chamber we have a system of 8 transition radiation detectors (TRD).

Each TRD consists of a radiator and a detector. The radiator is made from a $5.25\,in$ stack of fiber blankets. When a charged particle passes though the boundary of two media with different dielectric constants, electromagnetic radiation is given off in the form of X rays. The fiber blankets provided this material of alternating dielectric constants.

The probability of an x-ray being emitted is proportional to γ, so different types of particles at the same momentum will give off different amounts of transition radiation.

The X-rays produced convert into e^+e^- pairs which are detected by multi wire proportional chambers (MWPC). Each MWPC has two sense planes and three cathode planes (figure 2.2) running vertically.

The TRD chambers are filled with a 80/20 Xenon-CO_2 mixture. The size of the signal depends on the amount of radiative energy, hence the TRD can be used to distinguish pions from electrons. The TRDs are described in great detail elsewhere

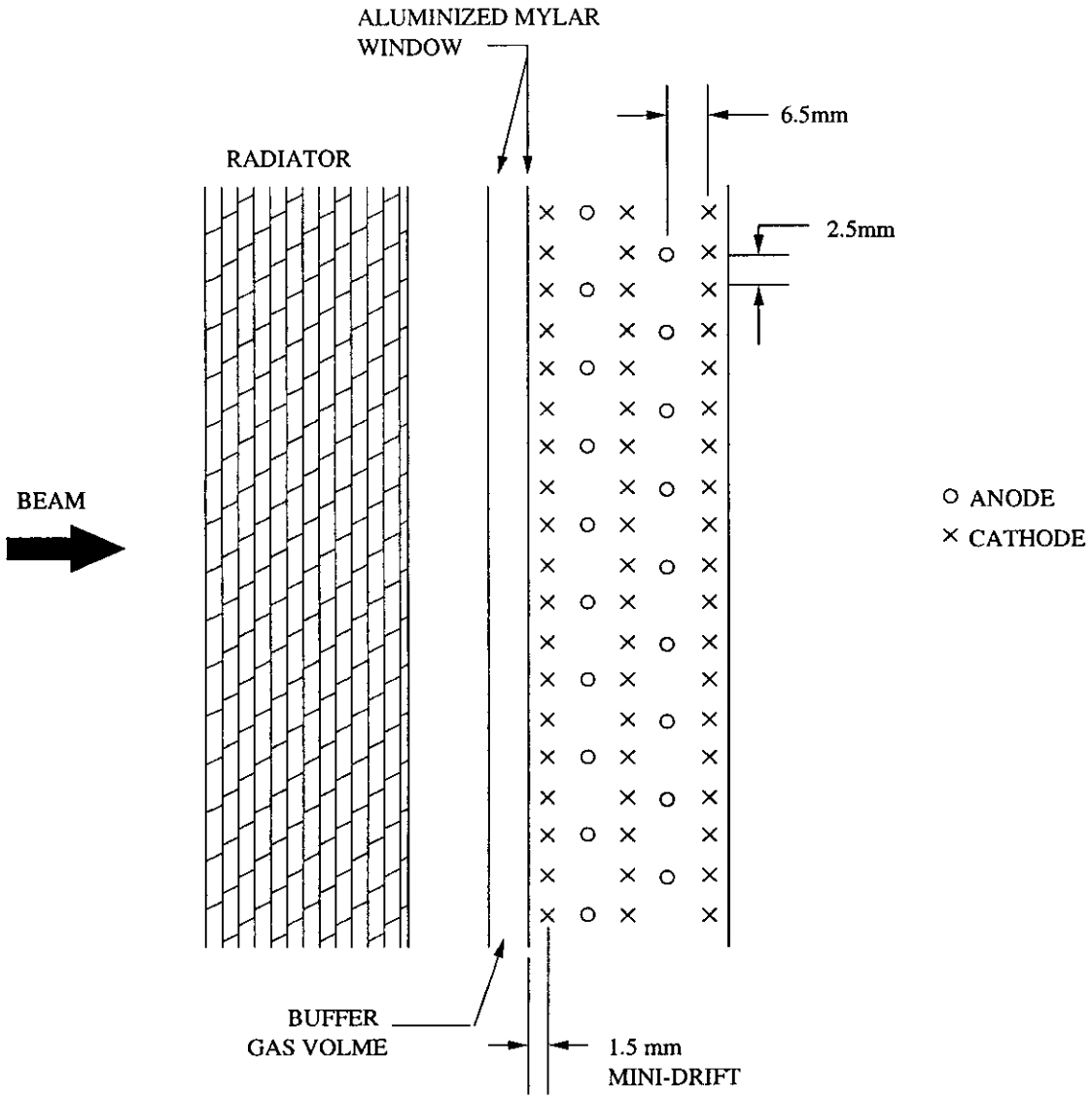

Figure 2.2: Diagram of TRD chamber and radiator.

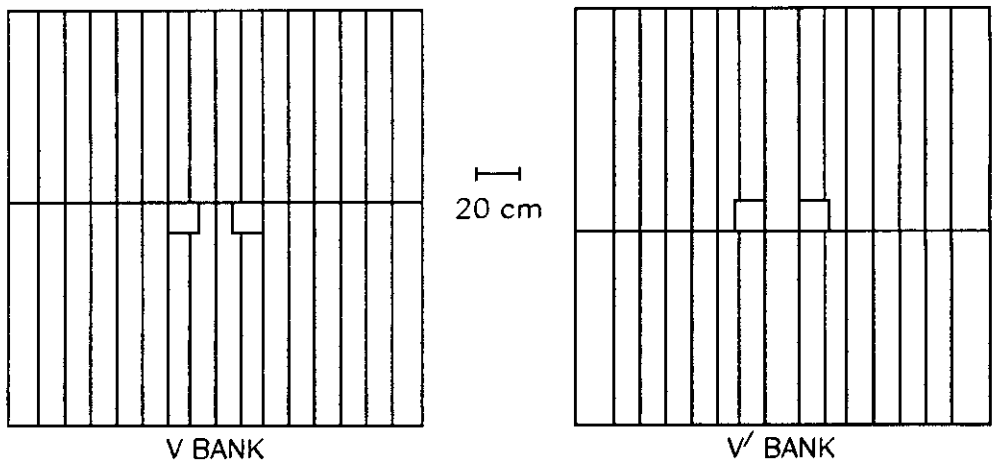

Figure 2.3: The V and V' banks. These scintillator banks are used to trigger on decays with charged particles.

[39].

2.8 The Trigger Hodoscopes

Following the TRD are the trigger hodoscopes (V and V' banks) these are long scintillator paddles which detect charged particles for the KTeV trigger.

Each bank consists of 32 paddles, aligned vertically, and split roughly in the middle. The different sized paddles are arranged in V and V' so gaps between paddles do not overlap, and holes are cut out for the neutral beams to pass through. (figure 2.3) [40].

The individual paddles are wrapped with mylar tape, and photo multiplier tubes are optically coupled to the ends of the paddles [41]. The timing and amplitude of the PMTs are used in the trigger and read out.

2.9 The Cesium Iodide Calorimeter (CsI)

An array of 3100 CsI blocks (the front face of which is located at $z = 186.01\,m$) is used to detect electromagnetic showers from electrons and photons (figure 2.4).

In the center region ($1.2 \times 1.2\,m^2$), the blocks are $2.5 \times 2.5\,cm^2$ in area, in the outer region, the blocks are $5 \times 5\,cm^2$ in area. All blocks are $50\,cm$ (27 radiation lengths) deep [34]. Most of the blocks are made from two $25\,cm$ crystals glued together. Part of each block is wrapped in aluminized mylar. The amount of each block wrapped, and the reflectivity is tuned for each block to achieve maximum resolution and linearity [35].

The light given off in the shower is detected by a photo-tube at the back of each crystal. The phototube signal is digitized by the KTeV Digital Photomultiplier Base (DPMT). The digitized DPMT information is recorded for 4 $19\,ns$ 'buckets', which records about 95 % of the shower energy.

The final energy resolution for electromagnetic showers was about 1 %, and the position resolution for electromagnetic showers was about $1\,mm$.

There are $15 \times 15\,cm^2$ beam holes on either side of the center of the calorimeter. The holes are in the vertical center of the calorimeter, and the center of each beam hole is displaced $15\,cm$ horizontally from the center of the CsI.

2.10 The Hole Counters and Hole Guards

In the beam hole, behind the CsI, there is a $16 \times 16\,cm^2$ thin ($1.5\,mm$) scintillator paddle [42]. Each paddle is wrapped in mylar tape and optically coupled to a PMT. When a charged particle passes through, the magnitude and the time of the signal is recorded.

2.11 Photon Vetoes

In order to detect photons from K decays leaving the detector, we have 10 photon veto counters , 5 Ring Counters (RC6-10), three Spectrometer Anti counters (SA2-4),

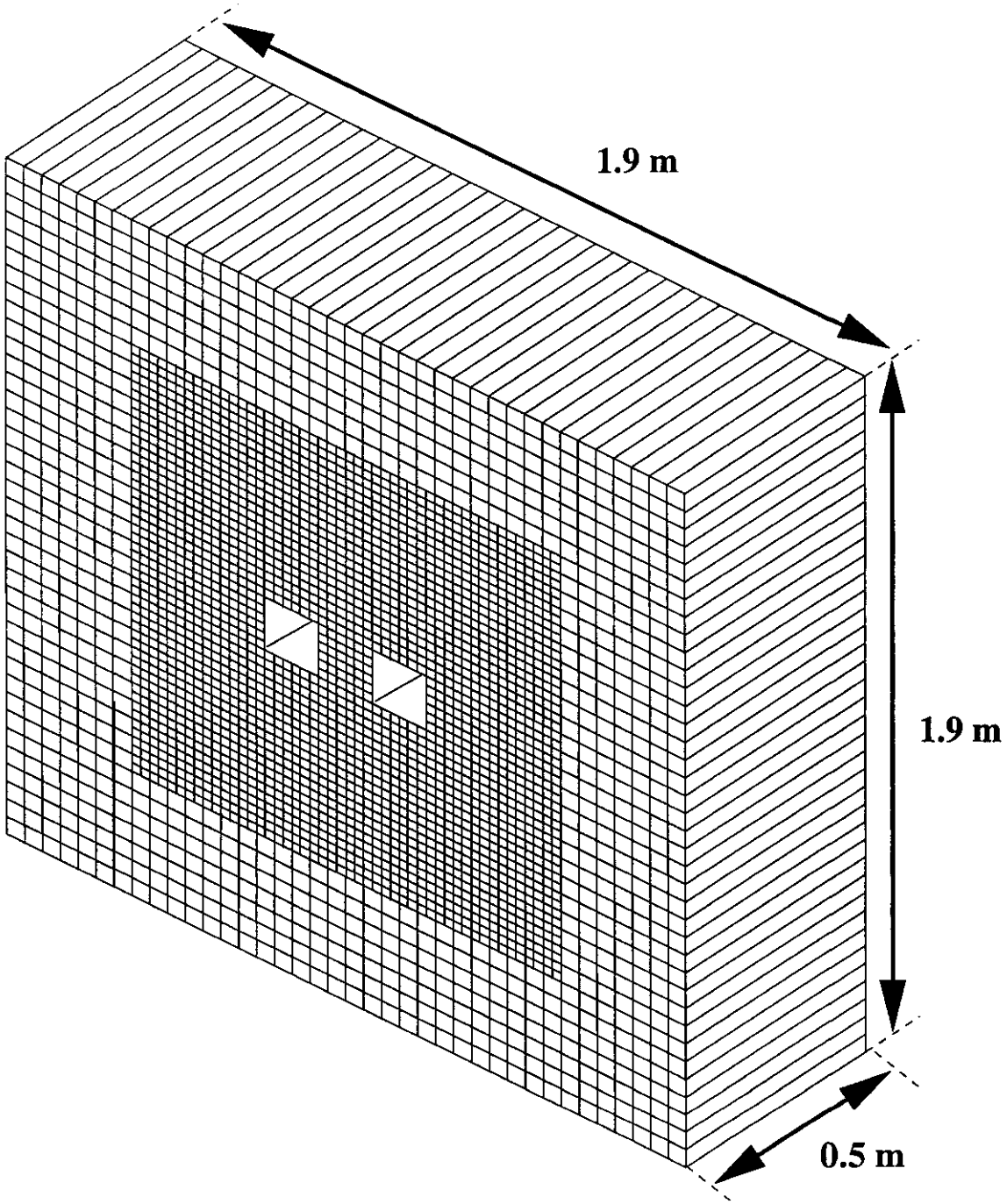

Figure 2.4: The CsI calorimeter consisting of 3100 50 *cm* long CsI crystals. The two beam holes allow the neutral beam (and protons from hyperon decays) to pass through.

a Cesium Iodide Anti (CIA), and the Collar Anti modules (CA).

The ring counters (RC) line the inside of the vacuum tank. The first, RC6, is located at $z = 132.6\,m$, the last, RC10, is located at $z = 158.6\,m$. Each ring counter is segmented, and each segment consists of 24 layers of Pb-scintillator sandwich [43]. The first 16 layers of lead are $0.5\,X_0(2.8\,mm)$ thick, and the last 8 layers of lead are $1.0\,X_0(5.6\,mm)$ thick. The RC are this thick so they can detect photons of energies down to $100\,MeV$, and reject backgrounds for rare decay searches.

The inner apertures are square (figure 2.5), $84 \times 84\,cm^2$ for RC 6 and 7, and $118 \times 118\,cm^2$ for RC 8, 9 and 10. Thus only RC7 and RC10 form limiting apertures.

Located just upstream of drift chambers 2-4 were the spectrometer anti counters (SA2 - 4). The SA apertures are square as well, their apertures are $154(x) \times 137(y)\,cm^2$ for SA2, $169(x) \times 160(y)\,cm^2$ for SA3, and $175(x) \times 175(y)\,cm^2$ for SA4. Each SA is segmented, and each segment consists of 32 $0.5\,X_0(2.8\,mm)$ thick layers of Pb-scintillator sandwich [43].

A fourth spectrometer anti, the cesium iodide anti (CIA) is located just upstream of the CsI. Its aperture is $184 \times 184\,cm^2$.

The beam hole boundaries of the CsI are covered by the collar anti (CA). The inner edges of the CAs frame the two beam holes, and the detector overlaps the innermost layer of CsI blocks by $1.5\,cm$. Each CA module consists of 3 layers of $1\,cm$ thick scintillator followed by $2.9\,X_0(1.0\,cm)$ of tungsten. Longitudinally, the CA begins $10\,cm$ upstream of the front face of the CsI [46, 47].

2.12 The Hadron Anti

Behind the CsI, there is a $10\,cm$ thick lead wall with a $60(x) \times 30(y)\,cm^2$ hole in the center to allow the neutral beam to pass through. Behind the lead wall, a set of scintillator paddles called the hadron anti (HA) detected hadronic showers (from charged pions) that started in the lead wall. This allowed us to reject events with a charged pion in the final state at trigger level. The active area of the HA is $2.24 \times 2.24\,m^2$ with a $64(x) \times 34(y)\,cm^2$ hole in the center to allow the neutral beam to pass through (figure 2.7) [48].

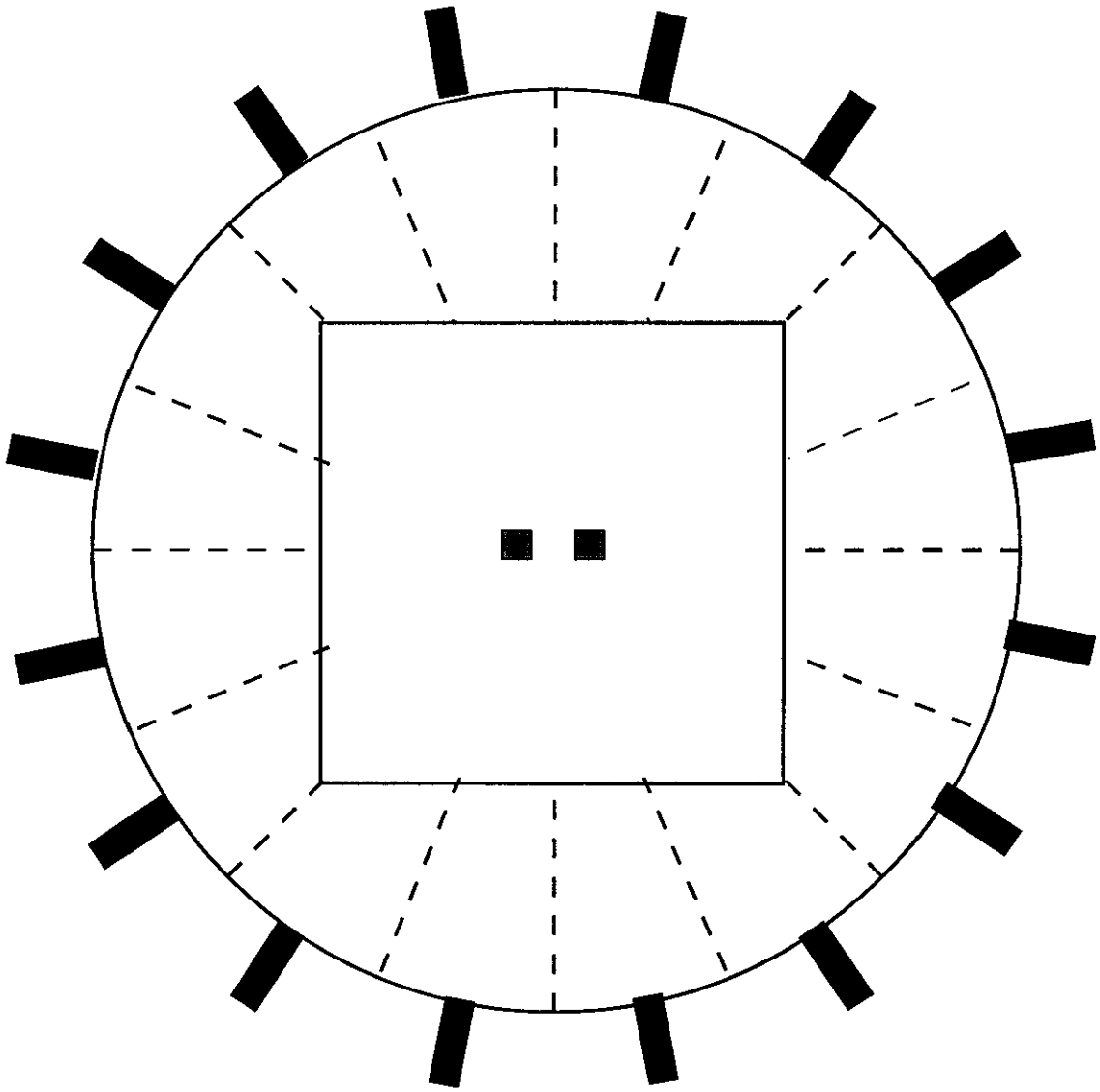

Figure 2.5: Diagram of a Ring Counter. There detectors veto events where a photon leaves the detector volume at trigger level.

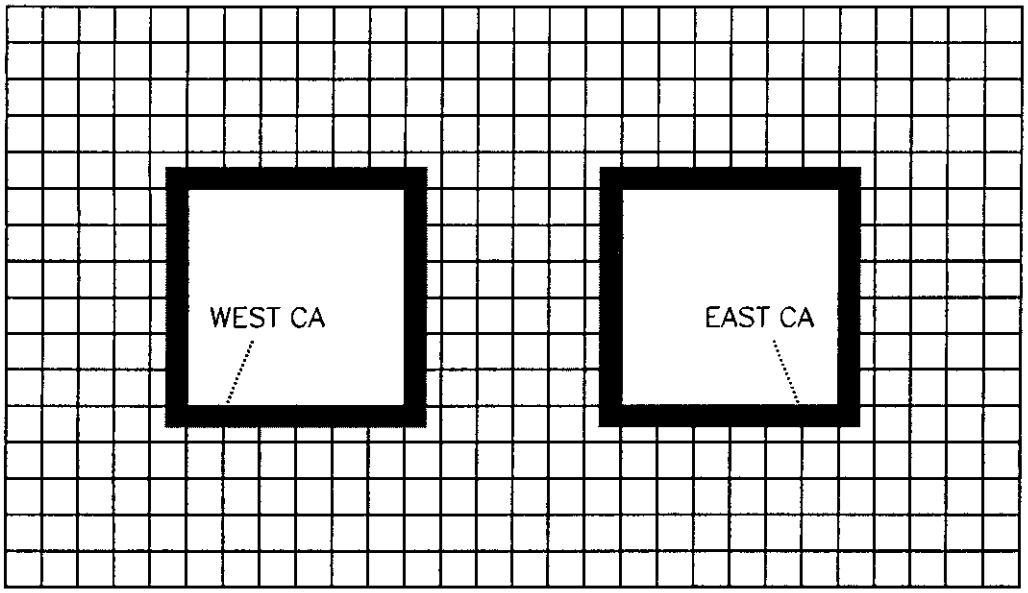

Figure 2.6: The Collar Anti (CA) viewed from the front, facing downstream.

2.13 The Muon System

A $1\,m$ block of steel covered the area behind the HA. The block of steel has a $64(x) \times 34(y)\,cm^2$ hole in the center to allow the neutral beam to pass through (the HC paddles are in this hole). Then there is small space where the back anti (BA) (not used here) is located. Behind that there is another $3\,m$ deep block of steel. Most hadronic showers range out by that distance, leaving muons with momentum $> 7\,GeV$. These muons are detected by a bank of vertical scintillator paddles (MU2). There is another $1m$ deep block of steel behind MU2, followed by a horizontal (MU3Y, at $z = 196.36\,m$) and a vertical (MU3X, at $z = 196.40\,m$) bank of scintillator paddles [49].

Figure 2.8 shows a 2 dimensional drawing of the KTeV detector configured for E799 running.

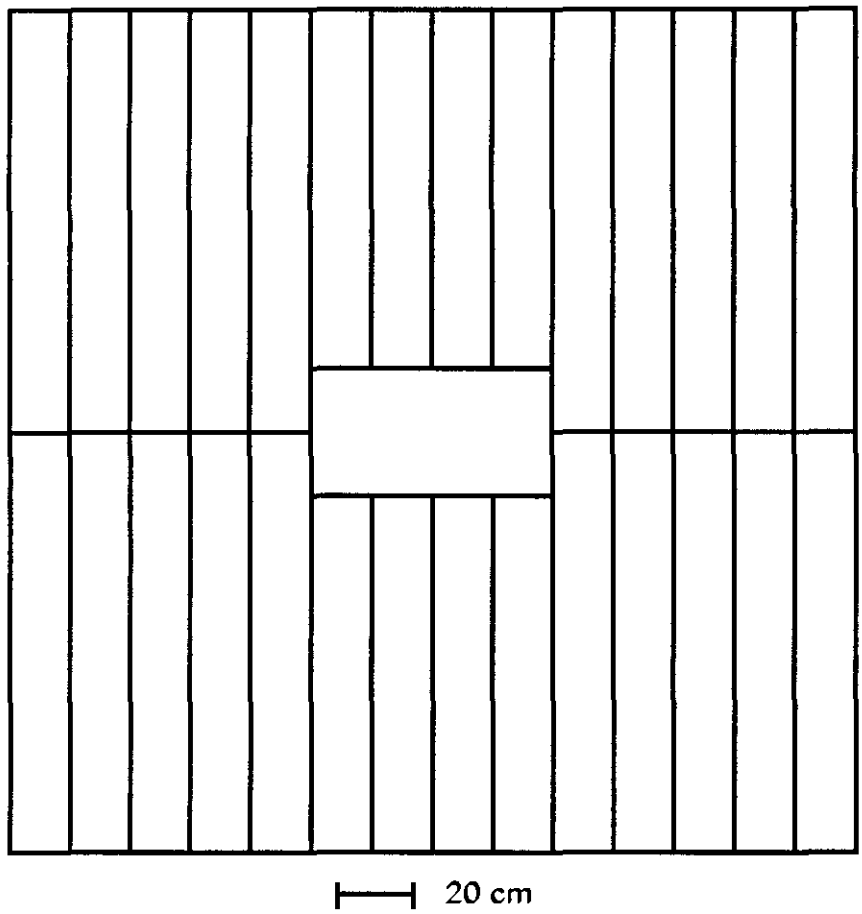

Figure 2.7: The Hadron Anti (HA) vetoes events where a charged pion starts to shower in the lead wall in front of it.

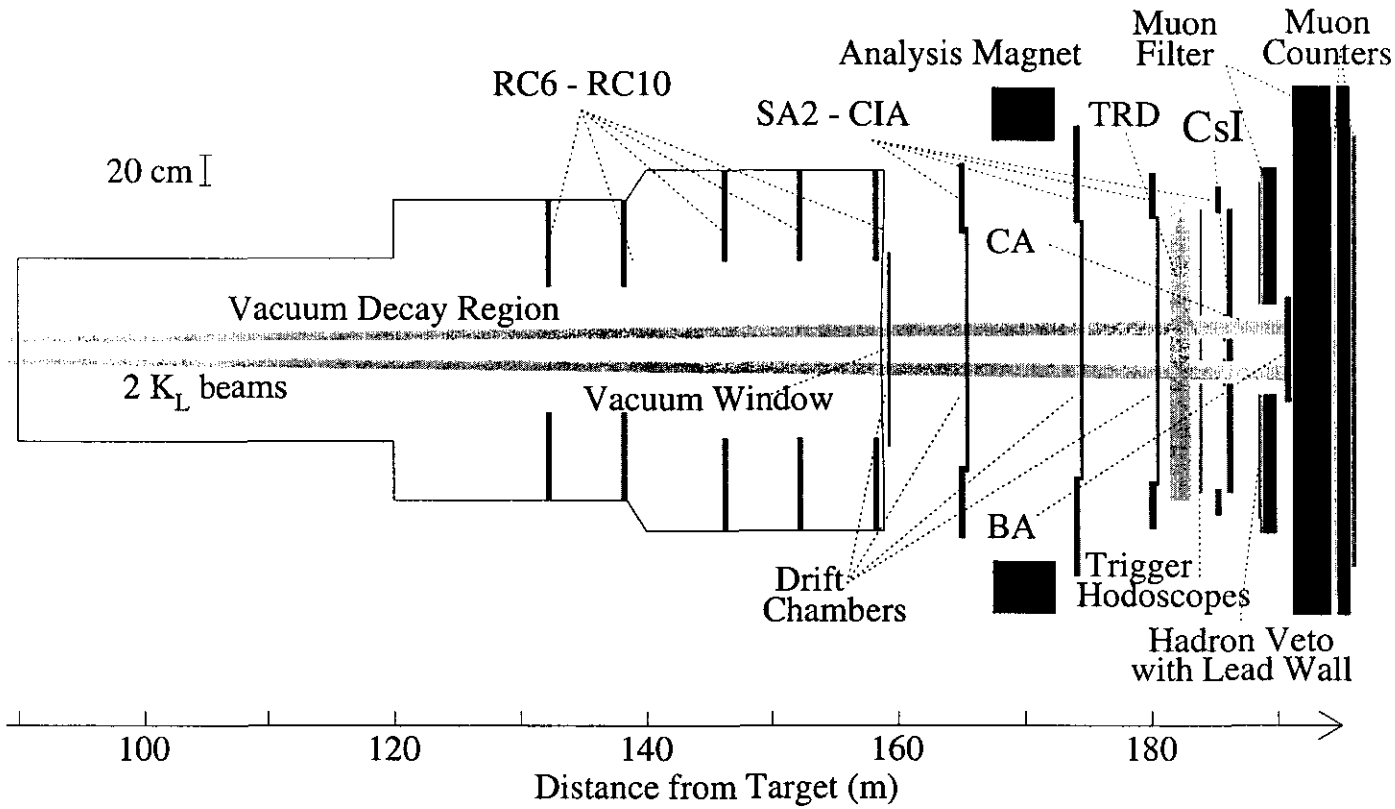

Figure 2.8: The KTeV Detector

Chapter 3

THE 1997 E799-II SUMMER DATA SET AND HYPERON TRIGGERS

In this chapter we discuss the trigger configuration and list the E799 runs used. While KTeV ran continuously (providing the detector and primary beam functioned), data taking was divided up into 'runs' lasting about 6-10 hours each. Runs were stopped to change data tapes, change the trigger configuration, or to fix detector problems.

3.1 The Hyperon Triggers

Rather than record the data in every detector for every $19\,ns$ bucket, we use an electronic 'trigger' to decide which buckets contain interesting physics events, and should be recorded. The KTeV trigger had a multi-level architecture. The first level was fast electronics, and not cause any dead time. The second trigger level required more time, and the trigger was inhibited from taking new data during the level 2 decision making time. Events passing the level 2 trigger get read out, and a rudimentary event reconstruction is performed on line. Events passing the on-line criteria are written to tape.

Most of the 15 triggers used for E799 running were dedicated to kaon decays, and are described elsewhere [50]. Three triggers were dedicated to collecting hyperon data. The decay chain for the signal mode is: $\Xi^0 \rightarrow \Sigma^+ e^- \overline{\nu}_e$ followed by $\Sigma^+ \rightarrow p\pi^0$, followed by $\pi^0 \rightarrow \gamma\gamma$. The final state consists of a proton, and electron, and two photons. Furthermore, the proton will carry most of the energy from the Ξ^0 . The trajectory of the proton will not change much due to the momentum kick of the analysis magnet, and hence the proton is likely to travel down one of the beam holes. With this in mind, the basic strategy of the hyperon trigger is to find events that have 1) a track in the beam region, traveling down a beam hole. 2) another track which hits the CsI 3) electromagnetic clusters in the CsI from $\pi^0 \rightarrow \gamma\gamma$.

$\Xi^0 \rightarrow \Sigma^+ e^- \overline{\nu}_e$ were collected in trigger 10:

Run	Date	Description
6753	October 29, 1996	Start of E832 running
8076	January 23, 1997	Start of E799 Winter Run
8913	March 24, 1997	End of E799 Winter Run
9060	April 2, 1997	Continue E832 running
10438	July 23, 1997	End E832 running
10463	July 24, 1997	Begin E799 Summer Run
10978	September 4, 1997	End E799 Summer Run

Table 3.1: The 1996-1997 KTeV Run

```
TRIG10[HYPERON] = GATE * 1V * L1HOLETRK * ET_THR2 * PHVBAR1  //
      * !HA_DC * !CA * 2HCY_LOOSE * LAMBDA_RA * HCC_GE2 : PS 1/1
```

$\Xi^0 \rightarrow \Lambda\pi^0$ with $\Lambda \rightarrow p\pi^-$ were collected in trigger 11:

```
TRIG11[LAMBDA-PPI] = GATE * 1V * L1HOLETRK * ET_THR1 //
           * PHVBAR1 *  LAMBDA_RA * HCCDUM : PS 1/50
```

$\Lambda \rightarrow p\pi^-$ were collected in trigger 12:

```
TRIG12[HYP-MINBI] = GATE * 1V * HC * STTDUM: PS 1/20000
```

3.1.1 Level 1 Hyperon Trigger Elements

Level 1:

- `GATE` On Spill
- `HC` A hit in either the left or right hole counter
- `1V` One hit in V or one hit in V' scintillator banks. This component of the trigger is satisfied by the e^- from the Ξ^0 vertex.
- `L1HOLETRK`

```
L1LEFTTRK = HC_LEFT * DC1X_LEFT_HOLE * DC2X_LEFT_HOLE
L1RGHTTRK = HC_RIGHT * DC1X_RIGHT_HOLE * DC2X_RIGHT_HOLE

L1HOLETRK = L1LEFTTRK + L1RGHTTRK
```

A hit in the hole counter `HC` and beam region DC FAST-OR paddles `DC1X_RIGHT_HOLE * DC2X_RIGHT_HOLE` on either beam hole. This component is satisfied by the high momentum proton traveling down one of the beam holes.

- `ET_THR`n ETOTAL. The energy in each CsI channel is summed and compared with predetermined thresholds ($12GeV$ for ET1, $18GeV$ for ET2). Satisfied by the electron and two photons in the final state.

- `PHVBAR1` Photon vetoes, except RC8. None of the photon vetoes can have energy in them above the pre set veto threshold (RC6,7,9,10, SA2, SA3, SA4, CIA). Reduces the rate from kaon decays where a photon leaves the fiducial volume of the detector.

- `!CA` Neither Collar Anti module above about $10\,GeV$. Ensures energy from the electro magnetic clusters is contained in the CsI.

- `!HA_DC` DC Coupled Hadron Anti Veto. Reduces rate from $K_L \rightarrow \pi^+ e^- \overline{\nu}_e$ events and other events having a charged pion in the final state.

Drift Chamber Fast Ors (DCFO)

In order to reduce the level 1 rate, the Drift Chamber Fast Ors (DCFO) were designed and built to quickly detect drift chamber hits present in an event. Each group of 16 wires (less on the ends) of each plane pair is connected to a single DCOR module. For chambers 1 and 2, both the x and y views. The module tells whether or not a

drift chamber hit is present in a 230 ns window. For hyperon decays, we require the proton to travel down the beam hole. Therefore it was possible for us to select the groups of wires in the beam regions of each chamber. Figure 3.1 shows the wires instrumented by the DCFOs in the beam region.

3.1.2 Level 2 Hyperon Trigger Elements

- `2HCY_LOOSE` Two Hits in Y view (using The Kumquat (KQ) and Banana (BAN) boards in every chamber, allowing a missing hit in Chamber 1 or Chamber 2.

- `LAMBDA_RA` The SUMMER STT, requires a hit in all 4 beam regions in either beam hole. The STT instrumented region consists of 11 wires in the upstream chambers, and 15 wires in the downstream chambers. There is also a 1/20 STT random accept implemented for summer data.

- `HCC_GE2` At least 2 HCC clusters

- `STTDUM` STT Dummy requirement, wait for STT to finish processing

Hit Counting in y

At level 2, special hardware boards (called 'Kumquats' (KQ) and 'Bananas' (BAN)) find in-time drift chamber hits on a wire-by-wire basis. They also pass this information on to other parts of the trigger, and count the total number of in time drift chamber hits in each view. Since our decays have two charged tracks, we should have two hits in all four y views. Chambers 3 and 4 are instrumented with kumquat boards, they look for either an isolated hit in one wire, or in-time hits in adjacent wires. Chambers 1 and 2 are instrumented with banana boards. Banana boards use a much more complicated algorithm to find in-time pairs, and actually calculate a drift distance at trigger level for two complimentary wires. As a result, we are more likely to miss a good drift chamber hit in chambers 1 and 2, and therefore allow for a missing hit in either chamber 1 or 2.

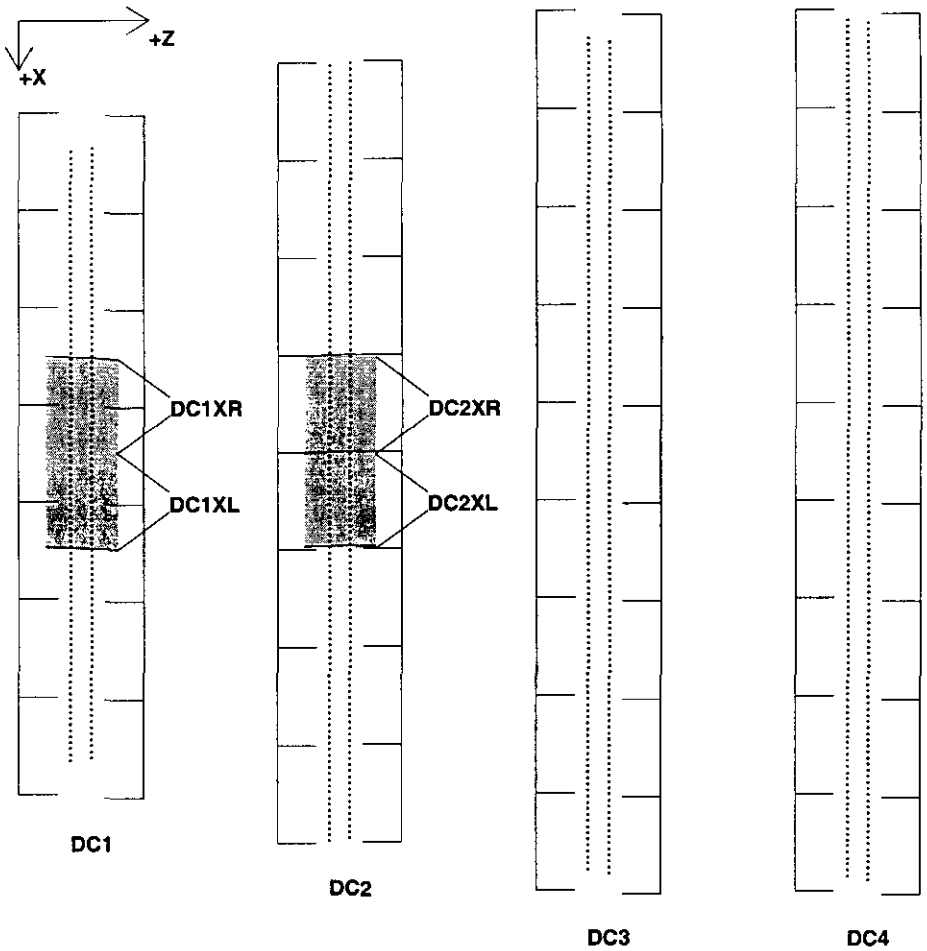

Figure 3.1: Wires instrumented by the beam region DC Fast Ors are in the shaded boxes.

```
2HCY_dum1  = 1HC1Y * 2HC2Y * 2HC3Y * 2HC4Y   # missing hit in CH1Y
2HCY_dum2  = 2HC1Y * 1HC2Y * 2HC3Y * 2HC4Y   # missing hit in CH2Y
2HCY_loose = ( 2HCY_dum1 + 2HCY_dum2 )
```

Hardware Cluster Counter (HCC)

The hardware cluster counter (HCC) quickly (about $2\,\mu s$) calculates the number of hardware clusters at level 2. Each of the 3100 blocks has a bit to assigned to it, which is on or off depending on whether or not there is at least $1\,GeV$ of energy in that block [52]. The HCC information is read out in the data stream and used in off-line clustering. Signal events have three clusters in the CsI.

The Stiff Track Trigger (STT)

The Stiff Track Trigger (STT) relied on inputs from the Kumquat and Banana boards to determine if there is a track in the beam region.

The STT used the KQ/BAN latches from the 11 (15) center-most wires with regard to each beam hole in chambers 1 and 2 (3 and 4). If there was a hit in all four chambers in either beam beam region, the event passed the STT. Additionally, every 20th event automatically passed the STT. Wires instrumented by the STT are shown in figure 3.2, a 'close-up' of figure 3.1.

The STT is described in greater detail in appendix B of this thesis and elsewhere [53, 86].

3.1.3 Level 3 Hyperon Trigger Elements

Level 3 processing is done in software. Events passing any hyperon trigger go though a 'filter' process, which decides whether or not to write them to tape.

For triggers 10 and 11, the filter code had the following requirements:

- At least 2 X and Y track candidates

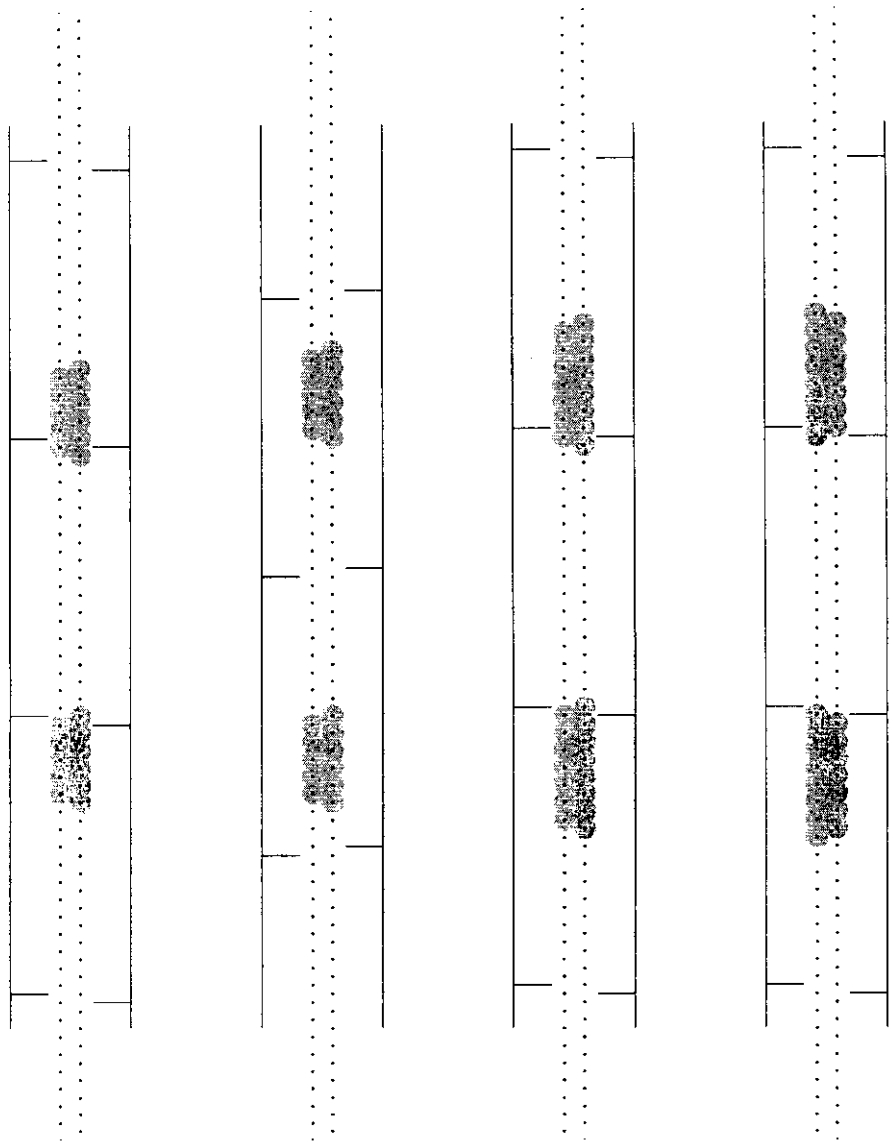

Figure 3.2: Wires instrumented by the STT are indicated by large light dots.

- At least 1 vertex candidate

- One track combination matching cluster, one matching beam hole

- At least one vertex candidate with the momentum of the positive track being at least 2.5 (or no more than 0.4, to allow for anti-hyperon decays) $\times$ the momentum of the negative track

- An X track candidate with momentum $> 85\,GeV$

- For each vertex candidate found above, the quantity

$$N_\tau = \frac{Z_{vtx} m_{\Xi^0}}{(\mid p_{hi} \mid + \mid p_{lo} \mid) c\tau_{\Xi^0}} \tag{3.1}$$

  is calculated. Here Z_{vtx} is the z position of the vertex candidate and p_{hi} and p_{lo} refer to the momenta of the tracks used for each candidate. One of the vertex candidates was required to have $N_\tau < 16$. This cut was changed to < 18 at run 10546, and not applied at all for runs 10788 and later.

- A track candidate pointing down the hole, one the x tracks was required to be between $x = 6\,cm$ and $x = 24\,cm$ (or $x = -24\,cm$ and $x = -6\,cm$) at $z = 186.17\,m$, and one the y tracks was required to be between $y = -8.5\,cm$ and $y = 8.5\,cm$ at $z = 186.17\,m$, this cut was not applied for runs 10788 and later.

Events which passed the 2 track requirement but failed the vertex candidate requirement were also saved.

The nominal trigger L1/L2 was used to collect 92.3 % (92.5 $\pm$ 1.0 %) of the $\Xi^0 \to \Lambda\pi^0$ ($\Xi^0 \to \Sigma^+ e^- \overline{\nu}_e$) events.

Trigger changes included removal of the CA veto in trigger 10, removal of SA3 from triggers 10 and 11, changing HA veto conditions, and removal of the hit counting in 4Y. Also, some of the L3 cuts were removed during various parts of the summer. The MC simulation was done with the tightest cuts used, and a signal loss of 8.7 $\pm$

2.0×10^{-4} was found. The cause of this loss is not known, but has a negligible effect on this result.

3.2 "Winter" and "Summer" Data

The E799 run period from January to March 1997 is referred to as the "winter" run. During this period, the upstream magnets were tuned to precess the Λ polarization to the $\pm y$ directions. The original intent was to measure the asymmetries from $\Lambda \to pe^-\overline{\nu}_e$. This measurement, however, required reduction of the $K_L \to \pi^+ e^- \overline{\nu}_e$ background. In order to do this, a device to distinguish pions from protons in the beam hole was built [54]. This device could not function in the beam hole environment, and was removed.

The hyperon triggers for the winter run were:

```
TRIG10[HYPERON] = GATE * 1V * L1HOLETRK * ET_THR1 * PHVBAR1 //
        * !HA_HI * 2HCY_LOOSE * LAMBDA * HCC_1234 : PS 1/2

TRIG11[LAMBDA-PPI] = GATE * 1V * L1HOLETRK * PHVBAR1 //
        * LAMBDA : PS 1/50

TRIG12[HYP-MINBI] = GATE * 1V * HC * STTDUM : PS 1/20000
```

The STT requirement for the winter was different in that there was no random accept as there was in the summer, and the STT algorithm was more complicated. The winter STT algorithm actually calculated the 'bend' in tracks in the STT instrumented region, but did not allow for extra hits in the STT instrumented region. as a result, the acceptance for high momentum tracks in the beam hole was very low ($\approx 30\%$), and our detector simulation does a poor job of mocking up this inefficiency (by about 25% of itself). For studying the decay of alternately polarized Λ this would not be a problem, since the bias would effectively cancel out [61].

Also, the ET threshold was lower, and the HCC requirement loosened (here HCC1234 means that the HCC had to find 1,2,3 or 4 clusters, very few hyperon triggers had more than 4). A prescale was applied to trigger 10 for most of the winter run. The level 3 code has some differences as well [86].

For the $\Xi^0 \to \Sigma^+ e^- \overline{\nu}_e$ observation paper [6]. The STT was the single largest contribution to the systematic error. We estimate that inclusion of the winter data would increase the useful $\Xi^0 \to \Sigma^+ e^- \overline{\nu}_e$ data sample by about 20%. However, given the lack of understanding of the loss due to the STT, most likely due to misunderstanding of accidental activity in the beam region, we do not include the winter data in this result.

3.3 Runs Used

Usable runs are defined as runs passing the spill quality cut to be described later, and having good $\Xi^0 \to \Lambda\pi^0$ with $\Lambda \to p\pi^-$events in trigger 11.

The usable runs are:

10463 10464 10477 10478 10482 10483 10491 10493 10494 10531
10532 10539 10540 10541 10544 10548 10549 10550 10552 10553
10554 10558 10559 10561 10563 10566 10567 10590 10593 10594
10601 10602 10604 10606 10608 10609 10610 10612 10618 10619
10620 10625 10627 10634 10635 10638 10643 10644 10647 10649
10656 10657 10658 10659 10660 10664 10666 10672 10673 10679
10680 10682 10684 10686 10703 10704 10705 10706 10707 10710
10715 10716 10717 10719 10720 10721 10724 10728 10732 10733
10736 10753 10757 10764 10766 10767 10769 10788 10790 10797
10798 10802 10818 10819 10825 10828 10933 10934 10937 10938
10947 10948 10950 10951 10952 *10957* 10959 10960 10962 10964
10967 10969 10970

3.4 Reduction of the Data Samples (Crunch)

During the data taking phase of the experiment, data that pass any level 3 trigger are written to digital linear tape (DLT). Each event is written to one of 10 DLTs, each DLT can hold about 15 Gigabytes of data.

At the conclusion of the experiment, all the hyperon triggers were split off to about 60 DLTs. In order to facilitate analysis, events having two x and y tracks and at least 2 extra clusters, were written to a set of 15 DLTs. That dataset was further reduced to 5 DLTs by selecting events which had one x and y track combination with an electron like $E/p > 0.8$ in trigger 10, and all events in trigger 11. All the events in trigger 12 having at least 2 tracks were sent to a different dataset of 2 DLTs. (Throughout this thesis, E/p refers to the amount of energy found in the CsI cluster associated with a track divided by the magnitude of the momentum of that track).

A check of the crunch procedure found that run 10957 was inadvertently omitted from the data reduction process. These events were recovered for the $\Xi^0 \rightarrow \Sigma^+ e^- \overline{\nu}_e$ analysis, which uses the 60 split tapes rather than the 5 crunch tapes. The $\Lambda \rightarrow p\pi^-$and $\Xi^0 \rightarrow \Lambda\pi^0$ data here *do not* include run 10957 (about .5% of the data).

Chapter 4
THE MONTE CARLO SIMULATION

4.1 Production of Ξ^0

The production of Ξ^0 by the proton beam is given by:

$$\begin{aligned}\frac{dN_{\Xi^0}}{dx_F dp_T} &= \frac{|\vec{p_\Xi}|}{E_\Xi} p_T EXP(C_1 + C_2 x_F^2 + C_3 x_F + C_4 x_F p_T + C_5 p_T^2 + C_6 p_T^4 + C_7 p_T^6) \\ &\quad \times (1 - x_F)^D (1 + a x_F)(1 + b p_T), \end{aligned} \tag{4.1}$$

where

$$D = C_8 + C_9 p_T^2, \tag{4.2}$$

x_F is the lab energy of the Ξ^0 divided by $800\,GeV$ and p_T is the momentum of the cascade perpendicular to the primary beam. The parameterization (minus the fudge factors a and b) is taken from [60].

$$\begin{aligned} C_1 &= -1.21 \\ C_2 &= 1.16 \\ C_3 &= -0.72 \\ C_4 &= -0.48 \\ C_5 &= -1.85 \\ C_6 &= 0.17 \\ C_7 &= -0.008 \\ C_8 &= 2.87 \\ C_9 &= 0.04 \\ a &= -.42 \\ b &= -.08 \end{aligned}$$

(4.3)

Most of the Ξ^0 produced do not survive to $z = 90\,m$. Figure 4.1 shows the energy spectrum of the Ξ^0 produced at the target, and the energy spectrum of Ξ^0 which survive to $z = 90\,m$. It is because only the highest energy Ξ^0 survive to $z = 90\,m$ that we base our triggering strategy on finding a high momentum track down the beam hole.

It is perhaps also worth mentioning that the correct value for the fudge factors will also depend somewhat on the lifetime of the Ξ^0 .

4.2 Simulation of Decay Processes

The Ξ^0 decay z positions are distributed according to their momenta and lifetimes in the specified decay volume and momentum range ($160\,m > z > 90\,m, 600\,GeV/c > p > 150\,GeV/c$). The distributions of the decay particles are produced and the polarizations of the decay products are set according to the MC physical parameters.

The decay products are traced through the detector and decay according to their lifetimes and momenta. The distribution of the grand-daughter particles depends on the calculated polarization of the daughter particles.

The physical response of the material in the detector to decay product particles is also simulated (i.e. conversion of photons, bremsstrahlung radiation of electrons, multiple scattering).

4.3 Simulation of KTeV Detector Elements

4.3.1 Drift Chambers

When a charged particle reaches the plane of a chamber, the position gets smeared by the measured resolution. The resolution has a Gaussian component ($\approx 100\,\mu m$) for each plane, and a region-by-region effective ionization density, which effectively produced an exponential tail in the resolution, (both measured from data). The smeared distance is translated into a drift time, and the drift time is recorded.

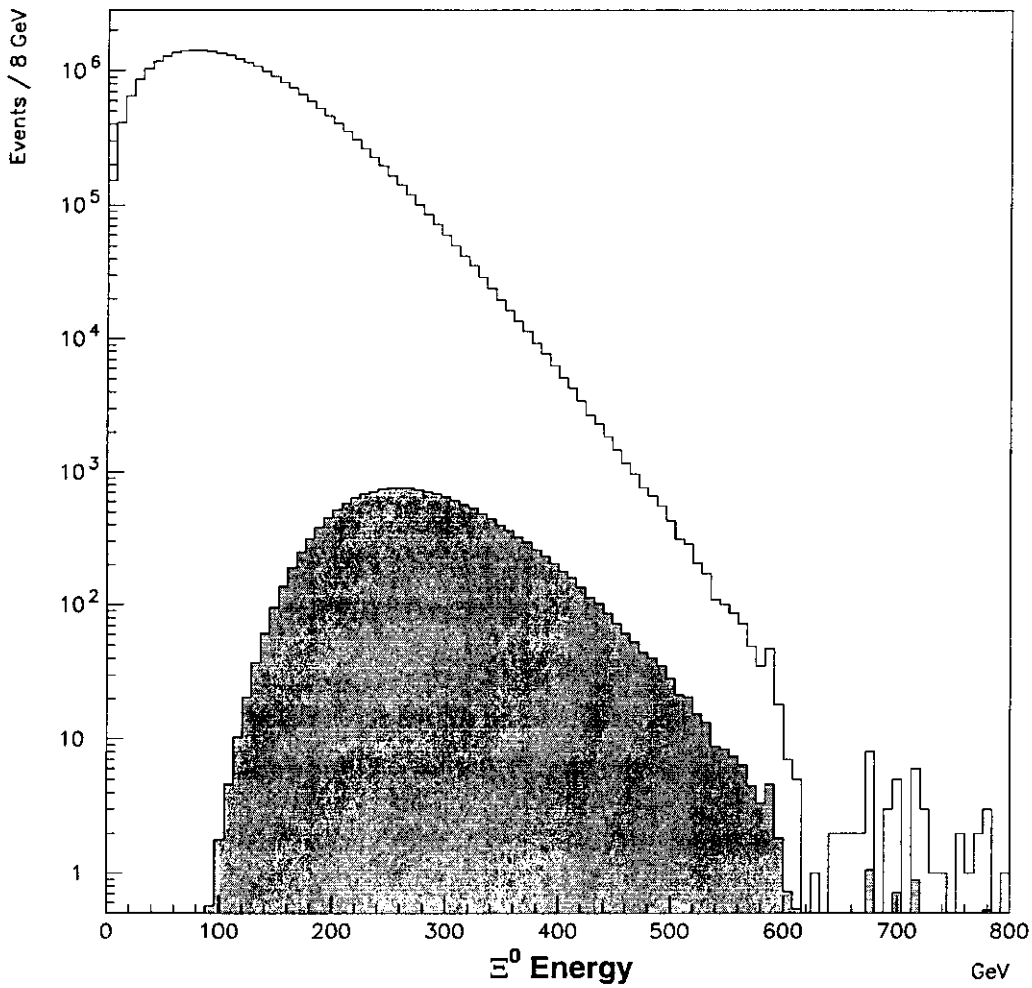

Figure 4.1: The energy spectrum of Ξ^0 produced at the KTeV target, using equation (4.1). The filled histogram shows Ξ^0 that survive to $z = 90\,m$.

The drift time is modified or dropped according to the inefficiency and hi-SOD probability. Also, delta rays (knock-on electrons) are also simulated, though they do not propagate across cells in the Monte Carlo.

4.3.2 Calorimeter

Electromagnetic showers involve a large number of particles, 2^t where t is the number of radiation lengths (X_0) traveled (CsI blocks are $27\,X_0$ long). Therefore, rather than simulate each shower from scratch, a shower is picked from a "library" of simulated showers made using GEANT, a shower simulation software package. The showers in the library are binned in energy (2,4,8,16,32, and 64 GeV) , transverse position (ranging from $0.7\,mm$ at the center of the crystal, and $0.2\,mm$ at the crystal boundaries), and longitudinal position (25 $2\,cm$ bins) [58]. Pion showers are handled in a similar manner, with different binning (12 energy bins, ranging from $4\,GeV$ to $64\,GeV$, 10 divisions in each lateral direction [59].

The HCC and ET trigger elements are simulated based on the resulting simulated energy in the calorimeter.

4.4 Accidental Overlays

There was a large neutron and kaon flux present in the experiment, resulting in an underlying activity in the detector, (extra drift chamber hits, extra clusters in the calorimeter, etc.). A special accidental trigger randomly sampled the activity in the detector at times when there was activity at the target. The accidental trigger was made from a series of three counters which instrumented a hole in the target setup. This trigger was prescaled by 25,000. These accidental events are overlaid with Monte Carlo physics event simulation to account for this activity.

4.5 Simulation of Hyperon Triggers

4.5.1 Hole Counters (HC)

In KTEVMC, if a charged particle is in the $16 \times 16\,cm^2$ box at $z = 189.61\,m$, the appropriate MC trigger bits are set. Each $16 \times 16\,cm^2$ hole counter paddle covers the entire beam hole.

The efficiency of the hole counter paddles in the Monte Carlo is assumed to be .96 across the entire surface of the paddle. Using two track events in the accidental trigger, we measure the hole counter efficiency to be $.950 \pm .005$ for the right hole counter, and $.952 \pm .005$ for the left hole counter. We see no significant variation across the surface of the hole counter paddles in x or y (Figure 4.2). We conclude our current simulation of the hole counters is adequate for this result.

4.5.2 Drift Chamber Fast Ors (DCFO)

In KTEVMC, any hit in the in time window sets the trigger bit for the appropriate DCFO paddle. The area of the drift chambers instrumented by the fast ors completely envelopes the area instrumented by the STT.

4.5.3 Stiff Track Trigger (STT)

The Banana and Kumquat boards are simulated in KTEVMC. The KTEVMC STT result is based on the simulated Kumquat and Banana data. KTEVMC also allows for an adjustable prescale, as was used in the data.

4.6 Simulation of Drift Chamber Inefficiencies and Hi-Sods

Maps of the spatial and time dependence of the hi-SOD probability and chamber inefficiencies were made for the summer E799 data using trigger 2 $K_L \rightarrow \pi^+ e^- \overline{\nu}_e$ decays [76].

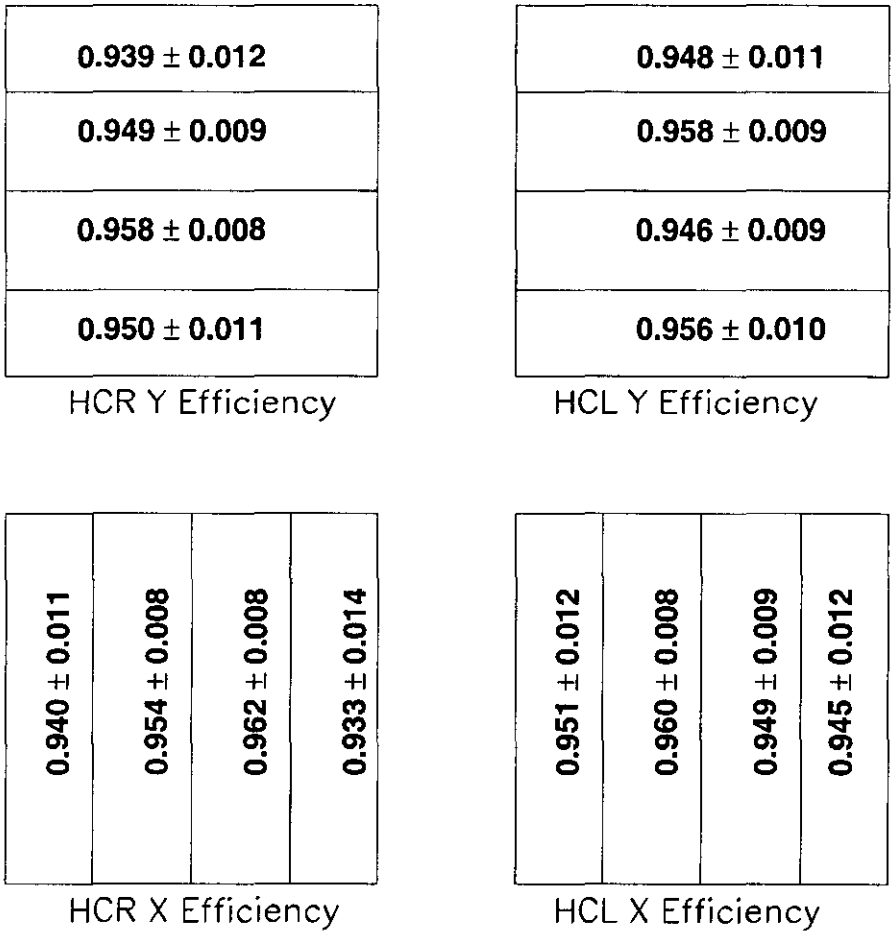

Figure 4.2: The efficiency of the hole counter paddles for the summer run, divided up into 4 slices in x and y.

Chapter 5
EVENT RECONSTRUCTION

In order to study the physics quantities of Ξ^0 decays, we need to reconstruct the momenta of the decay products, and the location of the decay vertices. Here we describe the reconstruction of charged tracks from the drift chamber information, and the reconstruction of electro magnetic clusters from the CsI data.

5.1 Track Finding

5.1.1 Hit Pairs

First 'pairs' of hits on complimentary wires are found. Each 'hit' is read out as a TDC time, which is converted into a distance from the wire. The distances from two complimentary wires should add up to distance between complimentary wires, this 'Sum of Distances' or 'SOD' is used to evaluate whether or not the 'pair' of hits should be used. In this context, 'pair' can mean either two hits on complimentary wires or a single isolated hit.

Y Track Candidates

All combinations of hit pairs that can reasonably form a track in y are evaluated. The 'pair values' are summed up over all four drift chambers, and the sum is used to determine whether or not that track can be used.

X Track Candidates

Since the tracks bend in the x plane, we find segments in the first two and last two chambers separately.

A similar procedure is followed to find these tracks, though the sum of pair values is taken for upstream and downstream segments separately.

5.1.2 Vertex Finding

For all decays studied here, there are two charged particles whose momenta we wish to reconstruct Furthermore, the two charged tracks physically originate from the same point (with the exception of $\Xi^0 \to \Sigma^+ e^- \overline{\nu}_e$, where the electron comes from the Ξ^0 vertex, and the proton comes from the Σ^+vertex, generally a few meters downstream of the Ξ^0 vertex).

Vertex Candidates

First pairs of x and y tracks are looped over. The z position of where each pair of x and y tracks are found. If they are within a specified distance of each other, a vertex candidate is found.

For each vertex, an attempt to match the tracks to clusters in the calorimeter is made. For most decay modes in KTeV, both tracks are required to match clusters in the calorimeter. However, for hyperon decays, one of the tracks points down the beam hole.

A quality value for each vertex candidate is calculated:

$$Q_{VTX} = \chi^2_{VTX} + \frac{1}{8}(\chi^2_{offmag,1} + \chi^2_{offmag,2}) + (16 - Ng_{x,1} - Ng_{x,2} - Ng_{y,1} - Ng_{y,2}) \quad (5.1)$$

where χ^2_{VTX} is the vertex χ^2 the goodness of fit for the upstream track segments to the hypothesis that both tracks originate from the same point in space [55]. The quantity χ^2_{offmag} is the OFFMAG χ^2. For each track, we define OFFMAG as the distance between the projections of the upstream and downstream track segments at the center of the analysis magnet. The expected error in OFFMAG is then calculated based on the distance resolution of the drift chambers. The OFFMAG χ^2 is just $OFFMAG^2/\sigma^2_{OFFMAG}$. The quantity $(16 - Ng_{x,1} - Ng_{x,2} - Ng_{y,1} - Ng_{y,2})$ is the number of single hits and bad-sod pairs.

The vertex candidate with the lowest Q_{VTX} is chosen as the charged vertex.

5.1.3 Calibration of Chambers

Transforming the timing information from the drift chambers into track momenta requires us to know: the relationship between TDC time and distance from the sense wire, and the position and orientation of each drift chamber in space. The time to distance relation is found from the data, assuming the illumination is constant over a cell. The position information is found from a multi stage procedure. First, using data from runs where the analysis magnet is turned off, and a beam stop covers the two neutral beams.

The result is a beam of muons which pass straight through the detector. The straight tracks are then over-constrained in x and y.

Since only two points are needed, two of the drift chambers (in this case chambers 1 and 3) are in the correct position then the offsets and rotations of the other two chambers are measured.

In general, the two chambers that are held fixed in the muon alignment process are not aligned with each other correctly. If the two chambers are rotated with respect to one another, there will be a 'corkscrew' rotation of the four chamber system.

Consider two tracks passing through the upstream chambers, we define the $\vec{r}_{1,2}$ as the vector connecting the points where the two tracks intersect the plane of chambers 1 and 2 (figure 5.1). The rotation of chamber 2 relative to chamber 1 is found from:

$$sin(\phi) = \frac{\vec{r}_1 \times \vec{r}_2}{\mid \vec{r}_1 \mid\mid \vec{r}_2 \mid} \tag{5.2}$$

The corkscrew rotation for chambers 3 and 4 is just proportional to the difference in the z positions:

$$\phi_3 = \phi \times \frac{Z_{DC3} - Z_{DC1}}{Z_{DC2} - Z_{DC1}} \tag{5.3}$$

$$\phi_4 = \phi \times \frac{Z_{DC4} - Z_{DC1}}{Z_{DC2} - Z_{DC1}} \tag{5.4}$$

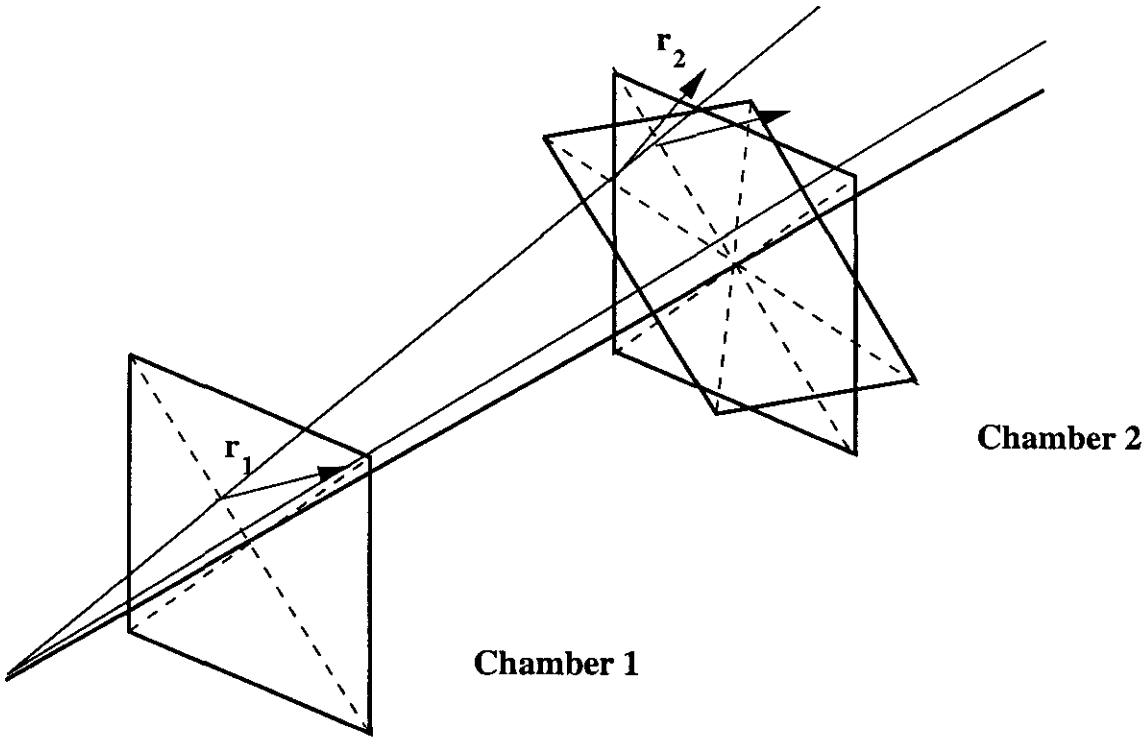

Figure 5.1: Illustration of 'Corkscrew' rotation between chambers 1 and 2.

At this point, all that remains in the global alignment of the chamber system with respect to the CsI and the target. Alignment with the CsI is accomplished by matching the electron tracks from $K_L \rightarrow \pi^+ e^- \overline{\nu}_e$ with their clusters in the CsI, and alignment with the target is accomplished by pointing the total momentum from $K \rightarrow \pi^+\pi^-$ decays back to $z = 0$. The procedure is described in more detail elsewhere [56, 57].

5.2 Cluster Finding

The blocks with the HCC bits on,that is, CsI channels with at least $\approx 1\,GeV$ in them are examined. A local maximum is found, that block is taken as a cluster 'seed'. The energy in that 3×3 large block (7×7 small block) region is summed up (in 4 $19\,ns$ 'slices' of time). We also look for 'software' clusters, that is, clusters *not* having a seed block with the HCC bit on. However, since we require that clusters

have at least $3\,GeV$ of energy in the final analysis, this is not important.

5.2.1 Corrections to Cluster Energy and Position

Overlap Separation

Often, two clusters share crystals. The energy in shared crystals is split up among the clusters, and the energy and position of the clusters are recalculated. The process is iterated until the energy on each crystal changes by less than $5\,MeV$, and the position of each crystal (both x and y) changes by less than $100\,\mu m$ (maximum of 20 iterations).

Neighbor Correction

This correction adjusts the energy of clusters if a nearby cluster could deposit a significant amount of energy to it, even though it is out of the 3×3 boundary.

Missing Block Correction

If a cluster is near a beam hole or the edge of the CsI array, the energy in the missing block(s) is inferred from the energy in the other blocks.

Threshold Correction

In the CsI, blocks below threshold (about $7\,MeV$) are not read out. This correction infers the energy present in such blocks in a cluster and adds it to the observed energy.

Intra-Block Correction

The response of each crystal was found to vary depending on the transverse position of the center of the shower. The intra-block correction compensates for this effect using the measured response to electrons (using the measured momentum) in 25 position bins in each crystal.

5.2.2 Calorimeter Calibration

The raw data from the CsI is just the number of DPMT counts. Two sets of constants are needed to convert the readout value to the correct energy. First, we must determine the number of DPMT counts we expect for a given PMT charge. Since the DPMT is a multi-range device, (8 ranges) with 4 'phases' (there are 4 capacitors on which charge is stored, each bucket cycles the charge through the next capacitor), the 32 relative gains must be determined. We also need the amount of charge on the PMT as a function of the electron energy. This is accomplished using electrons from $K_L \rightarrow \pi^+ e^- \overline{\nu}_e$ decays where the energy ($\approx$ momentum) of the electron is measured with the charged spectrometer

Chapter 6

THE DECAY $\Lambda \rightarrow p\pi^-$

In this chapter, we present the $\Lambda \rightarrow p\pi^-$data taken in trigger B12 for the summer E799 run.

6.1 Polarization of Λ

The Λ are produced with a polarization of about 10 % [61]. The direction of the polarization is normal to the production plane. The sweeping magnets are arranged to precess the polarization of Ξ^0 to the z direction. Since the magnetic moment of the Λ is only 1/2 that of the Ξ^0 , the polarization of the Λ only precesses half as much in the sweeping magnets.

6.2 Reconstruction and Event Selection

Spills flagged for problems in table 6.2 of severity code 1 were excluded (spills could either be flagged as severity code 1 ('severe') or 2 ('warning'), though in practice severity code 2 was never used).

Also, runs 10596 and 10599 were excluded as they had the incorrect `PTKICK` sign in the database.

These events are reconstructed by finding the two track $\Lambda \rightarrow p\pi^-$vertex.

Fiducialization cuts are applied to the Λ vertex and trigger verification cuts are applied:

- $158.0\,m > z_\Lambda > 95.0\,m$ - We require the Λ vertex to be downstream of any fringe fields from the final sweeping magnet, and upstream of the vacuum window.
- $.00124 >| x_\Lambda/z_\Lambda |> .000376$
- $.00043 >| y_\Lambda/z_\Lambda |$ - the Λ vertex must be located in the neutral beam.

Bit	Description
1	Trigger
2	DPMT ped exp > 0
5	Misc dead DPMT
9	Pipeline
10	Global CsI Problems
11	ETOT Problems
12	FERA Problems
13	Drift Chamber Problems
14	Veto Problems
15	V,V' Problems
17	HCC Problems
18	KQ/BAN Problems
20	Hyperon Trigger Problems
21	DAQ/L3 Problems
22	NOT 799 run
23	Short run
29	Beam Problems

Table 6.1: Bits used to reject bad spills for $\Lambda \rightarrow p\pi^-$and $\Xi^0 \rightarrow \Lambda\pi^0$ candidate events

- Absolute value of x position of proton between $.07\,m$ and $.22\,m$ at both $186.0\,m$ and $189.6\,m$
- y position of proton between $-.07\,m$ and $.07\,m$ at both $186.0\,m$ and $189.6\,m$ - the proton must travel down a beam hole
- The π^- is required to miss the beam holes by $.5\,cm$ - the π^-must hit the CsI
- Positive track passes through STT illuminated region, and appropriate Kumquat and Banana channels have hits in them (verify STT)
- Number of proper lifetimes reconstructed as $\Lambda \rightarrow p\pi^- < 10.0$ (verify L3)
- $375.0\,GeV/c > \mid p_p \mid > 110.0\,GeV/c$ (verify L3)
- $100.0\,GeV/c > \mid p_p \mid > 5.0\,GeV/c$ (verify L3)
- $\mid p_p \mid / \mid p_e \mid > 3.0$ (verify L3)

Kinematic and particle ID:

- $0.8 > E/p$ (negative track) - showers from charged pions tend to only deposit a fraction of their energy in the CsI, this cut eliminates nearly all events where the negative track is from an electron
- Neither track is allowed to match a hit in the muon counters (reject $\pi \rightarrow \mu$ decays)
- charged vertex $p_{\perp}^2$(VTXPT2) $< .0025\, GeV^2/c^2$
- $\mid m_{\pi^+\pi^-} - m_K(.4976\, GeV) \mid > .025\, GeV$ (Remove $K \rightarrow \pi^+\pi^-$ decays)

When all the selection criteria are applied, we find 12632 events in the data having a reconstructed $p\pi^-$ invariant mass within $.015\, GeV/c^2$ of the nominal Λ mass of $1.115684\, GeV/c^2$ [10].

The only background is considered from $K \rightarrow \pi^+\pi^-$, requiring the $\pi^+\pi^-$ mass be at least $25\, MeV$ away from the K_L mass effectively reduces this background (figure 6.1) to a negligible level.

In order to estimate the effect of lost tracks in the beam region, we have implemented a procedure to map out regions of the chamber where events are lost due to hi-SODs and inefficiencies [76].

The 'maps' are made from trigger 2 $K_L \rightarrow \pi^+ e^- \overline{\nu}_e$ decays. Then, in Monte Carlo, drift chamber hits are either then discarded or their simulated TDC times modified according the maps and a user specified weight. The Monte Carlo acceptance depends on the weight given to the hi-SOD and inefficiency maps. Trigger 12 has no Stiff Track Trigger requirement, so we can measure its acceptance with trigger 12 $\Lambda \rightarrow p\pi^-$ decays. In table 6.2 we show the STT acceptance and total Λ flux for different hi-SOD and inefficiency map weights. In the table "Geometry" refers to $\Lambda \rightarrow p\pi^-$ events where the proton is in the STT instrumented area in all four chambers, and "KQ-BAN" refers to the proton is in the STT instrumented area in all four chambers AND sufficient Kumquat and Banana channels record hits to satisfy the STT requirement. Increasing the hi-SOD map weighting in Monte Carlo increases

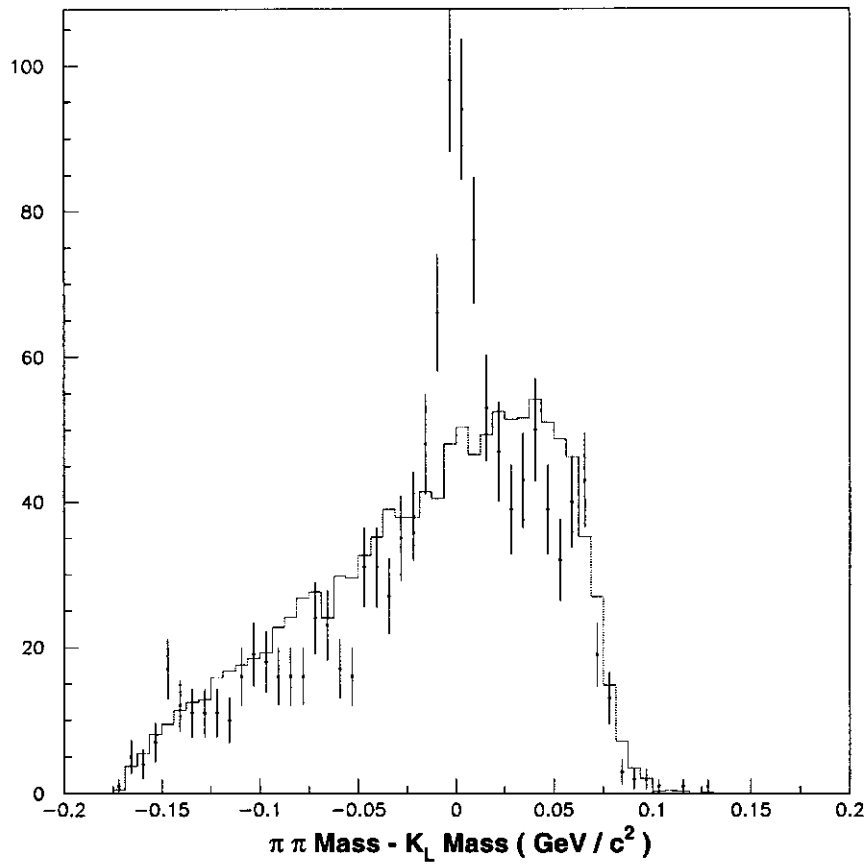

Figure 6.1: The $\pi^+\pi^-$ mass - K_L mass for events passing $\Lambda \to p\pi^-$selection criteria, the histogram are data events where the high momentum track is positive (scaled by 1/11), the dots are data events where the high momentum track is negative. Since $\overline{\Lambda}$ production is suppressed relative to Λ , and the decay $K \to \pi^+\pi^-$ is charge symmetric, we see that by cutting at $\pm 25\, MeV$ away from the K_L mass, we have a negligible $K_L \to \pi^+\pi^-$ background.

WGT	Geometry / Total	KQ-BAN / Geometry	ACC_{MC}	Λ flux ($\times 10^9$)
DATA	$.812 \pm .003$	$.952 \pm .002$	x	x
0.0	$.825 \pm .003$	$.980 \pm .002$	$.1963 \pm .0013$	$2.01 \pm .03$
0.5	$.818 \pm .003$	$.958 \pm .002$	$.1958 \pm .0013$	$2.02 \pm .03$
1.0	$.813 \pm .003$	$.944 \pm .002$	$.1850 \pm .0013$	$2.14 \pm .03$

Table 6.2: Λ flux

the probability of high SODs occurring in the beam region, which will in turn cause events to fail the STT - KQ/BAN requirement more often.

The flux is calculated according to:

$$Flux = \frac{N_{Data}}{BR \times PS \times Acc_{MC}} \tag{6.1}$$

We choose our 'nominal' hi-SOD/inefficiency weight to be 0.5 ± 0.5. Meaning that the probability for a Monte Carlo drift chamber hit to be lost or have its drift time modified is $.5\times$ the probability found for $K_L \rightarrow \pi^+ e^- \overline{\nu}_e$ decays in the data. Hence our measured Λ flux is $2.0 \pm .1 \times 10^9$.

6.3 Efficiency of Drift Chamber Fast Ors (DCFO)

The trigger 12 $\Lambda \rightarrow p\pi^-$decays present an opportunity to measure the efficiency of the DCFO trigger elements used in L1 for triggers 10 and 11. For events passing all cuts, and having the positive track travel down the STT instrumented area in all chambers (figure 6.2), we find 5078 of 5117 events in the left beam hole have the appropriate FAST-OR trigger bits set (efficiency = $.994 \pm .001$), and 5122 out of 5142 events in the right beam hole have the appropriate FAST-OR trigger bits set (efficiency = $.996 \pm .001$). No attempt to model this inefficiency is made in KTEVMC.

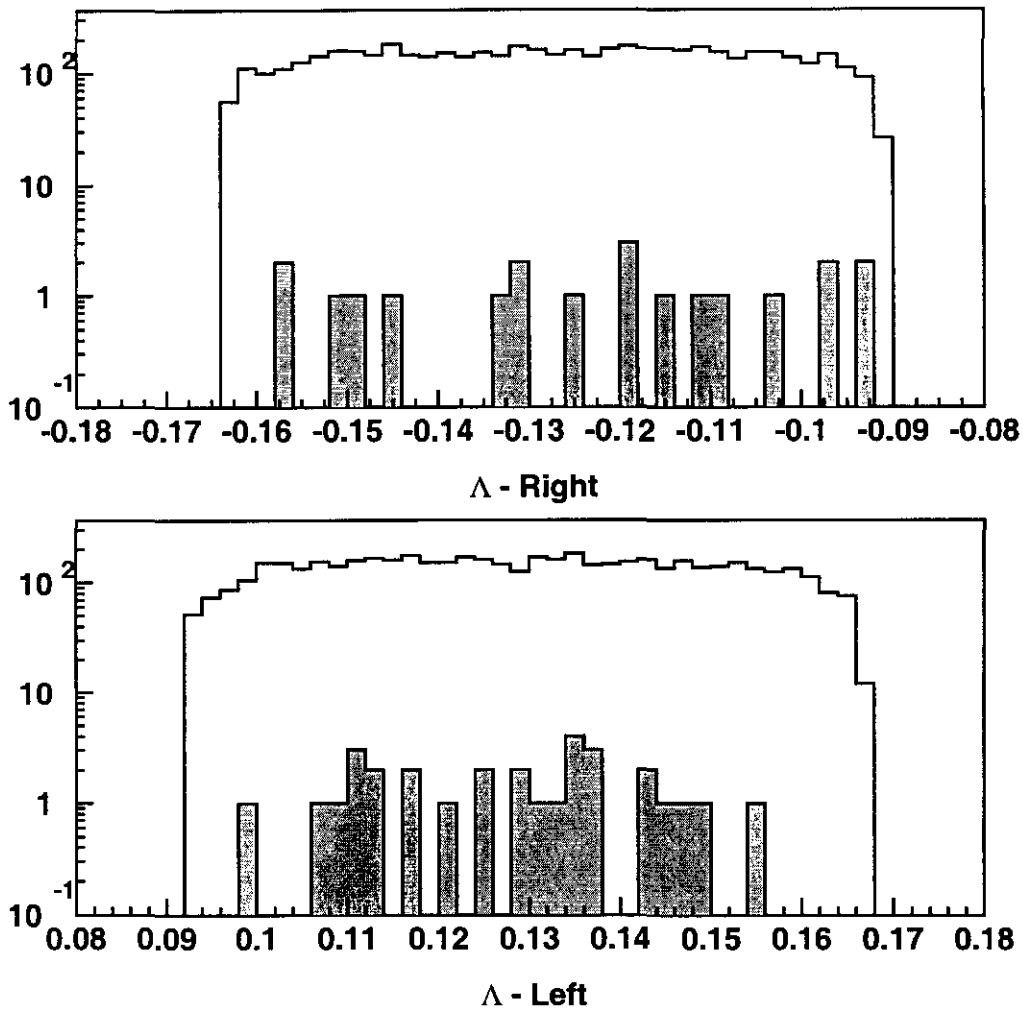

Figure 6.2: The X position of the positive track at DC1 for trigger 12 $\Lambda \rightarrow p\pi^-$ decays. The top plot is for $\Lambda \rightarrow p\pi^-$ where the proton travels down the right beam hole, the bottom plot is for $\Lambda \rightarrow p\pi^-$ where the proton travels down the left beam hole. In both plots, the unshaded histogram are data events passing all selection criteria, and the shaded histogram are data events where the appropriate DC Fast Or trigger bits are not set.

6.4 Data / Monte Carlo Comparisons

Figures 6.3 through 6.6 show data / Monte Carlo comparisons of various distributions for $\Lambda \rightarrow p\pi^-$decays.

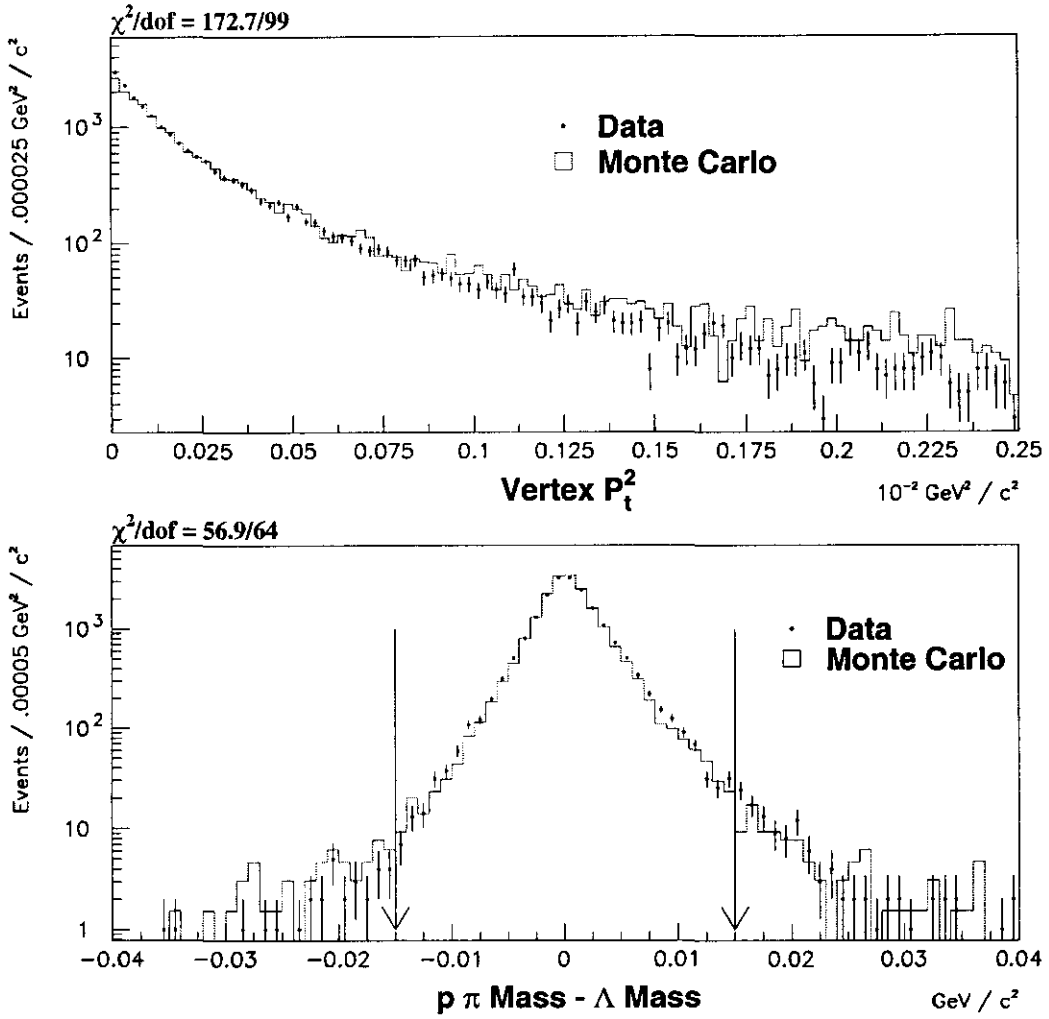

Figure 6.3: Data-Monte Carlo comparison of the Λ vertex $p_\perp^2$(top) and $p\pi^-$ mass $-\Lambda$ mass (bottom)(the dots are data and the histogram is Monte Carlo) .

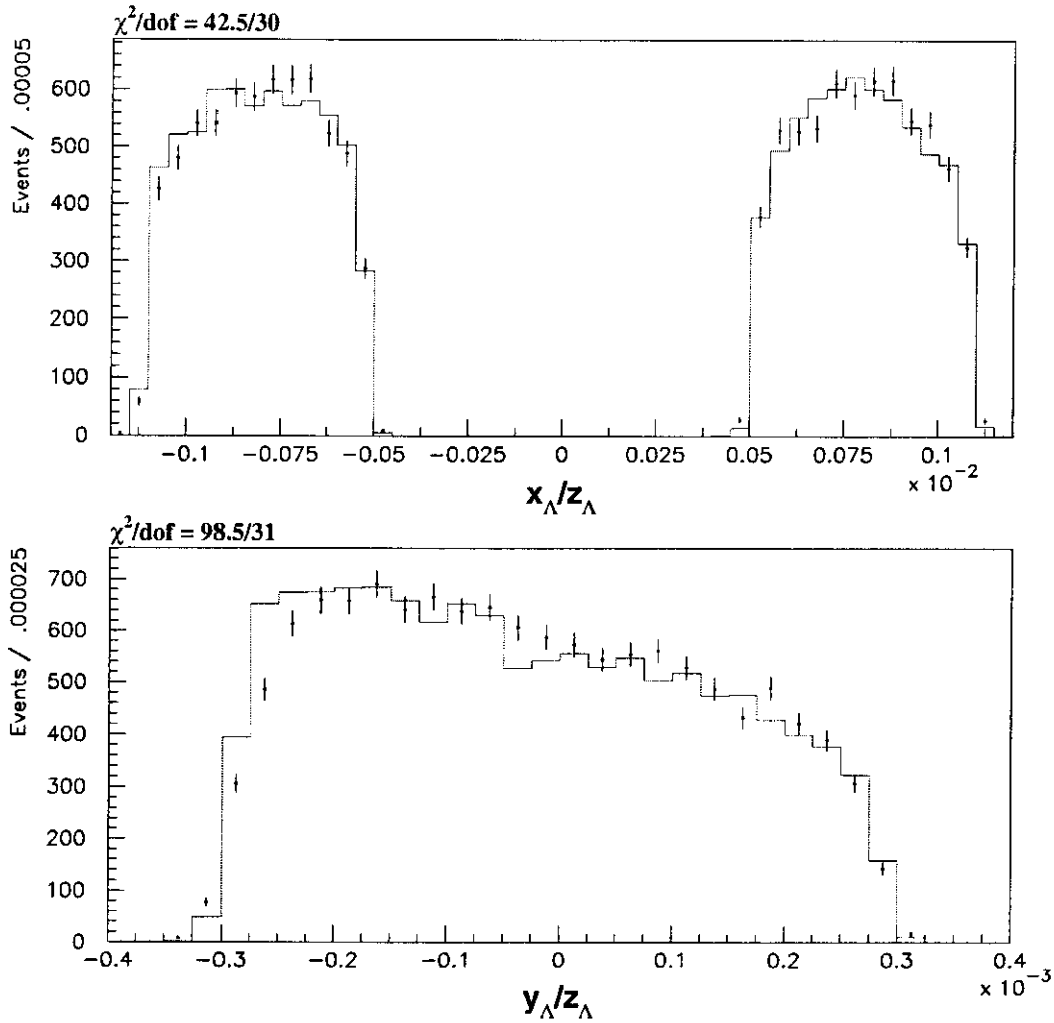

Figure 6.4: Data-Monte Carlo comparison of x/z of the Λ vertices (top) and y/z of the Λ vertices (bottom)(the dots are data and the histogram is Monte Carlo).

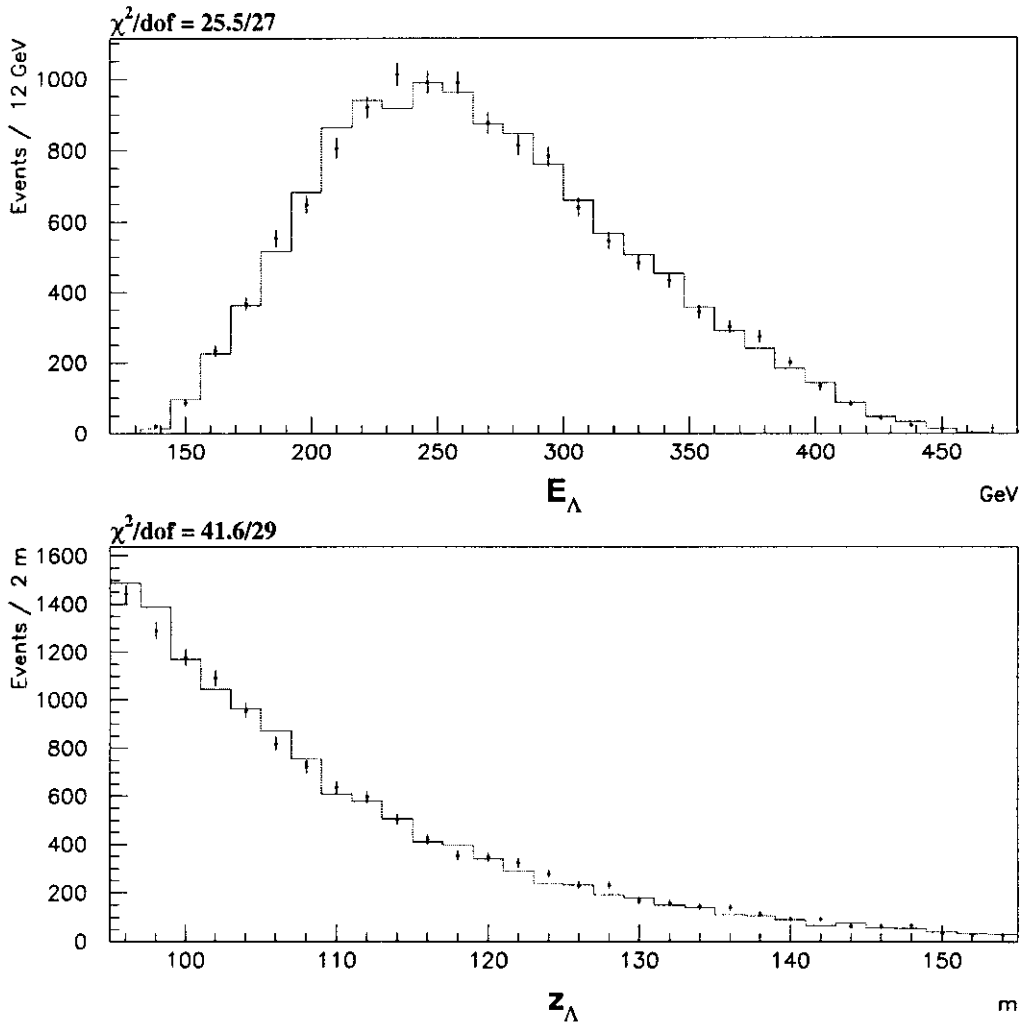

Figure 6.5: Data-Monte Carlo comparison of Λ energy (top) and z position of the Λ vertex (bottom)(the dots are data and the histogram is Monte Carlo).

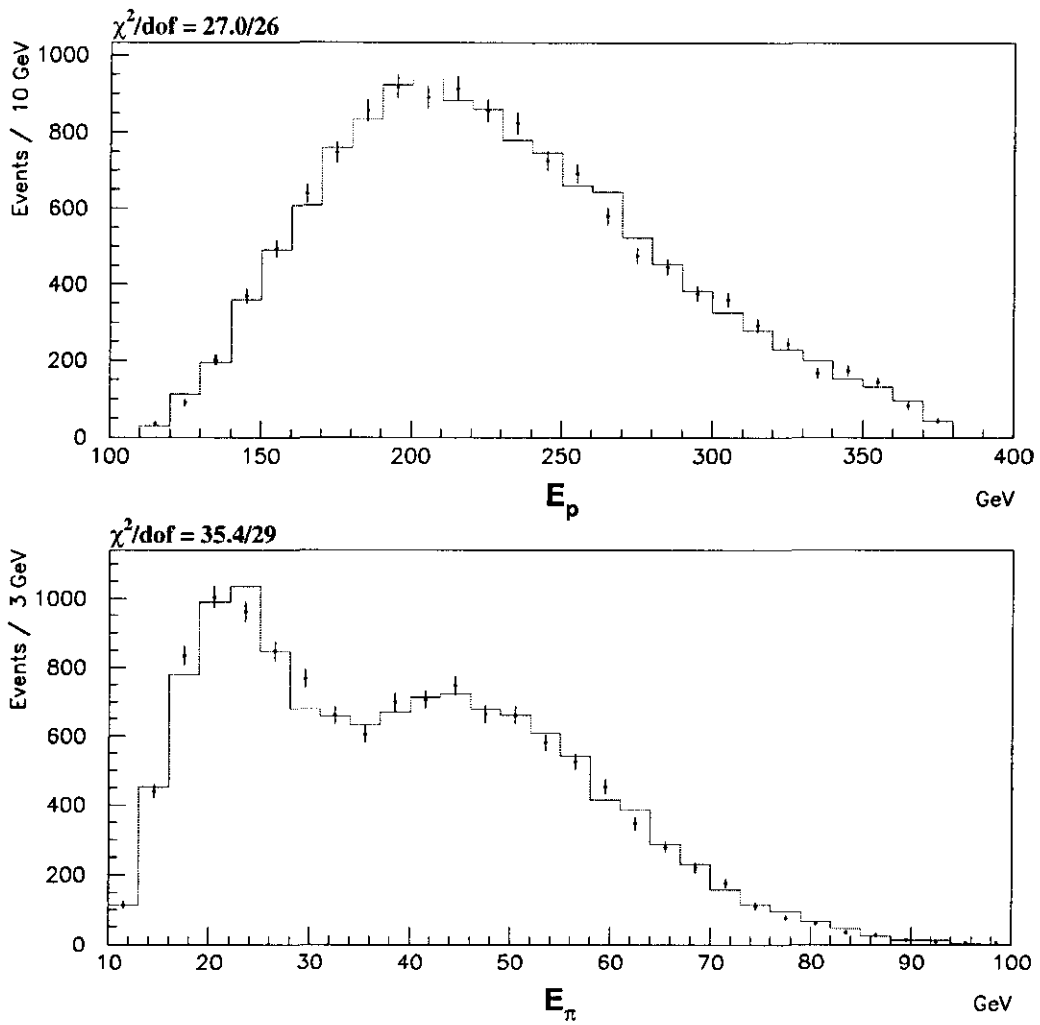

Figure 6.6: Data-Monte Carlo comparison of proton energy (top) and π^-energy (bottom)(the dots are data and the histogram is Monte Carlo).

Chapter 7

THE DECAY $\Xi^0 \to \Lambda\pi^0$ WITH $\Lambda \to p\pi^-$

In this chapter, we present the $\Xi^0 \to \Lambda\pi^0$ with $\Lambda \to p\pi^-$data obtained in trigger B11 during the E799 summer run.

7.1 Polarization of Ξ^0

The Ξ^0 are produced with a polarization of about 10 %. The direction of the polarization is normal to the production plane. The sweeping magnets are arranged to precess the polarization of the the Ξ^0 to the z direction. The spin rotator magnet ($NM2SR$) then rotates the polarization 90° to either the $+y$ or $-y$ direction. Care was taken to ensure that we had equal amounts of data taken with the two polarization settings, and we find that the number of events with the two settings are equal to one part in one hundred. Therefore, we can consider our Ξ^0 beam to be unpolarized for the summer dataset.

For the winter data set, the sweeping magnets were set to produce Λ polarized in the $\pm y$ directions. Since the magnetic moment of the Ξ^0 is about twice that of the Λ , the polarization of the Ξ^0 in the winter is somewhere in the $x - z$ plane. Details of the Λ and Ξ^0 polarization analyses in E799 can be found elsewhere [61, 62].

7.2 Phenomenology of $\Xi^0 \to \Lambda\pi^0$

The transition matrix for the process is:

$$\mathcal{M} = \overline{u}_\Lambda (A + B\gamma_5) u_{\Xi^0} + H.c., \tag{7.1}$$

containing both parity-violating (A) and parity-conserving (B) amplitudes [63]. Defining $\overline{B}$ by

$$\overline{B} = B\sqrt{\frac{E_\Lambda - m_\Lambda}{E_\Lambda + m_\Lambda}}, \tag{7.2}$$

where E_Λ is the energy of the lambda in the Ξ^0 frame, and m_Λ is the mass of the lambda.

The differential decay rate is

$$\frac{d\Gamma}{d\Omega_\Lambda} = \frac{\sqrt{(E_\Lambda^2 - m_\Lambda^2)}(E_\Lambda + m_\Lambda)}{16\pi^2 m_{\Xi^0}}(\mid A \mid^2 + \mid \overline{B} \mid^2)(1 + \alpha_{\Xi^0}\hat{\Lambda}\cdot\vec{P}_{\Xi^0}) \tag{7.3}$$

where $\vec{P_{\Xi^0}}$ is the polarization of the Ξ^0 and $\hat{\Lambda}$ is the direction of the Λ momentum in the Ξ^0 frame.

The asymmetry of the Ξ^0 decay is then

$$\alpha_{\Xi^0} = \frac{2Re(A^*\overline{B})}{\mid A \mid^2 + \mid \overline{B} \mid^2} \tag{7.4}$$

The polarization of the Λ from the decay is given by

$$\vec{P_\Lambda} = \frac{(\alpha_{\Xi^0} + \hat{\Lambda}\cdot\vec{P_{\Xi^0}})\hat{\Lambda} - \beta_{\Xi^0}(\hat{\Lambda}\times\vec{P_{\Xi^0}}) - \gamma_{\Xi^0}(\hat{\Lambda}\times\hat{\Lambda}\times\vec{P_{\Xi^0}})}{1 + \alpha_{\Xi^0}\hat{\Lambda}\cdot\vec{P_{\Xi^0}}} \tag{7.5}$$

with

$$\beta_{\Xi^0} = \frac{2Im(A^*\overline{B})}{\mid A \mid^2 + \mid \overline{B} \mid^2}, \tag{7.6}$$

$$\gamma_{\Xi^0} = \frac{\mid A \mid^2 - \mid \overline{B} \mid^2}{\mid A \mid^2 + \mid \overline{B} \mid^2}. \tag{7.7}$$

Notice that $\alpha_{\Xi^0}^2 + \beta_{\Xi^0}^2 + \gamma_{\Xi^0}^2 = 1$.

The polarization of the Λ can be observed via its two body decay $\Lambda \to p\pi^-$. If the Ξ^0 are unpolarized, the distribution of the proton in the lambda frame, relative to the direction of the Ξ^0 , (opposite to the π^0) in the Λ frame will follow

$$\frac{dN}{d(\hat{p}\cdot\hat{\pi^0})} = \frac{1}{2}(1 + \alpha_{\Xi^0}\alpha_\Lambda(-\hat{p}\cdot\hat{\pi^0})). \tag{7.8}$$

7.3 Reconstruction and Event Selection

These events are reconstructed by finding the two track $\Lambda \rightarrow p\pi^-$vertex, and extrapolating the position of the Λ to the z position of the $\pi^0$from the two extra clusters.

$$z_{\pi^0} = z_{CSISHM} - \frac{r_{12}}{m_{\pi^0}}\sqrt{E_1 E_2} \tag{7.9}$$

z_{CSISHM} is the mean z position used for the electromagnetic showers ($17\,cm$ downstream of the CsI front face). The quantity r_{12} is the distance between the two photon clusters in the CsI, m_{π^0} is the mass of the π^0, and E_1 and E_2 are the cluster energies.

Fiducialization cuts are applied to the Λ and Ξ^0 vertices, and trigger verification cuts are applied:

- $158.0\,m > z_\Lambda > 95.0\,m$
- $158.0\,m > z_{\Xi^0} > 95.0\,m$
- $.00124 >| x_{\Xi^0}/z_{\Xi^0} |> .000376$
- $.00043 >| y_{\Xi^0}/z_{\Xi^0} |$
- $.00124 >| x_\Lambda/z_\Lambda |> .000376$
- $.00043 >| y_\Lambda/z_\Lambda |$
- Absolute value of x position of proton between $.07\,m$ and $.22\,m$ at both $186.0\,m$ and $189.6\,m$
- y position of proton between $-.07\,m$ and $.07\,m$ at both $186.0\,m$ and $189.6\,m$
- The π^- is required to miss the beam holes by $.5\,cm$
- Both extra clusters are required to have both x and y positions greater then $9.5\,cm$ away from the edges of center of either beam hole
- The CA (`CAMX_ENE`) is required to have less than $1GeV$ of energy.

- $E_\gamma > 3.0\,GeV$ (verify HCC)
- $E_{\gamma 1} + E_{\gamma 2} > 18.0\,GeV$ (verify ET 1)
- Positive track passes through STT illuminated region, and appropriate Kumquat and Banana channels have hits in them (verify STT)
- Number of proper lifetimes reconstructed as $\Lambda \rightarrow p\pi^- < 14.0$ (verify L3)
- $375.0\,GeV/c > \mid p_p \mid > 110.0\,GeV/c$ (verify L3)
- $100.0\,GeV/c > \mid p_p \mid > 5.0\,GeV/c$ (verify L3)
- $\mid p_p \mid / \mid p_e \mid > 3.0$ (verify L3)

Kinematic and particle ID:

- $0.8 > E/p$ (negative track)
- Neither track is allowed to match a hit in the muon counters (reject $\pi \rightarrow \mu$ decays)
- $m_{K_L \rightarrow \pi^+\pi^-\pi^0} > 0.55\,GeV$ (reject $K_L \rightarrow \pi^+\pi^-\pi^0$)
- $\mid m_{p\pi^-} - 1.115684\,GeV \mid < .015\,GeV$
- charged vertex $p_\perp^2$(VTXPT2) $> .001\,GeV^2/c^2$ (reject target Λ with extra π^0)
- total Ξ^0 $p_\perp^2 < .01\,GeV^2/c^2$
- Both γ 's are at least $20\,cm$ away from where the π^- hits the calorimeter.

When all the selection criteria are applied, we find 67411 events in the data having a reconstructed $\Lambda\pi^0$ invariant mass within $.012\,GeV/c^2$ of the nominal Ξ^0 mass of $1.3149\,GeV/c^2$ [10].

The only backgrounds considered were $K_L \rightarrow \pi^+\pi^-\pi^0$ and $\Lambda \rightarrow p\pi^-$with accidental π^0. The $K_L \rightarrow \pi^+\pi^-\pi^0$ background is effectively eliminated by requiring that

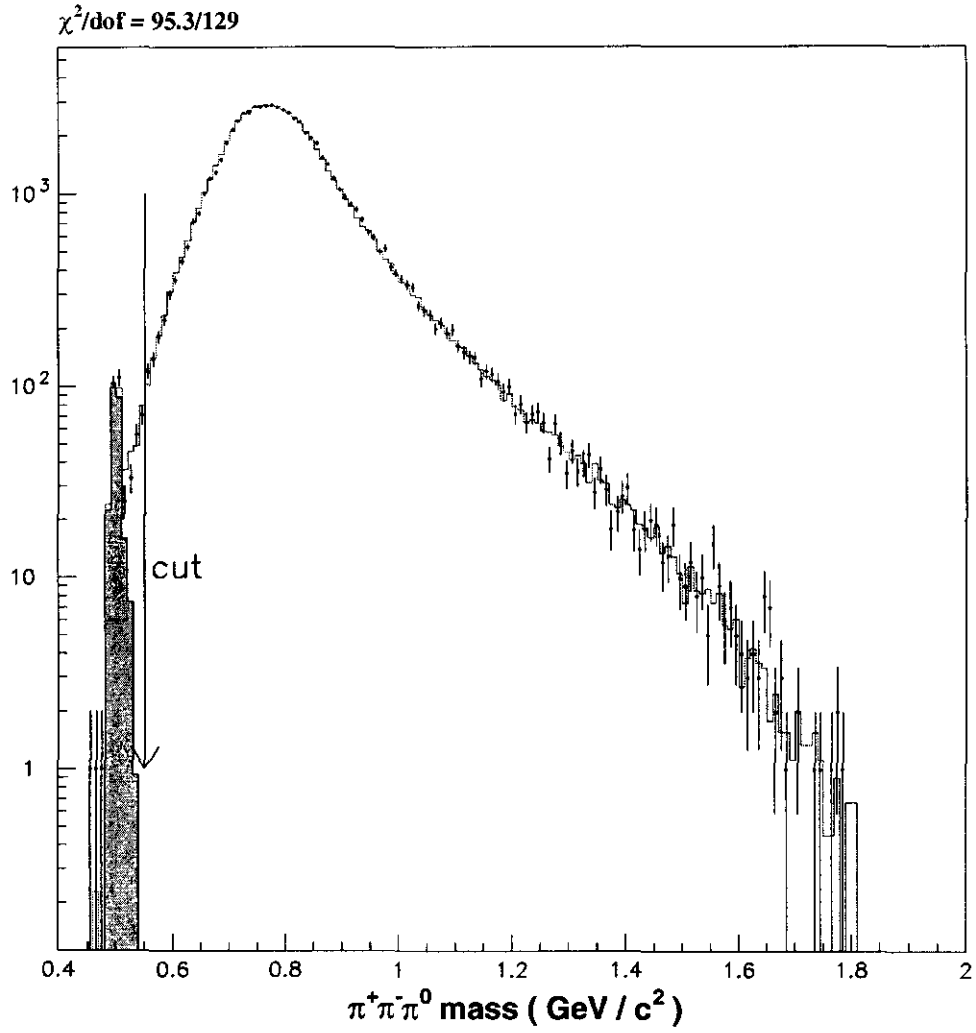

Figure 7.1: The $\pi^+\pi^-\pi^0$mass for Data (dots) compared with the distribution for $\Xi^0 \to \Lambda\pi^0$ Monte-Carlo (histogram) and $K_L \to \pi^+\pi^-\pi^0$ Monte Carlo normalized to measured K_L flux (filled histogram). All selection criteria have been applied except the requirement that the $\pi^+\pi^-\pi^0$mass be greater than $.55\,GeV/c^2$.

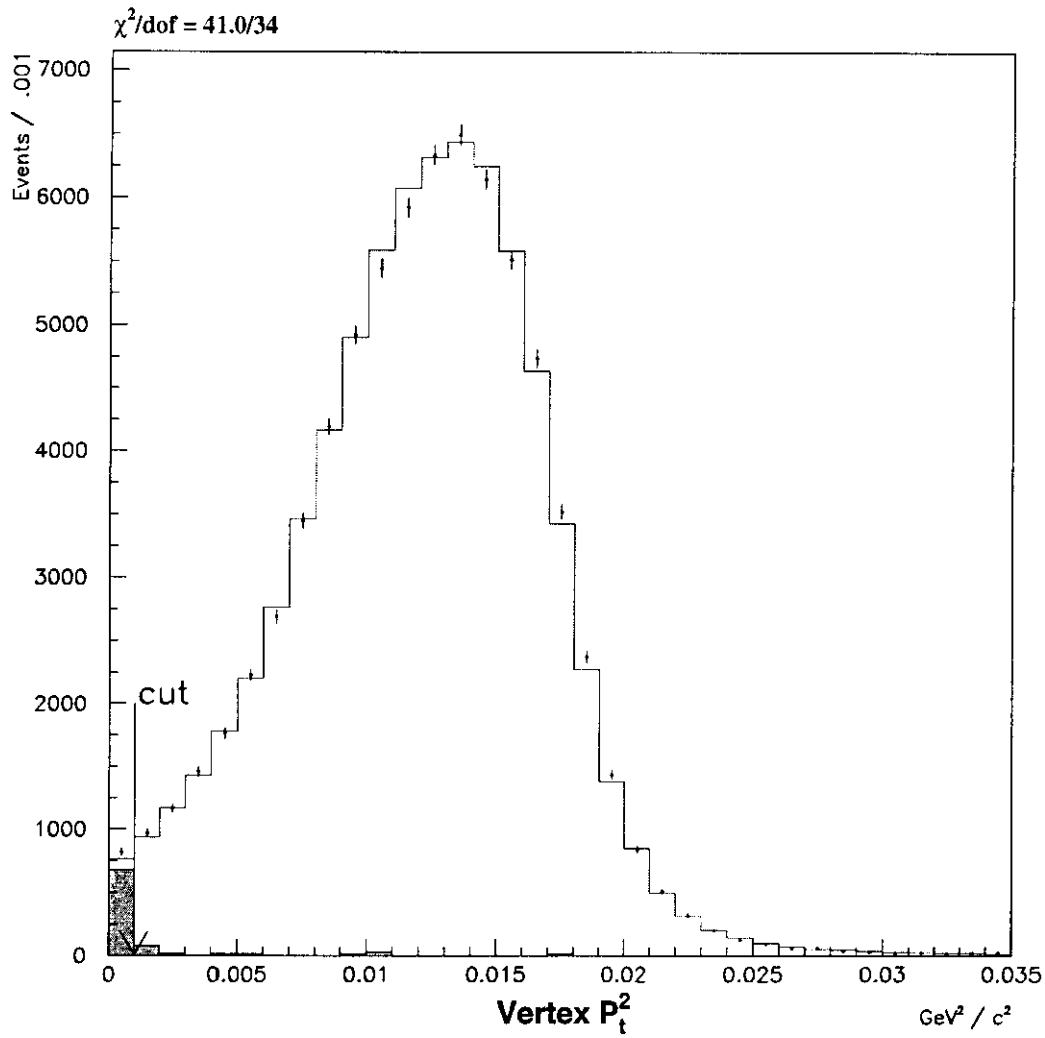

Figure 7.2: The charged vertex $p_\perp^2$ mass for Data (dots) compared with the distribution for $\Xi^0 \rightarrow \Lambda\pi^0$ Monte-Carlo (histogram), the $\Lambda \rightarrow p\pi^- +$ accidental π^0Monte-Carlo (*multiplied by 50*) is also shown (filled histogram). All selection criteria have been applied except the requirement that the charged vertex $p_\perp^2$ be greater than $.001\, GeV^2/c^2$.

WGT	Ξ^0 flux ($\times 10^8$)	ACC_{MC}
0.0	1.09	$.0492 \pm .0002$
0.5	1.14	$.0467 \pm .0001$
1.0	1.22	$.0437 \pm .0002$
1.5	1.30	$.0411 \pm .0002$

Table 7.1: Ξ^0 flux

$m_{K_L \to \pi^+\pi^-\pi^0} > 0.55\,GeV$ (figure 7.1). After all selection criteria are applied, we see no evidence for any non-negligible background to $\Xi^0 \to \Lambda\pi^0$ with $\Lambda \to p\pi^-$.

The Monte Carlo acceptance for the decay depends on the weighting given to hi-SOD and chamber inefficiency maps described in section 6.2.

Using the $\Xi^0 \to \Lambda\pi^0$ with $\pi^0 \to \gamma\gamma$ branching ratio of .629, we can calculate the total Ξ^0 flux:

$$Flux = \frac{N_{Data}}{BR \times PS \times Acc_{MC}} \tag{7.10}$$

Based in the STT acceptance for $\Lambda \to p\pi^-$we pick our hi-SOD and chamber inefficiency weight to be 0.5 ± 0.5, we thus have a systematic error of $.07 \times 10^8$ in the Ξ^0 flux.

The measured Ξ^0 flux for the summer for various hi-SOD and chamber inefficiency map weights is given in table 7.1. The hi-SOD inefficiency weight used could also potentially change the measured value of $\alpha_{\Xi^0}\alpha_\Lambda$, and $c\tau$(figure 7.3. The MC value of the Ξ^0 mass is not effected by the hi-SOD weight by more than $.02\,MeV$.

$$Flux = (1.14 \pm .004_{(BR)} \pm .004_{(Stat)} \pm .07_{(Syst)}) \times 10^8 \tag{7.11}$$

7.4 Events Lost Due to Bad Spills

The number of $\Xi^0 \to \Lambda\pi^0$ events actually lost due to the detector problems in table 6.2 are in table 7.2.

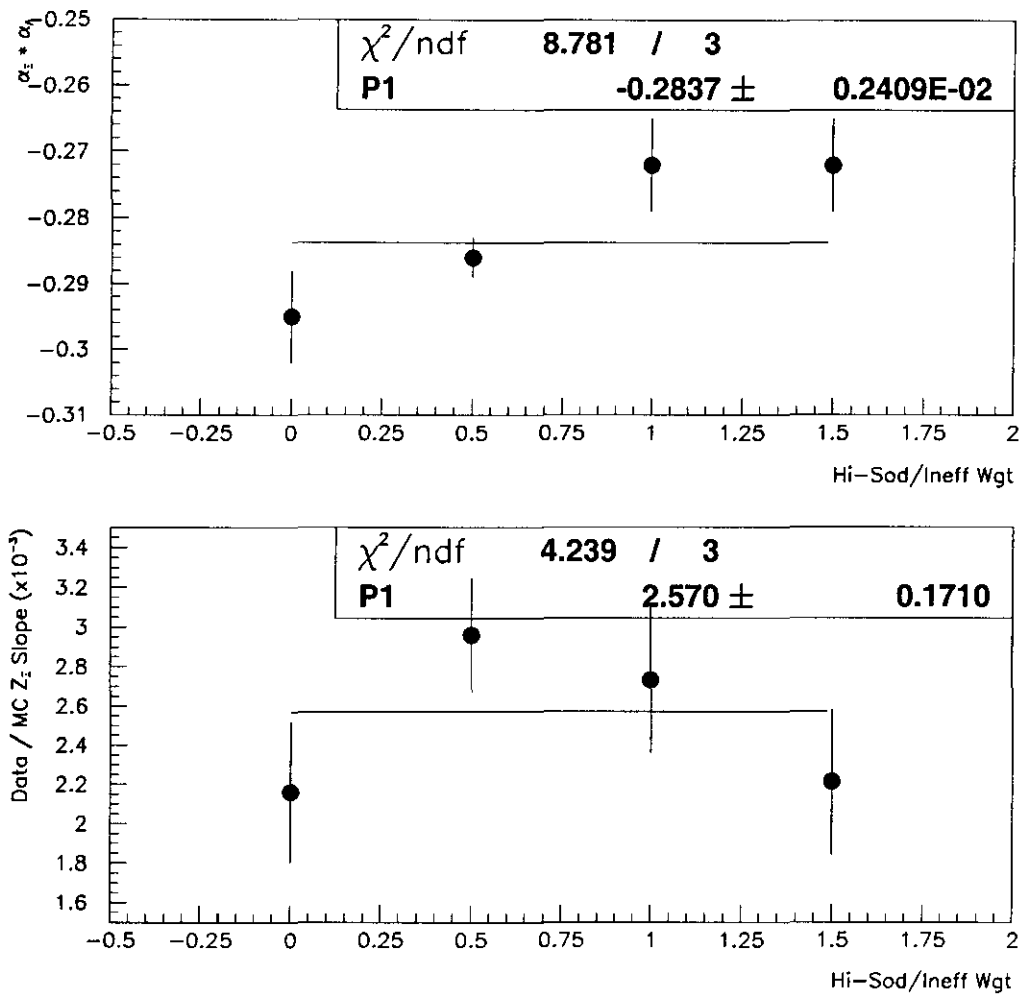

Figure 7.3: The measured value of $\alpha_{\Xi^0}\alpha_\Lambda$ for various Hi-SOD and chamber inefficiency map weights (top), and the Data / MC slope in Ξ^0 z vertex position (bottom).

Bit	Events	Comment
None	70806	Number of Events without Bad Spill Cuts
2	667	DPMT Ped EXP > 0
5	174	Dead DPMT
9	5	Pipeline
12	8	ADC
17	339	HCC
22	1549	Not 799 Run (Special Run)
23	594	Short Run
26	54	TRD: 1 Front Plane or 2 Back Planes Dead
28	510	TRD: Multiple Planes Dead
32	60	Spill = 0

Table 7.2: Ξ^0 Events Lost Due to Bad Spills

- *DPMT Ped EXP* > 0, *Dead DPMT and Pipeline Errors*

Refers to problems with the readout electronics of the CsI calorimeter.

- *HCC*

During run 10741, the HCC malfunctioned due to a bad crate controller in the E_{Total} system.

- *Non 799 run*

We do not include data from non-E799 runs. Runs 10742 and 10765 were used to scan over different targeting angles. Runs 10904, 10906 10909 and 10914 were special high intensity runs.

- *Short run*

We do not include short runs (aborted due to severe detector problems).

- *TRD Problems*

$\Xi^0 \rightarrow \Lambda\pi^0$ events with TRD problems are not removed, we include them in this table to illustrate the relative amount of data with this problem.

- *Spill 0*

Calibration constants are indexed in the database by run and spill number. Most entries start at spill 1. However, sometimes data is taken during spill 0 of a run. Due to this oversight, we exclude all events having a spill number 0.

Description	Error
Beam Shape	.003
Variation of $p_\perp^2$ cut	.006
DC Beam Hole Inefficiency	.013
MC Statistics	.004
Total	.015

Table 7.3: Systematic Error for $\alpha_{\Xi^0}\alpha_\Lambda$

7.5 Data / Monte Carlo Comparisons

Figures 7.4 through 7.9 show data / Monte Carlo comparisons of various distributions. Figure 7.11 shows the number of $\Xi^0 \to \Lambda\pi^0$ events found for each of the 112 runs listed in section 2.2. The 89th run used, run 10790, contributes 75.8 units to the total χ^2. This run contains .27%(.07%) of the Monte Carlo (Data) $\Xi^0 \to \Lambda\pi^0$ events. There are no $\Xi^0 \to \Sigma^+ e^- \overline{\nu}_e$ events passing the selection criteria in this run. We therefore determine that this discrepancy will not effect our result.

7.6 Extraction of $\alpha_{\Xi^0}\alpha_\Lambda$ from $\Xi^0 \to \Lambda\pi^0$ with $\Lambda \to p\pi^-$

MC $\Xi^0 \to \Lambda\pi^0$ decays are generated with the PDG value for $\alpha_{\Xi^0}\alpha_\Lambda$. The distribution (in the data) of the cosine of the angle between the proton and the π^0 in the Λ frame is then corrected for the geometrical acceptance, and fit to the functional form of equation (7.8).

From a sample of 67,411 data (298,869 MC) events, we measure:

$$\alpha_{\Xi^0}\,\alpha_\Lambda = -0.286 \pm .008(stat) \pm .015(syst)$$

The systematic errors for $\alpha_{\Xi^0}\alpha_\Lambda$ are tabulated in table 7.3.

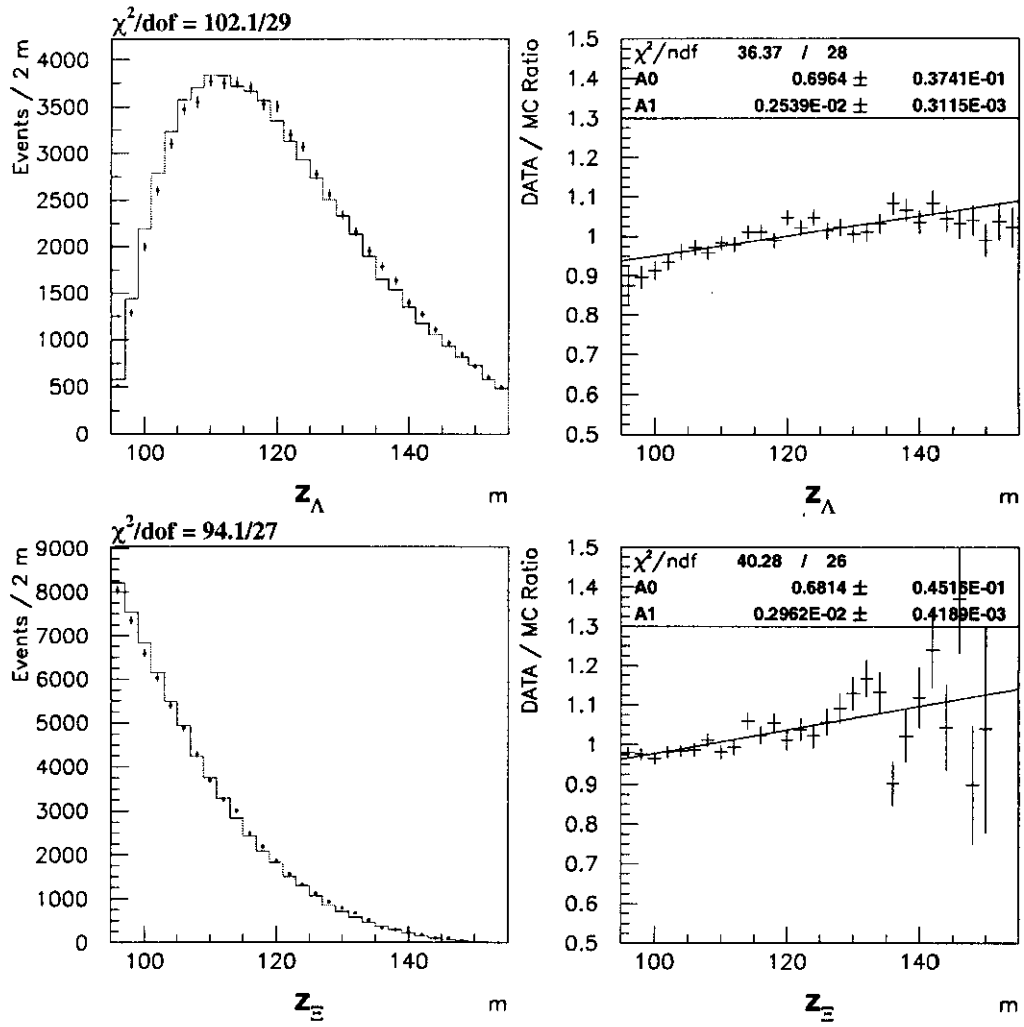

Figure 7.4: Data-Monte Carlo comparison of the z positions of the Ξ^0 (top) and Λ vertices (bottom) (the dots are data and the histogram is Monte Carlo) .

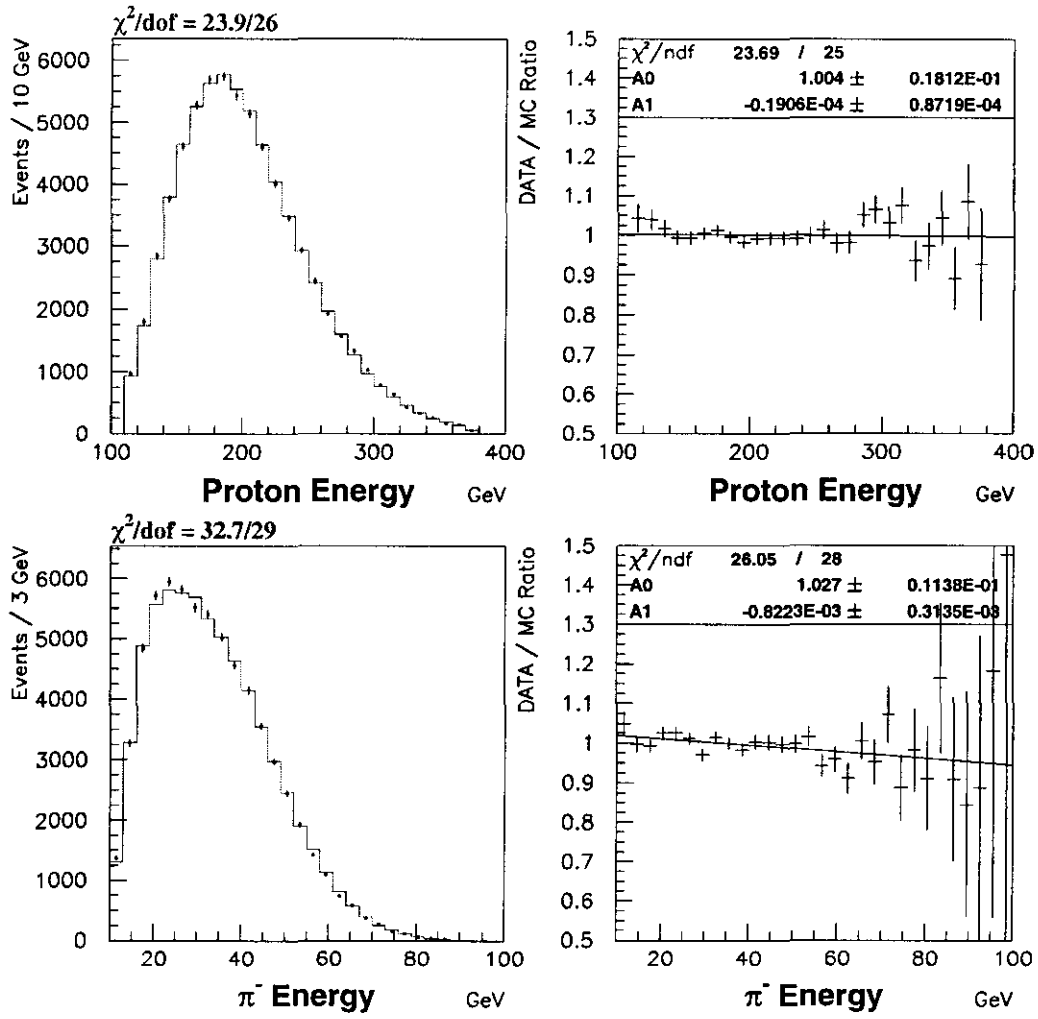

Figure 7.5: Data-Monte Carlo comparison of the proton (top) and π^-energies (bottom) (the dots are data and the histogram is Monte Carlo) .

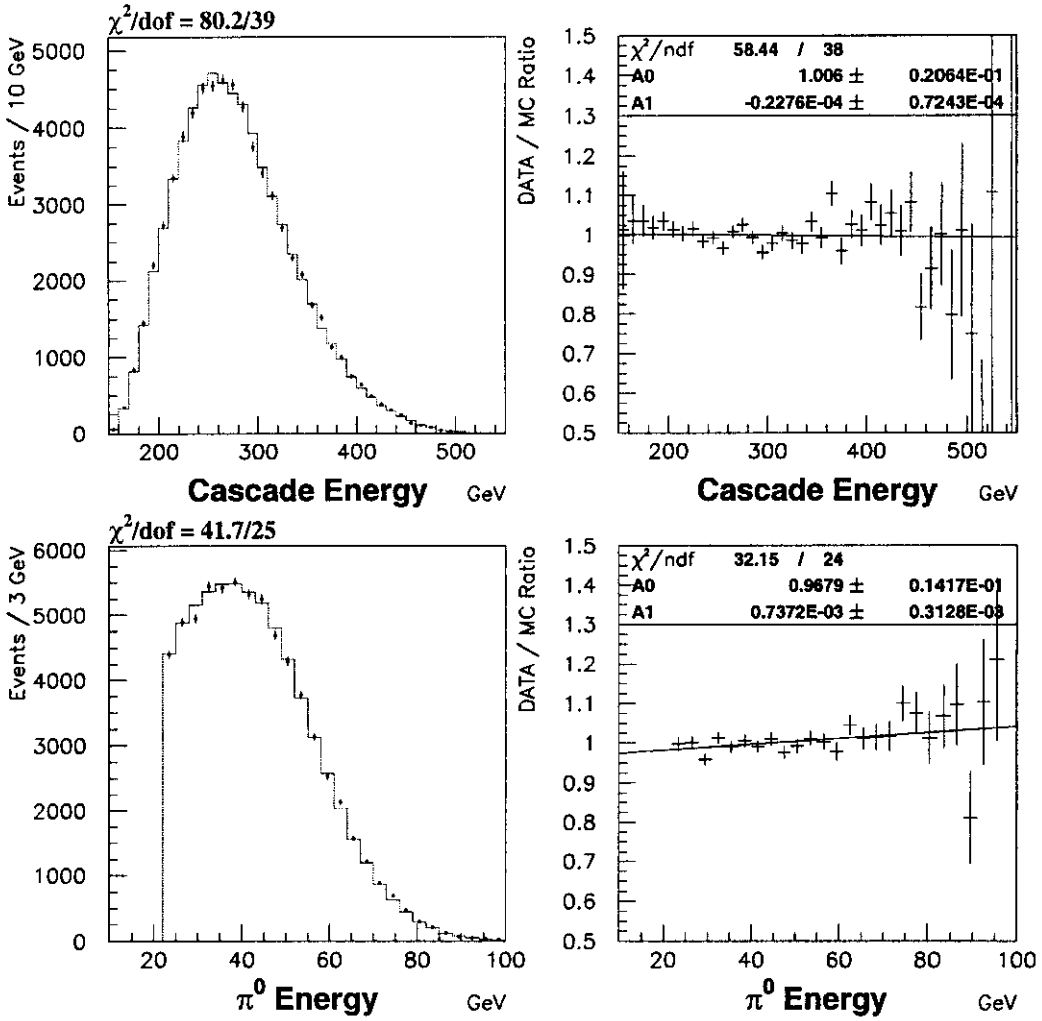

Figure 7.6: Data-Monte Carlo comparison of the π^0(top) and Ξ^0 energies (bottom)(the dots are data and the histogram is Monte Carlo) .

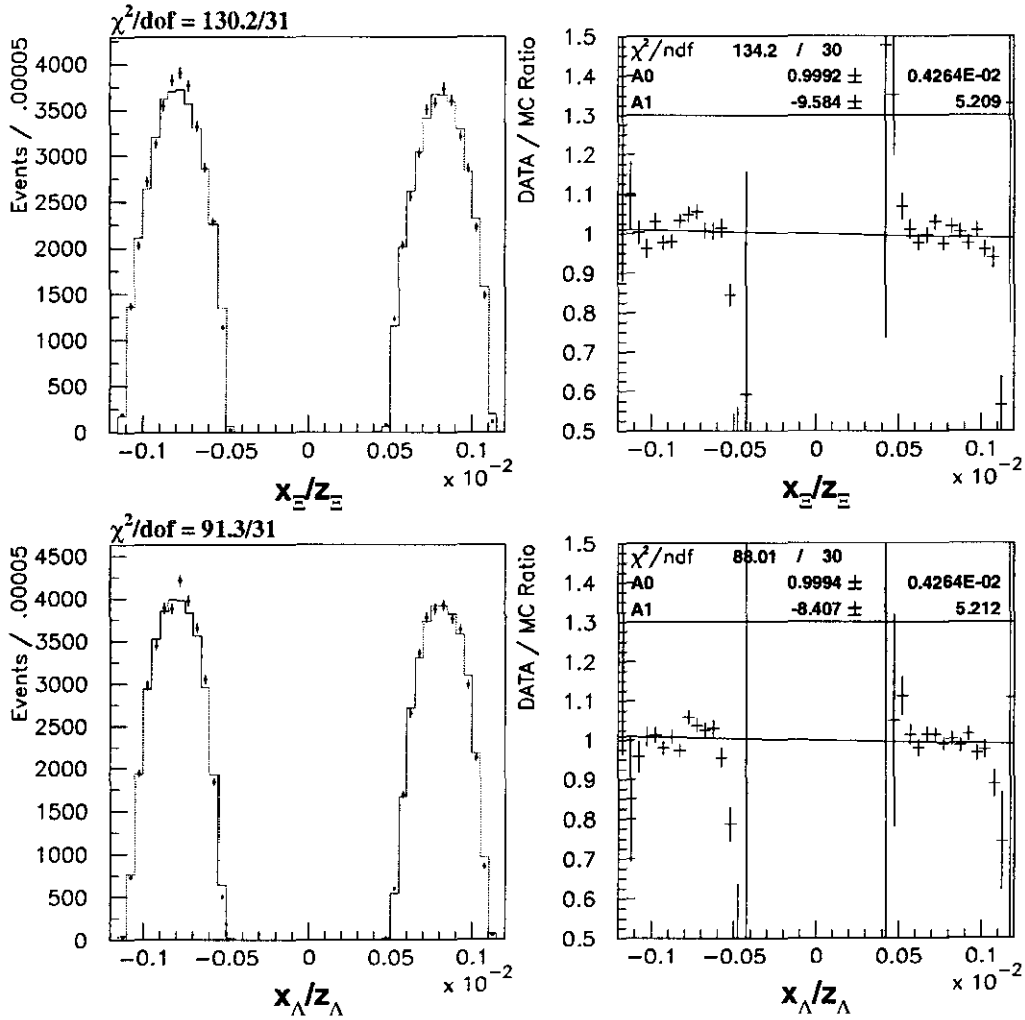

Figure 7.7: Data-Monte Carlo comparison of x/z of the Ξ^0 vertices (top) and Λ vertices (bottom) (the dots are data and the histogram is Monte Carlo).

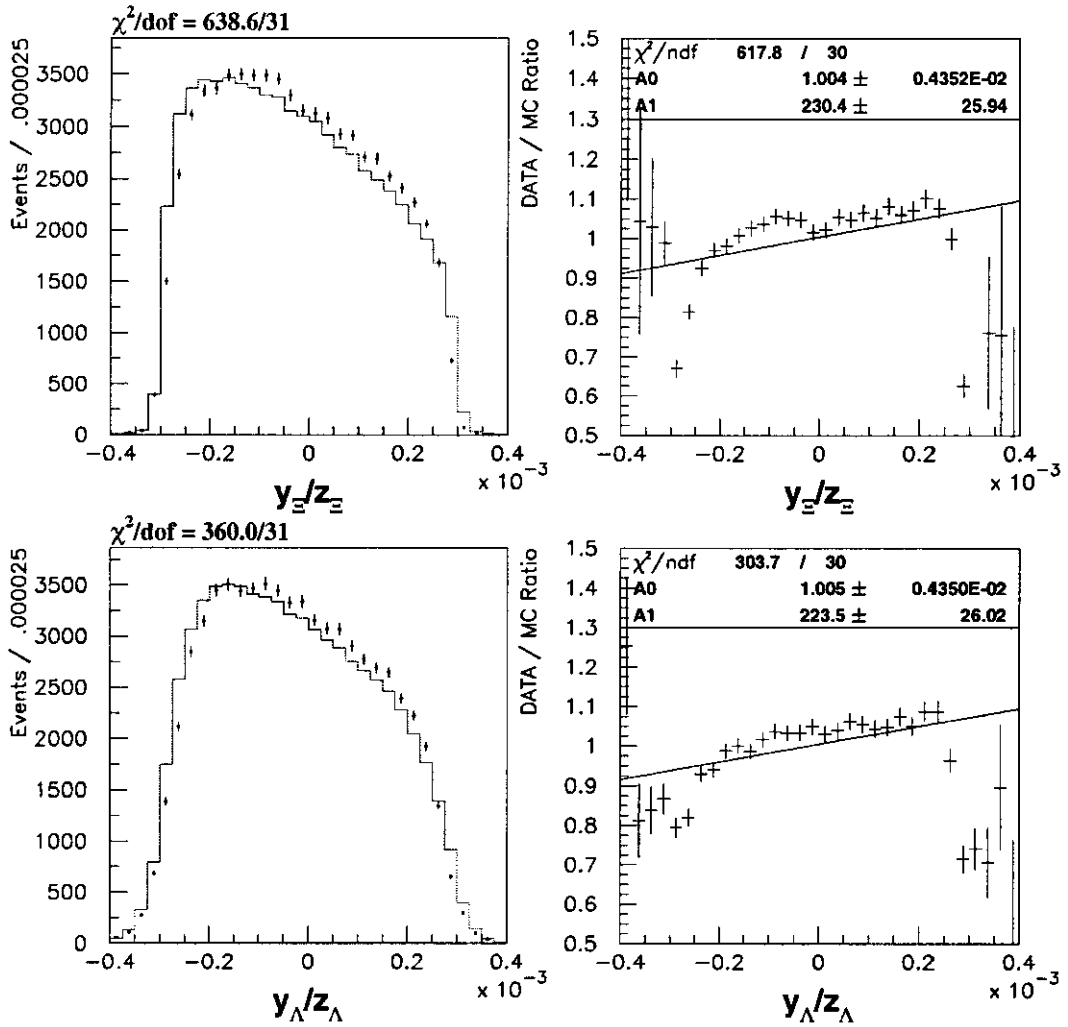

Figure 7.8: Data-Monte Carlo comparison of y/z of the Ξ^0 vertices (top) and Λ vertices (bottom) (the dots are data and the histogram is Monte Carlo).

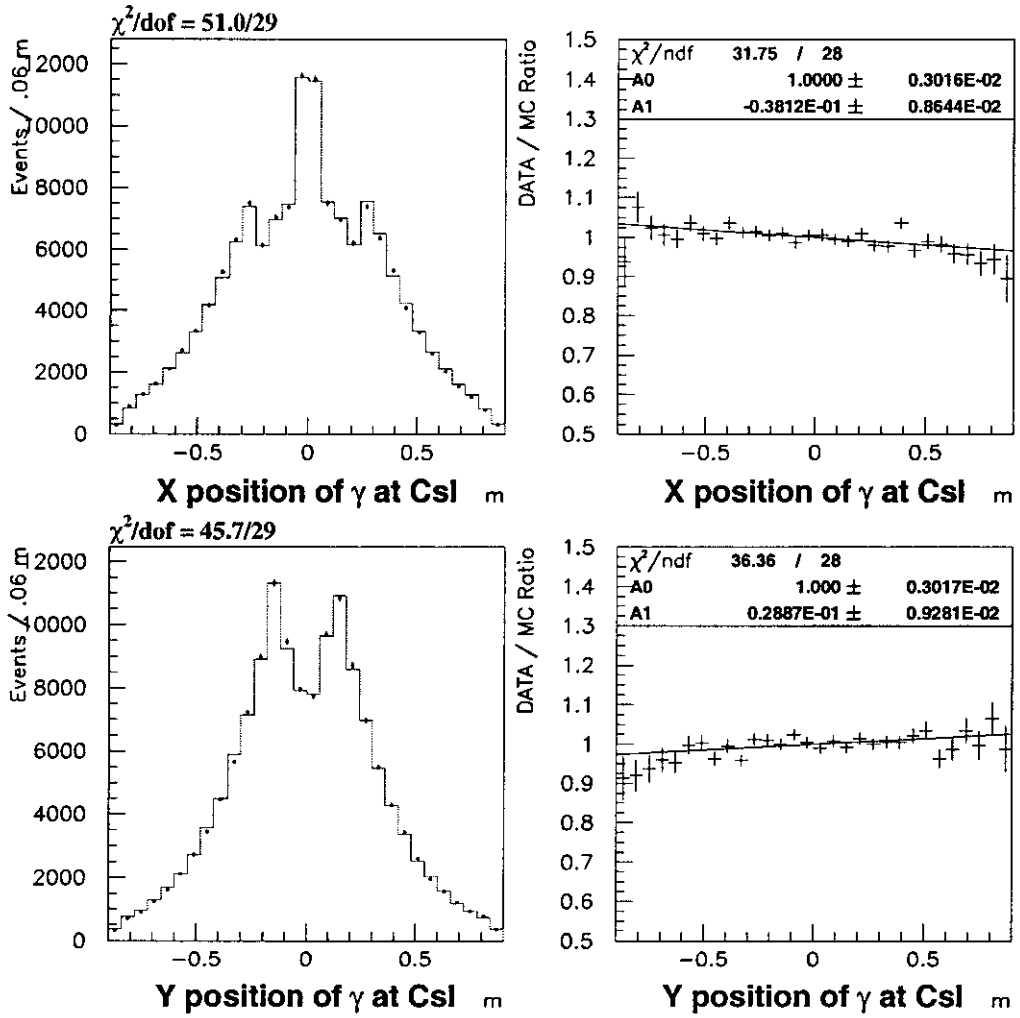

Figure 7.9: Data-Monte Carlo comparison of x (top) and y (bottom) positions of the photons at the CsI (the dots are data and the histogram is Monte Carlo).

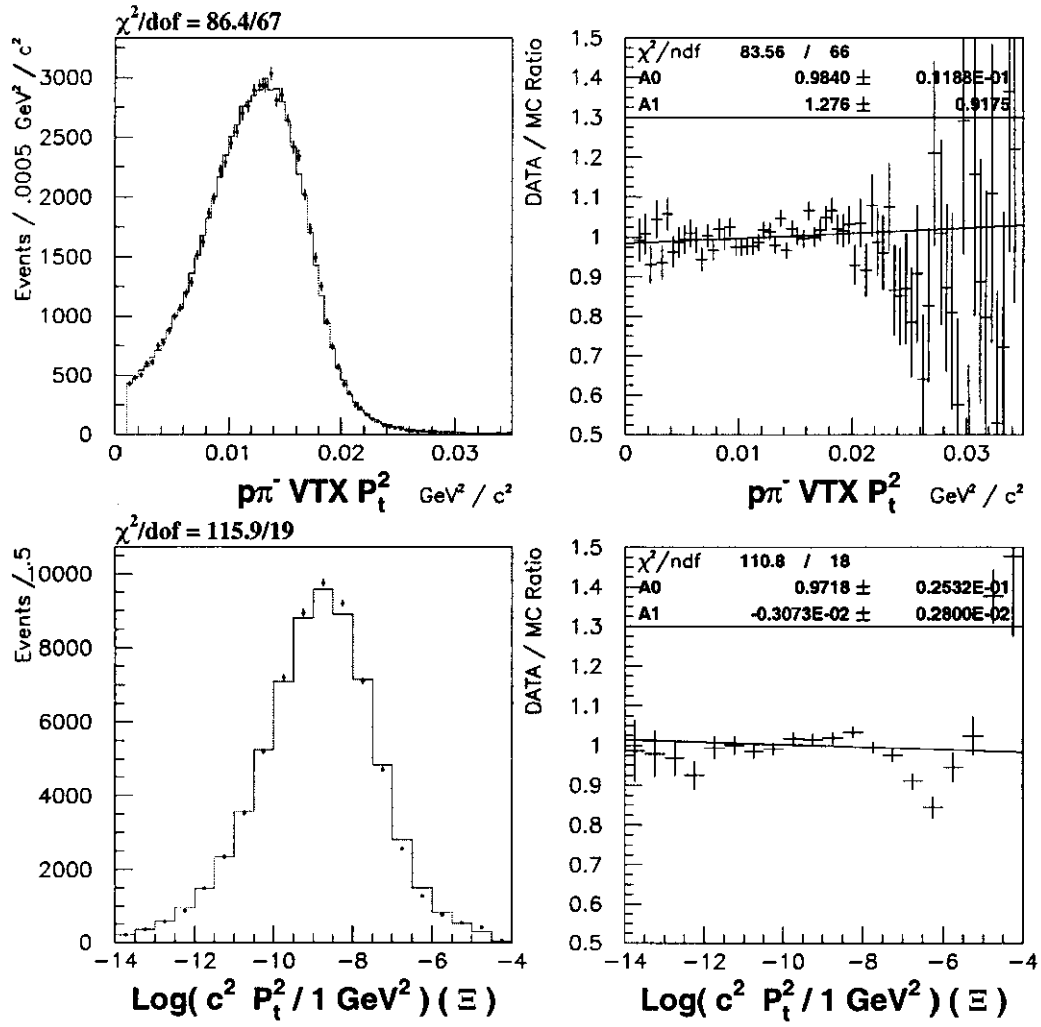

Figure 7.10: Data-Monte Carlo comparison of the charged vertex $p_\perp^2$(top), and the $\log p_\perp^2$ for the Ξ^0 vertex (bottom) (the dots are data and the histogram is Monte Carlo).

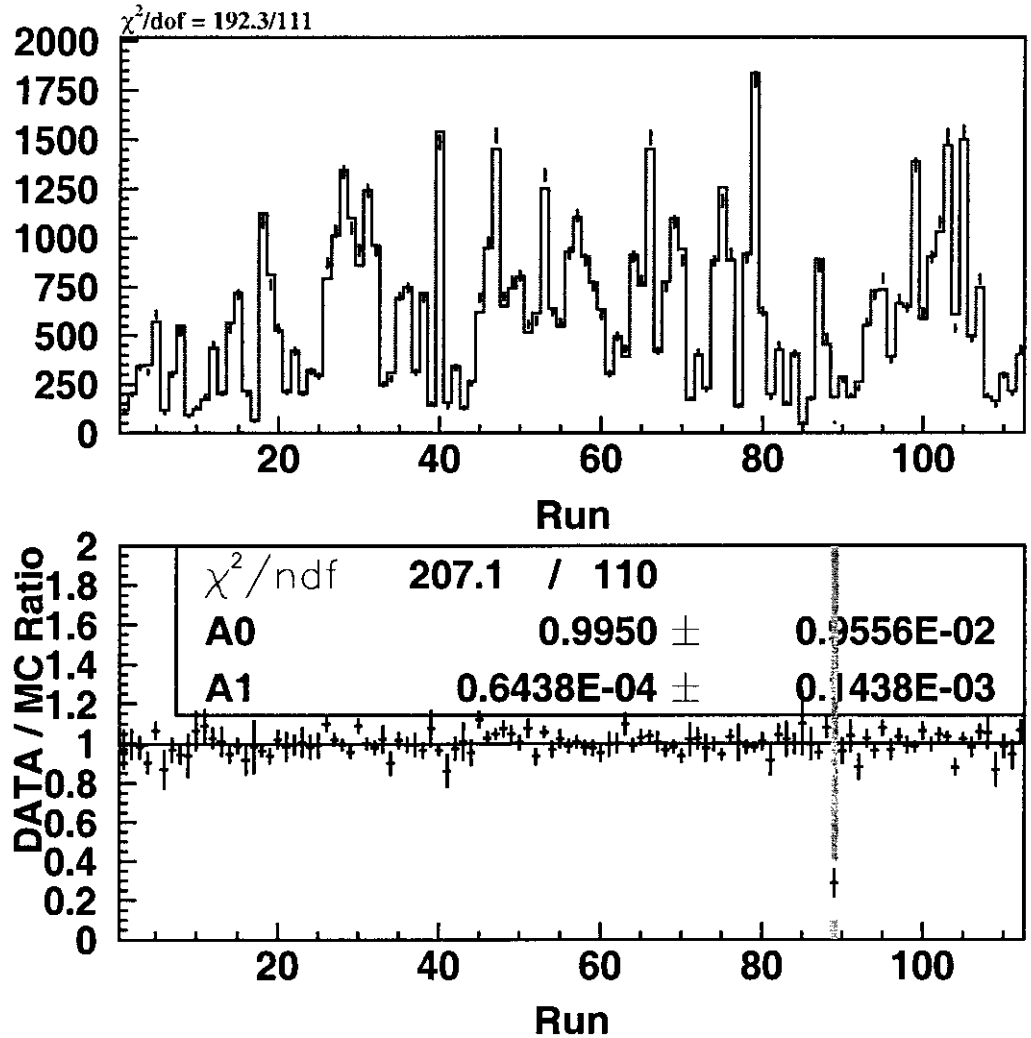

Figure 7.11: Data / Monte Carlo comparison of the number of $\Xi^0 \to \Lambda\pi^0$ events found in each run listed (in ascending order, excluding run 10957) in section 3.3 (the dots are data and the histogram is Monte Carlo).

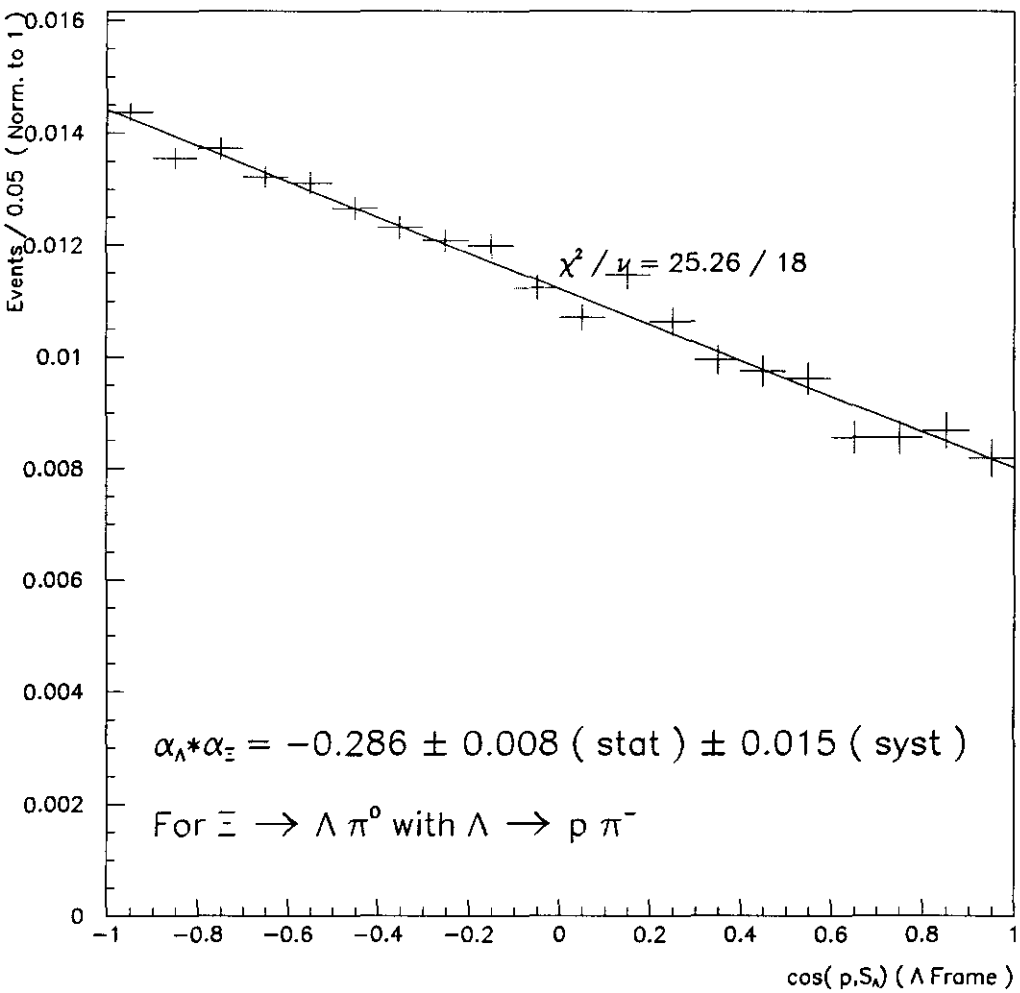

Figure 7.12: Acceptance corrected $(-\hat{p} \cdot \hat{\pi^0})^{\Lambda}$ distribution for $\Xi^0 \rightarrow \Lambda\pi^0$.

7.7 Other Physical Parameters of the Ξ^0

7.7.1 Ξ^0 Lifetime

In figure 7.13, we have the data / Monte Carlo comparison of the z positions of the Ξ^0 vertices. There is a slope in the data / Monte Carlo ratio which vanishes when the Monte Carlo events are re-weighted to increase the $c\tau$of the Ξ^0 by +5%. This corresponds to $c\tau$of 9.14 cm, the PDG value for the $c\tau$of the Ξ^0 is $8.71 \pm .27\,cm$.

7.7.2 Ξ^0 Mass

Figure 7.14 shows the reconstructed $\Lambda \rightarrow p\pi^-$mass for $\Xi^0 \rightarrow \Lambda\pi^0$events. The nominal Λ mass ($1.115684 GeV/c^2$) [10] is subtracted off, and the mass peak (in the -6 to $+6\,MeV$ range) is fit to a Gaussian. The Monte Carlo Λ mass is shifted by $.050 \pm .004\,MeV$, and the data Λ mass is shifted by $.032 \pm .008\,MeV$. The width of the Λ mass peak is $2.02\,MeV$ in data, and $2.12\,MeV$ in Monte Carlo.

Figure 7.15 shows the reconstructed $\Xi^0 \rightarrow \Lambda\pi^0$mass for $\Xi^0 \rightarrow \Lambda\pi^0$events. The nominal Ξ^0 mass ($1314.9\,MeV/c^2$) [10] is subtracted off, and the mass peak (in the -6 to $+6\,MeV$ range is fit to a Gaussian. The Monte Carlo Ξ^0 mass is shifted by $.020 \pm .004\,MeV$, and the Data Ξ^0 mass is shifted by $.593 \pm .008\,MeV$. The Particle Data Group uncertainty on the Ξ^0 mass is $\pm .6\,MeV$, so we cannot tell if this indicates some some systematic shift, or if the Ξ^0 mass shift is physical.

However, NA48 has recently published a value for the Ξ^0 mass,

$$M_{\Xi^0} = 1314.82 \pm 0.06(stat) \pm 0.2(syst)\,MeV/c^2, \tag{7.12}$$

based on a sample 3120 events [64]. Furthermore, a possible systematic effect on the Ξ^0 mass measurement at KTeV could be energy from the π^-clusters in the CsI leaking over the photon clusters. In figure 7.16 we have the plotted the Ξ^0 mass for various values for the π^--γ minimum distance cut. We see a significant shift in the Ξ^0 mass (about $-0.2\,MeV$) in the data when the π^--γ distance cut is increased from $20\,cm$ to $50\,cm$. Interestingly enough, when we require that the amount of energy in

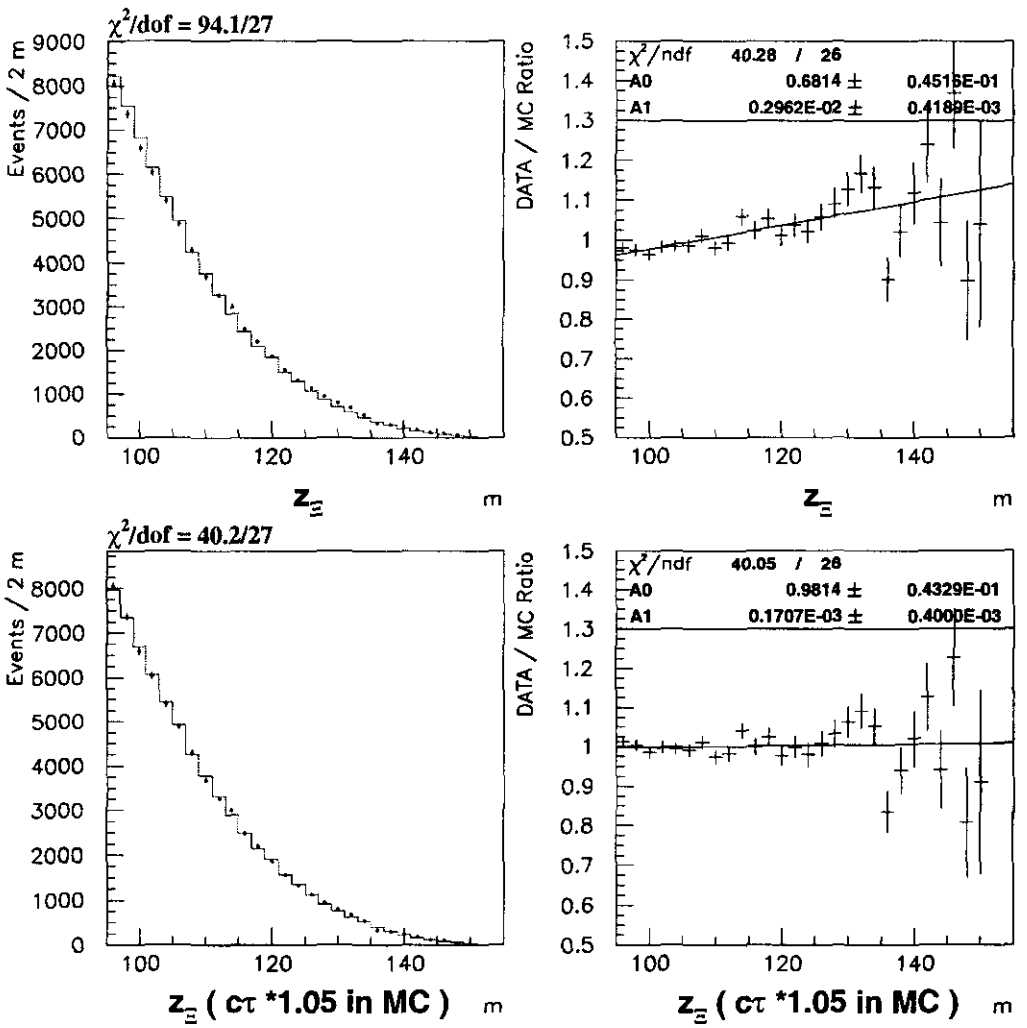

Figure 7.13: Data-Monte Carlo comparison of the z positions of the Ξ^0 vertices with the default Monte Carlo (top), and with Monte Carlo $c\tau$increased by 5 % (bottom).

WGT	Geometry / Total	KQ-BAN / Geometry
DATA	$.773 \pm .006$	$.960 \pm .003$
0.0	$.777 \pm .001$	$.978 \pm .001$
0.5	$.772 \pm .001$	$.960 \pm .000$
1.0	$.767 \pm .001$	$.942 \pm .001$
1.5	$.760 \pm .001$	$.924 \pm .001$

Table 7.4: STT Acceptance for $\Xi^0 \rightarrow \Lambda\pi^0$ events with the STT random accept bit set.

the CsI deposited in the π^-cluster is less than $1\,GeV$, we still see this effect (Figure 7.17).

Furthermore, we have found that a simple shift in the neutral energy scale would have to be of the order of 5% to shift the Ξ^0 mass by $\approx .16\,MeV$, this would also increase the width of the Ξ^0 mass to $3.8\,MeV$. The source of the Ξ^0 mass shift is not known at this point (assuming the NA48 value is correct).

7.8 STT Random Accepts

Because the STT had a 1/20 random accept for the summer run, we have a sample of 4502 $\Xi^0 \rightarrow \Lambda\pi^0$ events in the data with the random accept bit set. All $\Xi^0 \rightarrow \Lambda\pi^0$ event selection criteria are applied to these events except the STT verification requirement.

As with the $\Lambda \rightarrow p\pi^-$sample, we can check the STT acceptance from the geometry and KQ/BAN output for different hi-SOD/inefficiency weightings (table 7.4). In the data, there are 3342 STT random accept $\Xi^0 \rightarrow \Lambda\pi^0$ events which pass STT verification. All 3342 have the STT $DATA$ bit set in the trigger.

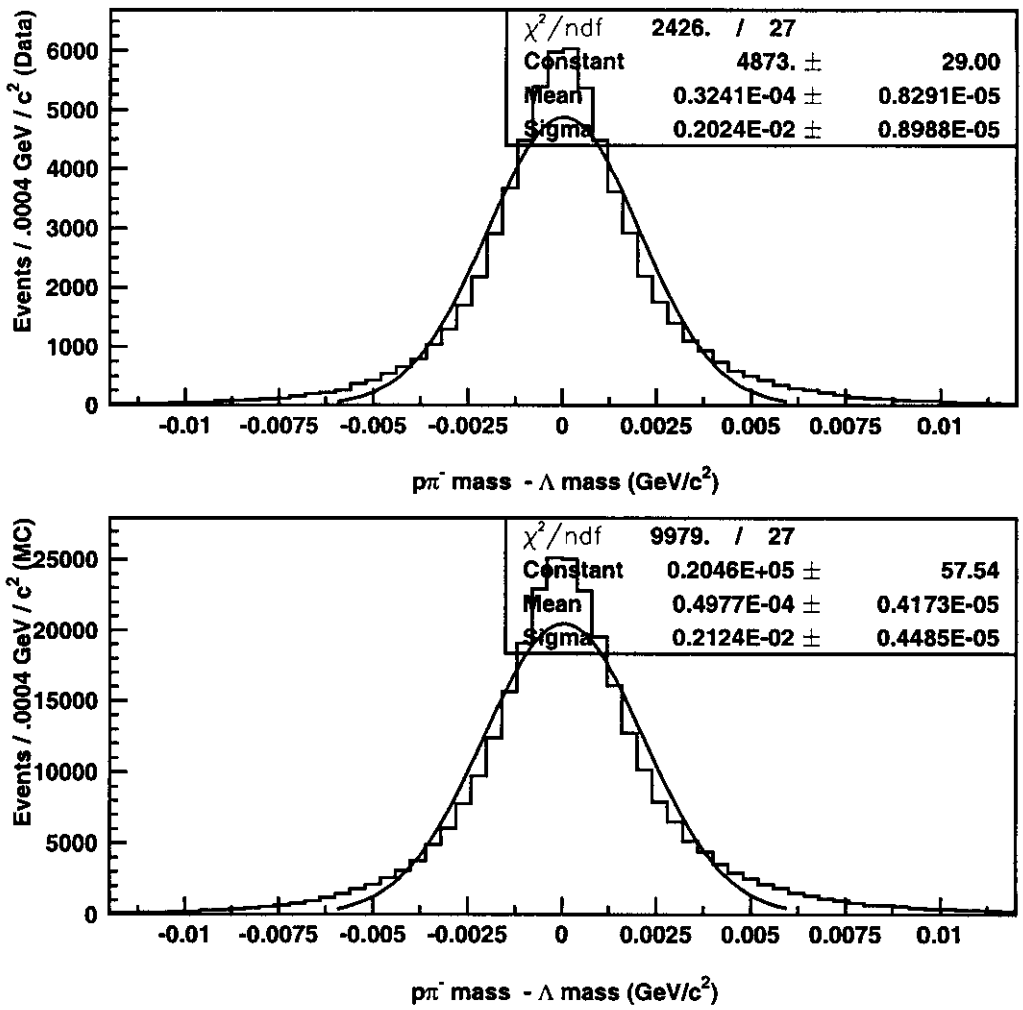

Figure 7.14: The proton π^- mass minus the Λ mass for all events passing the selection criteria. The top plot is data and the bottom plot is Monte Carlo.

FERMILAB
LIBRARY

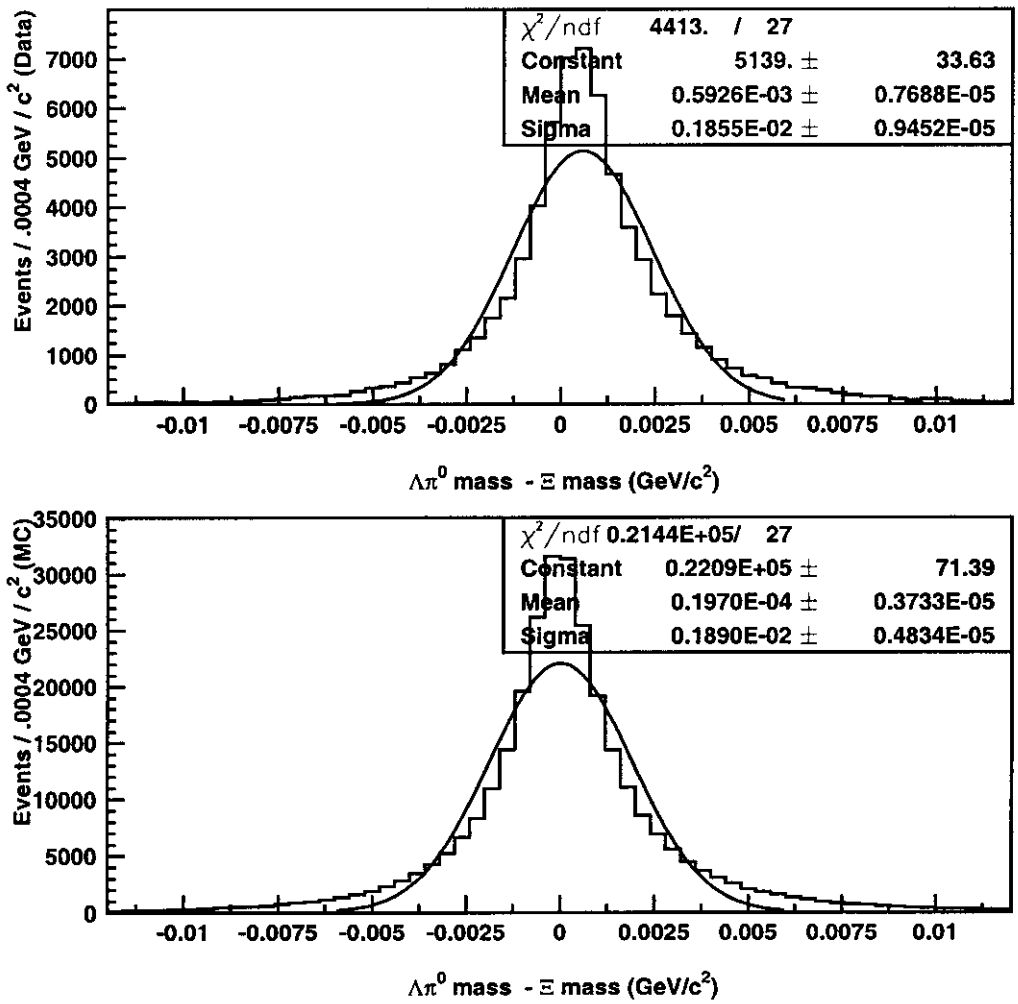

Figure 7.15: The Λ π^0mass minus the Ξ^0 mass for all events passing the selection criteria. The top plot is data and the bottom plot is Monte Carlo.

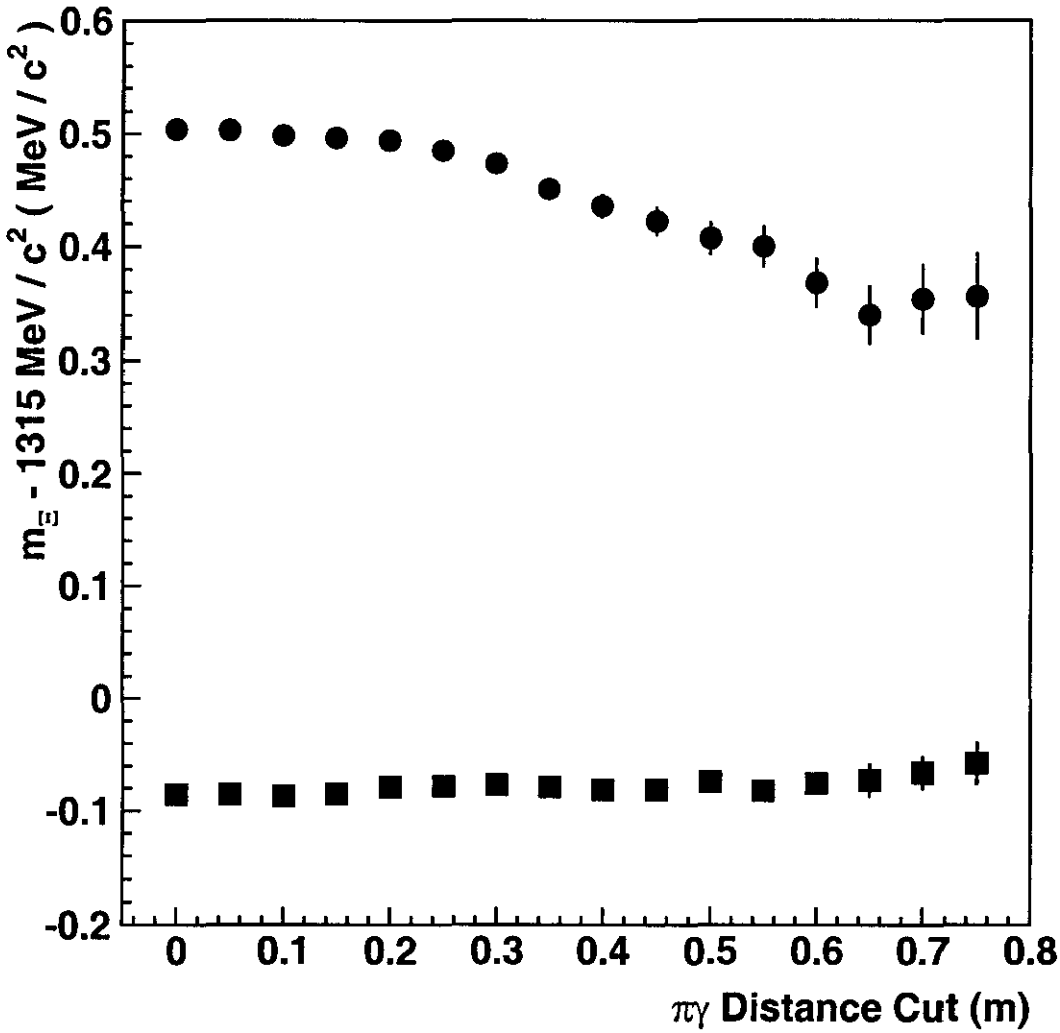

Figure 7.16: The Ξ^0 mass $-1315 MeV/c^2$ as a function of the $\pi^-\gamma$ separation cut. The circles are data, and the squares are Monte Carlo.

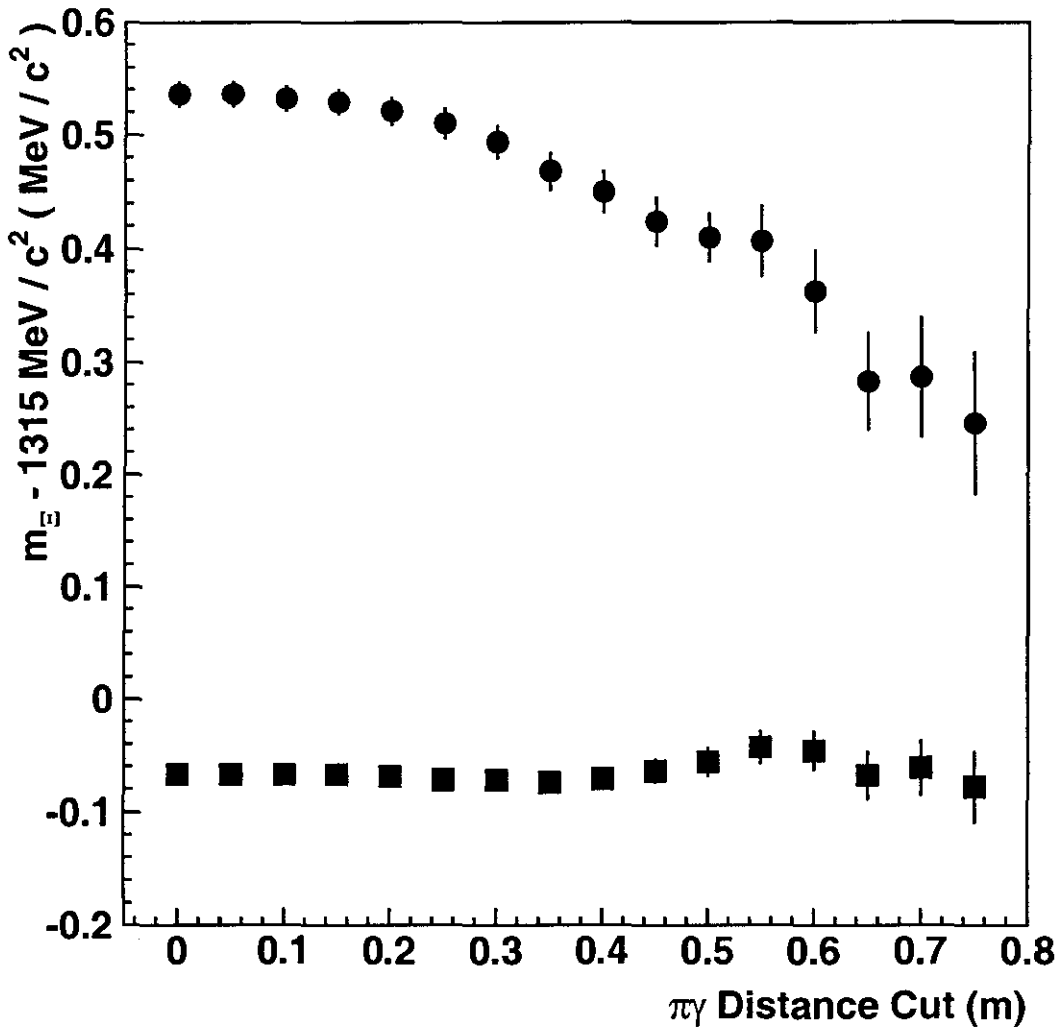

Figure 7.17: The Ξ^0 mass $-1315 MeV/c^2$ as a function of the $\pi^-\gamma$ separation cut, for $\Xi^0 \rightarrow \Lambda\pi^0$ events where the π^-deposited less than $1GeV$ of energy in the CsI. The circles are data, and the squares are Monte Carlo.

Chapter 8

THE DECAY $\Xi^0 \to \Sigma^+ e^- \overline{\nu}_e$ WITH $\Sigma^+ \to p\,\pi^0$

8.1 Simulation of $\Xi^0 \to \Sigma^+ e^- \overline{\nu}_e$ Decays

The matrix element used here for $\Xi^0 \to \Sigma^+ e^- \overline{\nu}_e$ neglects the mass of the electron, and terms of order δ^3 ($\delta = \frac{m_{\Xi^0} - m_{\Sigma^+}}{m_{\Xi^0}}$) [74]. The PDG values for the Ξ^0 mass ($1314.9\,MeV/c^2$), Σ^+mass ($1189.37\,MeV/c^2$), Ξ^0 lifetime ($2.90 \times 10^{-10}\,s\,, c\tau = 8.71\,cm$) , and Σ^+lifetime ($0.799 \times 10^{-10}\,s\,, c\tau = 2.396\,cm$) are used [10]. Time reversal invariance is assumed, (the form factors are real numbers) and the form factors can be varied at the generation level, or by re-weighting the generated Monte Carlo.

8.1.1 Radiative Corrections to $\Xi^0 \to \Sigma^+ e^- \overline{\nu}_e$

Full matrix element used can be found in Ref. [74] or Appendix A. The matrix element will be modified by radiative processes. Only radiative corrections of order α are considered. Furthermore, radiative terms of order δ are ignored.

Virtual Radiative Corrections

The virtual radiative corrections are separated into a model dependent and model independent part [65]. The model independent part is finite in the ultraviolet, and contains the infra-red divergence. The model dependent part contains all the complications due to the strong interaction, and the ultraviolet divergence. The model dependent part of the virtual correction can be reduced to:

$$f_1(q^2 = 0) = f_1^{bare}(q^2 = 0) + \frac{\alpha_{EM}}{\pi} c_{MD} \tag{8.1}$$

$$g_1(q^2 = 0) = g_1^{bare}(q^2 = 0) + \frac{\alpha_{EM}}{\pi} d_{MD} \tag{8.2}$$

Estimates for $\frac{\alpha_{EM}}{\pi} c_{MD}$ and $\frac{\alpha_{EM}}{\pi} d_{MD}$ are of order 1%. Any study of hyperon beta

decay form factors *measures* $f_1(q^2=0)$ and $g_1(q^2=0)$, the presence of this model dependent term presents a further complication.

Real Radiative Corrections

The entire model dependent portion of the inner-bremsstrahlung process will be proportional to $\frac{\alpha_{EM}}{\pi}\delta$ and is neglected.

The model independent part of the inner-bremsstrahlung corrections contains an infra-red divergent part which cancels that of the virtual corrections.

Radiative Corrections to Differential Decay Rate

For an unpolarized Ξ^0 , the differential decay rate is modified from equation (A.11) to

$$\begin{aligned}\frac{d\Gamma}{de\,d\Omega_e\,d\Omega_\nu} &= \xi([1+\frac{\alpha_{EM}}{\pi}(\phi_1+\theta_1)]+a[1+\frac{\alpha_{EM}}{\pi}(\phi_2+\theta_2)]\hat{e}\cdot\hat{\nu}) \\ &\times\ (\frac{M_\Sigma+E_\Sigma}{2M_\Xi})(\frac{e^2\nu^3}{e^{max}-e}) \qquad (8.3)\end{aligned}$$

where the model independent quantities $\phi_1+\theta_1$ and $\phi_2+\theta_2$ are

$$\begin{aligned}\phi_1+\theta_1 &= 2(\frac{1}{\beta}tanh^{-1}(\beta)\ -1)[\frac{e^{max}-e}{3e}-\frac{3}{2}+ln(\frac{2(e^{max}-e)}{m_e})]+\frac{2}{\beta}L(\frac{2\beta}{1+\beta}) \\ &+\ \frac{1}{2\beta}[2(1+\beta^2)+\frac{(e^{max}-e)^2}{6e^2}-4tanh^{-1}(\beta)\,] \\ &-\ \frac{3}{8}+\frac{\pi^2}{\beta}+\frac{3}{2}ln(\frac{M_{\Sigma^+}}{m_e}) \qquad (8.4) \\ \phi_2+\theta_2 &= 2(\frac{1}{\beta}tanh^{-1}(\beta)\ -1)[\frac{e^{max}-e}{3\beta^2e}+\frac{(e^{max}-e)^2}{24\beta^2e^2}-\frac{3}{2}+ln(\frac{2(e^{max}-e)}{m_e})] \\ &+\ \frac{2}{\beta}L(\frac{2\beta}{1+\beta})+\frac{1}{2\beta}tanh^{-1}(\beta)\,(tanh^{-1}(\beta)\ -1) \\ &-\ \frac{3}{8}+\frac{\pi^2}{\beta}+\frac{3}{2}ln(\frac{M_{\Sigma^+}}{m_e}) \qquad (8.5)\end{aligned}$$

Where e is the energy of the e^-in the Ξ^0 frame, m_e is the mass of the e^-, M_{Σ^+} is the mass of the Σ^+, and e^{max} is the maximum energy of the e^-in the Ξ^0 frame

$$e^{max} = \frac{M^2_{\Xi^0} - M^2_{\Sigma^+}}{2M_{\Xi^0}} \tag{8.6}$$

and β is the velocity of the e^-in the Ξ^0 frame

$$\beta = \frac{\sqrt{e^2 - m_e^2}}{e} \tag{8.7}$$

and $L(x)$ is the Spence function

$$L(x) = \int_0^x \frac{dtln(1-t)}{t} \tag{8.8}$$

Radiative Corrections to Final State Polarization

We make the following changes to equation (A.7):

$$A + A'\hat{e}\cdot\hat{\nu} \rightarrow (A + A'\hat{e}\cdot\hat{\nu})(1 + \frac{\alpha_{EM}}{\pi}(\hat{\phi}_2 + \hat{\theta}_2)) \tag{8.9}$$

$$B + B'\hat{e}\cdot\hat{\nu} \rightarrow (B + B'\hat{e}\cdot\hat{\nu})(1 + \frac{\alpha_{EM}}{\pi}(\hat{\phi}_1 + \hat{\theta}_1)) \tag{8.10}$$

$$1 + a\hat{e}\cdot\hat{\nu} \rightarrow 1 + \frac{\alpha_{EM}}{\pi}(\hat{\phi}_1 + \hat{\theta}_1) + a(1 + \frac{\alpha_{EM}}{\pi}(\hat{\phi}_2 + \hat{\theta}_2)\hat{e}\cdot\hat{\nu}) \tag{8.11}$$

The quantities $\hat{\phi}_1 + \hat{\theta}_1$ and $\hat{\phi}_2 + \hat{\theta}_2$ are now defined in the Σ^+frame

$$\begin{aligned}
\hat{\phi}_1 + \hat{\theta}_1 &= 2(\frac{1}{\beta}tanh^{-1}(\beta) - 1)[\frac{e^{max} - e}{3e} - \frac{3}{2} + ln(\frac{2(e^{max} - e)}{m_e})] + \frac{2}{\beta}L(\frac{2\beta}{1+\beta}) \\
&+ \frac{1}{2\beta}[2(1+\beta^2) + \frac{(e^{max} - e)^2}{6e^2} - 4tanh^{-1}(\beta)] \\
&- \frac{3}{8} + \frac{\pi^2}{\beta} + \frac{3}{2}ln(\frac{M_{\Sigma^+}}{m_e}) \qquad (8.12) \\
\hat{\phi}_2 + \hat{\theta}_2 &= 2(\frac{1}{\beta}tanh^{-1}(\beta) - 1)[\frac{e^{max} - e}{3\beta^2 e} + \frac{(e^{max} - e)^2}{24\beta^2 e^2} - \frac{3}{2} + ln(\frac{2(e^{max} - e)}{m_e})]
\end{aligned}$$

$$+ \quad \frac{2}{\beta}L(\frac{2\beta}{1+\beta}) + \frac{1}{2\beta}tanh^{-1}(\beta)\,(tanh^{-1}(\beta) \; - 1)$$
$$- \quad \frac{3}{8} + \frac{\pi^2}{\beta} + \frac{3}{2}ln(\frac{M_{\Sigma^+}}{m_e}) \tag{8.13}$$

but now e and e^{max} refer to the energy and maximum energy of the electron in the Σ^+frame

$$e^{max} = \frac{M^2_{\Xi^0} - M^2_{\Sigma^+}}{2M_{\Sigma^+}} \tag{8.14}$$

Integrated Observables

The distributions of angular variables do not change significantly with the addition of radiative corrections. However, the energy spectrum of the electron does (figure 8.1). As a result, the total rate is increased by $2.3 \pm .2\%$ for $\Xi^0 \rightarrow \Sigma^+ e^- \overline{\nu}_e$ by radiative corrections.

Real photons produced in the process are integrated over in the Monte Carlo, and hence not traced through the detector, nor do we attempt to find $\Xi^0 \rightarrow \Sigma^+ e^- \overline{\nu}_e \gamma$ events in the data. The fraction of $\Xi^0 \rightarrow \Sigma^+ e^- \overline{\nu}_e$ events with a real photon produced above the infra-red cutoff λ (in GeV) is

$$r = -\frac{ln(440\lambda)}{50}, \tag{8.15}$$

small enough to ignore real photons from $\Xi^0 \rightarrow \Sigma^+ e^- \overline{\nu}_e \gamma$ in the Monte Carlo.

Radiative corrections to hyperon beta decays are discussed in much detail in chapter 5 of Ref., [2] and elsewhere [68, 69, 70, 71, 72, 73].

8.2 Reconstruction

In reconstructing $\Xi^0 \rightarrow \Sigma^+ e^- \overline{\nu}_e$ events, the vertex finding routine was modified to allow for the fact that the proton and electron the decay generally do not come from the same point. Instead of calculating a vertex χ^2 in the usual way, the closest approach of the sigma and the electron is calculated DSEL and χ^2_{VTX} = (DSEL/.003)$*$

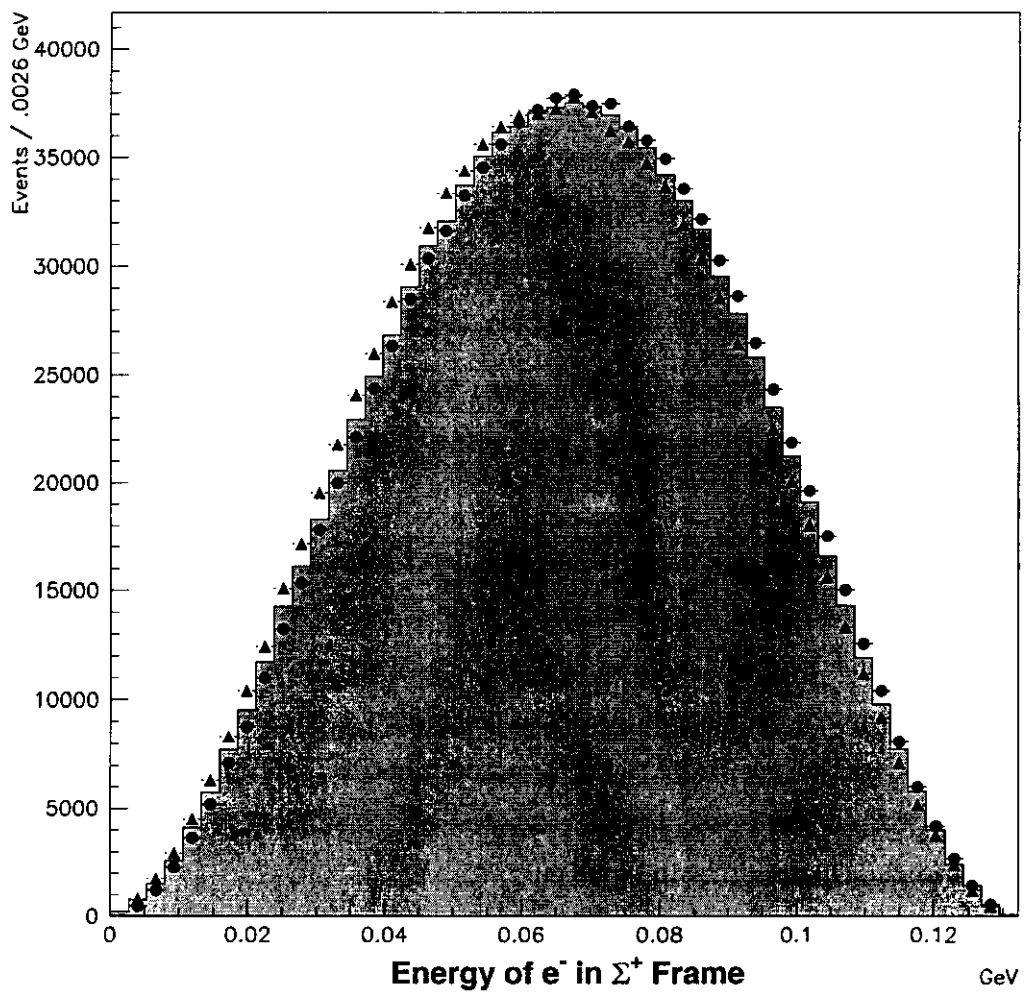

Figure 8.1: The Monte Carlo generated spectrum of the energy of the e^-in the Σ^+frame. The filled histogram is for $f_2/f_1 = 2.6$, the circles are for $f_2/f_1 = 2.6$ *without* the radiative corrections described above implemented, and the triangles are for $f_2/f_1 = 1.3$ (with the radiative corrections).

Decay	Branching Ratio	Number
$\Xi^0 \to \Sigma^+ e^- \overline{\nu}_e$ with $\Sigma^+ \to p\,\pi^0$ and $\pi^0 \to \gamma\gamma$	$\approx 1.3 \times 10^{-4}$	$\approx 15 \times 10^3$
$\Xi^0 \to \Lambda\pi^0$ with $\Lambda \to p\pi^-$ and $\pi^0 \to \gamma\gamma$	$.628 \pm .005$	72×10^6
$\Xi^0 \to \Lambda\pi^0$ with $\Lambda \to pe^-\overline{\nu}_e$ and $\pi^0 \to \gamma\gamma$	$8.18 \pm .14 \times 10^{-4}$	93×10^3
$\Xi^0 \to \Lambda\pi^0$ with $\Lambda \to p\pi^-$ and $\pi^0 \to e^+e^-\gamma$	$7.62 \pm .21 \times 10^{-3}$	870×10^3
$\Xi^0 \to \Lambda\pi^0$ with $\Lambda \to pe^-\overline{\nu}_e$ and $\pi^0 \to e^+e^-\gamma$	$9.97 \pm .31 \times 10^{-6}$	1100
$\Xi^0 \to \Sigma^0\gamma$ with $\Sigma^0 \to \Lambda\gamma$ and $\Lambda \to p\pi^-$	$2.2 \pm .3 \times 10^{-3}$	260×10^3
$\Xi^0 \to \Sigma^0\gamma$ with $\Sigma^0 \to \Lambda\gamma$ and $\Lambda \to pe^-\overline{\nu}_e$	$2.9 \pm .3 \times 10^{-6}$	330
$\Xi^0 \to \Lambda^0\gamma$ with $\Lambda \to p\pi^-$	$6.8 \pm 1.0 \times 10^{-4}$	78×10^3
$\Xi^0 \to \Lambda^0\gamma$ with $\Lambda \to pe^-\overline{\nu}_e$	$8.8 \pm 1.3 \times 10^{-7}$	100

Table 8.1: Number of Ξ^0 decays

$*2$ is substituted into equation (5.1).

Also, the routine matching tracks to clusters (`T3MTACH`) was modified to preferentially pair x and y tracks to have one track going down the hole, and one hitting the calorimeter.

Events with 2 corrected tracks, a hardware cluster matching the negative track, and 2 extra hardware clusters are reconstructed as $\Xi^0 \to \Sigma^+ e^- \overline{\nu}_e$ events. 4 vectors for the proton and electron are calculated using the upstream segments of the corrected tracks. 4 vectors for the photons are calculated from the point along the upstream segment of the positive track give a two photon invariant mass equal to the π^0mass, and the cluster position at the calorimeter (`ZCSISHM`) is used to define the z position of the clusters (as in equation (7.9)).

8.3 Backgrounds

8.3.1 Background from Ξ^0 Decays

Using the total calculated Ξ^0 flux of $1.14 \pm .07(syst) \times 10^8$, we can determine the number of decays of each type that should occur in the decay volume.

$\Xi^0 \to \Lambda\pi^0$ with $\Lambda \to p\pi^-$ and $\pi^0 \to \gamma\gamma$

This decay mode occurs about 4500 times more often than $\Xi^0 \to \Sigma^+ e^- \overline{\nu}_e$. However, there is a π^- in the final state that will be misidentified as an electron a small fraction of the time. Also, the topology of this decay is different than $\Xi^0 \to \Sigma^+ e^- \overline{\nu}_e$ in two very important respects. First, the π^0decay is always upstream of the Λ decay, so the reconstructed Σ^+ vertex will usually be upstream of the Ξ^0 vertex. Also, the maximum $p\pi^0$ invariant mass that can be reconstructed is 1161.2 MeV, which is 28 MeV below the Σ^+ mass. Thus, if the proton track, and $\pi^0$are correctly reconstructed, there can be no $\Xi^0 \to \Lambda\pi^0$ decays under the Σ^+mass peak. Of course, reconstruction is not perfect in the detector, and mis-measurement of the proton and π^0can cause $\Xi^0 \to \Lambda\pi^0$ events to fall in the Σ^+peak.

$\Xi^0 \to \Lambda\pi^0$ with $\Lambda \to pe^-\overline{\nu}_e$ and $\pi^0 \to \gamma\gamma$

This decay occurs about 6 times more often than $\Xi^0 \to \Sigma^+ e^- \overline{\nu}_e$. Like $\Xi^0 \to \Lambda\pi^0$ with $\Lambda \to p\pi^-$, the maximum kinematically allowed proton π^0invariant mass is 1161 MeV and the reconstructed "Σ^+" vertex will usually be upstream of the Ξ^0 vertex.

$\Xi^0 \to \Sigma^0\gamma$ with $\Sigma^0 \to \Lambda\gamma$ and $\Lambda \to p\pi^-$

This decay occurs about 10 times more often than $\Xi^0 \to \Sigma^+ e^- \overline{\nu}_e$ with $\Sigma^+ \to p\,\pi^0$, however, it has a π^-in the final state, and due to its event topology, it is not likely to resemble $\Xi^0 \to \Sigma^+ e^- \overline{\nu}_e$.

$\Xi^0 \to \Sigma^0\gamma$ with $\Sigma^0 \to \Lambda\gamma$ and $\Lambda \to pe^-\overline{\nu}_e$

This decay is quite rare, and due to its event topology, it is not likely to resemble $\Xi^0 \to \Sigma^+ e^- \overline{\nu}_e$.

Decay	Branching Ratio	Number
$\Lambda \rightarrow p\pi^-$ with $\Lambda \rightarrow p\pi^-$ and ($\pi^0 \rightarrow \gamma\gamma$)	$1.4 \times 10{-}3$	2.8×10^6
$\Lambda \rightarrow pe^-\overline{\nu}_e$ with $\Lambda \rightarrow pe^-\overline{\nu}_e$ and ($\pi^0 \rightarrow \gamma\gamma$)	1.8×10^{-6}	3.7×10^3

Table 8.2: Number of Λ decays estimated to occur during the Summer E799 run. The branching ratios are multiplied by 2.2×10^{-3} to account for the fraction of accidental events found to have two hardware clusters.

$$\Xi^0 \rightarrow \Lambda\pi^0 \text{ with } \pi^0 \rightarrow e^+e^-\gamma \text{ (and } \Lambda \rightarrow p\pi^- \text{or } \Lambda \rightarrow pe^-\overline{\nu}_e \text{)}$$

For this decay to reconstructed as a $\Xi^0 \rightarrow \Sigma^+ e^- \overline{\nu}_e$, the $\pi^-$from the decay must be lost either outside the fiducial volume or down one of the beam holes, with one the Dalitz electron faking the primary vertex electron, and the Dalitz e^+ faking a photon by virtue of missing drift chamber hits. This background is not expected to be large.

8.3.2 Background from Λ Decays

Using the total calculated Λ flux of $2.0 \pm .1 \times 10^9$, we can determine the number of decays of each type that should occur in the decay volume. All of these decays must be accompanied by accidental activity in order to fake the two extra clusters.

In order to simulate such decays with the required accidental activity, we split off the accidental events having two extra clusters forming a good π^0 z position.

8.3.3 Background from K_L Decays

It turns out that K_L decays are the source of most of the background to $\Xi^0 \rightarrow \Sigma^+ e^- \overline{\nu}_e$. Since we require that the momentum of the high track be at least $120\,GeV/c$, only the highest energy K_L decays contribute to the background. In all background studies we assume that only K_L with momenta of at least $100\,GeV/c$ contribute to the background.

We measure the K_L flux above $150\,GeV$ using $K_L \rightarrow \pi^+\pi^-\pi^0$ decays in the trigger B11, (our level 3 code has a minimum track momentum cut, we are only able to measure the flux of K_L above $150\,GeV$ for $K_L \rightarrow \pi^+\pi^-\pi^0$ in the hyperon triggers).

The event selection criteria are identical to the $\Xi^0 \rightarrow \Lambda\pi^0$ selection criteria except:

- $| p_p | / | p_\pi | > 3.0 \rightarrow | p_p | / | p_\pi | > 2.6$
- $| m_{p\pi^-} - 1.115684\,GeV | < .015\,GeV \rightarrow | m_{p\pi^-} - 1.115684\,GeV | > .010\,GeV$ (remove $\Xi^0 \rightarrow \Lambda\pi^0$)
- Remove $m_{K_L \rightarrow \pi^+\pi^-\pi^0} > 0.55\,GeV$ cut
- Add $| z_{\Xi^0} - z_\Lambda | < 3.0\,m$ cut

Applying all the criteria, we find 1410 events in the data within $20\,MeV$ of the nominal K_L mass. From a MC sample of 10 Million $K_L \rightarrow \pi^+\pi^-\pi^0$ decays (with $E_K > 150\,GeV$) we find 1592 events within $20\,MeV$ of the nominal K_L mass. A sample of $\Xi^0 \rightarrow \Lambda\pi^0$ decays of equal statistics to the summer run gives a prediction of 0 $\Xi^0 \rightarrow \Lambda\pi^0$ events in the $\pm 20\,MeV$ mass window.

Using the $K_L \rightarrow \pi^+\pi^-\pi^0$ with $\pi^0 \rightarrow \gamma\gamma$ branching ratio (BR) of .124, and the trigger 11 prescale (PS) of .02, we have

$$Flux = \frac{N_{Data}}{BR \times PS \times Acc_{MC}} \tag{8.16}$$

The Measured K_L flux above $150\,GeV$ for the summer is

$$Flux(E_K > 150\,GeV) = (3.57 \pm .09_{(Stat)} \pm .24_{(Syst)}) \times 10^9 \tag{8.17}$$

$$Flux(E_K > 100\,GeV) = (1.39 \pm .04_{(Stat)} \pm .10_{(Syst)}) \times 10^{10} \tag{8.18}$$

$$Flux(220\,GeV > E_K > 20\,GeV) = (1.06 \pm .03_{(Stat)} \pm .07_{(Syst)}) \times 10^{11} \tag{8.19}$$

Figure 8.2 shows data / Monte Carlo comparisons of the $K_L \rightarrow \pi^+\pi^-\pi^0$ mass, K_L energy and z vertex positions for $K_L \rightarrow \pi^+\pi^-\pi^0$ candidates in trigger B11.

In all K_L MC generation, only events with a charged decay product having at least $90\,GeV$, and the high momentum track having at least $2.4\times$ the momentum of the low momentum track are actually traced through the detector (`MCUSER`).

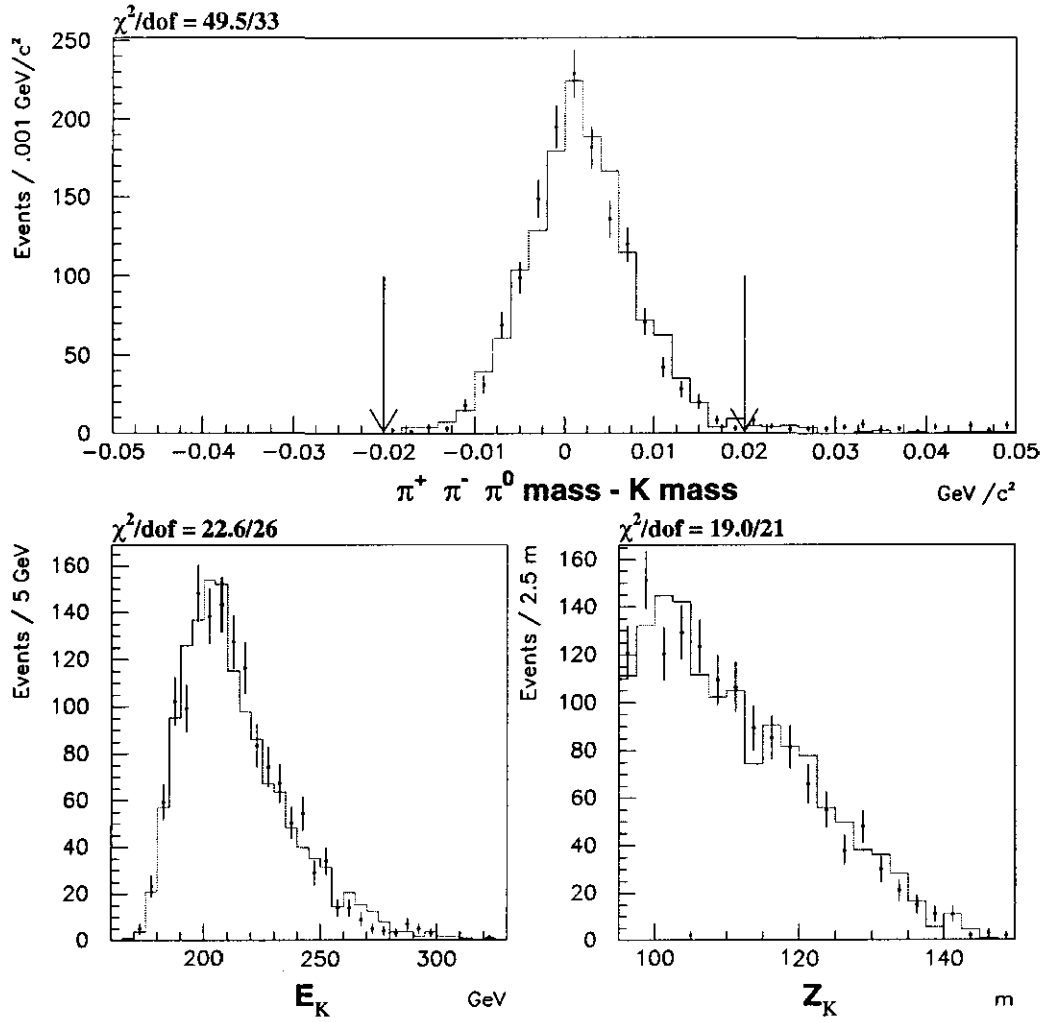

Figure 8.2: Data (dots) / Monte Carlo (histogram) comparison for $K_L \to \pi^+\pi^-\pi^0$ mass for B11 $K_L \to \pi^+\pi^-\pi^0$ candidates (Top). Also shown are comparisons for total K_L energy (bottom left) and K_L z vertex position (bottom right).

$K_L \rightarrow \pi^+\pi^-\pi^0$

Requiring the $\pi^+\pi^-\pi^0$mass to be greater than $.57\,GeV$ is highly effective in reducing this background. From a sample corresponding to .42 of the summer run, no events pass the selection criteria, with the addition of the TRD cut, we estimate this background to be $< .4$ Figure 8.3 shows the $m_{K_L \rightarrow \pi^+\pi^-\pi^0}$ distribution for data.

$K_L \rightarrow \pi^0\pi^+e^-\overline{\nu}_e$

For kaons with $p > 100\,GeV/c$ this decay occurs 730,000 times. Since we do not distinguish between protons and pions traveling down the beam hole, this decay effectively has the same final state as our signal.

The charged and neutral vertices of this decay are always physically at the same point (in contrast with the Σ^+- Ξ^0 vertex separation in $\Xi^0 \rightarrow \Sigma^+\,e^-\,\overline{\nu}_e$). In figure 8.4, we see that a 2 dimensional cut on the $K_L \rightarrow \pi^0\pi^+e^-\overline{\nu}_e$ mass and the difference in the z positions of the $\Sigma^+$and Ξ^0 vertices removes most of the $K_L \rightarrow \pi^0\pi^+e^-\overline{\nu}_e$ background and only removes a small part ($\approx 7\%$) of the signal.

$K_L \rightarrow \pi^+e^-\overline{\nu}_e$

In order for this decay to pass the $\Xi^0 \rightarrow \Sigma^+\,e^-\,\overline{\nu}_e$ selection criteria, there must be accompanying accidental extra clusters. To facilitate simulation of these, accidental events with no tracks, and two extra clusters forming a π^0 z position in the fiducial volume were spooled from the 4 accidental tapes from the summer. This corresponded to 2.2×10^{-3} of all accidental events.

$K_L \rightarrow \pi^+e^-\overline{\nu}_e\gamma$

These events require an extra photon, the IR cutoff for photons is set to $1.56\,MeV$, so the radiative fraction is .0992. $K_L \rightarrow \pi^+e^-\overline{\nu}_e\gamma$ events having an energetic γ and an accidental photon can fake a $\Xi^0 \rightarrow \Sigma^+\,e^-\,\overline{\nu}_e$ signal. To save computing time, only $K_L \rightarrow \pi^+e^-\overline{\nu}_e\gamma$ events having a lab photon energy of at least $2.5\,GeV$ are traced through the detector. Radiative photons from the decay will tend to follow the

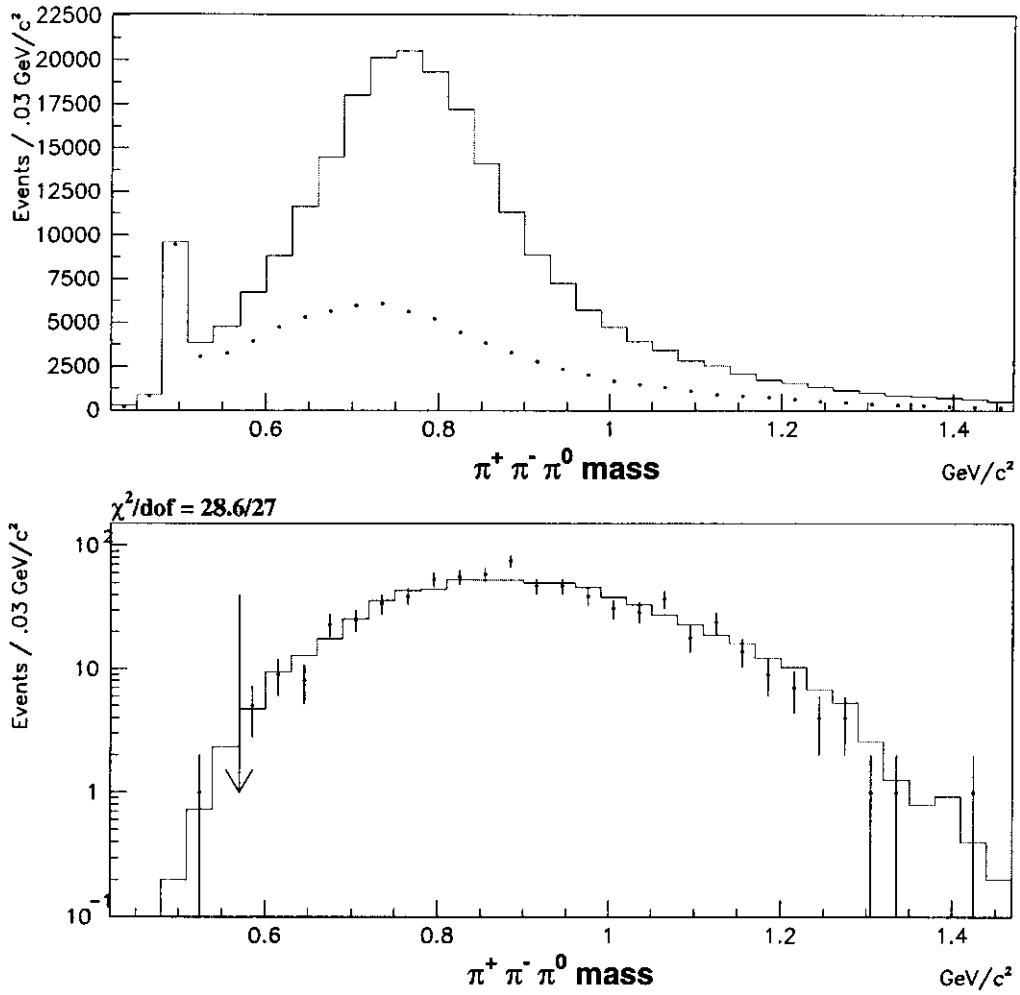

Figure 8.3: The top plots shows the $K_L \rightarrow \pi^+\pi^-\pi^0$ mass distribution for all trigger 10 data events having a high momentum track in the hole, two extra clusters, and a negative track with $1.15 > E/p > 0.85$. The histogram is events where the high momentum track is negative, the are events with the high momentum track being positive. The bottom plot shows the data (dots) and Monte Carlo (histogram) distribution for the $K_L \rightarrow \pi^+\pi^-\pi^0$ mass when all cuts are applied, expect the requirement that $M_{K_L \rightarrow \pi^+\pi^-\pi^0} > 0.57\,GeV$.

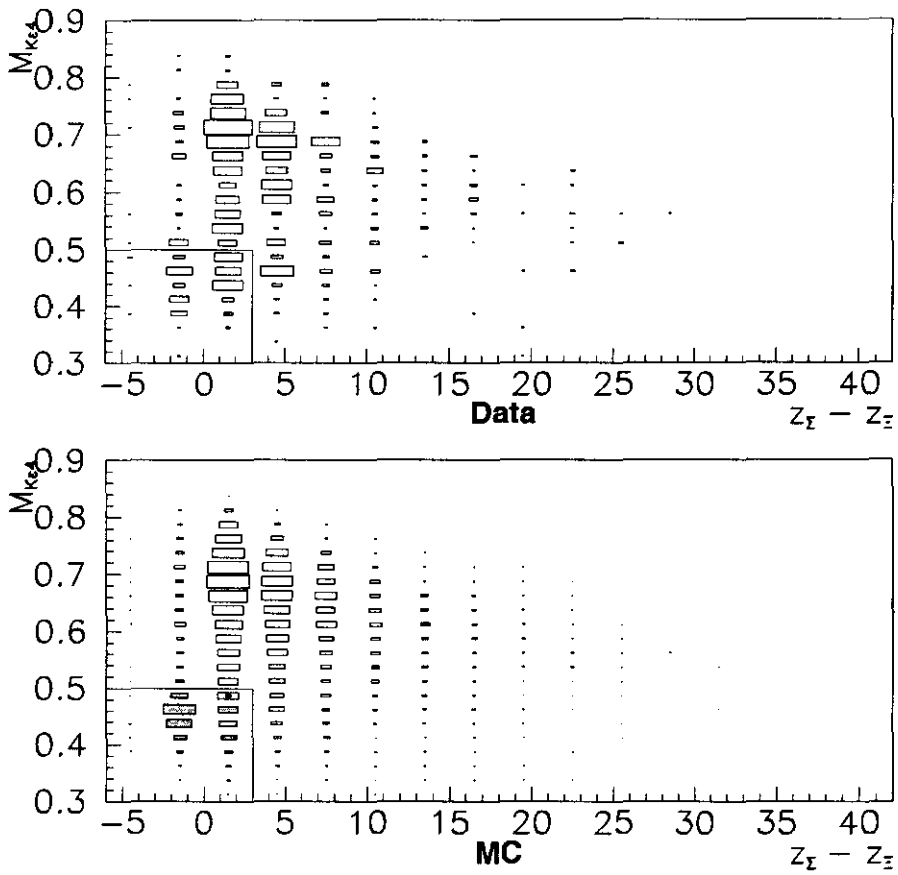

Figure 8.4: The top plots shows the distribution if the difference in the z positions of the $\Sigma^+$and Ξ^0 vertices vs. $M_{K_L \to \pi^0\pi^+e^-\overline{\nu}_e}$ for data. The bottom plot shows the same distribution for $\Xi^0 \to \Sigma^+ e^- \overline{\nu}_e$ Monte Carlo, and for $K_L \to \pi^0\pi^+e^-\overline{\nu}_e$ Monte Carlo (shaded) scaled by 5 for visibility. In both plots all selection criteria have been applied except the requirement that $M_{K_L \to \pi^0\pi^+e^-\overline{\nu}_e} > 0.50\,GeV\,OR\,z_\Sigma - z_{\Xi^0} > 3.0\,m$. Events removed by that cut are in the box in the lower left hand corner of each plot.

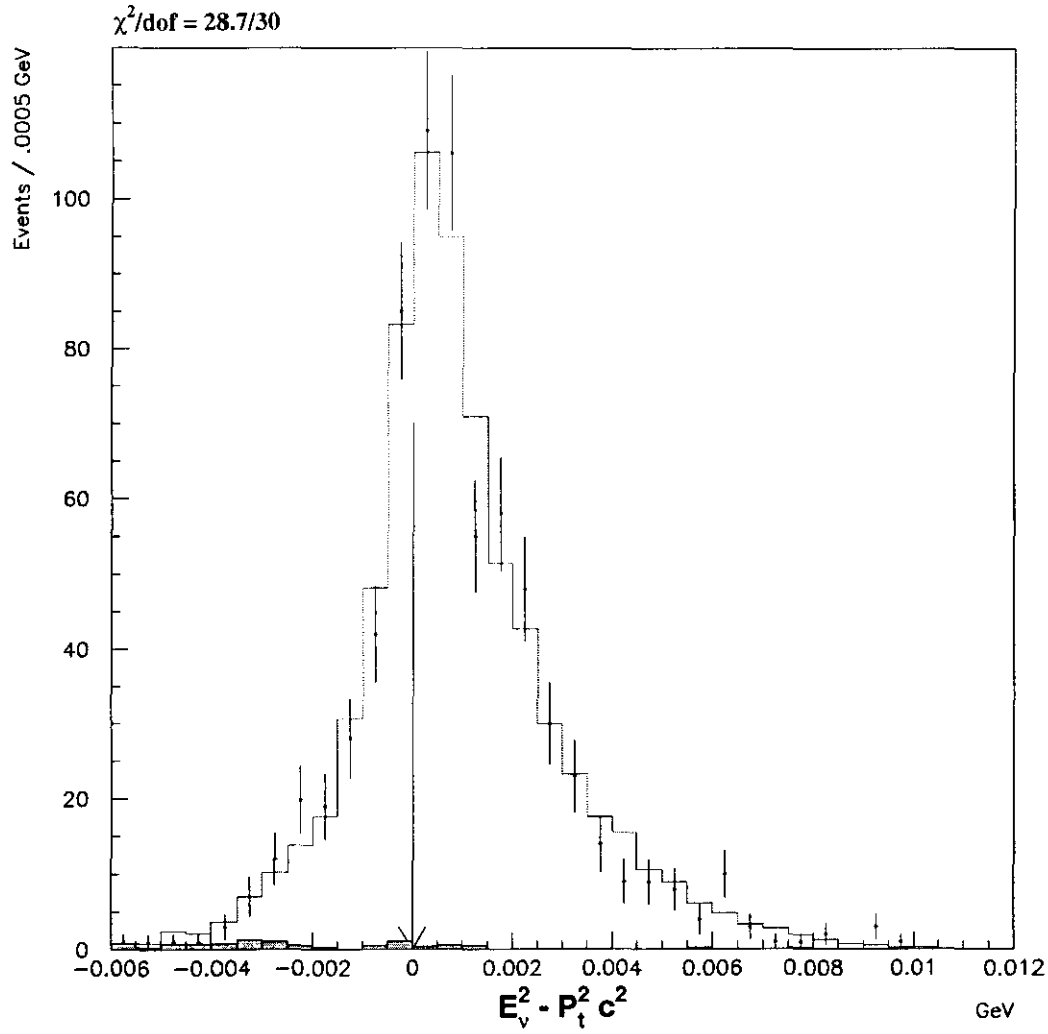

Figure 8.5: Data / Monte Carlo comparison of $p^2_{\nu||}$, the square of the longitudinal momentum of the neutrino in the Ξ^0 frame. The shaded histogram is the predicted $K_L \to \pi^+ e^- \overline{\nu}_e$ background. Events to the left of the arrow do not have a physical solution for the neutrino momentum direction in the Ξ^0 frame and are not used for the $g_1/f_1$and g_2/f_1measurement.

Decay	Branching Ratio	Number
$K_L \rightarrow \pi^0\pi^+e^-\overline{\nu}_e$ and $\pi^0 \rightarrow \gamma\gamma$	$5.2 \times 10{-}5$	7.3×10^5
$K_L \rightarrow \pi^+e^-\overline{\nu}_e$ ($\pi^0 \rightarrow \gamma\gamma$)	8.6×10^{-4}	1.2×10^7
$K_L \rightarrow \pi^+e^-\overline{\nu}_e\gamma$ (γ)	.0385	5.4×10^8
$K_L \rightarrow \pi^+\pi^-\pi^0$	.124	1.7×10^9

Table 8.3: Number of K_L decays estimated to occur during the Summer E799 run (for $E_K > 100\,GeV$). The branching ratio for $K_L \rightarrow \pi^+e^-\overline{\nu}_e$ is multiplied by 2.2×10^{-3} to account for the fraction of accidental events found to have two hardware clusters, and the $K_L \rightarrow \pi^+e^-\overline{\nu}_e\gamma$ branching ratio is for a center of mass photon energy cutoff of $1.56\,MeV$.

Bit	Description
26	1 Dead TRD Front Plane or 2 Dead TRD Back Planes
28	Many planes dead or other severe TRD problem

Table 8.4: Bits used to reject bad spills for $\Xi^0 \rightarrow \Sigma^+\, e^-\, \overline{\nu}_e$ (in addition to those in Table 2).

electron in the lab, We create the quantity *Brem* which is the distance between the upstream segment of the electron projected to the CsI and the closer of the two extra clusters. Events having $Brem < .02\,cm$ are removed (Figure 8.6).

8.4 Event Selection

Selection criteria are applied in order to ensure that the decays in occur in the proper fiducial volume of the detector, and to reject the above mentioned background.

Spills flagged for problems in tables 6.2 and 8.4 of severity code 1 were excluded.

Also, runs 10596 and 10599 were excluded as they had the incorrect `PTKICK` sign in the database.

Events are then selected by Fiducialization of $\Sigma^+$and Ξ^0 vertices and trigger verification:

- $158.0\,m > z_\Sigma > 95.0\,m$
- $158.0\,m > z_{\Xi^0} > 95.0\,m$
- $.00124 >| x_{\Xi^0}/z_{\Xi^0} |> .000376$

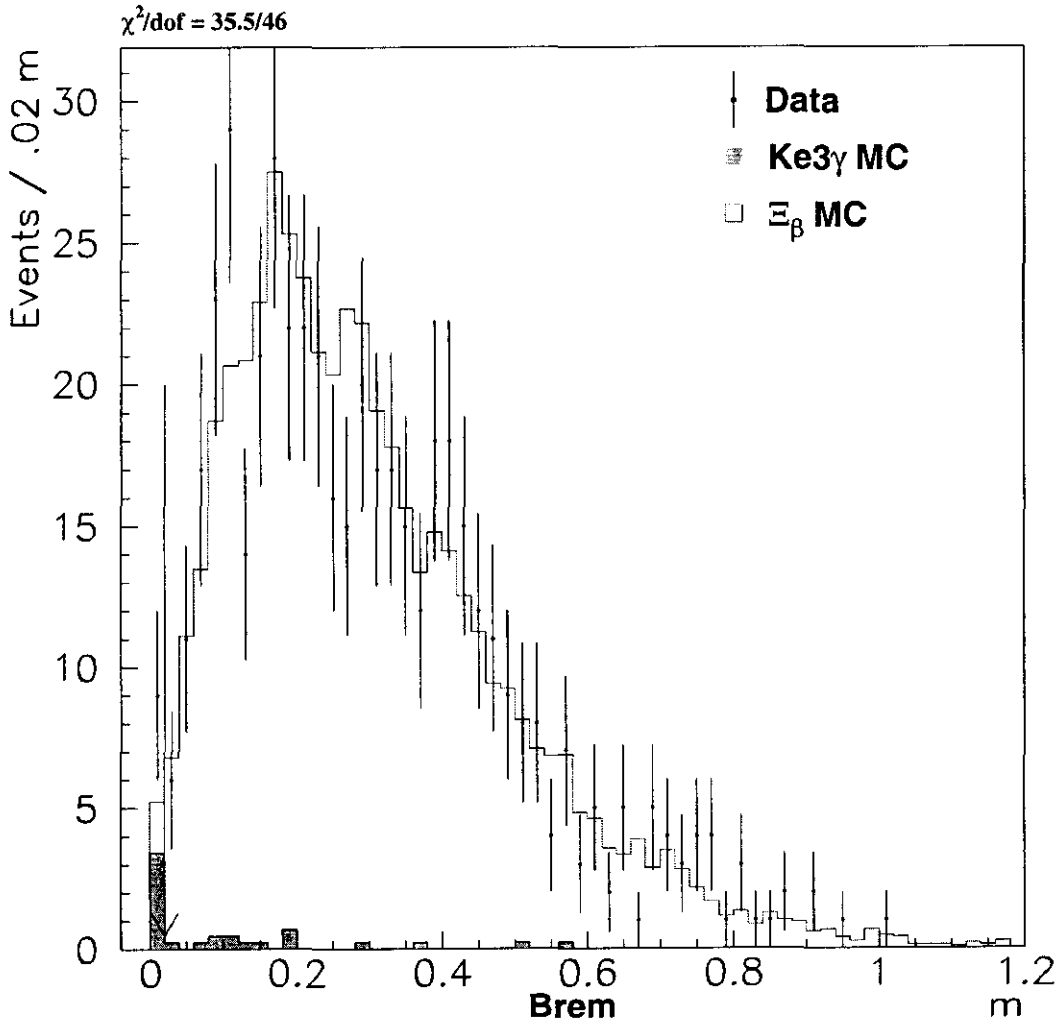

Figure 8.6: Data / Monte Carlo comparison of $Brem$ (described in the text). Here all selection criteria have been applied except the $Brem < .02\,cm$ requirement. The shaded histogram is the predicted $K_L \to \pi^+ e^- \overline{\nu}_e \gamma$ background. Events to the left of the arrow are removed

- $.00043 >| y_{\Xi^0}/z_{\Xi^0} |$
- $.00124 >| x_\Sigma/z_\Sigma |> .000376$
- $.00043 >| y_\Sigma/z_\Sigma |$
- Absolute value of x position of proton between $.07\,m$ and $.22\,m$ at both $186.0\,m$ and $189.6\,m$
- y position of proton between $-.07\,m$ and $.07\,m$ at both $186.0\,m$ and $189.6\,m$
- The e^- is required to be $7.5\,cm$ away from the center of either beam hole at chamber 4.
- Both extra clusters are required to have both x and y positions greater then $9.5\,cm$ away from the edges of center of either beam hole
- The CA (`CAMX_ENE`) is required to have less than $1\,GeV$ of energy.
- $E_\gamma > 3.0\,GeV$ (verify HCC)
- $E_{\gamma 1} + E_{\gamma 2} + E/p_{e^-} \times | p_{e^-} |> 18.0\,GeV$
- Positive track passes through STT illuminated region, and appropriate Kumquat and Banana channels have hits in them (verify STT)
- Number of proper lifetimes reconstructed as $\Lambda \rightarrow p\pi^- < 14.0$ (verify L3)
- $400.0\,GeV/c >| p_p |> 120.0\,GeV/c$ (verify L3)
- $50.0\,GeV/c >| p_e |> 5.0\,GeV/c$ (verify L3 , TRD)
- $| p_p | / | p_e |> 3.6$ (verify L3)

Kinematic and particle ID:

- $40.0\,m > z_\Sigma - z_{\Xi^0} > -6.0\,m$
- $1.1 > E/p_{e^-} > 0.9$

- $M_{K_L \to \pi^+\pi^-\pi^0} > 0.57\,GeV$ (reject $K_L \to \pi^+\pi^-\pi^0$)
- $M_{K_L \to \pi^0\pi^+e^-\overline{\nu}_e} > 0.50\,GeV\,OR\,z_\Sigma - z_{\Xi^0} > 3.0\,m$ (reject $K_L \to \pi^0\pi^+e^-\overline{\nu}_e$)
- Distance between either photon and upstream segment of electron at calorimeter $> 0.02\,m$ (reject $K_L \to \pi^+e^-\overline{\nu}_e\gamma$)
- $.010 > p^2_{\nu\|} > -.005(GeV^2)$ (Longitudinal momentum of neutrino in Ξ^0 frame, kinematic limits are 0.0 and $0.12\,GeV$)
- energy of electron in Σ^+frame $< 0.13\,GeV$
- total $p^2_T < .02\,GeV^2$
- Number of proper Ξ^0 lifetimes < 10.0
- No extra hits in X views in upstream chambers (reject γ conversions in vacuum window)
- $ppion < 0.1$ (gives about 9:1 π/e rejection)

We can obtain the energy of the neutrino in the Ξ^0 frame ($E_\nu^{[\Xi]}$) , the component of the neutrino momentum in the Ξ^0 frame perpendicular to the Ξ^0 momentum in the lab ($\vec{p}_{\nu\perp}$), and the magnitude of the component of the neutrino momentum in the Ξ^0 frame parallel to the Ξ^0 momentum in the lab ($p_{\nu\|}$).

$$E_\nu^{[\Xi]} = \sqrt{\frac{(m^2_\Xi - m^2_{\Sigma e})^2}{4m^2_\Xi}} \tag{8.20}$$

$$\vec{p}_{\nu\perp} = -\vec{p}_\perp \tag{8.21}$$

$$p^2_{\nu\|} = (E_\nu^{[\Xi]})^2 - p^2_\perp \tag{8.22}$$

Finally, for the determination of $g_1/f_1$and g_2/f_1, we will exclude events having an unphysical longitudinal neutrino momentum, $p^2_{\nu\|} < 0.0$. This cut removes about 31% of the signal (figure 8.5), and reduces the background under the peak by about a factor of 3.

Mode	Low Band	Peak	High Band
$\Xi^0 \to \Sigma^+ e^- \overline{\nu}_e$	6.0 ± 0.6		4.8 ± 0.6
$\Xi^0 \to \Lambda\pi^0$ with $\Lambda \to p\pi^-$ and $\pi^0 \to \gamma\gamma$	4.0 ± 1.9	1.4 ± 1.1	0.2 ± 0.3
$\Xi^0 \to \Lambda\pi^0$ with $\Lambda \to pe^-\overline{\nu}_e$ and $\pi^0 \to \gamma\gamma$	12.1 ± 1.1	1.0 ± 0.3	0.1 ± 0.1
$\Xi^0 \to \Lambda\pi^0$ with $\Lambda \to p\pi^-$ and $\pi^0 \to e^+e^-\gamma$	0.3 ± 0.2	1.0 ± 0.4	0.0 ± 0.0
$\Xi^0 \to \Sigma^0\gamma$ with $\Sigma^0 \to \Lambda\gamma$ and $\Lambda \to p\pi^-$	0.2 ± 0.2	0.2 ± 0.2	0.0 ± 0.0
$\Xi^0 \to \Sigma^0\gamma$ with $\Sigma^0 \to \Lambda\gamma$ and $\Lambda \to pe^-\overline{\nu}_e$	0.3 ± 0.1	0.3 ± 0.1	0.0 ± 0.0
$\Lambda \to p\pi^-$ with accidental $\gamma\gamma$	0.2 ± 0.3	0.4 ± 0.5	0.0 ± 0.0
$\Lambda \to pe^-\overline{\nu}_e$ with accidental $\gamma\gamma$	0.4 ± 0.1	0.4 ± 0.1	0.1 ± 0.0
$K_L \to \pi^+e^-\overline{\nu}_e$	7.4 ± 1.2	10.8 ± 1.5	1.8 ± 0.6
$K_L \to \pi^+e^-\overline{\nu}_e\gamma$	3.9 ± 0.9	7.5 ± 1.3	1.4 ± 0.6
$K_L \to \pi^0\pi^+e^-\overline{\nu}_e$ with $\pi^0 \to \gamma\gamma$	0.1 ± 0.1	0.6 ± 0.1	0.2 ± 0.1
SUM of MC Bkg	34.9 ± 2.8	23.6 ± 2.4	8.7 ± 1.8
DATA	48		5

Table 8.5: Tabulated Background where events with unphysical neutrino momentum are kept. Low Band $= m_{p\pi^0} - m_{\Sigma^+}$ between -30 and $-20\,MeV$, Peak $= m_{p\pi^0} - m_{\Sigma^+}$ between -15 and $+15\,MeV$, High Band $= m_{p\pi^0} - m_{\Sigma^+}$ between 20 and $30\,MeV$.

8.4.1 Backgrounds After Selection Criteria

We tabulate the remaining background with the above cuts applied, for the case of the events with $p^2_{\nu\|} < 0.0$ being excluded and kept. Figure 8.7 shows the proton π^0mass for the predicted Monte Carlo background compared with the data after all selection criteria have been applied. Figure 8.8 shows the proton π^0mass for the predicted Monte Carlo background compared with the data after all selection criteria have been applied, except the requirement that $p^2_{\nu\|} > 0$.

When events with $p^2_{\nu\|} < 0.0$ are excluded, we have a background of 7.4 events under the peak (about 2 %).

8.5 Data / Monte Carlo Comparisons

Figures 8.9 through 8.14 show data / Monte Carlo comparisons of various $\Xi^0 \to \Sigma^+ e^- \overline{\nu}_e$ distributions.

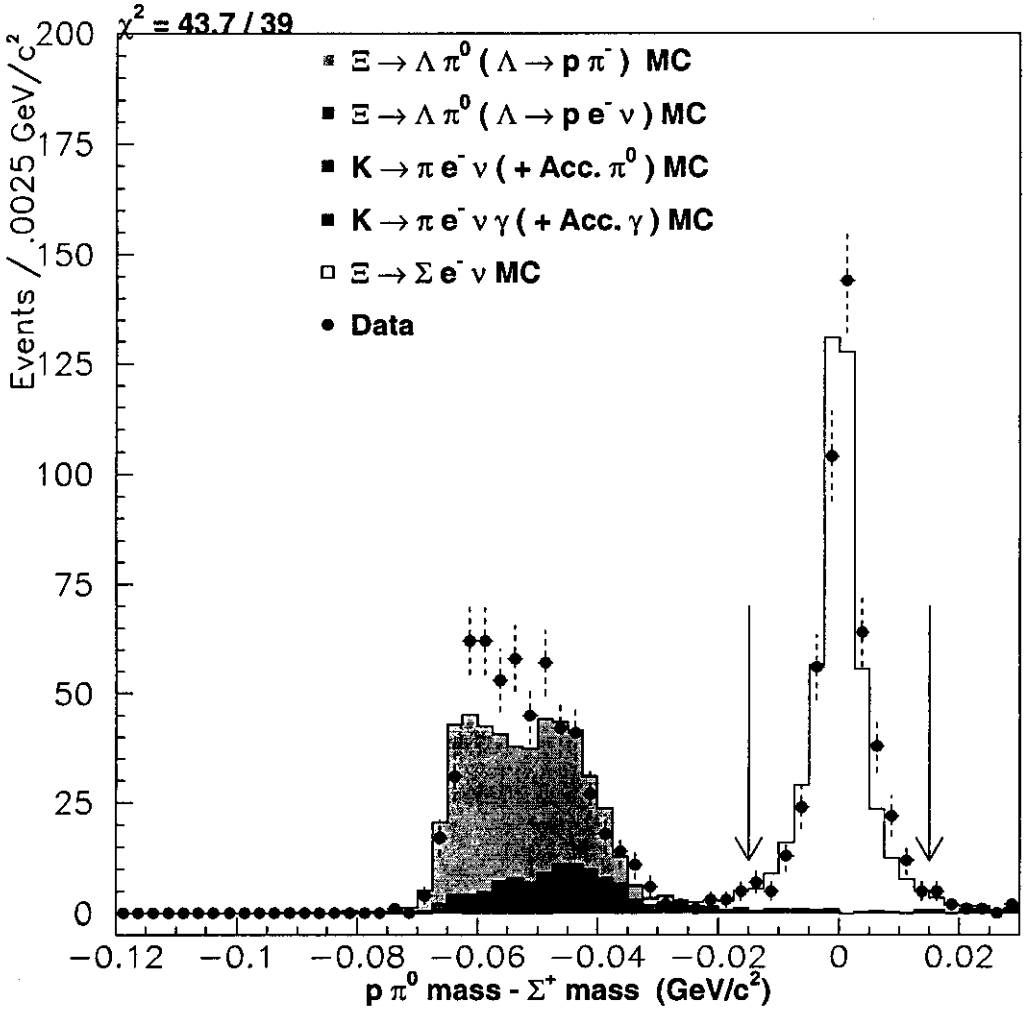

Figure 8.7: Data and Monte Carlo background, based on measured K_L and Ξ^0 flux. All selection criteria have been applied.

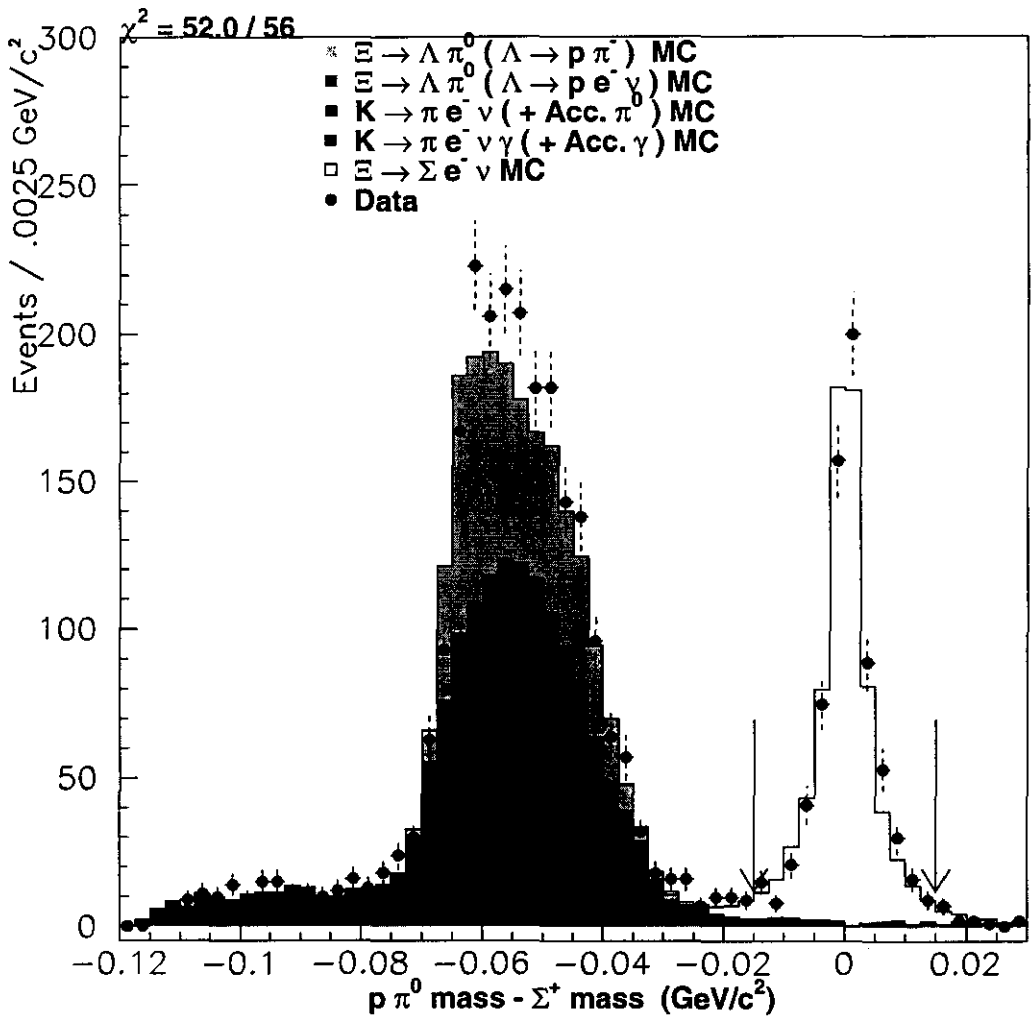

Figure 8.8: Data and Monte Carlo background, based on measured K_L and Ξ^0 flux. All selection criteria have been applied, expect events having $p^2_{\nu\|} < 0$ are kept.

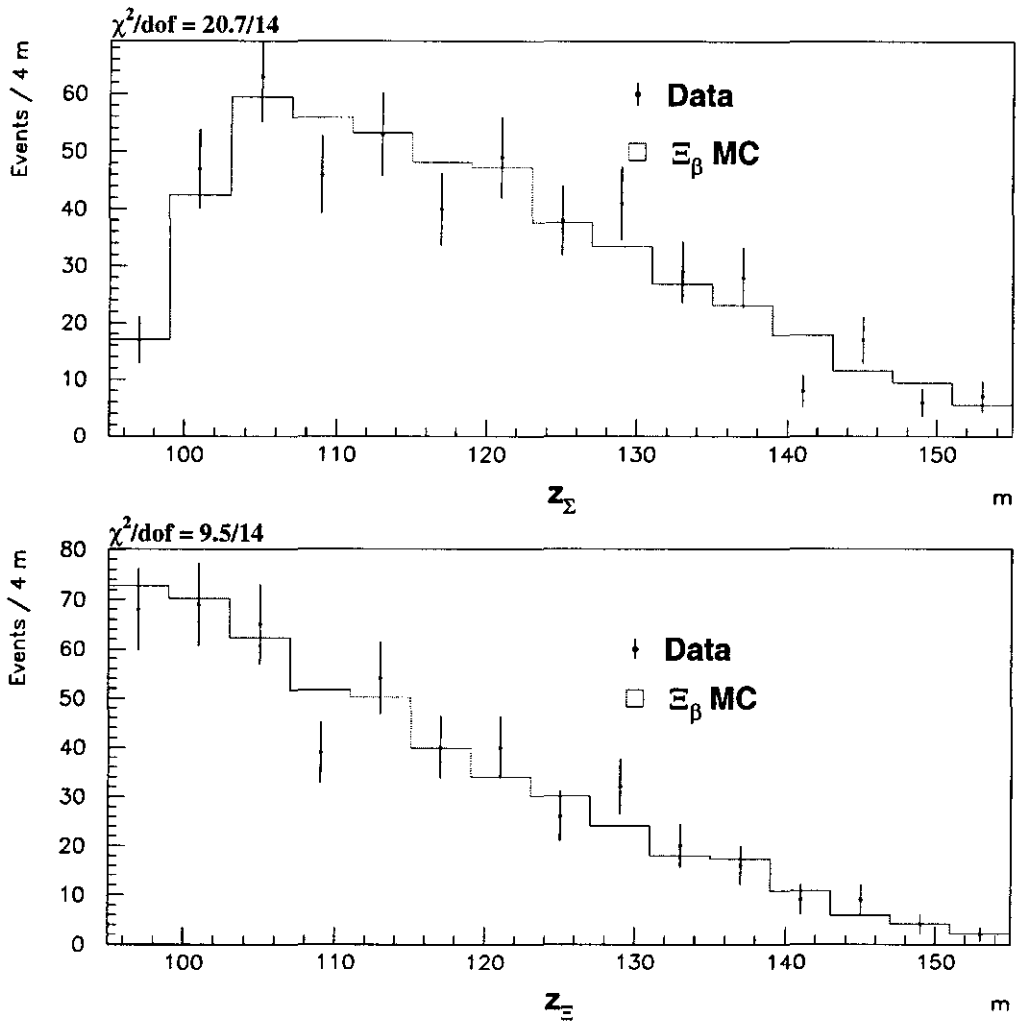

Figure 8.9: Data-Monte Carlo comparison of the z positions of the Σ^+(top) and Ξ^0 vertices (bottom).

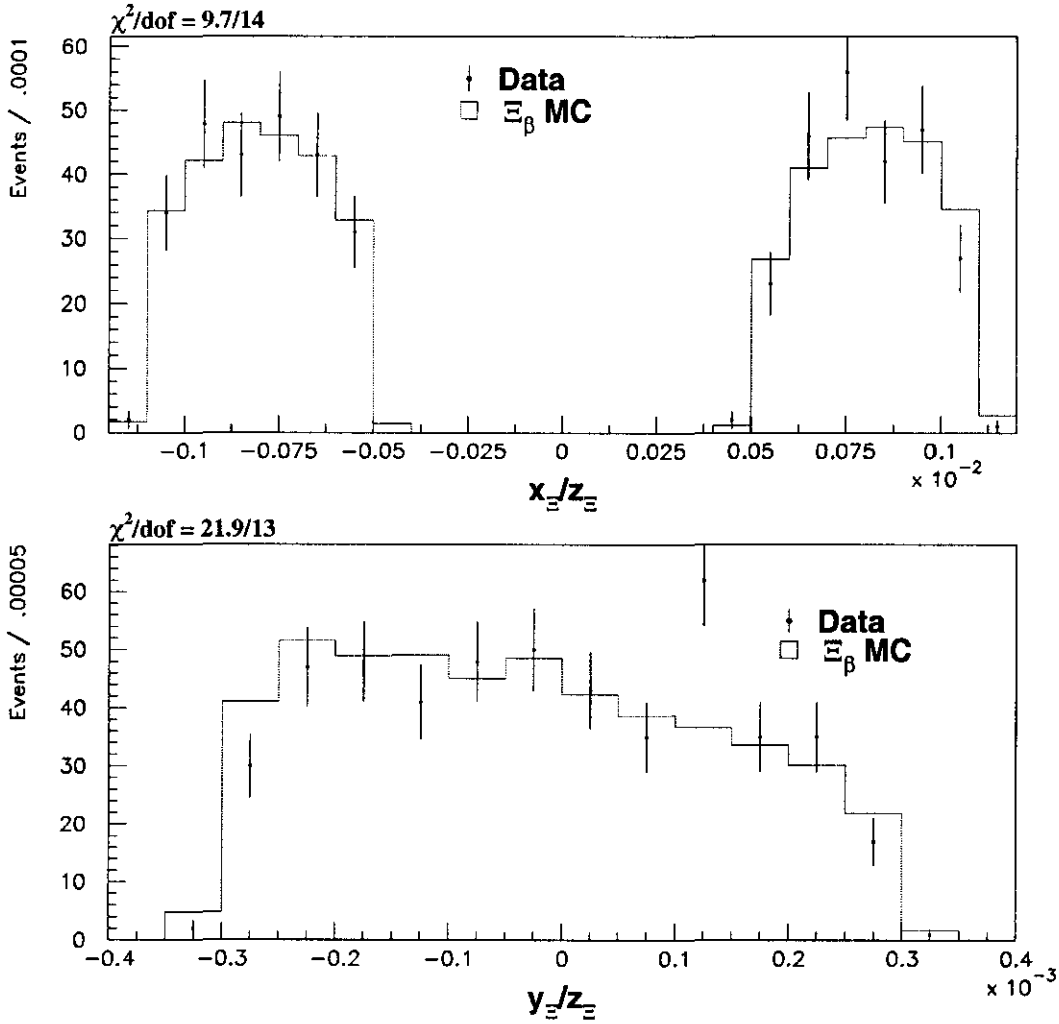

Figure 8.10: Data-Monte Carlo comparison of x/z of the Ξ^0 vertices (top) and y/z of the Ξ^0 vertices (bottom).

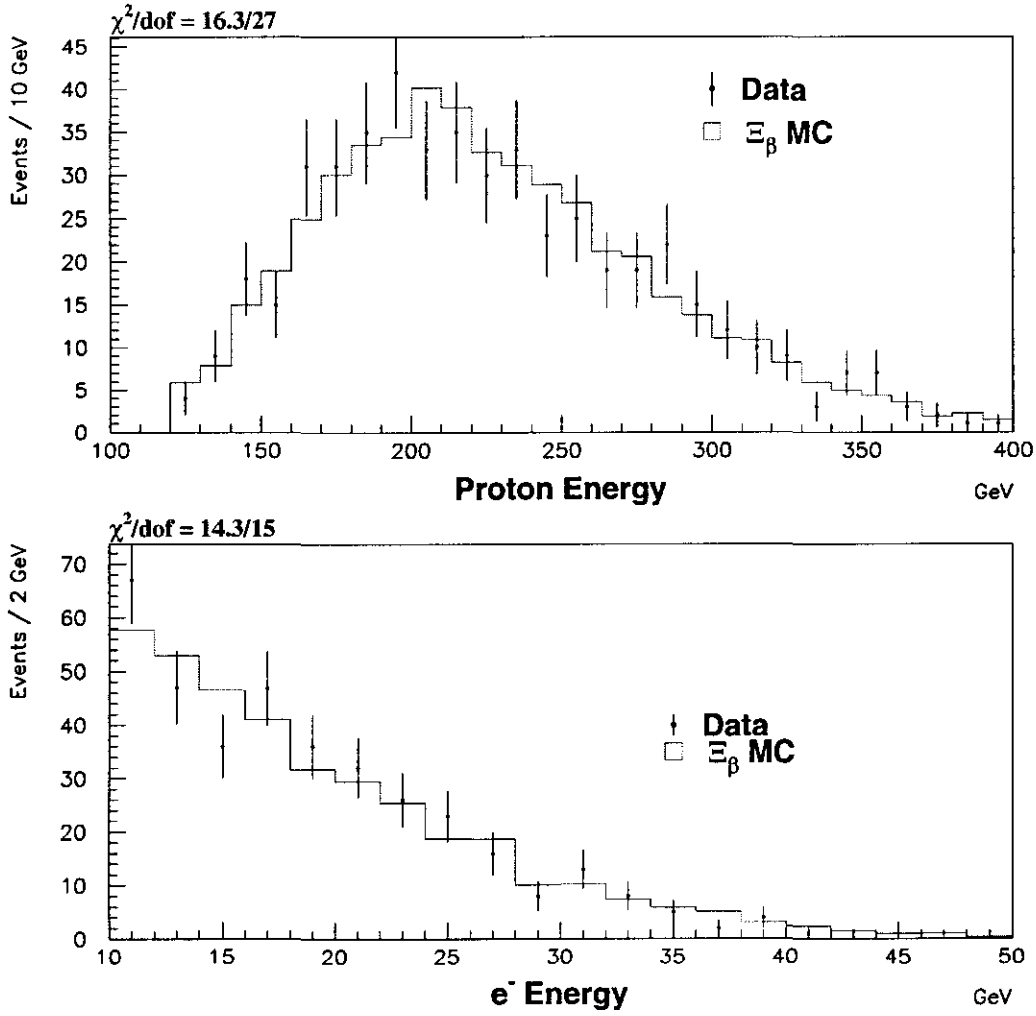

Figure 8.11: Data-Monte Carlo comparison of the proton (top) and e^-energies (bottom).

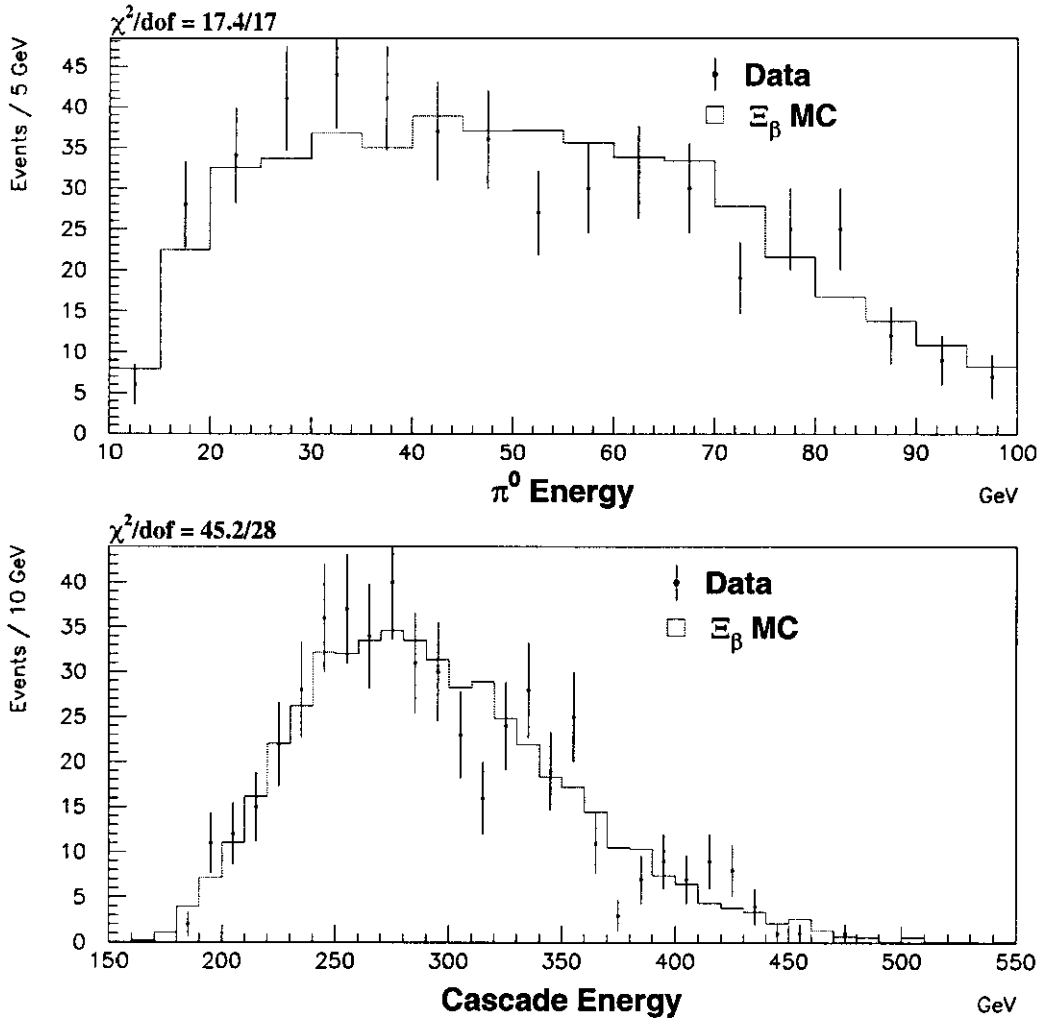

Figure 8.12: Data-Monte Carlo comparison of the π^0(top) and Ξ^0 energies (bottom).

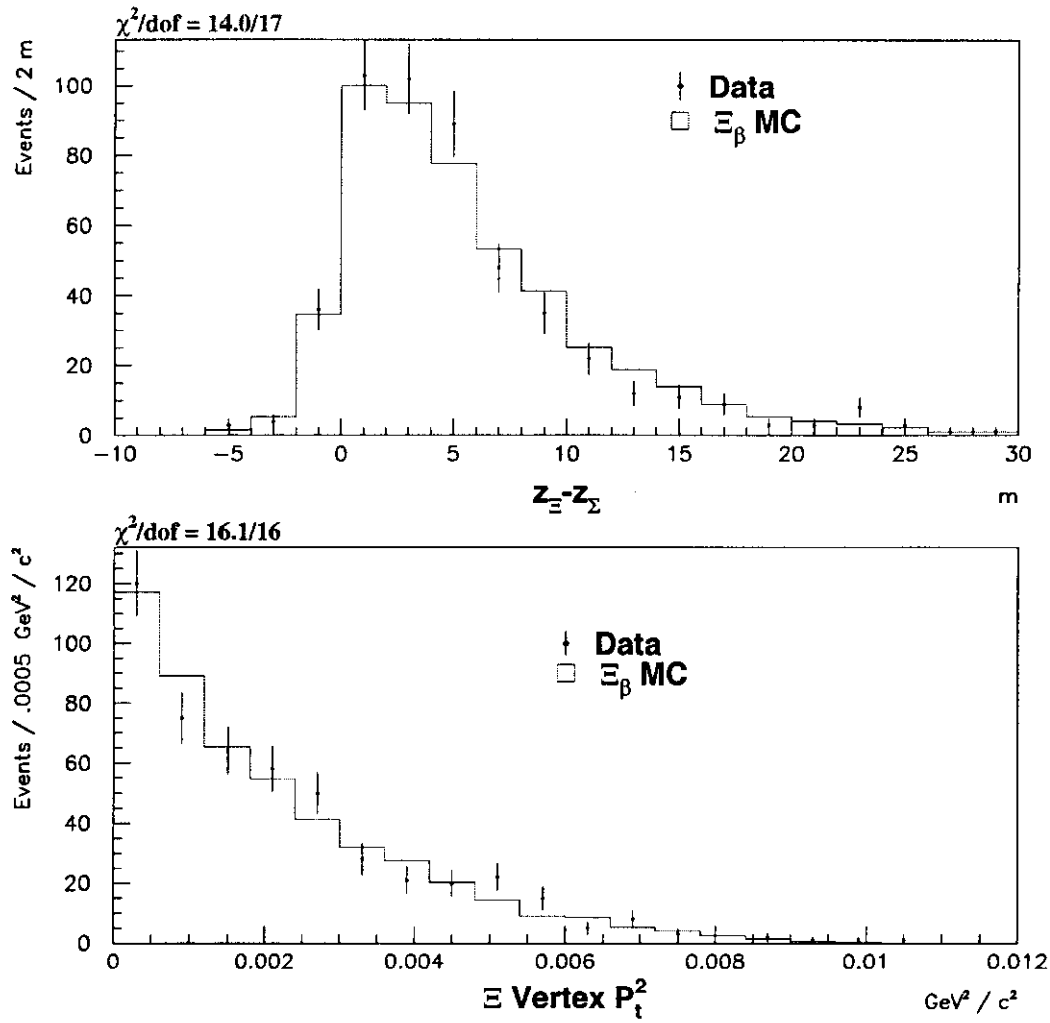

Figure 8.13: Data-Monte Carlo comparison of the difference between the Ξ^0 and Σ^+z vertex positions (top) and total Ξ^0 $p_\perp^2$(bottom).

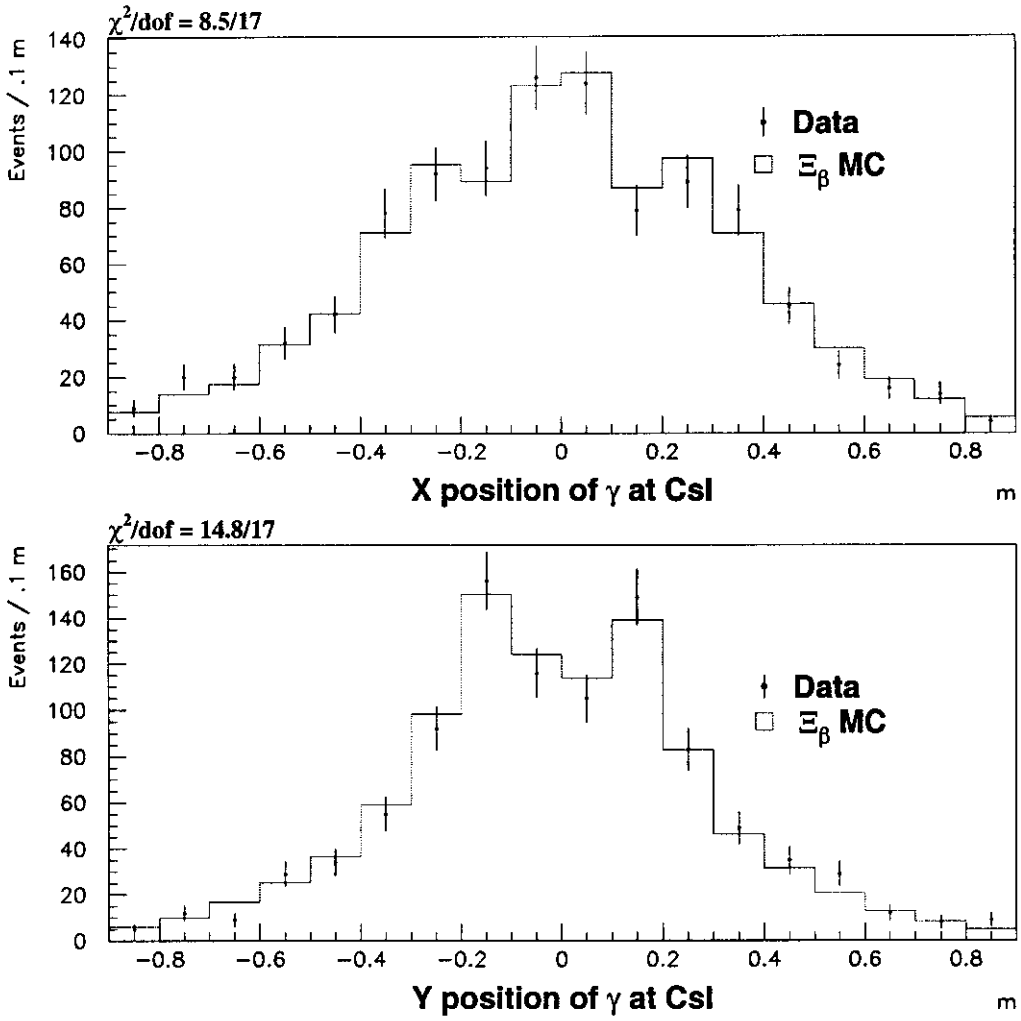

Figure 8.14: Data-Monte Carlo comparison of x (top) and y (bottom) positions of the photons at the CsI.

Mode	Low Band	Peak	High Band
$\Xi^0 \to \Sigma^+ e^- \overline{\nu}_e$	3.3 ± 0.5		3.2 ± 0.5
$\Xi^0 \to \Lambda\pi^0$ with $\Lambda \to p\pi^-$ and $\pi^0 \to \gamma\gamma$	2.5 ± 1.5	0.1 ± 0.3	0.1 ± 0.3
$\Xi^0 \to \Lambda\pi^0$ with $\Lambda \to pe^-\overline{\nu}_e$ and $\pi^0 \to \gamma\gamma$	2.1 ± 0.4	0.2 ± 0.1	0.0 ± 0.0
$\Xi^0 \to \Lambda\pi^0$ with $\Lambda \to p\pi^-$ and $\pi^0 \to e^+e^-\gamma$	0.0 ± 0.0	0.7 ± 0.3	0.0 ± 0.0
$\Xi^0 \to \Sigma^0\gamma$ with $\Sigma^0 \to \Lambda\gamma$ and $\Lambda \to p\pi^-$	0.1 ± 0.2	0.1 ± 0.1	0.0 ± 0.0
$\Xi^0 \to \Sigma^0\gamma$ with $\Sigma^0 \to \Lambda\gamma$ and $\Lambda \to pe^-\overline{\nu}_e$	0.0 ± 0.0	0.0 ± 0.0	0.0 ± 0.0
$\Lambda \to p\pi^-$ with accidental $\gamma\gamma$	0.1 ± 0.2	0.2 ± 0.3	0.0 ± 0.0
$\Lambda \to pe^-\overline{\nu}_e$ with accidental $\gamma\gamma$	0.1 ± 0.0	0.1 ± 0.0	0.0 ± 0.0
$K_L \to \pi^+e^-\overline{\nu}_e$	2.2 ± 0.7	2.0 ± 0.6	0.8 ± 0.4
$K_L \to \pi^+e^-\overline{\nu}_e\gamma$	2.0 ± 0.7	3.4 ± 0.9	1.1 ± 0.5
$K_L \to \pi^0\pi^+e^-\overline{\nu}_e$	0.1 ± 0.1	0.6 ± 0.1	0.2 ± 0.1
SUM of MC Bkg	12.5 ± 1.9	7.4 ± 1.2	5.4 ± 0.9
DATA	8		4

Table 8.6: Tabulated Background where events with unphysical neutrino momentum are excluded. Low Band = $m_{p\pi^0} - m_{\Sigma^+}$ between -30 and $-20\,MeV$, Peak = $m_{p\pi^0} - m_{\Sigma^+}$ between -15 and $+15\,MeV$, High Band = $m_{p\pi^0} - m_{\Sigma^+}$ between 20 and $30\,MeV$.

Chapter 9

EXTRACTION OF THE FORM FACTORS OF $\Xi^0 \to \Sigma^+ e^- \overline{\nu}_e$

In this chapter, we discuss the extraction of the form factors for the signal and the evaluation of systematic errors.

9.1 Kinematic Variables

There are 4 variables required to completely describe the decay chain $\Xi^0 \to \Sigma^+ e^- \overline{\nu}_e$ with $\Sigma^+ \to p\pi^0$, assuming the Ξ^0 is unpolarized.

- The angle between the electron and neutrino in the Ξ^0 frame ($x_{e\nu}^{[\Xi]} = \cos(\theta_{e-\nu})$)
- The energy of the electron in the Σ^+frame (e = $E_e^{[\Sigma]}$);
- The angle between the proton and the electron in the Σ^+frame ($x_{pe}^{[\Sigma]} = \cos(\theta_{p-e})$)
- The angle between the proton and the neutrino in the Σ^+frame ($x_{p\nu}^{[\Sigma]} = \cos(\theta_{p-\nu})$)

9.2 Integrated Observables

The total rate for the process is given by:

$$
\begin{aligned}
R &= R_0[(1-\frac{3}{2}\delta)f_1^2 + (3-\frac{9}{2}\delta)g_1^2 - (4\delta)g_1 g_2], \\
R_0 &= \frac{G_F^2 \mid V_{CKM} \mid^2 (M_{\Xi^0} - M_{\Sigma^+})^5}{60\pi^3} \qquad (9.1) \\
\delta &= \frac{M_{\Xi^0} - M_{\Sigma^+}}{M_{\Xi^0}} \qquad (9.2)
\end{aligned}
$$

The ensemble polarization of the Σ^+along the electron direction ($\times$ the total rate) is:

$$\begin{aligned} R\mathsf{S}_e &= R_0[(2-\frac{10}{3}\delta)g_1^2+(2-\frac{7}{3}\delta)f_1g_1-(\frac{1}{3}\delta)f_1^2 \\ &\quad -(\frac{2}{3}\delta)f_1f_2+(\frac{2}{3}\delta)f_2g_1-(\frac{2}{3}\delta)f_1g_2-(\frac{10}{3}\delta)g_1g_2+\mathcal{O}(\delta^2)] \end{aligned} \tag{9.3}$$

Thus, the distribution of the proton relative to the electron in the Σ^+frame is

$$\frac{dN}{dx_{pe}^{[\Sigma]}}=\frac{1}{2}(1+\alpha_{\Sigma^+}\mathsf{S}_e x_{pe}^{[\Sigma]}), \tag{9.4}$$

where α_{Σ^+} is the $\Sigma^+ \to p\,\pi^0$ two body asymmetry.

Similarly, the polarization of the Σ^+along the neutrino direction is:

$$\begin{aligned} R\mathsf{S}_\nu &= R_0[(-2+\frac{10}{3}\delta)g_1^2+(2-\frac{7}{3}\delta)f_1g_1+(\frac{1}{3}\delta)f_1^2 \\ &\quad +(\frac{2}{3}\delta)f_1f_2+(\frac{2}{3}\delta)f_2g_1-(\frac{2}{3}\delta)f_1g_2+(\frac{10}{3}\delta)g_1g_2+\mathcal{O}(\delta^2)]. \end{aligned} \tag{9.5}$$

We define the electron-neutrino correlation (in the Ξ^0 frame) as:

$$\alpha_{e\nu}=2\frac{N(\theta_{e\nu}>\pi/2)-N(\theta_{e\nu}<\pi/2)}{N(\theta_{e\nu}>\pi/2)+N(\theta_{e\nu}<\pi/2)}, \tag{9.6}$$

where $N(\theta_{e\nu}>\pi/2)$ refers to the number of decays observed where the angle between the electron and neutrino is greater than $\pi/2$. The electron-neutrino correlation ($\times$ the total rate) is equal to:

$$R\alpha_{e\nu} = R_0[(-1-\frac{3}{2}\delta)g_1^2+(1-\frac{5}{2}\delta)f_1^2+(4\delta)g_1g_2+\mathcal{O}(\delta^2)]. \tag{9.7}$$

In addition, the spectrum of the electron in the $\Sigma^+$is frame is roughly:

$$\frac{dN}{dE_e^{[\Sigma]}} = cE_e^{[\Sigma]^2}(E_{e(MAX)}^{[\Sigma]} - E_e^{[\Sigma]})^2[1 + \frac{E_e^{[\Sigma]}}{M_\Sigma}\frac{(-2f_1^2 - 10g_1^2 + 4f_1g_1 + 8f_2g_1)}{f_1^2 + 3g_1^2}]R_{em}(E_e^{[\Sigma]}) \tag{9.8}$$

Where $R_{em}(E_e^{[\Sigma]})$ is due to radiative corrections, discussed in [2], and $E_{e(MAX)}^{[\Sigma]}$is the maximum energy of the electron in the Σ^+frame.

Although we do not use the integrated observables S_e , S_ν and $\alpha_{e\nu}$ here, we see that the distributions of $x_{pe}^{[\Sigma]}$, $x_{p\nu\perp}^{[Q]}$, and $x_{e\nu\perp}^{[Q]}$are most sensitive to g_1/f_1. Also, we see that the beta spectrum has the greatest sensitivity to f_2/f_1.

To a good approximation, the term f_2/f_1can be determined from the distribution of $E_e^{[\Sigma]}$, and $g_1/f_1$and g_2/f_1can be determined from the distributions in the other three variables.

9.3 Transverse Kinematic Variables

Determining $x_{pe}^{[\Sigma]}$from the lab momenta of the observed particles is simple:

$$E_p^{[\Sigma]} = \frac{p_p \cdot p_\Sigma}{M_\Sigma} \tag{9.9}$$

$$|\vec{p_p}^{[\Sigma]}| = \sqrt{(E_p^{[\Sigma]})^2 - M_p^2} \tag{9.10}$$

$$E_e^{[\Sigma]} = \frac{p_e \cdot p_\Sigma}{M_\Sigma} \tag{9.11}$$

$$x_{pe}^{[\Sigma]} = \frac{E_p^{[\Sigma]}E_e^{[\Sigma]} - p_e \cdot p_p}{E_e^{[\Sigma]}|\vec{p_p}^{[\Sigma]}|} \longleftrightarrow \mathsf{S}_e \tag{9.12}$$

In order to determine $x_{e\nu}^{[\Xi]}$and $x_{p\nu}^{[\Sigma]}$, we must find the momentum of the neutrino in the Ξ^0 frame. Using the measured lab four-momenta of the observable particles ($p_e, p_p, p_\Sigma = p_p + p_{\pi^0}$) ,the $\vec{p}_\perp$of the decay and the constraints of momentum and energy conservation.

The $\vec{p}_\perp$of the decay is the component of the observed Ξ^0 momentum ($\vec{P_{obs}}$) transverse to a vector pointing from the target to the Ξ^0 vertex($\vec{V}$). That is,

$$\vec{p}_\perp = \vec{P_{obs}} - (\vec{P_{obs}} \cdot \vec{V})\vec{V}/(\vec{V} \cdot \vec{V}). \tag{9.13}$$

We can obtain the energy of the neutrino in the Ξ^0 frame ($E_\nu^{[\Xi]}$) , the component of the neutrino momentum in the Ξ^0 frame perpendicular to the Ξ^0 momentum in the lab ($\vec{p}_{\nu\perp}$), and the magnitude of the component of the neutrino momentum in the Ξ^0 frame parallel to the Ξ^0 momentum in the lab ($p_{\nu\|}$).

$$E_\nu^{[\Xi]} = \sqrt{\frac{(m_\Xi^2 - m_{\Sigma e}^2)^2}{4m_\Xi^2}} \tag{9.14}$$

$$\vec{p}_{\nu\perp} = -\vec{p}_\perp \tag{9.15}$$

$$p_{\nu\|} = \pm\sqrt{(E_\nu^{[\Xi]})^2 - p_\perp^2} \tag{9.16}$$

In determining $p_{\nu\|}$, there is an ambiguity as to whether the positive or negative solution is to be used. For a monochromatic beam, the sign can be determined by virtue of the fact that the two solutions will give different total Ξ^0 energies. At KTeV, the distribution of Ξ^0 momenta is wide enough to completely wash out any information about the sign of the longitudinal component. Additionally, we must have the condition $p_{\nu\|}^2 > 0$ in order to obtain a real value for $p_{\nu\|}$, events failing this requirement due to detector resolution must therefore be excluded.

Given these disadvantages, we will make use of the TRANSVERSE component of the neutrino momentum only, following the analysis of $\Lambda \to pe^-\overline{\nu}_e$ decays by Dworkin *et al.* [75].

We define

$$p_Q = p_e + p_\Sigma \tag{9.17}$$

$$m_Q^2 = p_Q \cdot p_Q \tag{9.18}$$

Quantities in the Q frame will be denoted with a $^{[Q]}$. The momentum of the

electron in the Q frame is

$$\vec{p_e}^{[Q]} = \vec{p_e}^{[LAB]} - \frac{(\vec{p_e}^{[LAB]} \cdot \vec{p_q}^{[LAB]})}{\vec{p_q}^{[LAB]} \cdot \vec{p_q}^{[LAB]}} \vec{p_q}^{[LAB]} \tag{9.19}$$

And the energy of the electron in the Q frame is

$$E_e{}^{[Q]} = \frac{m_Q^2 - m_\Sigma^2}{2m_Q} \tag{9.20}$$

The momentum of the neutrino in the Q frame, transverse to the Ξ^0 direction is simply the $\vec{p}_\perp$of the decay.

$$\vec{p}_{\nu\perp}^{[Q]} = -\vec{p}_\perp \tag{9.21}$$

The energy of the neutrino in the Q frame is

$$E_\nu{}^{[Q]} = \frac{m_\Xi^2 - m_Q^2}{2m_Q} \tag{9.22}$$

We then have the unambiguous kinematic quantities

$$x_{e\nu\perp}^{[Q]} = \frac{\vec{p_e}^{[Q]} \cdot \vec{p_{\nu\perp}}^{[Q]}}{E_e{}^{[Q]} E_\nu{}^{[Q]}} \longleftrightarrow \alpha_{e\nu} \tag{9.23}$$

$$x_{p\nu\perp}^{[Q]} = \frac{\vec{p_p}^{[Q]} \cdot \vec{p_{\nu\perp}}^{[Q]}}{\mid \vec{p_p}^{[Q]} \mid E_\nu{}^{[Q]}} \longleftrightarrow \mathsf{S}_\nu \tag{9.24}$$

9.4 Extraction of g_1/f_1

For each data event,$x_{pe}^{[\Sigma]}$, $x_{e\nu\perp}^{[Q]}$and $x_{p\nu\perp}^{[Q]}$are calculated and put into a $10 \times 10 \times 10$ bin histogram. A corresponding histogram is made for different values of g_1/f_1(we used the interval $(0.3, 2.6)$ in intervals of .02). The histograms for the different values of $g_1/f_1$are obtained by re-weighting the differential decay rate in [74] using the *GENERATED* Monte Carlo (MC)kinematic variables. We then calculate the

log likelihood for each g_1/f_1 by

$$\mathcal{L}(g_1/f_1) = \Sigma_{ijk} D_{ijk} \log MC(g_1/f_1)_{ijk} \tag{9.25}$$

Where the MC histograms are all appropriately normalized. The central value is the value of g_1/f_1 which maximizes $\mathcal{L}$. With the standard errors being determined by change in g_1/f_1 which changes $\mathcal{L}$ by 1/2 (figure 9.1). The errors are asymmetric due to the non-linear dependence of g_1/f_1 on the integrated observables. A DATA-MC comparison of the one dimensional distributions of $x_{pe}^{[\Sigma]}$, $x_{e\nu\perp}^{[Q]}$ and $x_{p\nu\perp}^{[Q]}$ is in figure 9.2.

9.4.1 Correcting for Background

Our best background estimate with this selection criteria is 7.4 ± 3.7 events (about $2 \pm 1\%$ of the signal), the background being almost entirely due to $K_L \to \pi^+ e^- \overline{\nu}_e$ and $K_L \to \pi^+ e^- \overline{\nu}_e \gamma$ decays. We estimate the effect of this background by adding MC background events to MC signal events and observing the change in the measured value of g_1/f_1 in the MC samples. We used 30 'data sized' $\Xi^0 \to \Sigma^+ e^- \overline{\nu}_e$ Monte Carlo samples with 9 values of g_1/f_1 ranging from .9 to 1.6. The recovered values with no background added were compared to the values with background added. We estimate the error on the correction by adding background with both the high momentum track being positive and negative, and observing the difference, and by scaling the background by 1.5. Averaging the corrections from MC samples with g_1/f_1 of 1.2, 1.25 and 1.3 gives a correction of $-.014 \pm .039$. Neglecting background we find the maximum value for $\mathcal{L}$ at $g_1/f_1 = 1.332$. Thus our final value for g_1/f_1 is 1.32. The systematic error due to background is subtraction is taken to be .039.

9.5 Systematic Errors on g_1/f_1

9.5.1 Backgrounds

Determined in the above section to be .039.

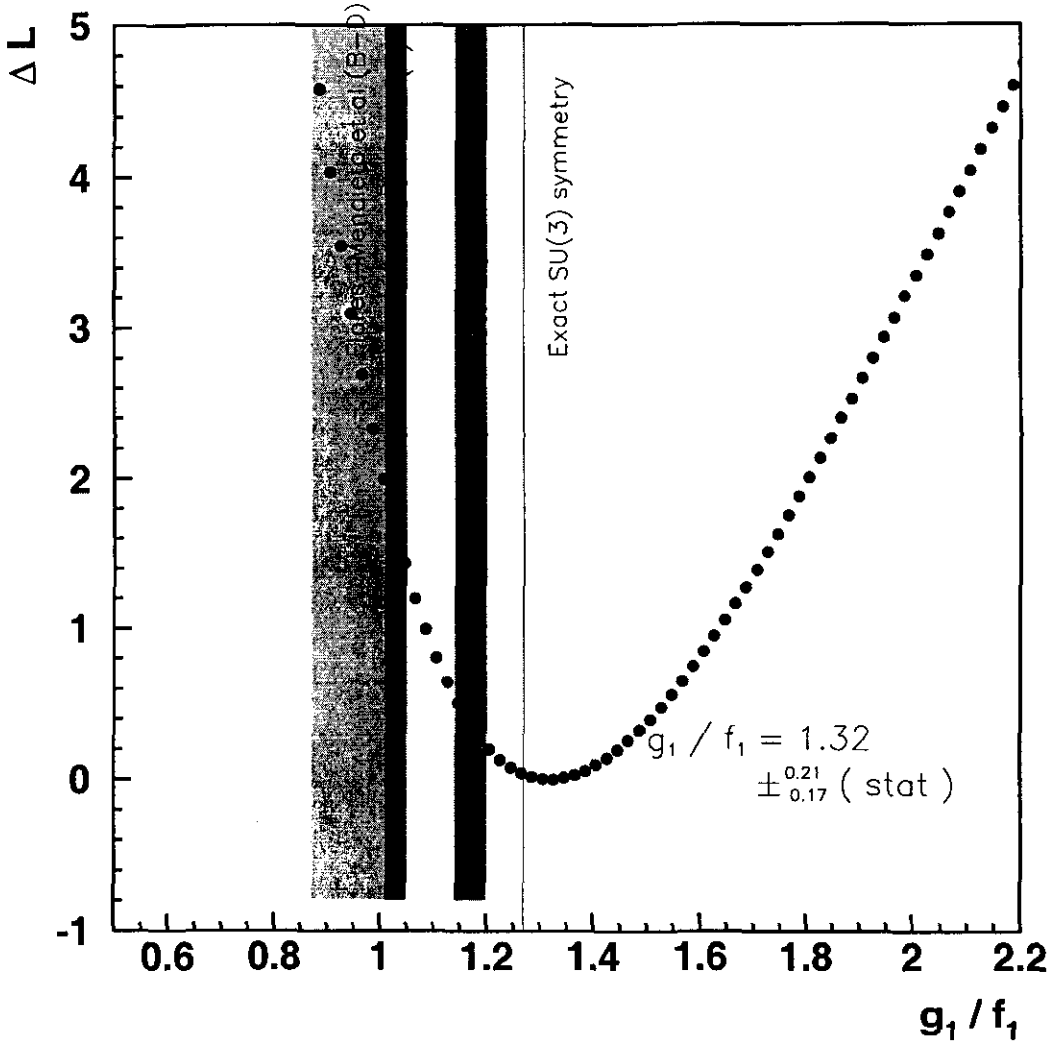

Figure 9.1: Maximum Likelihood fit to g_1/f_1corrected for background.

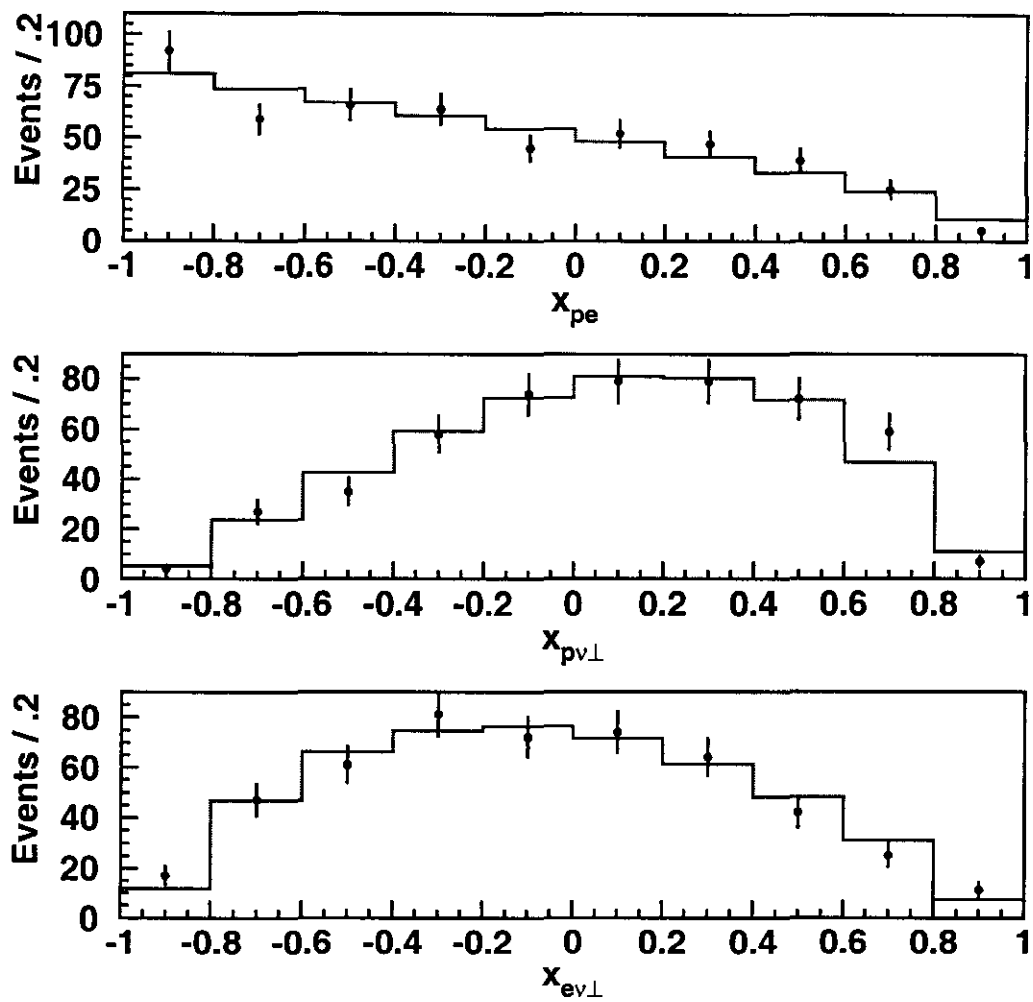

Figure 9.2: g_1/f_1Comparison of DATA-MC distributions of $x_{pe}^{[\Sigma]}$, $x_{p\nu\perp}^{[Q]}$and $x_{e\nu\perp}^{[Q]}$(MC generated with g_1/f_1= 1.27).

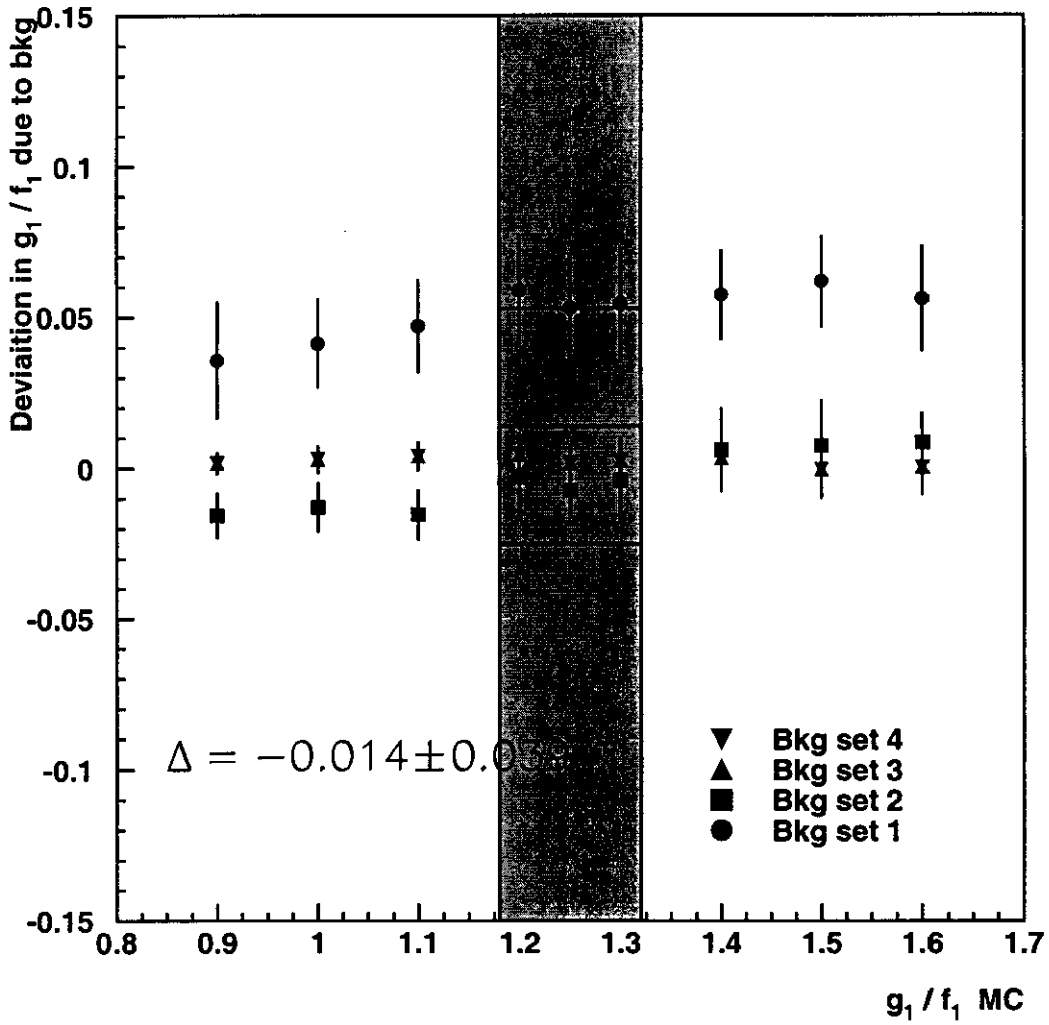

Figure 9.3: Background Correction to g_1/f_1, the filled circles are the corrections found with the MC background with the high momentum track being positive.

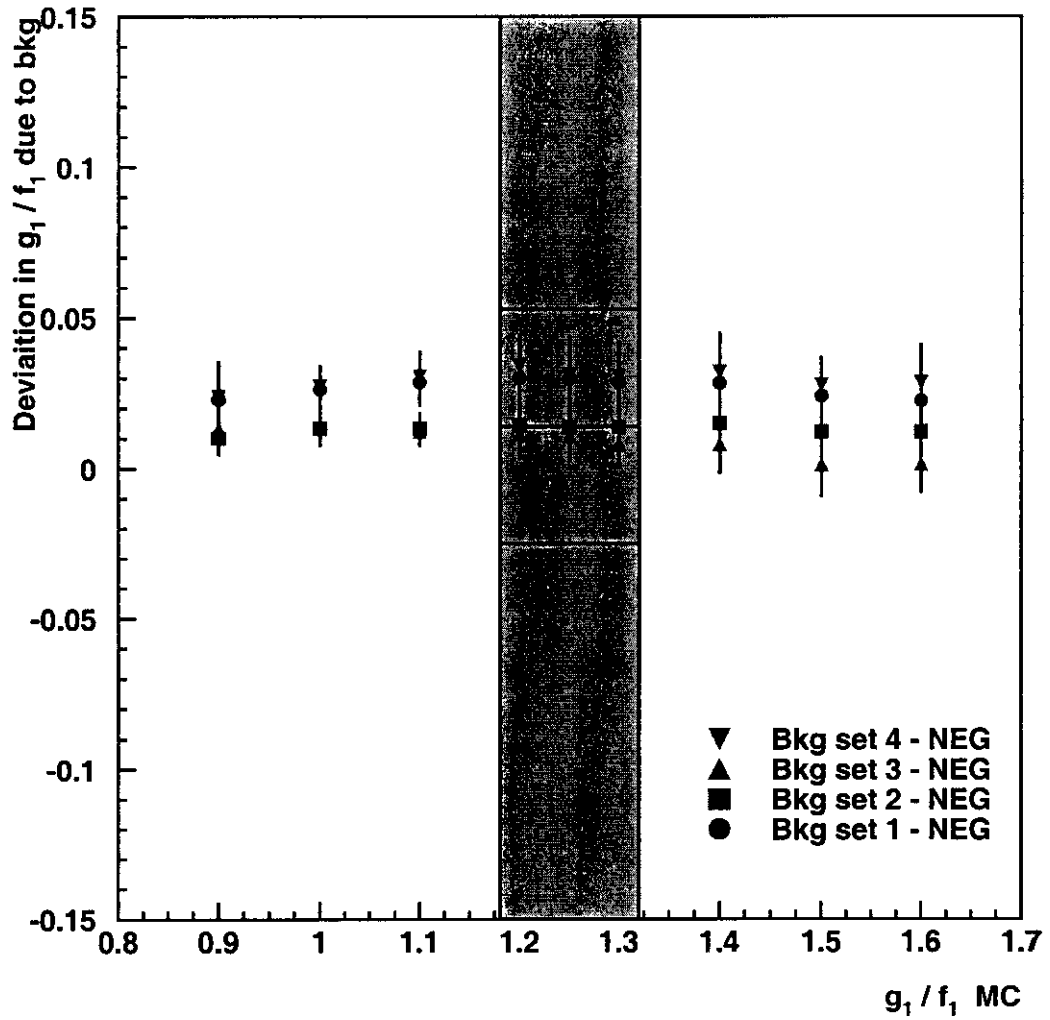

Figure 9.4: Background Correction to g_1/f_1, the filled circles are the corrections found with the MC background with the high momentum track being negative (for K_L background).

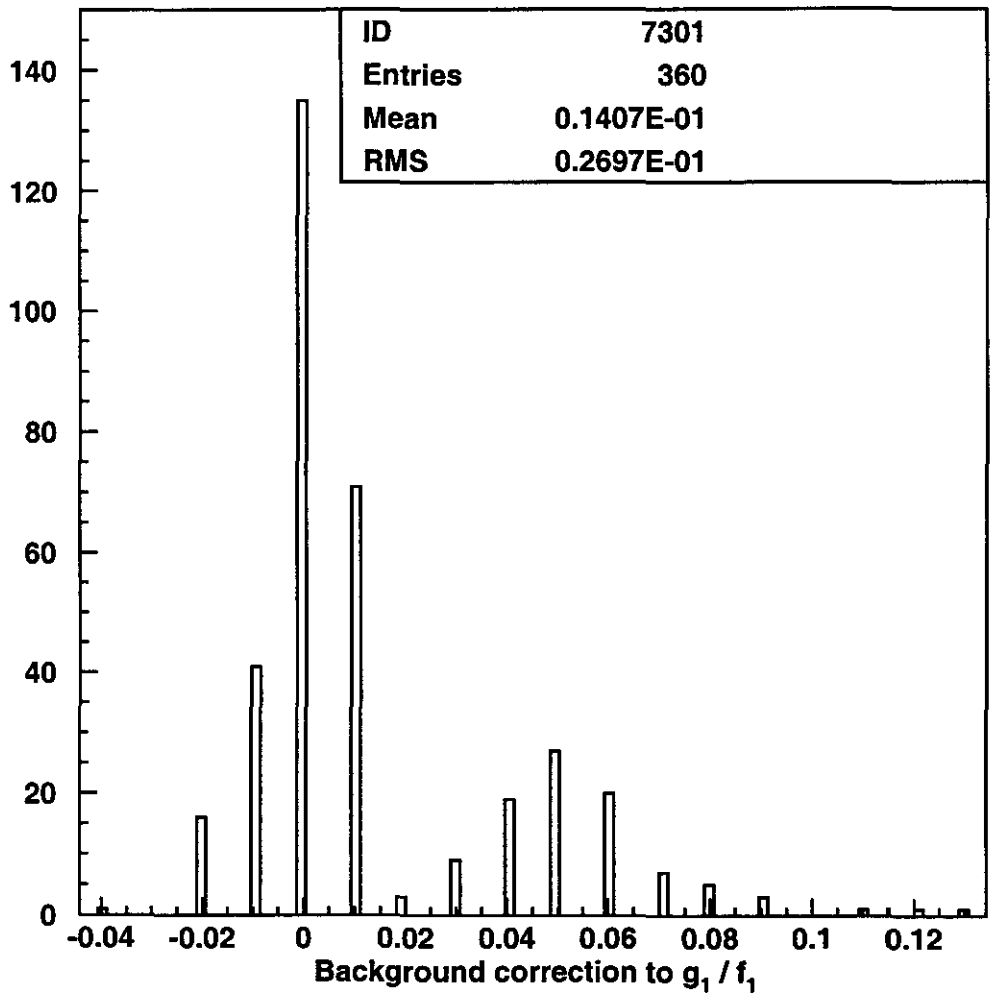

Figure 9.5: The background correction to $g_1/f_1$is evaluated by taking the mean of the corrections from the 4 background sets to the 90 Monte Carlo data sized datasets (360 total).

9.5.2 Residual Errors in Drift Chamber Alignment

For $\Xi^0 \to \Lambda\pi^0$ with $\Lambda \to p\pi^-$ we find a small offset of unknown origin in OFFMAG. We estimate the size of this effect by re-analyzing the CM sample with offsets in the x and y positions of DC 1 by $\pm 20\,\mu m$. Adding the average deviations from x and y offsets in quadrature gives a systematic error of .020 due to Drift Chamber Alignment. Adding a $100\,\mu rad$ Non-orthogonality to DC 1 does not alter the value of g_1/f_1.

9.5.3 Mass of the Ξ^0

We generated a MC $\Xi^0 \to \Sigma^+ e^- \overline{\nu}_e$ with $\Sigma^+ \to p\,\pi^0$ sample with the mass of the Ξ^0 being $1315.5\,GeV/c^2$ (the PDG mass of the Ξ^0 is $1314.9 \pm .6\,MeV/c^2$, and the recent NA48 result for the Ξ^0 mass is $1314.82 \pm 0.06(stat) \pm 0.2(syst)\,MeV/c^2$ [64]) and found the value of g_1/f_1 changed by +.017, consistent with the MC statistical error of .02.

9.5.4 $Z_{\Sigma^+} - Z_{\Xi^0}$ cut

We varied the value of this cut from its nominal value of $-6\,m$ to $+1\,m$ and found no significant variation in the value of g_1/f_1 (figure 9.8).

9.5.5 HA

We have not considered any systematic effect due to $\Xi^0 \to \Sigma^+ e^- \overline{\nu}_e$ events being vetoed by the Hadron Anti veto at L1.

9.5.6 Lifetime of the Ξ^0

Using $\Xi^0 \to \Lambda\pi^0$ with $\Lambda \to p\pi^-$ our data indicates that the $c\tau$ of the Ξ^0 is about 5 % higher than its PDG value. (Or, that we do not accurately model the acceptance of Ξ^0 decays in z at the 5% level) We estimate the effect of this by re-weighting the $\Xi^0 \to \Sigma^+ e^- \overline{\nu}_e$ with $\Sigma^+ \to p\,\pi^0$ MC events to change the $c\tau$ of the Ξ^0 by

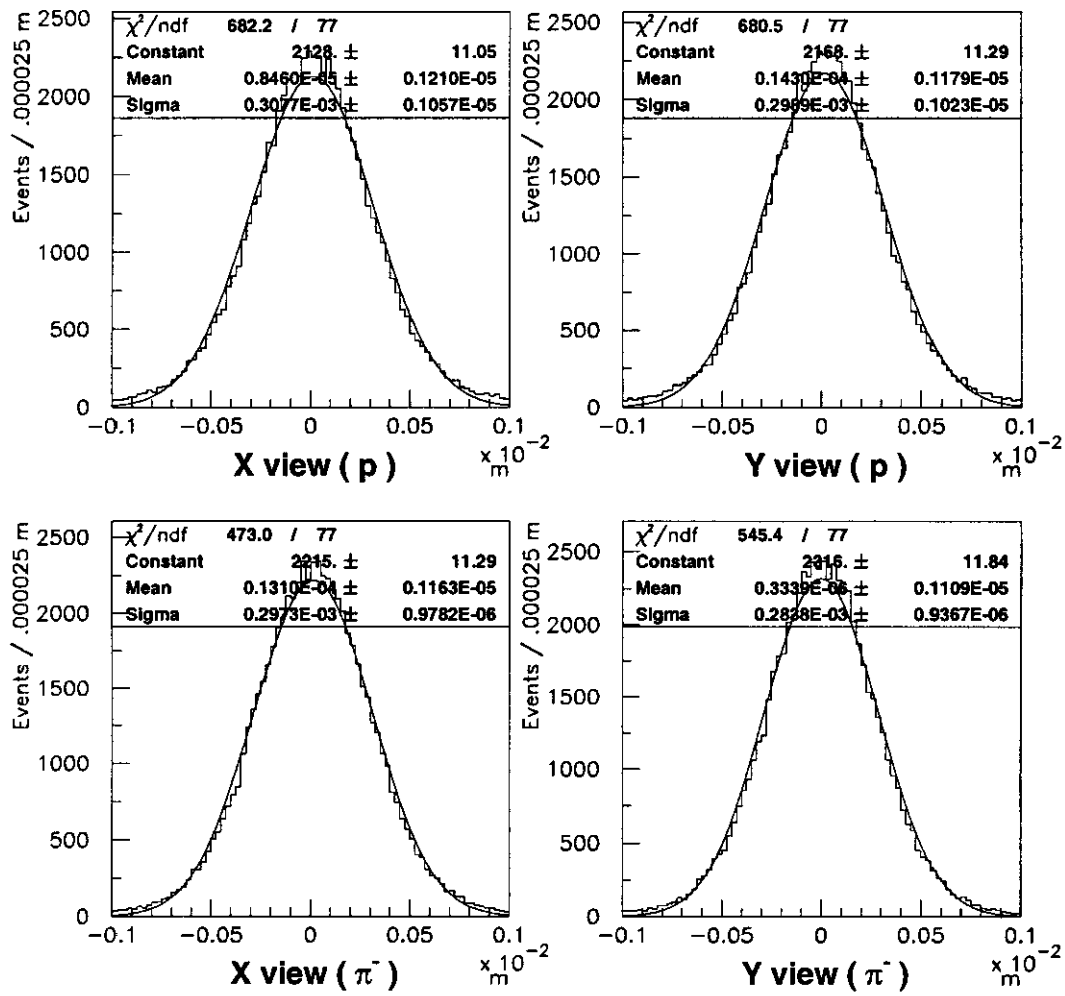

Figure 9.6: OFFMAG for $\Xi^0 \rightarrow \Lambda\pi^0$ events, the top plots are for the high momentum track (proton), the bottom plots are for the low momentum track (pion). The plots on the right are for the Y view, the plots on the left are for the X view.

+5%(−5%) and find the value g_1/f_1changes by −.008(.009). We assign a systematic error of ±.009 to g_1/f_1due to this effect.

9.5.7 Neutral Energy Scale

Even with our limited data sample, we see a clear mismatch between data and MC for the E/p of the negative track. The mean E/p in MC is .003 too high. We estimate the error from this effect by re-analyzing the MC with the energy of every cluster scaled by 1.003 (.997) and find that the value for g_1/f_1changes by .011(.007). We assign a systematic error of .009 from this effect.

9.5.8 TRD Inefficiency

We step through the cut on the distance of the negative track from the TRD dead region at DC 4, and find find that the changes in $g_1/f_1$are consistent with statistical variations. Furthermore, removing the TRD requirement altogether changes the value of $g_1/f_1$by .006.

9.5.9 $p^2_{\nu||}$ Cut

The requirement $p^2_{\nu||} > 0$ removed about 30 % of the data. Also, this quantity directly depends on the reconstructed $p^2_\perp$, thus any cut on this quantity deserves careful scrutiny. We vary the value of this cut from -.005 to .0005 (GeV^2/c^2), and find the change in the value of $g_1/f_1$is consistent with statistical variations (see figure 9.8.)

9.5.10 Measured CsI Non-orthogonality

In performing the global alignment of the drift chambers to the CsI, it was found that there is a 300 μrad residual apparent non-orthogonality in the calorimeter. Re-analyzing the MC with with cluster position at the calorimeter modified by $x \rightarrow x + (-)300 \times 10^{-6} y$ changed the measured value of $g_1/f_1$by 0.000(−.001). We determine the systematic error due to this effect to be negligible.

9.5.11 Radiative Corrections

Radiative corrections have been explicitly determined not to effect the final state polarization and electron-neutrino correlation in hyperon beta decays [2].

9.5.12 Beam Shape / Edges

There is still a significant mismatch in the shape of the beam in y for summer data. We estimate the size of this effect on $g_1/f_1$by reanalyzing the data, prescaling events having y/z of the Ξ^0 vertex $< -.0002$ (See figure 9.7.) The value for g_1/f_1changes by $-.015$.

9.5.13 Drift Chamber Inefficiency

In order to estimate the effect of lost tracks in the beam region, we have implemented the hi SOD mapping procedure described in [76].

The 'maps' are made from trigger 2 $K_L \rightarrow \pi^+ e^- \overline{\nu}_e$ decays. Then, in Monte Carlo, drift chamber hits are either then discarded or their simulated TDC times modified according the maps and a user specified weight. We generated signal MC for weights of 0.0 , 0.5 and 1.0 respectively. We find that a weight of 1.0 over-predicts the number of observed $\Xi^0 \rightarrow \Lambda\pi^0$ events missing hits in the beam region and the resolution in $p_\perp^2$observed for Ξ^0 with $\Lambda \rightarrow p\pi^-$decays.

The value for g_1/f_1obtained in the data for the three MC samples are consistent with the statistical variation.

9.5.14 Error on α_{Σ^+}

The PDG value of the asymmetry of the decay $\Sigma^+ \rightarrow p\,\pi^0$ is $-.980\pm^{.017}_{.015}$. Re-weighting the MC to give values of α_{Σ^+}equal to $-.963(-.995)$ changes the value of $g_1/f_1$by $-.018(.008)$. We assign an (external) systematic error of .013 due to the uncertainty in α_{Σ^+}.

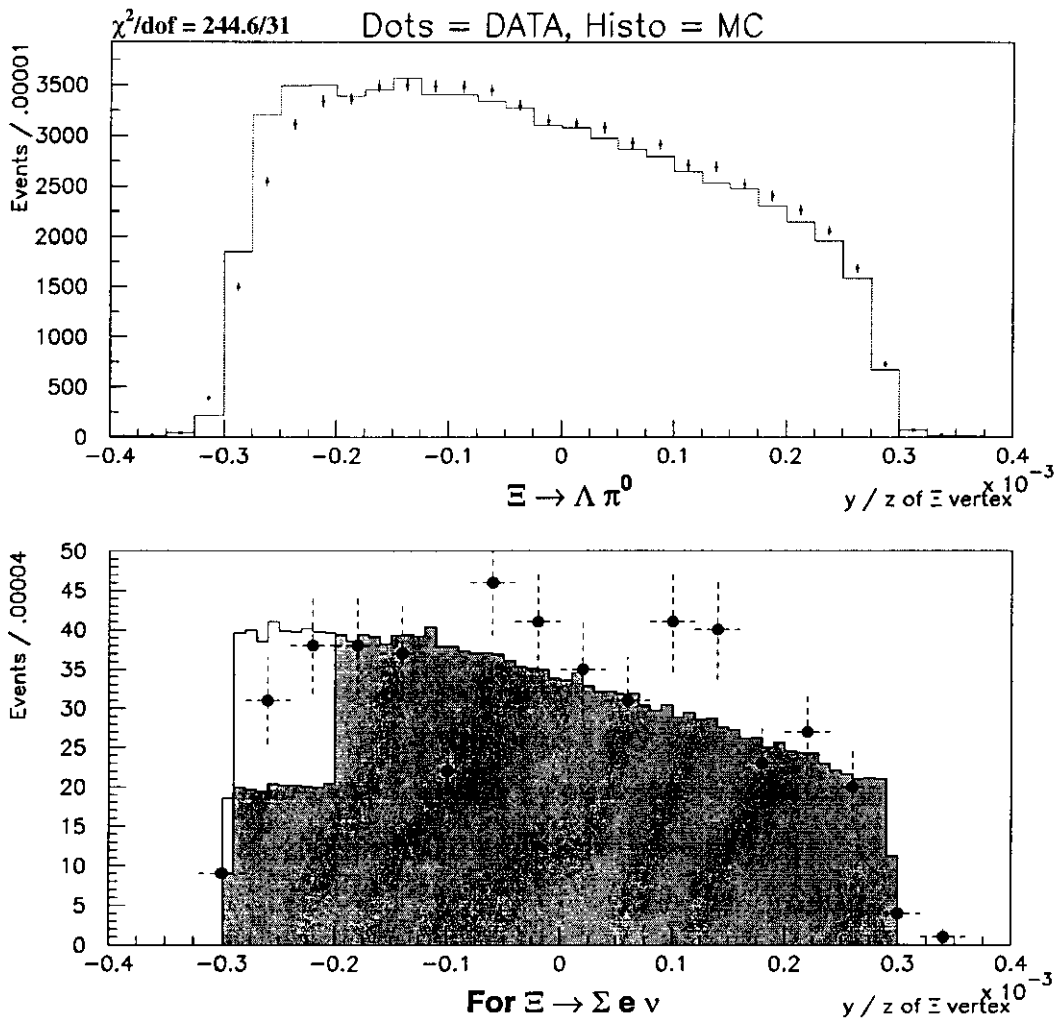

Figure 9.7: Beam shape. The top plot is a DATA-MC comparison of y_{Ξ^0}/z_{Ξ^0} for $\Xi^0 \to \Lambda\pi^0$ with $\Lambda \to p\pi^-$events. The bottom plot shows the distribution of y_{Ξ^0}/z_{Ξ^0} for signal MC events (histogram), signal MC with events having $y_{\Xi^0}/z_{\Xi^0} < -.0002$ by 2 (filled histogram), and data (dots).

9.5.15 q^2 Dependence of f_1 and g_1

The standard q^2($q^2 = (p_e + p_\nu)^2$) dependence of f_1 and g_1 is

$$\begin{aligned} f_1(q^2) &= f_1(0) \cdot (1 - \frac{q^2}{M_V^2})^{-2} \\ g_1(q^2) &= g_1(0) \cdot (1 - \frac{q^2}{M_A^2})^{-2} \end{aligned} \tag{9.26}$$

with

$$M_V = 0.970\, GeV/c^2, M_A = 1.250\, GeV/c^2 \tag{9.27}$$

Typical values for $\sqrt{q^2}$ are $0 - .09\, GeV/c^2$. The change in $g_1/f_1$with different q^2dependences is given in table 9.1.

M_V	M_A	$\Delta g_1/f_1$
$0.485\, GeV/c^2$	$0.625\, GeV/c^2$	-.029
$0.970\, GeV/c^2$	$1.250\, GeV/c^2$	0.000
$1.940\, GeV/c^2$	$2.500\, GeV/c^2$	+.002
∞	∞	+.007

Table 9.1: Variation of $g_1/f_1$with M_V and M_A

9.5.16 Misc. Checks for g_1/f_1

In table 9.3 we present the g_1/f_1fit results with some changes made in the selection criteria for DATA ONLY. Figure 9.9 shows the value for $g_1/f_1$with different selection criteria in data and Monte Carlo, we find these changes to be consistent with statistical variations.

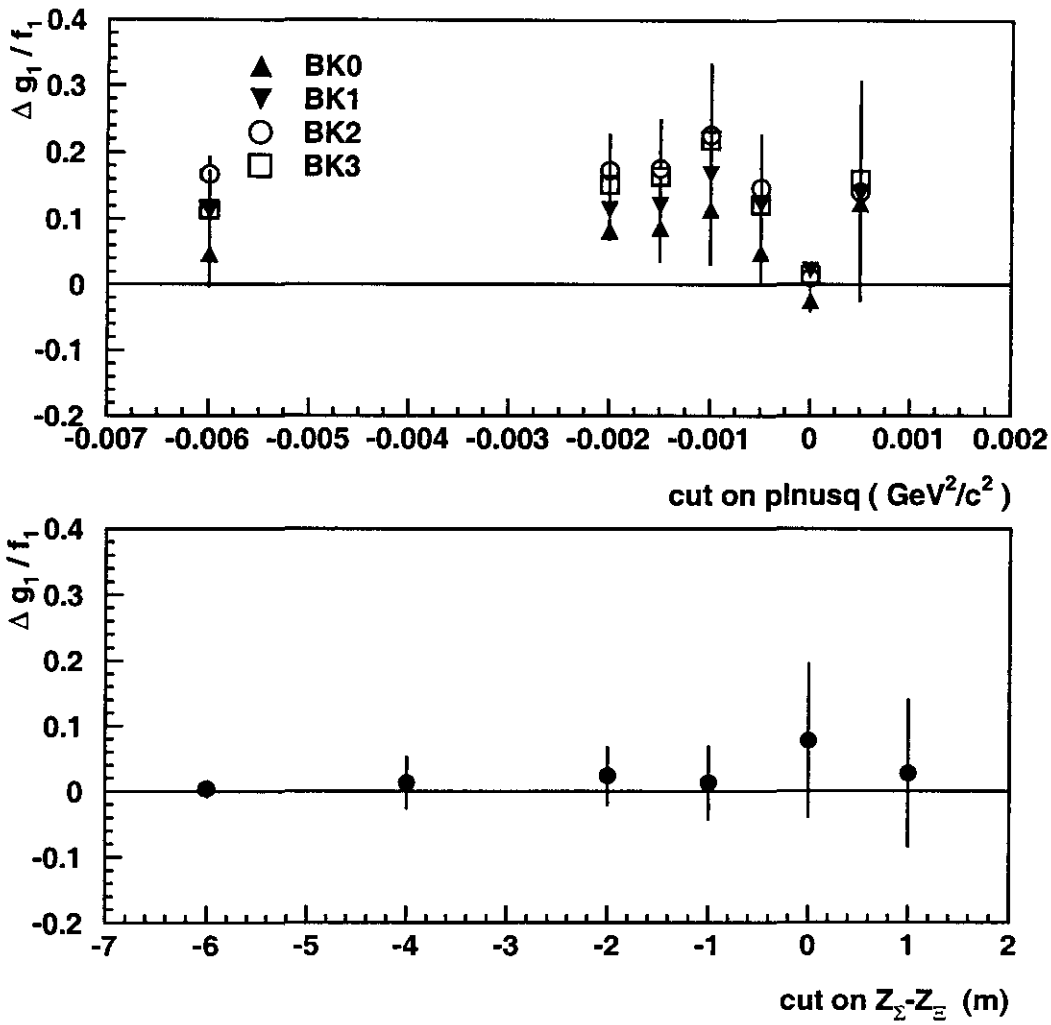

Figure 9.8: The measured value for g_1/f_1as a function of the $p^2_{\nu\|}$cut (top), and a function of the $z_{\Sigma^+} - z_{\Xi^0}$ cut (bottom).

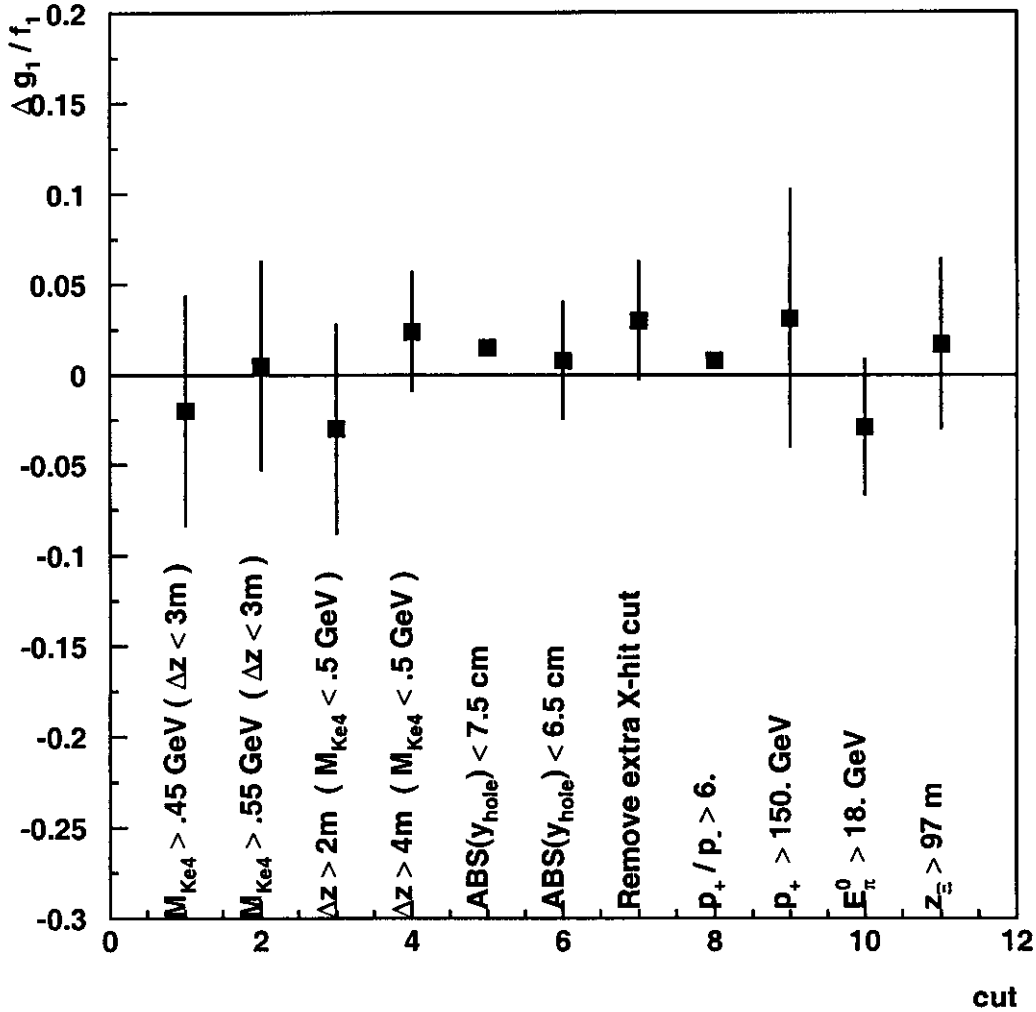

Figure 9.9: The measured value for $g_1/f_1$with different selection criteria.

Description	Error
Background	.039
Beam Shape	.015
MC Statistics	.020
DC Alignment	.020
$c\tau$of Ξ^0 (z slope)	.009
Energy Scale	.009
Delta z	NEG
DC Beam Hole Inefficiency	NEG
$p^2_{\nu\parallel}$cut	NEG
CsI Non-orthogonality	NEG
TRD	NEG
mass of Ξ^0	NEG
Error on $\alpha_{\Sigma+}$	.013
Total Systematic Error	.054 (.05)

Table 9.2: Systematic Error for g_1/f_1

9.6 Extraction of g_2/f_1

We follow the same procedure as in determining g_1/f_1, only we allow $g_2/f_1$to vary as well. The background correction is determined in a similar manner as g_1/f_1, only for simplicity we use the correction found from MC with $g_1/f_1 = 1.25, g_2/f_1 = 0.0$.

We follow the same procedure used to estimate the error on g_1/f_1. The largest contribution is due to the background (.33).

Our value for $g_2/f_1$is $-1.7 \pm^{2.1}_{2.0} (stat) \pm .5(syst)$. We thus find no evidence for a non-zero second-class current term in our data sample (figure 9.10).

9.7 Extraction of $f_2/f_1$from Beta Spectrum

While the electron spectrum depends on $g_1/f_1$and $f_2/f_1$to lowest order,the other integrated observables do not. We can operationally separate determination of $f_2/f_1$from $g_1/f_1$and $g_2/f_1$by determining $g_1/f_1$and $g_2/f_1$from the distribution of $x^{[\Sigma]}_{pe}$, $x^{[Q]}_{e\nu\perp}$, and $x^{[Q]}_{p\nu\perp}$, and determining $f_2/f_1$from the distribution of $E^{[\Sigma]}_e$.

To determine the distribution of $E^{[\Sigma]}_e$, there is no need to remove events with

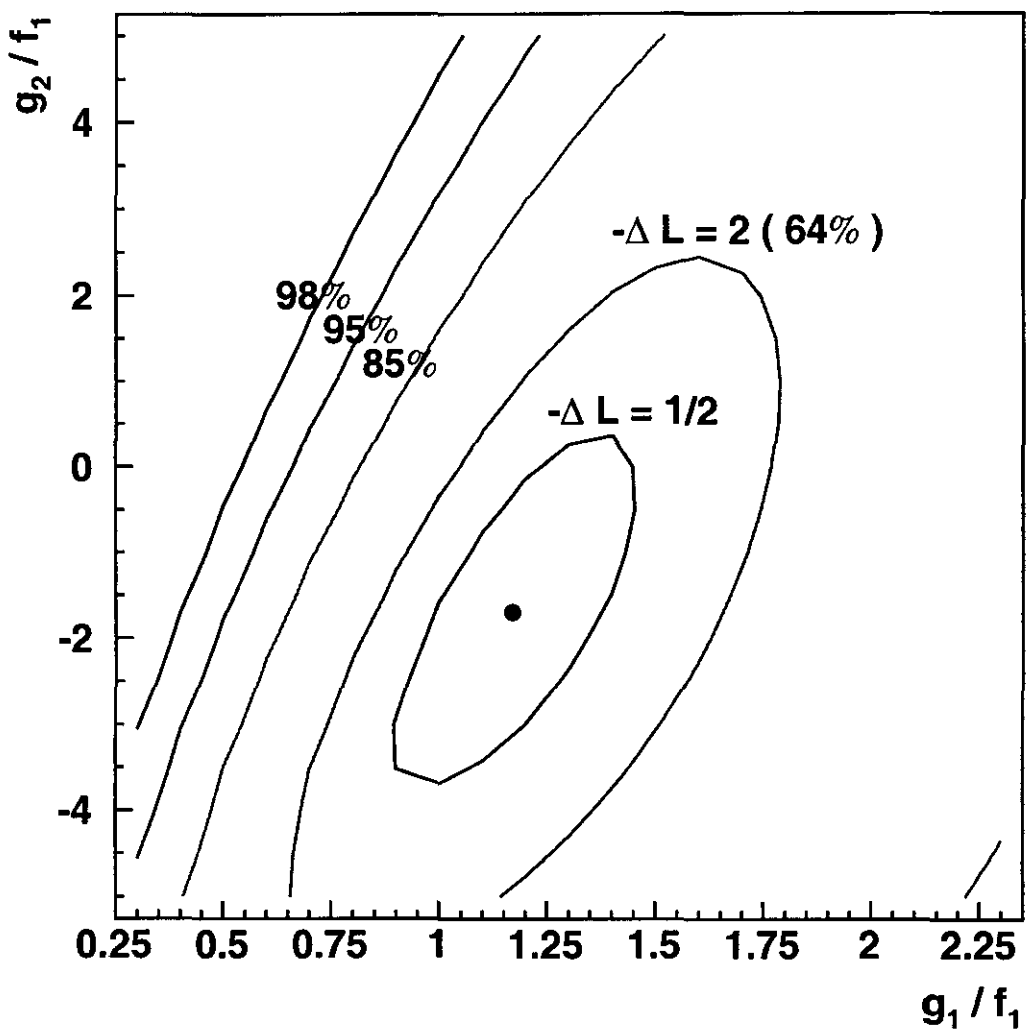

Figure 9.10: Confidence interval plot for g_1/f_1-g_2/f_1.

Description	ΔN	$\Delta\ g_1/f_1$
Standard	0	0.000
Using 'Old' x(t) maps	+11	0.00*
Remove ppion < .1 (TRD)	+9	+0.006
Require $z_\Sigma - z_\Xi > -3\,m$ (from $-6\,m$)	-5	+0.009
Require $z_\Xi > 97\,m$ (from $95\,m$)	-27	-0.006
Changing m_Σ window from $\pm 12\,MeV$ to $\pm 15\,MeV$	-16	-0.011
Require shape $\chi^2 < 10$ for extra clusters	-23	+0.018
Narrow E/p_{e^-} cut window to $\pm .05$ (from $\pm .10$)	-11	-0.030
Requiring E-M energy deposited to be $28\,GeV$ (from $18\,GeV$)	-14	0.000

Table 9.3: Changes in Data Selection criteria. The fit using the 'Old' x(t) maps only obtains g_1/f_1in increments of .02.

$p^2_{\nu\|} < 0$. We are only using a one dimensional distribution, and we will determine f_2/f_1using a one dimensional maximum likelihood fit 9.11. Using the nominal background subtraction, we measure $f_2/f_1$to be $2.0 \pm 1.2(stat) \pm 0.5(syst)$. Figure 9.14 shows the value for $g_1/f_1$with different selection criteria in data and Monte Carlo, we find these changes to be larger than statistical variations, but still within the estimated systematic error.

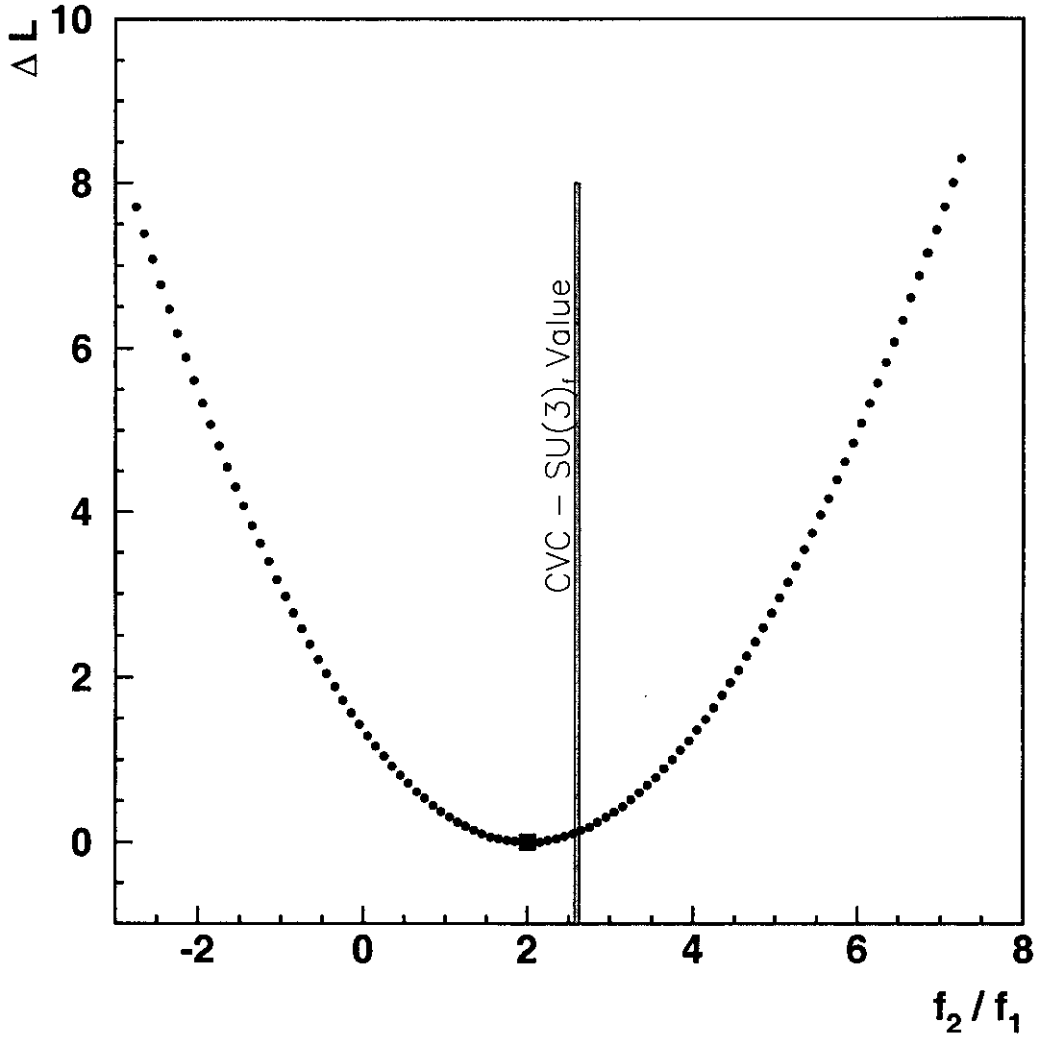

Figure 9.11: Extraction of f_2/f_1using maximum likelihood of energy spectrum of electron in Σ^+frame ($E_e^{[\Sigma]}$).

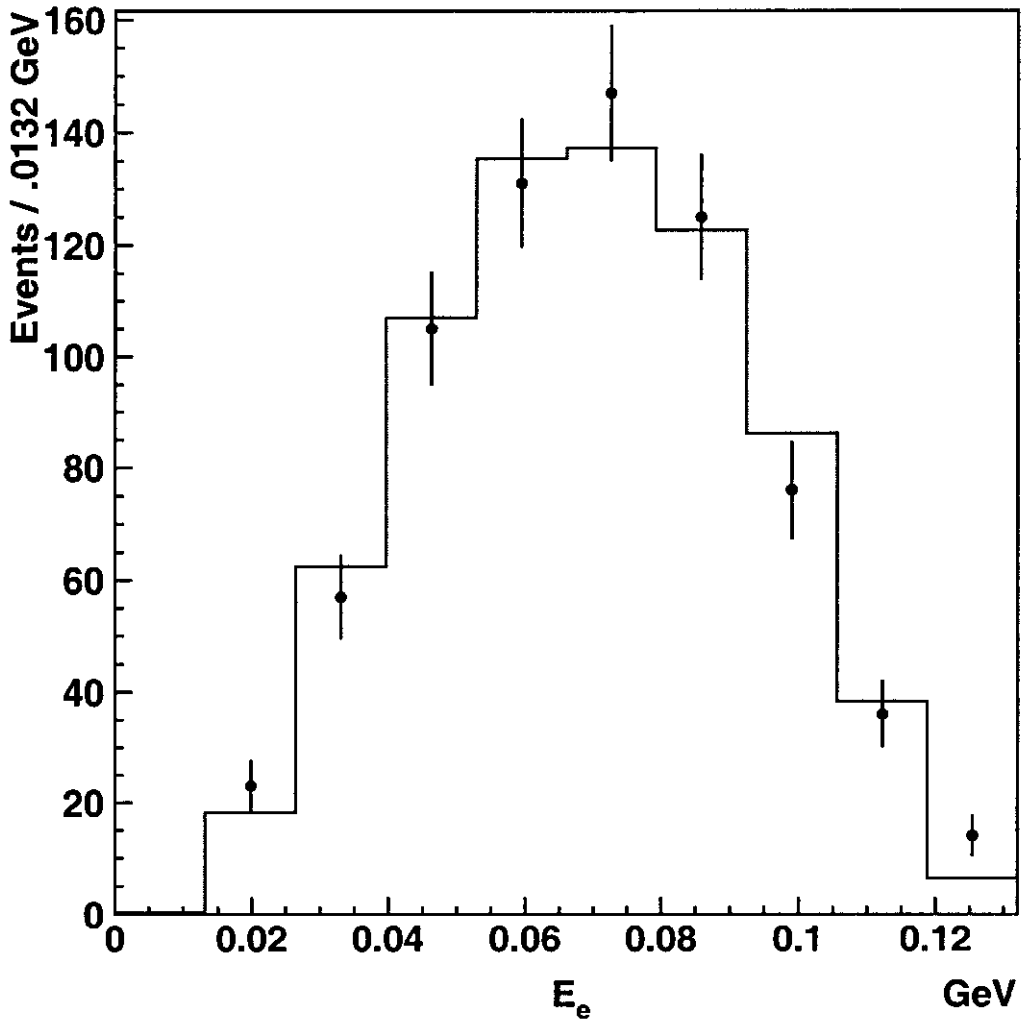

Figure 9.12: Energy spectrum of electron in Σ^+frame ($E_e^{[\Sigma]}$).

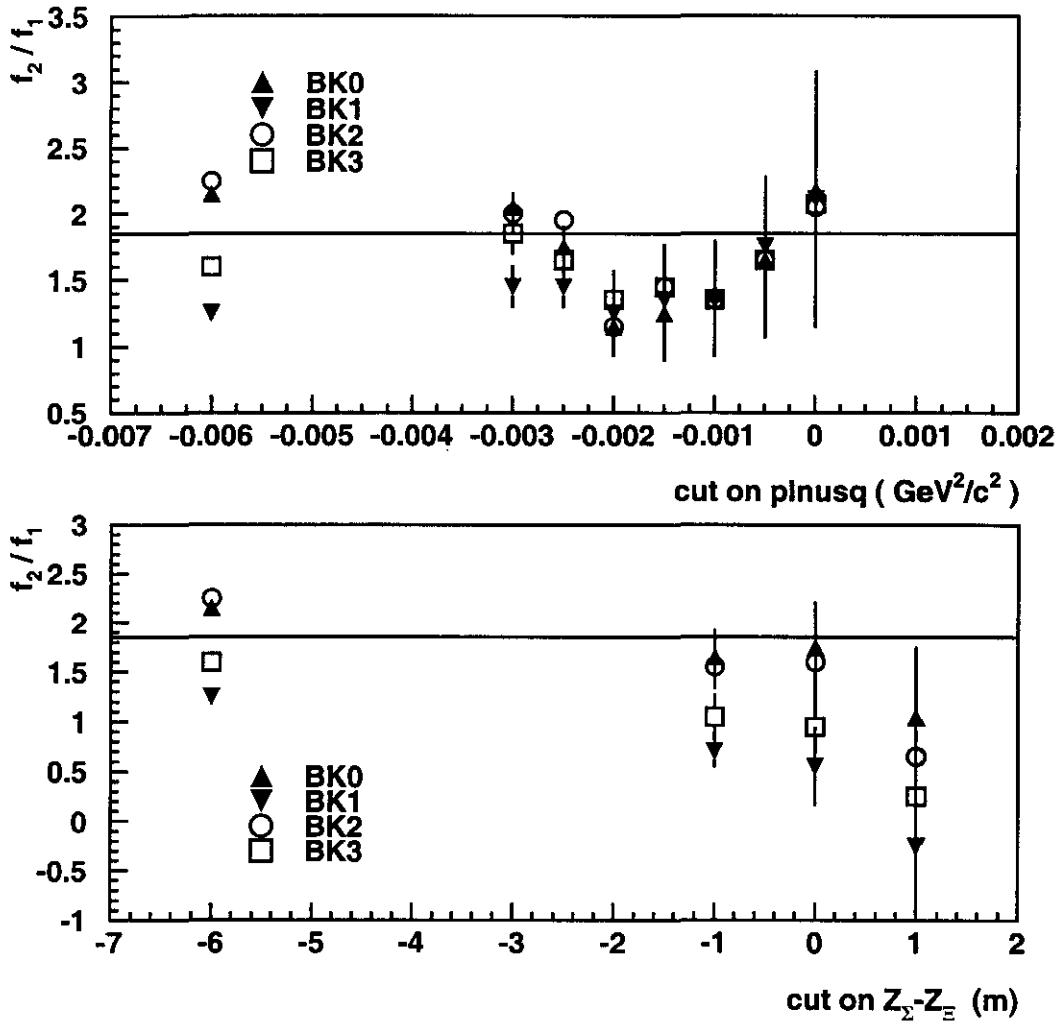

Figure 9.13: The measured value for f_2/f_1as a function of the $p^2_{\nu\|}$cut (top), and a function of the $z_{\Sigma^+} - z_{\Xi^0}$ cut (bottom).

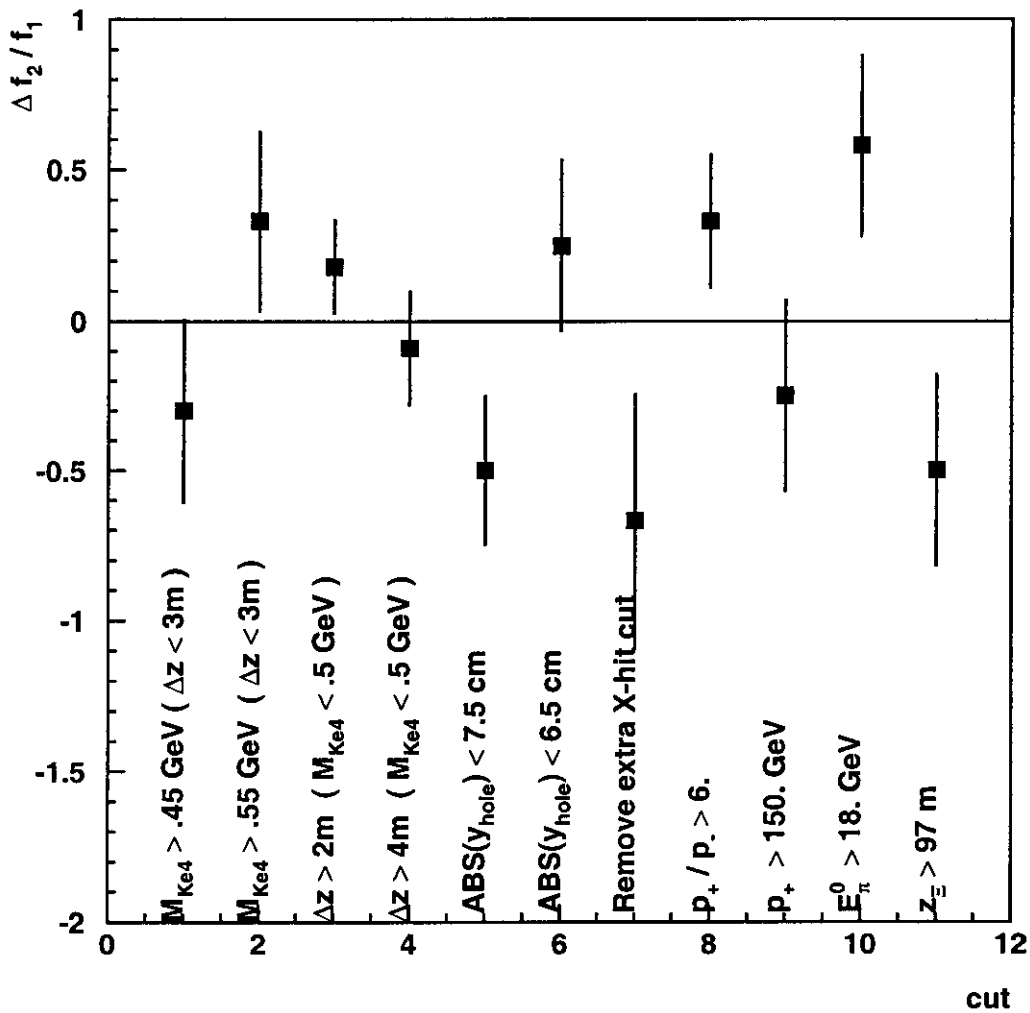

Figure 9.14: The measured value for f_2/f_1as a function of different selection criteria.

Description	Error
Background	.33
Beam Shape	.13
MC Statistics	.18
DC Alignment	.22
$c\tau$of Ξ^0 (z slope)	.10
Energy Scale	.07
Delta z	NEG
DC Beam Hole Inefficiency	NEG
$p^2_{\nu\parallel}$cut	NEG
CsI Non-orthogonality	.20
TRD	NEG
Error on α_{Σ^+}	.12
mass of Ξ^0	NEG
Total Systematic Error	.52 (.5)

Table 9.4: Systematic Error for g_2/f_1

Description	Error
Background	.30
Beam Shape	.02
MC Statistics	.06
DC Alignment	NEG
Energy Scale	.08
DC Beam Hole Inefficiency	.15
CsI Non-orthogonality	NEG
Radiative Corrections	.08
Statistical Error in g_1/f_1	.30
mass of Ξ^0	.25
$c\tau$of Ξ^0 (z slope)	.06
Total Systematic Error	.53 (.5)

Table 9.5: Systematic Error for f_2/f_1

Chapter 10
CONCLUSIONS

10.1 Results for g_1/f_1

Our result of $g_1/f_1 = 1.32 \pm^{.21}_{.17} (stat) \pm .05(syst)$assumes that:

- The f_2/f_1term is equal to its CVC value (2.6)
- There is NO second class current term ($g_2/f_1 = 0$)

In this case, our result for $g_1/f_1$is quite clearly consistent with exact $SU(3)_f$ symmetry, and the $SU(3)_f$ breaking predictions put forth by Ratcliffe [23]. Our result does not significantly favor the exact $SU(3)_f$ solution over those of Ratcliffe [23]. Table 10.1 rehashes the theoretical predictions, this time with the change in maximum likelihood included. The number of 'standard errors' this represents is obtained by $\Delta/\sigma = \sqrt{2\Delta\mathcal{L}}$. Neglecting any systematic error then, the predictions of Flores-Mendieta *et al.* which allow for the renormalization of f_1 are disfavored at the 2.3 σ to 2.8 σ level. The $SU(3)_f$ braking fit in Flores-Mendieta *et al.* which *does not* allow for the renormalization of f_1 is only marginally disfavored (at the 1.8σ level).

Theory	f_1	g_1	g_1/f_1	$\Delta\mathcal{L}$
Exact $SU(3)_f$ and CVC	1.00	1.27	1.27	0.0
Flores-Mendieta (A) [24]	1.00	1.03 ± .02	1.03 ± .02	1.6
Flores-Mendieta (B) [24]	1.12 ± .05	1.02 ± .02	.91 ± .04	3.9
Flores-Mendieta (C) [24]	1.12 ± .05	1.02 ± .03	.91 ± .05	3.9
Flores-Mendieta (D) [24]	1.12 ± .05	1.07 ± .03	.96 ± .05	2.7
Ratcliffe (A) [23]	1.00	1.17 ± .03	1.17 ± .03	0.3
Ratcliffe (B) [23]	1.00	1.14 ± .03	1.14 ± .03	0.5

Table 10.1: Predictions for g_1/f_1

A non-zero g_2/f_1would change our value for g_1/f_1as shown in figure 9.10. A value of f_2/f_1different from 2.6 would change our value for g_1/f_1as well.

We find that a unit change in f_2/f_1changes $g_1/f_1$by .05, that is

$$g_1/f_1 = (f_2/f_1 - 2.6) \times .05 + 1.32 \tag{10.1}$$

10.2 Results for g_2/f_1

Our value for g_2/f_1($-1.7 \pm^{2.1}_{2.0} (stat) \pm .5(syst)$) is consistent with zero. Since predictions for $g_2/f_1$are of the order 0.1, we are not sensitive to any realistic standard model non-zero second class current.

10.3 Results for f_2/f_1

Our result of $2.0 \pm 1.2(stat) \pm 0.5(syst)$is consistent with the CVC value, and does not distinguish between the predictions in the range of the ' normalization ambiguity ', nor do we definitively establish a non-zero f_2/f_1term for this decay.

10.4 Extraction of f_1 and g_1 Separately

In order to extract f_1 and g_1 we need to have the total rate for the decay. As mentioned previously, the total rate is equal to

$$\begin{aligned} R &= \frac{G_F^2 \mid V_{us} \mid^2 (M_{\Xi^0} - M_{\Sigma^+})^5}{60\pi^3} \\ &\times \ [(1 - \frac{3}{2}\delta) f_1^2 + (3 - \frac{9}{2}\delta) g_1^2 - (4\delta) g_1 g_2 + \mathcal{O}(\delta^2)] \end{aligned} \tag{10.2}$$

To experimentally get the rate, we measure the branching ratio, the fraction of the time a Ξ^0 decays via the $\Xi^0 \rightarrow \Sigma^+ e^- \overline{\nu}_e$ mode divided by the total number of Ξ^0 decays. The rate is the branching ratio divided by the Ξ^0 lifetime.

In order to get a quantity that depends on the form factors, we need to know: 1) The Branching Ratio 2) The Ξ^0 lifetime 3) the *difference* between the Ξ^0 mass and the Σ^+mass.

The branching ratio has been previously measured at KTeV [6] to be:

$$BR(\Xi^0 \rightarrow \Sigma^+ e^- \overline{\nu}_e) = (2.71 \pm 0.22_{stat} \pm 0.31_{syst}) \times 10^{-4} \tag{10.3}$$

The fractional error on $M_{\Xi^0} - M_{\Sigma^+}$ is 0.5%, but since this quantity enters in

at the 5th power, this translates to a 2.5% error on the form factors. There is also a 3 % error from the Ξ^0 lifetime uncertainty. The total relative error on the published $\Xi^0 \to \Sigma^+ e^- \overline{\nu}_e$ branching ratio is 14%. To fit for f_1 and g_1, we include an additional error on the branching ratio of 0.11×10^{-4} to account for the error due to the uncertainty in the Ξ^0 mass and lifetime.

The fitted values are

$$\begin{aligned} f_1 &= 0.99 \pm .14 \\ g_1 &= 1.30 \pm .10 \end{aligned} \tag{10.4}$$

An analysis of the $\Xi^0 \to \Sigma^+ e^- \overline{\nu}_e$ branching ratio using the summer data set is in progress [77].

10.5 Future Prospects

The KTeV experiment successfully took data during the 1999-2000 Fermilab fixed target run. We obtained about 4× the summer 1997 $\Xi^0 \to \Sigma^+ e^- \overline{\nu}_e$ statistics. With these additional data, it should be possible to measure g_1/f_1 to ± 0.1.

As far as extracting f_1 and g_1 separately, the statistical error from the *1997* data on the branching ratio is already as small as the external systematic error from the Ξ^0 mass and lifetime. additionally, the current *preliminary* value for the branching ratio of $\Xi^0 \to \Sigma^+ e^- \overline{\nu}_e$ is systematically limited [77]. Further improvement to that measurement cannot happen without a better measurement of either quantity. An improved Ξ^0 mass measurement should be possible with the existing data. An improved Ξ^0 lifetime measurement should also be possible with the 1.4 Million (!) $\Xi^0 \to \Lambda\pi^0$ decays collected in trigger 11 during the KTeV99 run.

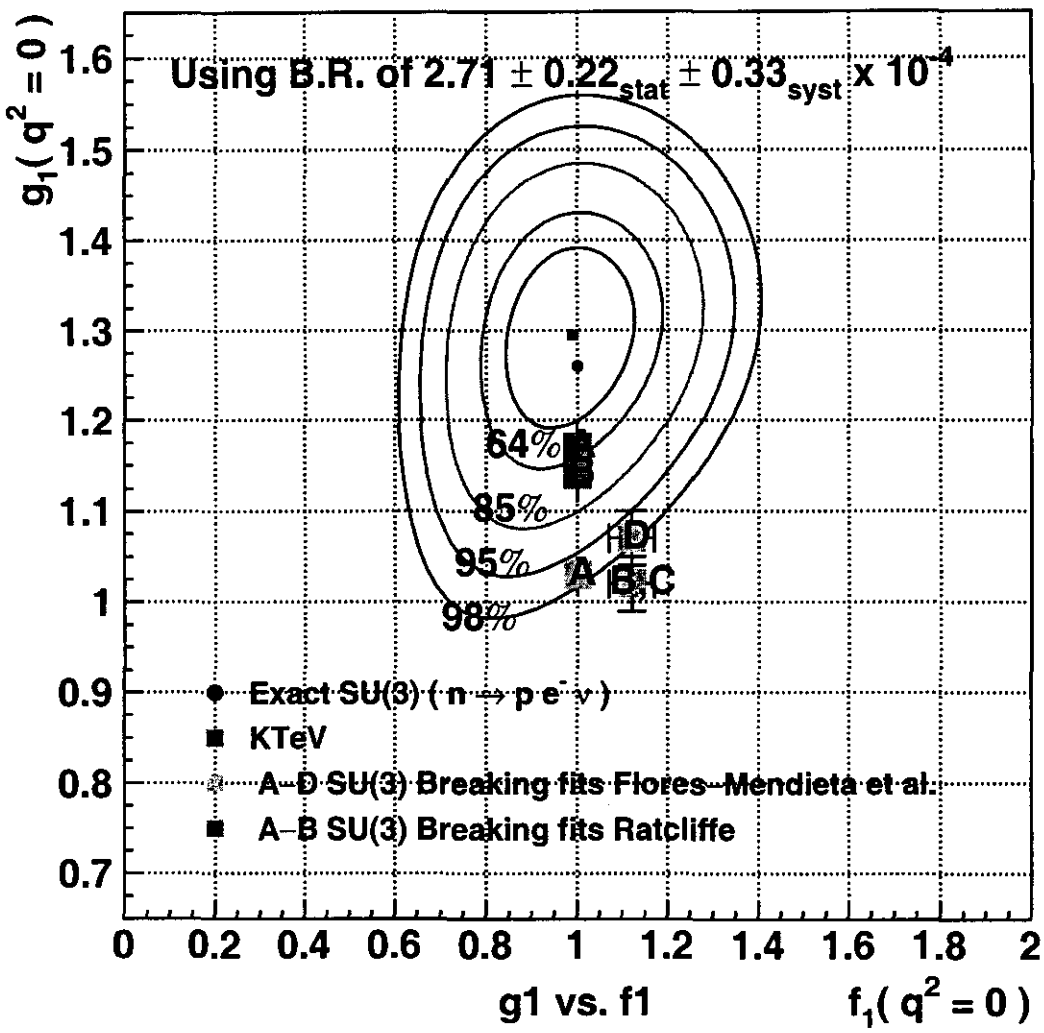

Figure 10.1: Confidence interval plot for f_1 and g_1.

Appendix A
DERIVATION OF ASYMMETRIES

The exact formulae for the decay distributions for hyperon semileptonic decay have been calculated, but the resulting expressions are quite opaque, and, as a result, the physical content is hidden.

Using a method introduced by Primakoff for muon capture [81, 82], we keep only terms through second order in the recoil velocity of the initial baryon (in the rest frame of the final baryon).

Starting from the transition matrix in equation (A.1), we introduce the effective Hamiltonian by

$$\mathcal{M} = \langle be \mid \mathcal{H}_{\text{eff}} \mid B\nu \rangle \sqrt{2e\, 2\nu\, 2M_b\, (E_B + M_B)} \tag{A.1}$$

with

$$\begin{aligned} \frac{\sqrt{2}}{2}\mathcal{H}_{\text{eff}} &= G_S \frac{1}{2}(1 - \sigma_\ell \cdot \hat{e})\, [G_V + G_A \sigma_\ell \cdot \sigma_b \\ &\quad + G_P^e \sigma_b \cdot \hat{e} + G_P^\nu \sigma_b \cdot \hat{\nu}]\, \frac{1}{2}(1 - \sigma_\ell \cdot \hat{\nu}). \end{aligned} \tag{A.2}$$

Here $\hat{e}$ and $\hat{\nu}$ are unit vectors along the electron and antineutrino directions, while e, ν, and E_B are the energies of the electron, antineutrino, and initial baryon (all quantities are in the rest frame of b). The spin operators σ_ℓ and σ_b act respectively on the lepton and baryon states (represented by two-component spinors).

The effective coupling coefficients G_V, G_A, G_P^e, and G_P^ν are functions of the form factors in equation (A.2):

$$\begin{aligned} G_V &= f_1 + \delta f_2 - \frac{\nu + e}{2M_B}(f_1 + \Delta f_2), \\ G_A &= -g_1 + \delta g_2 + \frac{\nu - e}{2M_B}(f_1 + \Delta f_2), \\ G_P^e &= \frac{e}{2M_B}(-(f_1 + \Delta f_2) - g_1 + \Delta g_2), \end{aligned}$$

$$G_P^\nu = \frac{\nu}{2M_B}(f_1 + \Delta f_2 - g_1 + \Delta g_2), \tag{A.3}$$

where $\delta = (M_B - M_b)/M_B$ and $\Delta = (M_B + M_b)/M_B = 2 - \delta$. Since the form factors f_3 and g_3 always appear with a multiplier of the electron mass divided by M_B, they are neglected throughout. Note also that f_2 and g_2 always appear multiplied by a quantity of order δ, so their q^2 dependence is not relevant to our order δ^2 approximation. However, the q^2 dependence of f_1 and g_1 does need to be included [2] in calculations to maintain a completely consistent order of approximation.

Electron and antineutrino spins are not usually observed, and this analysis focuses on measurement of the final baryon polarization. We therefore sum over the electron and antineutrino spins and average over initial baryon spin:

$$\sum_{\nu \text{ spins}, B \text{ spins}} |\langle be|\, \mathcal{H}_{\text{eff}} \,|\, B\nu\rangle|^2 = \langle be|\, \mathcal{H}_{\text{eff}}\mathcal{H}_{\text{eff}}^\dagger \,|\, be\rangle \tag{A.4}$$

and

$$\sum_{e \text{ spins}} \langle be|\, \mathcal{H}_{\text{eff}}\mathcal{H}_{\text{eff}}^\dagger \,|\, be\rangle = Tr((1 + \sigma_{\mathbf{b}} \cdot \mathbf{P}_b)\mathcal{H}_{\text{eff}}\mathcal{H}_{\text{eff}}^\dagger). \tag{A.5}$$

By projecting out the spin of the final baryon and taking the trace, we obtain

$$\begin{aligned}
|\mathcal{M}|^2 &= \xi[1 + a\hat{e}\cdot\hat{\nu} + A\mathbf{P}_b\cdot\hat{e} + B\mathbf{P}_b\cdot\hat{\nu} \\
&\quad + A'(\mathbf{P}_b\cdot\hat{e})(\hat{e}\cdot\hat{\nu}) + B'(\mathbf{P}_b\cdot\hat{\nu})(\hat{e}\cdot\hat{\nu}) \\
&\quad + D\mathbf{P}_b\cdot(\hat{e}\times\hat{\nu})] \\
&\quad \cdot(2e)(2\nu)(2M_b)(E_B + M_B)G_S^2, \\
\xi &= |G_V|^2 + 3|G_A|^2 - 2Re(G_A^*(G_P^e + G_P^\nu)) \\
&\quad + |G_P^e|^2 + |G_P^\nu|^2, \\
\xi a &= |G_V|^2 - |G_A|^2 - 2Re(G_A^*(G_P^e + G_P^\nu)) \\
&\quad + |G_P^e|^2 + |G_P^\nu|^2 + 2Re(G_P^{e*}G_P^\nu)(1 + \hat{e}\cdot\hat{\nu}), \\
\xi A &= -2Re(G_V^*G_A) + 2|G_A|^2 \\
&\quad + 2Re(G_V^*G_P^e - G_A^*G_P^\nu),
\end{aligned}$$

$$
\begin{aligned}
\xi B &= -2Re(G_V^* G_A) - 2\,|G_A|^2 \\
&\quad +2Re(G_V^* G_P^\nu + G_A^* G_P^e), \\
\xi A' &= 2Re(G_P^{e*}(G_V - G_A)), \\
\xi B' &= 2Re(G_P^{\nu*}(G_V + G_A)), \\
\xi D &= 2Im(G_V^* G_A) + 2Im(G_P^{e*} G_P^\nu)(1 + \hat{e}\cdot\hat{\nu}) \\
&\quad +2Im(G_A^*(G_P^e - G_P^\nu)).
\end{aligned} \tag{A.6}
$$

The polarization of the final baryon may be expressed explicitly as

$$
\mathbf{P}_b = \frac{(A + A'\hat{e}\cdot\hat{\nu})\hat{e} + (B + B'\hat{e}\cdot\hat{\nu})\hat{\nu} + D\hat{e}\times\hat{\nu}}{1 + a\hat{e}\cdot\hat{\nu}}. \tag{A.7}
$$

The components of this polarization can readily be measured when the outgoing baryon b is a hyperon which undergoes a subsequent weak decay $b \to b'\pi$ with a non-zero decay asymmetry parameter $\alpha_{b'}$. The distribution of the b' direction relative to any axis defined by a unit vector $\hat{i}$ is given by

$$
\frac{1}{\Gamma}\frac{d\Gamma}{d\Omega_{b'}} = \frac{1}{4\pi}(1 + \mathsf{S}_i \alpha_{b'}\hat{i}\cdot\hat{b}'), \tag{A.8}
$$

where $\mathsf{S}_i = \langle \mathbf{P}_b \cdot \hat{i}\rangle$ is the average polarization of b in the $\hat{i}$ direction. Conceptually, it is advantageous to employ the orthonormal basis

$$
\begin{aligned}
\hat{\alpha} &= \frac{\hat{e} + \hat{\nu}}{\sqrt{2(1 + \hat{e}\cdot\hat{\nu})}}, \\
\hat{\beta} &= \frac{\hat{e} - \hat{\nu}}{\sqrt{2(1 - \hat{e}\cdot\hat{\nu})}}, \\
\hat{\gamma} &= \hat{\alpha}\times\hat{\beta}.
\end{aligned} \tag{A.9}
$$

Experimentally, it may be more advantageous to determine the polarization components along one or more of the outgoing particle directions $(\hat{e}, \hat{\nu}, \hat{b})$.

To gauge the importance of the recoil contributions, in Fig A.1 we compare values of several integrated observables calculated from our expressions with the

corresponding zero-recoil values for the decay $\Xi^0 \to \Sigma^+ e^- \overline{\nu}$. For these calculations, we assumed $V_{us} = 0.2205$, $f_1(0) = 1.0$, $f_2 = 2.6$, and $g_2 = 0.0$. Comparing values of integrated observables obtained from our expressions with exact values from tables in Ref.[2], we find that the decay rates agree to better than 1 %, and that polarizations and asymmetries agree to better than 0.004. We have not included electromagnetic corrections, which are discussed in Ref.[2].

Finally, the analytic expressions for the integrated observables to order δ in the final state rest frame, assuming real form factors are

$$\begin{aligned}
R &= R_0[(1-\frac{3}{2}\delta)f_1^2 + (3-\frac{9}{2}\delta)g_1^2 - (4\delta)g_1g_2], \\
R\mathsf{S}_e &= R_0[(2-\frac{10}{3}\delta)g_1^2 + (2-\frac{7}{3}\delta)f_1g_1 - (\frac{1}{3}\delta)f_1^2 \\
&\quad -(\frac{2}{3}\delta)f_1f_2 + (\frac{2}{3}\delta)f_2g_1 - (\frac{2}{3}\delta)f_1g_2 - (\frac{10}{3}\delta)g_1g_2], \\
R\mathsf{S}_\nu &= R_0[(-2+\frac{10}{3}\delta)g_1^2 + (2-\frac{7}{3}\delta)f_1g_1 + (\frac{1}{3}\delta)f_1^2 \\
&\quad +(\frac{2}{3}\delta)f_1f_2 + (\frac{2}{3}\delta)f_2g_1 - (\frac{2}{3}\delta)f_1g_2 + (\frac{10}{3}\delta)g_1g_2], \\
R\mathsf{S}_\alpha &= R_0[(\frac{8}{3}-\frac{52}{15}\delta)f_1g_1 + (\frac{16}{15}\delta)f_2g_1 - (\frac{16}{15}\delta)f_1g_2], \\
R\mathsf{S}_\beta &= R_0[(\frac{8}{3}-4\delta)g_1^2 - (\frac{8}{15}\delta)f_1^2 - (\frac{16}{15}\delta)f_1f_2 \\
&\quad -(\frac{64}{15}\delta)g_1g_2],
\end{aligned} \tag{A.10}$$

where

$$R_0 = \frac{G_S^2(\delta M_B)^5}{60\pi^3}.$$

As can be seen in Ref. [78], the zero-recoil ($\delta = 0$) expression for $\mathsf{S}_e(\mathsf{S}_\nu)$ is the same as the that for the neutrino (electron) asymmetry for a polarized initial baryon [2]. Also, $R\mathsf{S}_\alpha$ depends only on $V \times A$ cross terms, and $R\mathsf{S}_\beta$ depends only on $V \times V$ and $A \times A$ terms, as required by a theorem due to Weinberg [85].

The correct order δ^2 expressions are obtained by adding

$$
\begin{aligned}
R(\delta^2) &= R_0\delta^2(\frac{6}{7}f_1^2 + \frac{12}{7}g_1^2 + 6g_1g_2 \\
&\quad +\frac{6}{7}f_1f_2 + \frac{4}{7}f_2^2 + \frac{12}{7}g_2^2), \\
RS_e(\delta^2) &= R_0\delta^2(\frac{55}{42}g_1^2 + \frac{17}{21}f_1g_1 + \frac{19}{42}f_1^2 + \frac{4}{3}f_1f_2 - \frac{10}{21}f_2g_1 \\
&\quad +\frac{10}{21}f_1g_2 + \frac{116}{21}g_1g_2 + \frac{4}{21}f_2^2 + \frac{4}{3}g_2^2 - \frac{16}{21}f_2g_2), \\
RS_\nu(\delta^2) &= R_0\delta^2(-\frac{55}{42}g_1^2 + \frac{17}{21}f_1g_1 - \frac{19}{42}f_1^2 - \frac{4}{3}f_1f_2 - \frac{10}{21}f_2g_1 \\
&\quad +\frac{10}{21}f_1g_2 - \frac{116}{21}g_1g_2 - \frac{4}{21}f_2^2 - \frac{4}{3}g_2^2 - \frac{16}{21}f_2g_2), \\
RS_\alpha(\delta^2) &= R_0\delta^2(\frac{316}{245}f_1g_1 - \frac{752}{735}f_2g_1 + \frac{752}{735}f_1g_2 - \frac{128}{105}f_2g_2), \\
RS_\beta(\delta^2) &= R_0\delta^2(\frac{422}{735}f_1^2 + \frac{88}{49}f_1f_2 + \frac{8}{35}f_2^2 \\
&\quad +\frac{362}{245}g_1^2 + \frac{1576}{245}g_1g_2 + \frac{8}{5}g_2^2)
\end{aligned}
$$

to $R, RS_e, RS_\nu, RS_\alpha$ and RS_β, respectively in equation (A.10).

Finally, note that the total rate is the same *to order* δ in either the final or initial baryon rest frame [2].

Operationally, it is more convenient to calculate the Dalitz plot variables for the Ξ^0 decay in the Ξ^0 frame. We use the result of reference [83]. For an unpolarized Ξ^0 , the differential decay rate for $\Xi^0 \to \Sigma^+ e^- \overline{\nu}_e$ in the Ξ^0 frame is:

$$
\frac{d\Gamma}{de\, d\Omega_e\, d\Omega_\nu} = \xi(1 + a\hat{e}\cdot\hat{\nu})(\frac{M_\Sigma + E_\Sigma}{2M_\Xi})(\frac{e^2\nu^3}{e^{max} - e}) \tag{A.11}
$$

Where

$$
\begin{aligned}
\xi &= |G_V|^2 + 3\,|G_A|^2 + |G_P^e|^2 + |G_P^\nu|^2 \\
&\quad -2Re(G_A^*(G_P^e + G_P^\nu)), \\
\xi a &= |G_V|^2 - |G_A|^2 + |G_P^e|^2 + |G_P^\nu|^2 \\
&\quad -2Re(G_A^*(G_P^e + G_P^\nu)) + 2Re(G_P^{e*}G_P^\nu)(1 + \hat{e}\cdot\hat{\nu}),
\end{aligned}
$$

(A.12)

and

$$
\begin{aligned}
G_V &= f_1 - \delta f_2 + \frac{\nu + e}{2M_\Sigma}(f_1 + \Delta f_2), \\
G_A &= -g_1 + \delta g_2 + \frac{\nu - e}{2M_\Sigma}(f_1 + \Delta f_2), \\
G_P^e &= \frac{e}{2M_\Sigma}(-(f_1 + \Delta f_2) + g_1 + \Delta g_2), \\
G_P^\nu &= \frac{\nu}{2M_\Sigma}(f_1 + \Delta f_2 + g_1 + \Delta g_2).
\end{aligned}
\tag{A.13}
$$

Then , the polarization of the $\Sigma^+$is calculated according to equation (A.7).

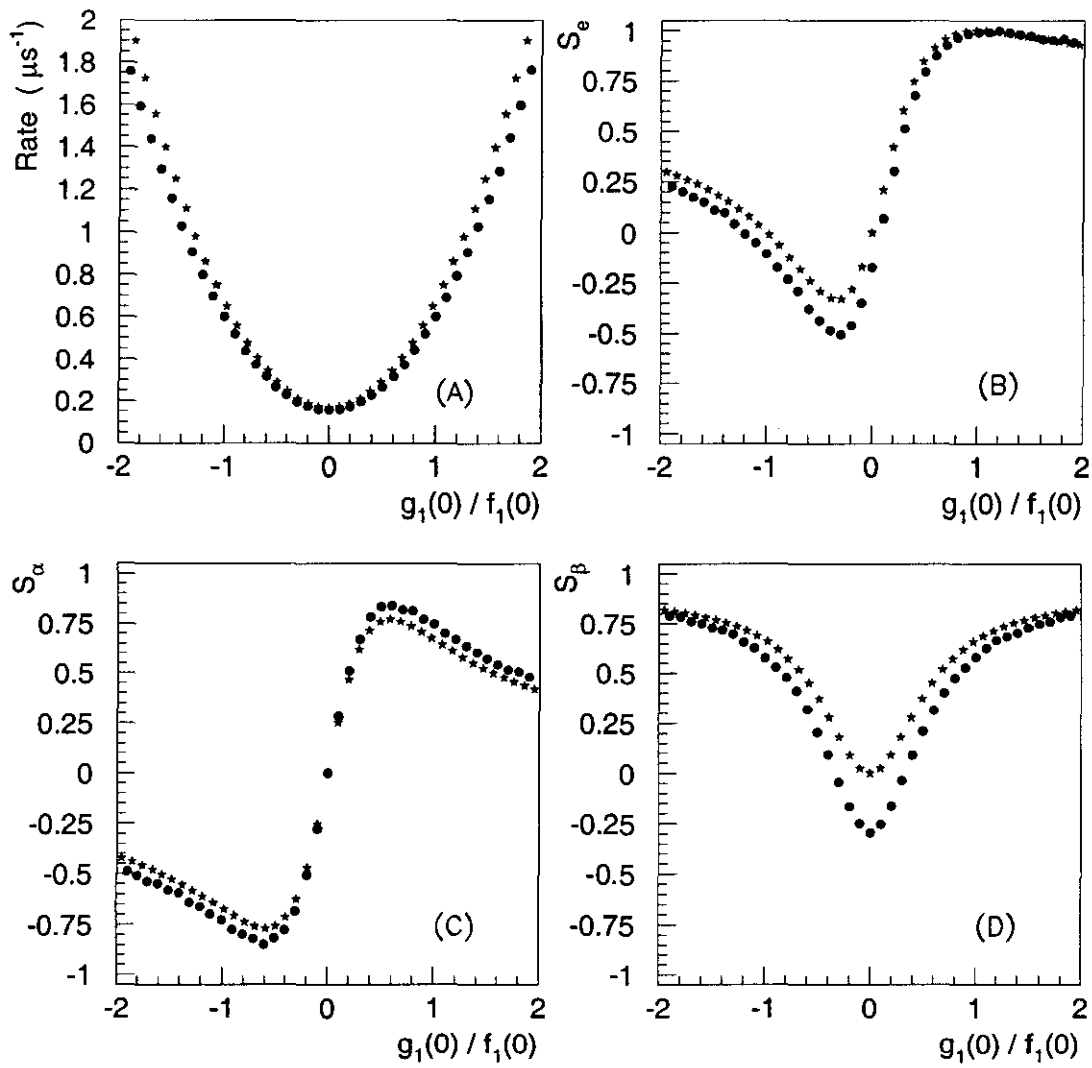

Figure A.1: Integrated observable quantities for the decay $\Xi^0 \to \Sigma^+ e^- \overline{\nu}_e$ as a function of g_1/f_1 : A) The total decay rate (μs^{-1}); B) The polarization of the Σ^+in the e^- direction ($S_e = \langle \mathbf{P}_b \cdot \hat{e} \rangle$); C) The polarization of the Σ^+in the α direction ($S_\alpha = \langle \mathbf{P}_b \cdot \hat{\alpha} \rangle$); D) The polarization of the Σ^+in the β direction ($S_\beta = \langle \mathbf{P}_b \cdot \hat{\beta} \rangle$). The stars ($\star$) are zero recoil values, and circles ($\bullet$) are values obtained by numerical integration of our formulae.

Appendix B
THE STIFF TRACK TRIGGER

As stated in section 3.1.2, the purpose of the STT is to select high momentum tracks traveling down the beam hole. Here we describe in detail the design and implementation of the STT, and the algorithm used in both the summer and winter data sets.

B.1 Hardware

The LeCroy 2366 module is a CAMAC module with 59 front panel input/output (I/O) pin pairs , and contains a programmable XILINX chip.

The chip is programmed using the XILINX software package XACT, along with WORKVIEW, a schematic drawing program. The circuit schematic is created using WORKVIEW (the schematic drawings can be found in Ref. [86]), and XACT translates the drawing into a binary file which is loaded to the XILINX chip via the CAMAC backplane interface. Of the 59 front panel pin pairs, 52 are data inputs, there are also `START` and `CLEAR` inputs as well as `BUSY`, `DONE`, and `DATA` outputs. There is one unused output pin.

Before the 2366 module can be used, the input/output pins must be correctly configured. Front panel pins A1 through A4 are to be configured as output pins.

The front panel pins can be selected as input or output in groups of 4 for pins A1 - A8,B1-B16,C1-C16, and D1-D16. Pins B17,C17, and D17 can each be selected as input or output.

B.2 STT Algorithm (Summer)

When the module is in its quiescent state, `START`, `CLEAR`, and `BTRDVETO` inputs are FALSE, the `BUSY` and `DONE` outputs are FALSE as well, the `DATA` output may or may not be FALSE. When the level 1 trigger is activated, the `START` signal is sent to the STT. When the STT gets the `START` signal, the `BUSY` output becomes TRUE

Front Panel Pin Outputs	Name	Description
A1	BUSY	TRUE while STT is processing
A2	DATA	TRUE if dsl is within bounds
A3	NOT DONE	FALSE CDEL ticks after START
A4	RANDOM	STT Random Accept
Front Panel Pin Inputs	**Name**	**Description**
A5	START	
A6	CLR	clear, resets module
A7	Unused	veto from beam TRD
A8	C0-01	most negative x wire from DC 1
B1-B10	C0-03 - C0-21	other wires from DC 1
B11-B17	C1-01 - C1-13	
C1-C4	C1-15 - C1-21	
C5-C17	C2-01 - C2-25	
D1-D2	C2-27 - C2-29	
D3-D17	C3-01 - C3-29	

Table B.1: Description of STT front panel inputs and outputs. C0 refers to signals mapped from drift chamber 1, etc.

and the 7 bit counter begins counting off 20 MHz (50 ns) ticks. *NOTE: ALL front panel inputs and outputs are inverted at the front panel of the 2366, hence the extra inverters.* The NOT DONE outputs for the 2 STT modules are ORed together. The DATA signals from the two modules are ORed together externally, as are the BUSY and RANDOM outputs. This simplified algorithm just looks for a hit in each chamber.

B.2.1 CAMAC Read/Write Bits

There are 23 bits of STT setup data which are written to the 2366 module through the CAMAC backplane. The quantity ADELAY is the number of (50 ns) ticks to wait before passing the signals from chambers 1 and 2, BDELAY is the number of ticks to wait before passing the signals from chambers 3 and 4 and CDELAY is the number of ticks to wait before the calculation is assumed to finish and the DONE signal becomes TRUE. PRESC is the STT prescale, every PRESCth START produced a TRUE value for RANDOM.

Bits	Quantity	Value Used
CAM_W1 - CAM_W5	ADELAY	28
CAM_W6 - CAM_W10	BDELAY	20
CAM_W11 - CAM_W15	CDELAY	31
CAM_W16 - CAM_W23	PRESC	20

Table B.2: CAMAC Read/Write bits for STT (Summer)

B.3 Integration With the KTeV Trigger System

Each group of 16 wires as shown in figure 3.1 is grouped together on a 17 pin-pair ECL output connector at the front of the KQ/BAN modules (each KQ/BAN module processes 32 chamber wires, so there are 2 such connectors on each KQ/BAN module). The wires we wish to instrument for the STT (figure 3.2) do not map on this grouping, and the STT front panel uses all 17 pin pairs (the 17th pair is ground for the KQ/BAN connectors). We re-map the signal using a wire recombination box, consisting of 17 pin pair ECL connectors on the front and back, with single pair cables connected the two. The re-mapped signals (3 groups of 17 wires for each, with two single pair outputs for the last wire) are routed to the front panel of the STT.

The remaining inputs come from the KTeV trigger system. The `START` signal becomes true whenever an event passes one of the KTeV level 1 triggers. The `CLEAR` input is sent to the STT after all the required level 2 processors have finished, it resets the STT to its quiescent state.

The four outputs from the STT are sent to the KTeV trigger system. The `BUSY` signal becomes true after the STT receives the start signal, and stays on until the `CLEAR` signal is received. When the level 2 trigger is processing an event, the KTeV trigger is inhibited. This is decided by the OR of `BUSY` signals from all the level 2 processors used for the triggers which passed level 1 for that event. The level 2 processor does not decide to pass an event until all the `DONE` signals are received from all the level 2 processors used for the triggers which passed level 1 for that event. The `DATA` and `RANDOM` signals are used by the level 2 trigger as part of the decision criteria.

B.4 STT Algorithm (Winter)

The original STT algorithm was somewhat more complicated. The basic idea of the algorithm is to convert the drift chamber hit pattern in each of the 4 mapping areas to an x position $(x1, x2, x3, x4)$ for the 2 beams. Then the two 2366 modules calculate

$$dsl = (x4 - x3) - (x2 - x1) \tag{B.1}$$

for their respective beams. Since the difference in z (along the beam) between chambers 3 and 4 is the same as the difference in z between chambers 1 and 2, this quantity dsl is proportional to the change in slope, which is in turn proportional to the bending angle for small angles. A valid hit pattern is if only one cell is active, or if only two adjacent cells are active. The inputs for chamber 1 are labeled C0-01 through C0-21, using odd numbers. If only one wire is active, say C0-09, then that number is the position x1. If two adjacent wires are active, then the x position is the average of the two wire numbers, for example, if wires C0-09 and C0-11 are active then x1 is 10.

In figure B.1 we have an example of STT operation. On the right side (R) the particle travels between the 3rd and 4th wires. The x value is calculated to be 6. In most cases, there is a hit in two adjacent wires, rather than a single isolated wire, so the x position is even most of the time. The x position is 10,16 and 16 at chambers 2, 3 and 4, respectively. The change in slope is $(16 - 16) - (10 - 6) = -4$. This is within the bounds of -7 and 8, this event passes the STT (assuming there are no other hits present anywhere in the instrumented regions in the right beam hole). On the left side (L) the particle does not pass through the instrumented region in the upstream chambers, so the STT will automatically not pass that event.

Thus the x position of the particle at the drift chamber is represented as a number between 1 and 21 inclusive. Similarly, the x position at chambers 2 and 3 is represented by a number from 1 to 29 inclusive. If more than two cells on any one chamber are active, or two non-adjacent cells are active, the event is vetoed. Also,

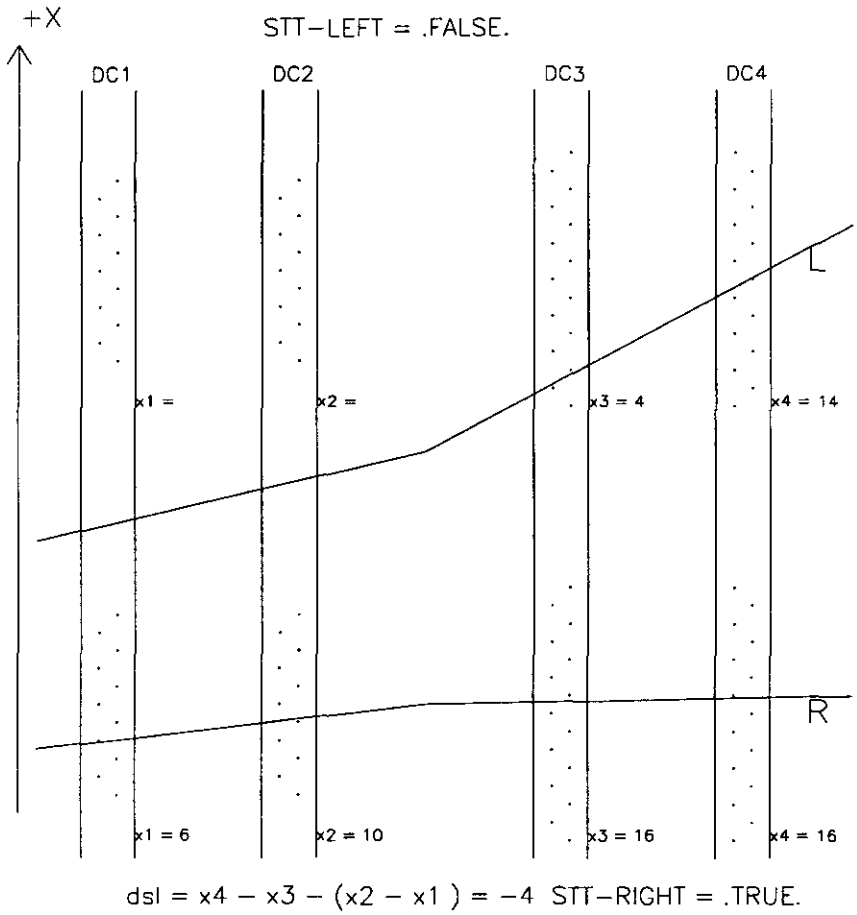

Figure B.1: STT Winter Algorithm

if the output is 0 after a fixed amount of time, the event is vetoed. The quantity *dsl* is calculated as described above (See Figure 1).

If that number is within limits set by the user, and sent to the module via CAMAC, the output DATA is true. The DONE signal becomes true when a fixed amount of time has elapsed, that fixed time is specified by the user.

Chambers 1 and 2 were instrumented with banana boards in the x view, and chambers 3 and 4 were instrumented with kumquat boards in the x view. About $300\,ns$ after `START` becomes true, the drift chamber signals for chambers 2 and 3 reach the STT, and the signals for chambers 0 and 1 reach the STT about $700\,ns$ after `START` becomes true. The algorithm takes an additional $250\,ns$ to complete.

B.4.1 CAMAC Read/Write Bits for Winter STT

There are 23 write bits which are written to the STT module through the CAMAC backplane. The quantity ADELAY is the number of ($50\,ns$) ticks to wait before passing the signals from chambers 1 and 2, BDELAY is the number of ticks to wait before passing the signals from chambers 3 and 4 and CDELAY is the number of ticks to wait before the calculation is assumed to finish and the `DONE` signal becomes TRUE. The quantities LI and UI are the lower and upper bounds (inclusive) for *dsl* defined above.

Bits	Quantity	Value Used
CAM_W1 - CAM_W5	ADELAY	28
CAM_W6 - CAM_W10	BDELAY	20
CAM_W11 - CAM_W15	CDELAY	31
CAM_W16 - CAM_W19	UI	8
CAM_W20 - CAM_W23	LI	-7

Table B.3: CAMAC Read/Write bits for STT (Winter)

For each quantity, the MSB is the highest numbered write bit. UI and LI are integers from -7 to +8, negative integers being represented as 2's complement. When the direction of the magnetic field is reversed the quantities UI and LI must be set to the appropriate new values. Also, by executing a CAMAC read F=0, A=1 on the

STT module, one can see if the bit file is loaded or not. If the .BIT file is loaded into the memory, the CAMAC read will give DATA = 65530. This was be used as a quick check to see if the .BIT file is loaded during the experiment.

Bibliography

[1] E. D. Commins and P. H. Bucksbaum *Weak Interactions of Leptons and Quarks* (Cambridge, 1983).

[2] A. García and P. Kielanowski, *The Beta Decay of Hyperons*, Lecture Notes in Physics Vol. 222 (Springer-Verlag, Berlin, 1985).

[3] E. Swallow, *KTeV Memo 655* (unpublished) (1999).

[4] H. Leutwyler and M. Roos, Z. Phys. C **25**, 91 (1984).

[5] N. Cabibbo, Phys. Rev. Lett. **10**, 531 (1963).

[6] A. Affolder *et al.*, Phys. Rev. Lett. **82**, 3751 (1999).

[7] Yeh *et al.*, Phys. Rev. D **10**, 3545 (1974).

[8] Dauber *et al.*, Phys. Rev. **179**, 1262 (1969).

[9] Hubbard, Ph.D. Thesis, UCRL 11510 (1966).

[10] Particle Data Group, C. Caso *et al.*, Eur. Phys. J. C **3**, 1 (1998).

[11] H. Abele *et al.*, Phys. Lett. B **407**, 212 (1997).

[12] P. Liaud *et al.*, Nucl. Phys. A **612**, 53 (1997).

[13] Yerozolimsky *et al.*, Phys. Lett. B **412**, 240 (1997).

[14] P. Bopp *et al.*, Phys. Rev. Lett. **56**, 919 (1986).

[15] M. Ademollo and R. Gatto, Phys. Rev. Lett. **13**, 264 (1964).

[16] A. Krause, Helv. Phys. Acta **63**, 3 (1990).

[17] J. Anderson and M. A. Luty, Phys. Rev. D **47**, 4975 (1993).

[18] J. Donoghue, B. Holstein and S. Klimt, Phys. Rev. D **35**, 934 (1987).

[19] F. Schlumpf, Phys. Rev. D **51**, 2262 (1995).

[20] L. Carson *et al.*, Phys. Rev. D **37**, 3197 (1988).

[21] A. García, R. Huerta and P. Kielanowski, Phys. Rev. D **45**, 879 (1992).

[22] R. Flores-Mendieta, A. García and G. Sanchez-Colon, Phys. Rev. D **54**, 6855 (1996).

[23] P. G. Ratcliffe, Phys. Rev. D **59**, 014038 (1999).

[24] R. Flores-Mendieta *et al.*, Phys. Rev. D **58**, 094028 (1998).

[25] L. J. Carson, R. J. Oakes and C. R. Wilcox, Phys. Rev. D **33**, 1356 (1986).

[26] J. F. Donoghue and R. Holstein, Phys. Rev. D **25**, 206 (1982).

[27] K. Kubodera *et al.*, Nucl. Phys. A **439**, 695 (1985).

[28] Ø. Lie-Sevendsen and H. Høgaasen, Z. Phys. C **35**, 239 (1987), and Ø. Lie-Sevendsen *ibid*, **31**, 443 (1986).

[29] S. Y. Hseuh, *et. al.*, Phys. Rev. D **38**, 2056 (1988).

[30] A. Alavi-Harati *et al.*, Phys. Rev. Lett. **83** 22 (1999).

[31] A. Alavi-Harati *et al.*, Phys. Rev. Lett. **83** 922 (1999).

[32] J. Adams *et al.*, Phys. Rev. Lett. **80** 4123 (1998).

[33] A. Alavi-Harati *et al.*, Phys. Rev. Lett. **84** 408 (2000).

[34] K. Arisaka, *et al.*, *KTeV Design Report* (unpublished) (1992).

[35] A. Roodman, *Internal KTeV Memo 518* (1997).

[36] R. Coleman, *KTeV Memo 220* (unpublished) (1994).

[37] L. Gibbons, PhD. Thesis, The University of Chicago (1993).

[38] R. Briere, PhD Thesis, The University of Chicago (1995).

[39] G. Graham, PhD Thesis, The University of Chicago (1999).

[40] J. Belz *et al.*, *KTeV Memo 200* (unpublished) (1994).

[41] J. Belz and G. Thomson, *KTeV Memo 157* (unpublished) (1993).

[42] P. Krolak *et al.*, *KTeV Memo 267* (unpublished) (1994).

[43] Y. B. Hsiung, *KTeV Memo 121* (unpublished) (1993).

[44] K. Hanagaki, PhD Thesis, Osaka University (1998).

[45] T. Barker and U. Nauenberg, *KTeV Memo 132* (unpublished) (1993).

[46] K. Hanagaki and T. Yamanaka *KTeV Memo 177* (unpublished) (1993).

[47] A. Roodman *KTeV Memo 209* (unpublished) (1994).

[48] S. Schnetzer *KTeV Memo 191* (unpublished) (1994).

[49] R. Tesarek and S. Schnetzer, *KTeV Memo 215* (unpublished) (1994).

[50] E. Zimmerman, PhD Thesis, The University of Chicago (1999).

[51] T. Alexopoulos and A. Erwin, *KTeV Memo 264* (unpublished) (1994).

[52] C. Bown *et al*, Nucl. Inst. and Meth. A **369**, 248 (1996).

[53] S. Bright, *KTeV Memo 369* (unpublished) (1996).

[54] N. Solomey *et al*, Nucl. Inst. and Meth. A **367**, 252 (1995).

[55] P. Shawhan, *KTeV Memo 328* (unpublished) (1995).

[56] J. Graham, *KTeV Memo 467* (unpublished) (1997).

[57] C. Qiao, *KTeV Memo 470* (unpublished) (1997).

[58] A. Roodman, *Internal KTeV Memo 317* (1995).

[59] K. Senyo, PhD Thesis, Osaka University (1999).

[60] L. Pondrom, *Hyperon Experiments at Fermilab* , Phys. Rep. **122**, 1 (1985).

[61] E. J. Ramberg *et al.*,Phys. Lett. B **338**, 403 (1994).

[62] A. Alavi-Harati *et al.*, in preparation.

[63] J. Donoghue, E. Golowich and B. Holstein, *Dynamics of the Standard Model* , Cambridge Monographs on Particle Physics, Nuclear Physics and Cosmology, Vol. 2 (Cambridge University Press, Cambridge, 1992).

[64] V. Fanti *et al.*, Eur. Phys. J. C **12**, 69 (2000).

[65] A. Sirlin, Phys. Rev. **164**, 1767 (1967).

[66] A. García, Phys. Rev. D **25**, 1348 (1982).

[67] A. García, Phys. Rev. D **28**, 1659 (1983).

[68] A. Sirlin, Phys. Rev. Lett. **32**, 966 (1974).

[69] K. Tóth *et al.*, Phys. Rev. D **33**, 3306 (1986).

[70] F. Glück and K. Tóth *et al.*, Phys. Rev. D **46**, 2090 (1992).

[71] A. García and M. Maya, Phys. Rev. D **17**, 1376 (1978).

[72] D. M. Tun *et al.*, Phys. Rev. D **40**, 2967 (1989).

[73] R. Flores-Mendieta *et al.*, Phys. Rev. D **55**, 5702 (1997).

[74] S. Bright *et al.*, Phys. Rev. D **60**, 117505 (1999).

[75] J. Dworkin *et al.*, Phys. Rev. D **41**, 780 (1999).

[76] P. Shawhan, Ph.D. Thesis, University of Chicago (1999).

[77] A. Alavi-Harati, PhD Thesis, The University of Wisconsin (1999).

[78] W. Alles, Nuovo Cimento **26**, 1429 (1962).

[79] P. S. Desai, Phys. Rev. **179**, 1327 (1969) and references therein.

[80] V. Linke, Nuc. Phys. **B12**, 669 (1969).

[81] H. Primakoff, Rev. Mod. Phys. **31**, 802 (1959).

[82] A. Fujii and H. Primakoff, Nuovo Cimento **12**, 327 (1959).

[83] J. M. Watson and R. Winston, Phys. Rev. **181**, 1907 (1969). Their normalization convention differs from ours in that each spinor has the normalization $\sqrt{E+m}$ factored out into their phase space term. Also, in order to make their phase space correct to second order, one must replace M_b/M_B with $(E_b + M_b)/2M_B$.

[84] We employ the metric and γ matrix conventions of Ref. [2], so that g_1/f_1 is **positive** for neutron beta decay. They differ from those of J. D. Bjorken and S. D. Drell,*Relativistic Quantum Mechanics*, (McGraw-Hill, New York, 1964) only in that γ_5 has the opposite sign, and that there is no i in the definition of $\sigma_{\alpha\beta}$.

[85] S. Weinberg, Phys. Rev. **115**, 481 (1959).

[86] S. Bright *KTeV Memo 683* (unpublished) (2000).